Heavy-quark Effects in Factorization and Resummation

Dissertation

zur Erlangung des Doktorgrades an der Fakultät für Mathematik, Informatik und Naturwissenschaften

Fachbereich Physik

der Universität Hamburg

vorgelegt von Rebecca Olga von Kuk

Hamburg 2025

Gutachter:innen: Dr. Frank Tackmann

Prof. Dr. Gudrid Moortgat-Pick

Zusammensetzung der Prüfungskommission: Dr. Frank Tackmann

Prof. Dr. Gudrid Moortgat-Pick

Prof. Dr. Jürgen Reuter

Prof. Dr. Christian Schwanenberger

Prof. Dr. Sven-Olaf Moch

Vorsitzender der Prüfungskommission: Prof. Dr. Sven-Olaf Moch

Datum der Disputation: 06.05.2025

Vorsitzender des Fach-Promotionsauschusses PHYSIK: Prof. Dr. Wolfgang J. Parak

Leiter des Fachbereichs PHYSIK: Prof. Dr. Markus Drescher

Dekan der Fakultät MIN: Prof. Dr.-Ing. Norbert Ritter

Eidesstattliche Versicherung

Hiermit versichere ich an Eides statt, die vorliegende Dissertationsschrift selbst verfasst und keine anderen als die angegebenen Hilfsmittel und Quellen benutzt zu haben.

Sofern im Zuge der Erstellung der vorliegenden Dissertationsschrift generative Künstliche Intelligenz (gKI) basierte elektronische Hilfsmittel verwendet wurden, versichere ich, dass meine eigene Leistung im Vordergrund stand und dass eine vollständige Dokumentation aller verwendeten Hilfsmittel gemäß der guten wissenschaftlichen Praxis vorliegt.

Ich trage die Verantwortung für eventuell durch die gKI generierte fehlerhafte oder ve	erzerrte
Inhalte, fehlerhafte Referenzen, Verstöße gegen das Datenschutz- und Urheberrecht oder P	lagiate.

Hamburg, den 21.03.2025	
0,	
	Rebecca von Kuk

Abstract

In this thesis, we study different aspects of heavy-quark effects in factorization and resummation using the methods of effective field theories. As the quark masses are much lighter than the hard scale of processes at the LHC, they are considered subleading and usually neglected. However, with high-precision measurements from the experiments at the LHC more precise theory predictions are needed and quark-mass effects can no longer be ignored. In this thesis we study two different aspects of heavy-quark effects.

One part of this thesis focuses on quark-mass effects in the Higgs transverse momentum spectrum. This kinematic distribution is of particular interest as its shape can be used extract the quark Yukawa couplings appearing in Higgs production processes. We present a new state-of-the-art prediction for quark initiated Higgs production where we consider bottom, charm and strange quarks in the initial state. We provide results at three-loop order in resummed perturbation theory and match this prediction to an approximate next-to-next-to-next-to-leading order prediction. Moreover, we study the resummation of transverse variables in the Monte Carlo event generator GENEVA using one-jettiness, \mathcal{T}_1 , and the transverse momentum, q_T , as resolution variables. This presents a first step towards an NNLO prediction matched to a parton shower for this process. Further, we study bottom-mass effects in the transverse momentum spectrum for the gluon fusion process. In gluon fusion, the dominant contribution comes from a massive top-quark loop, with contributions from other quarks often neglected. However, to fully exploit high-precision measurements at the LHC, it becomes essential to account for subleading effects. In particular, the contribution from the bottom quark can no longer be ignored. The interference between the top- and bottom-quark contributions plays a significant role and is crucial for measuring the bottom-Yukawa coupling in Higgs production. So far these effects have only been studied for the form factor where we have two scales, the Higgs mass and the bottom-quark mass. The measurement of the transverse momentum introduces a third scale to the problem which makes the factorization much more subtle: the bottom and the Higgs mass of course still have the same scaling as in the form factor calculation but the transverse can have different scalings. Hence, we have to consider different kinematic regimes and write down a factorization theorem for each of them.

In the second part, we consider transverse momentum dependent (TMD) fragmentation functions (FFs) for heavy quarks. The heavy-quark mass provides a perturbative scale in the otherwise nonperturbative dynamics of the fragmentation process. We demonstrate that applying boosted Heavy-Quark Effective Theory to TMD FFs gives rise to novel, universal matrix elements describing the nonperturbative transverse dynamics of light QCD degrees of freedom in the presence of a heavy quark. We further calculate all TMD parton distribution functions for the production of heavy quarks from polarized gluons within the nucleon. We use these results to make phenomenological predictions for cross sections in e^+e^- collisions and semi-inclusive deep inelastic scattering, which are relevant for existing B-factories and the future EIC, respectively. Additionally we calculate all TMD FFs involving heavy quarks and the associated TMD matrix element in heavy-quark effective theory to next-to-leading order in the strong coupling.

Zusammenfassung

In dieser Arbeit werden verschiedene Aspekte von Quarkmasseneffekten in Faktorisierung und Resummierung unter Verwendung von effektiven Feldtheorien untersucht. Da Quarkmassen deutlich leichter sind als die typischen Energieskalen am LHC, gelten sie als unterdrückt und werden normalerweise vernachlässigt. Mit den Hochpräzisionsmessungen am LHC werden jedoch immer genauere Theorievorhersagen benötigt und Quarkmasseneffekte werden relevant. Diese Arbeit beschäftigt sich mit zwei unterschiedlichen Aspekten von Quarkmasseneffekten.

Ein Teil dieser Arbeit konzentriert sich auf Quarkmasseneffekte im Transversalimpulsspektrum des Higgs-Bosons. Diese kinematische Verteilung ist wichtig, da sich aus ihrer Form die Quark-Yukawa-Kopplungen extrahieren lassen, die in Higgs-Produktionsprozessen auftreten. Diese Arbeit enthält eine neue, hochpräzise Vorhersage für Higgs-Produktion durch Quarkannihilation, bei der Bottom-, Charm- oder Strange-Quarks als Anfangszustände betrachtet werden. Die Präzision der Vorhersage für dieses Spektrum wird bis zur dritten Ordnung in der starken Kopplung in resummierter Störungstheorie berechnet. Diese Vorhersage wird mit einer genäherten Vorhersage der nächst-zu-nächst-zu-führenden Ordnung kombiniert. Darüber hinaus wird die Resumierung von transversalen Variablen mit dem Monte-Carlo-Eventgenerator GENEVA untersucht. Hier werden die 1-Jettiness-Variable, \mathcal{T}_1 , und der Transversalimpulse, q_T , als Auflösungsvariablen genutzt. Dies ist ein erster Schritt in Richtung einer NNLO Vorhersage für diesen Prozess, die mit einem Partonenschauer kombiniert ist. Darüber hinaus werden Bottom-Quark-Masseneffekte im transversalen Impulsspektrum für den Gluonenfusionsprozess untersucht. Der dominante Beitrag im Gluonfusionsprozess kommt von einer schweren Top-Quark-Schleife. Hierbei werden die Beiträge von anderen Quarks meistens vernachlässigt. Um jedoch die Hochpräzisionsmessungen am LHC voll ausschöpfen zu können, ist es wichtig auch unterdrückte Effekte zu berücksichtigen. Insbesondere der Beitrag des Bottom-Quarks sollte in Zukunft miteinbezogen werden. Die Interferenz zwischen den Beiträgen des Top- und des Bottom-Quarks spielt eine wichtige Rolle und hat einen nicht zu vernachlässigenden Beitrag für die Messung der Bottom-Yukawa-Kopplung in Higgs-Produktionsprozessen. Bisher wurden diese Effekte nur für den Formfaktor untersucht, bei dem zwei Skalen relevant sind: die Higgs-Masse und die Bottom-Quark-Masse. Die Messung des transversalen Impulses fügt eine dritte Skala hinzu, die die Faktorisierung wesentlich komplizierter macht: Die Bottom-Quark und die Higgs-Masse haben immer noch das gleiche Verhältnis wie in der Formfaktorberechnung, aber der Transversalimpuls kann unterschiedliche Skalierungen haben. Daher müssen verschiedene kinematische Regime betrachtet werden, welche je ein Faktorisierungtheorem benötigen.

Der zweite Teil beschäftigt sich mit transversalimpulsabhängigen (TMD) Fragmentierungsfunktionen (FFs) für massive Quarks. Die Masse der Quarks fungiert als perturbative Skala im sonst nicht-perturbativen Fragmentierungsprozess. Die Anwendung von boosted Heavy-Quark Effective Theory auf TMD FFs führt zu neuen, universellen Matrixelementen, die die nicht-perturbative Dynamik von leichten Freiheitsgraden in Anwesenheit eines massiven Quarks beschreiben. Außerdem werden alle TMD-Partondichtefunktionen für die Produktion massiver Quarks aus einem polarisierten Gluon im Nukleon berechnet. Diese Ergebnisse werden verwendet um phenomenologische Vorhersagen für Wirkungsquerschnitte in e^+e^- -Kollisionen und in semi-inklusiver tiefinelastischer Streuung. Diese können für B-Fabriken sowie den zukünftigen EIC genutzt werden. Darüber hinaus werden alle TMD FFs massiver Quarks sowie die entsprechenden TMD Matrixelemente zur nächst führenden Ordnung in der starken Kopplung berechnet.

List of Publications

Journal articles:

- [1] R. von Kuk, J. K. L. Michel and Z. Sun, Transverse momentum-dependent heavy-quark fragmentation at next-to-leading order, JHEP 07 (2024) 129, arXiv: 2404.08622
- [2] P. Cal, R. von Kuk, M. A. Lim and F. J. Tackmann, q_T spectrum for Higgs boson production via heavy quark annihilation at $N^3LL'+aN^3LO$, Phys. Rev. D. 110(2024) 076005, arXiv: 2306.16458
- [3] R. von Kuk, J. K. L. Michel and Z. Sun, Transverse momentum distributions of heavy hadrons and polarized heavy quarks, JHEP 09 (2023) 205, arXiv: 2305.15461

Preprint:

[4] R. von Kuk, K. Lee, J. K. L. Michel and Z. Sun, Towards a Quantum Information Theory of Hadronization: Dihadron Fragmentation and Neutral Polarization in Heavy Baryons, arXiv: 2503.22607

In preparation:

- [5] R. von Kuk, J. K. L. Michel, I. W. Stewart, Z. Sun and F. J. Tackmann, Bottom mass effects in Higgs production at small q_T
- [6] A. Gavardi, R. von Kuk and M. A. Lim, Resumming transverse observables for NNLO+PS matching in GENEVA

This thesis is based on refs. [1-3,5,6] reflecting the author's contribution.

Contents

1	Intr	roduction	1
2	The	eoretical Framework	9
	2.1	Basics of QCD	9
	2.2	Higgs production at hadron colliders	13
		2.2.1 Higgs production channels at hadron colliders	13
	2.3	99 1	17
	2.4		19
		· · · · · · · · · · · · · · · · · · ·	21
		2.4.2 Symmetries of SCET	24
			28
			29
			31
	2.5		33
	_		33
		0 0	35
			37
			40
	2.6	·	42
			42
			43
		8 1	45
		0	46
		2.011 This processes at comment 1.11.11.11.11.11.11.11.11.11.11.11.11.1	10
3	$Th\epsilon$	q_T spectrum in Higgs Production via Quark Annihilation	49
	3.1	Motivation	49
	3.2	Resummed prediction	50
		3.2.1 Canonical scales and resummation in b_T space	51
		3.2.2 Profile scales and matching to fixed order	52
		3.2.3 Perturbative uncertainties	53
	3.3	Fixed-order contributions	54
		3.3.1 LO_1 and NLO_1	55
		3.3.2 Estimation of the matching uncertainties	60
		9	64
			66
	3.4	**	68
	3.5		73

${\bf Contents}$

4	\mathbf{Res}	summing transverse observables in GENEVA	7 5
	4.1	Motivation	75
	4.2	The GENEVA method	76
	4.3	One-jettiness with generalized measures	79
	4.4	Results	81
		4.4.1 Validation	81
		4.4.2 Resummed q_T and \mathcal{T}_1 distributions	81
	4.5	Summary and Outlook	83
5	Bot	tom Mass Effects in the Higgs Production via Gluon Fusion	85
	5.1	Motivation	85
	5.2	Operator basis and calculation of the LO contribution	87
		5.2.1 Leading-order collinear contribution	88
		5.2.2 Soft LO_0	92
		5.2.3 Leading-order hard contribution	93
		5.2.4 Combine results	94
	5.3	Bare factorization theorems	95
		5.3.1 Factorization theorem for $q_T \ll m_b \ll m_H$	95
		5.3.2 Factorization theorem for $q_T \sim m_b \ll m_H$	96
		5.3.3 Factorization theorem for $m_b \ll q_T \ll m_H$ and $m_b \ll m_H \lesssim q_T$	98
	5.4	Collinear emission diagrams	98
		5.4.1 Triple-gluon-vertex emission diagrams	100
		5.4.2 Vertex emission diagrams	101
		5.4.3 Loop emission diagrams	104
	5.5	Cancellation of endpoint divergences	106
		5.5.1 Collinear emission	107
		5.5.2 Soft emission	107
	5.6	Summary	108
6	Tra	nsverse Momentum Distributions of Heavy Quarks and Heavy Hadrons	109
	6.1	Motivation	109
	6.2	TMDs for heavy quark fragmentation into a heavy hadron	110
		6.2.1 Calculational setup and parametric regimes	110
		6.2.2 boosted Heavy-Quark Effective Theory	111
		6.2.3 Calculating TMD FFs from bHQET for $\Lambda_{\rm QCD} \lesssim k_T \ll m$	112
		6.2.4 Matching TMD FFs onto bHQET for $\Lambda_{\rm QCD} \ll m \lesssim k_T$	117
		6.2.5 Consistency between regimes for $\Lambda_{\rm QCD} \ll k_T \ll m$	
		6.2.6 Model functions and numerical results	
	6.3	Polarized heavy-quark TMD PDFs	122
		6.3.1 Calculational setup	122
		6.3.2 Matching onto twist-2 collinear PDFs	123
		6.3.3 One-loop evaluation of matching coefficients	
		6.3.4 Consistency with the light-quark limit	
		6.3.5 Numerical results for TMD PDFs	
	6.4	Towards phenomenology with heavy-quark TMDs	
		6.4.1 Accessing heavy-quark TMDs in e^+e^- collisions	
		6.4.2 Accessing heavy-quark TMDs at the future EIC	

	6.5	Summary	. 137
7	TM	D heavy-quark fragmentation at NLO	141
	7.1	Motivation	. 141
	7.2	Theoretical framework	. 142
		7.2.1 Heavy-quark TMD FFs	. 142
		7.2.2 Nonvalence contributions	. 143
		7.2.3 bHQET fragmentation factors and the large-mass limit	. 143
		7.2.4 Consistency conditions in the light-quark limit	. 144
	7.3	Partonic heavy-quark TMD fragmentation at NLO	. 145
		7.3.1 Bare real-emission diagrams and distributional expansion	. 146
		7.3.2 Virtual contributions and UV renormalization	
		7.3.3 Cumulant space and position space results	
		7.3.4 Nonvalence channels at $\mathcal{O}(\alpha_s)$	
	7.4	Consistency checks in the large and small-mass limits	
	-	7.4.1 Large-mass limit	
		7.4.2 Small-mass limit	
	7.5	Summary	
	1.0		. 102
8	Con	nclusion	153
\mathbf{A}	Not	ation and conventions	157
	A.1	Lightcone coordinates	. 157
	A.2	Fourier transforms	. 158
В	Per	turbative ingredients	159
	B.1	Anomalous dimensions	. 159
	B.2	Hard function and quark scalar-current matching coefficient	. 160
		B.2.1 Quark scalar-current matching coefficient	. 161
	B.3	Heavy and light matching coefficients	. 162
		B.3.1 Large-mass limit	. 162
		B.3.2 Small-mass limit	. 163
\mathbf{C}	Plus	s distributions	165
D	\mathbf{Add}	litional figures	167
${f E}$	Fey	nman rules	169
_	<i>C</i> 1		1 71
\mathbf{F}		culational details	171
	F.1	Leading-order soft contribution	
	F.2	Leading-order hard contribution	
	F.3	NLO loop emission diagrams	. 173
Re	efere	nces	176
Ac	knov	wledgements	199

Chapter 1

Introduction

The Standard Model of particle physics (SM) [7–10] is the current theory describing all known elementary particles as well as their interactions. With the discovery of the Higgs boson in 2012 the by the ATLAS and CMS experiments [11,12] at the Large Hadron Collider (LHC) the last missing piece of the Standard Model was found. This marks a major success in theoretical and experimental particle physics as the Higgs boson was postulated 50 years before its discovery [13–18]. Remarkably, the Higgs discovery completed the SM after so many years and is celebrated as one of the greatest successes of particle physics but, on the other hand, a non-discovery of the Higgs boson could have meant the end of the Standard Model: In the SM contributions of the Higgs boson are needed in order to cancel divergences in W boson scattering in order to guarantee the unitarity of the theory which makes the Higgs boson such a crucial component.

After the Higgs discovery, there are still many open questions which cannot be addressed within the Standard Model, such as the existence and origin of Dark Matter (DM). As far as we know, DM particles do not share any interaction (besides gravitational) with SM particles. Therefore, DM particles are invisible or "dark" for SM particles. From astrophysical observables, we know that ordinary matter only makes up for a minor contribution of the total matter density of the universe whereas the majority (84.4%) comes from DM [19]. There exist multiple Dark Matter candidates and even alternative approaches to explain the overwhelming empirical evidence of Dark Matter. However, as of today none of the searches for DM particles have been successful and its origin remains unknown. Also, the Standard Model neither includes a quantum description of gravity nor masses for neutrinos which both clearly exist. It might be less apparent for the neutrino masses, but their masses are required to explain neutrino oscillation [20, 21]. The SM also fails to explain the matter-antimatter asymmetry which is for the reason for our whole existence.

To tackle these issues, we need *New Physics* or physics beyond the Standard Model (BSM). For a long time supersymmetry [22] was a promising candidate as it does not just provide us with whole set of possible DM particles but also offers an elegant solution to some of the aesthetic problems of the SM such as the hierarchy problem. However, sadly or maybe even shockingly for some in the physics community, no supersymmtric particles were found at the LHC. Not only were no new particles found, the SM also seems to pass every test. Neither the experiments at the LHC nor other experiments have been able to find any significant deviations from the SM predictions to this day. Given this lack of direct evidence for new particles, a promising avenue to discover BSM physics is to compare experimental measurements and theoretical predictions and look for even the tiniest deviations from the SM expectations. This requires equally precise

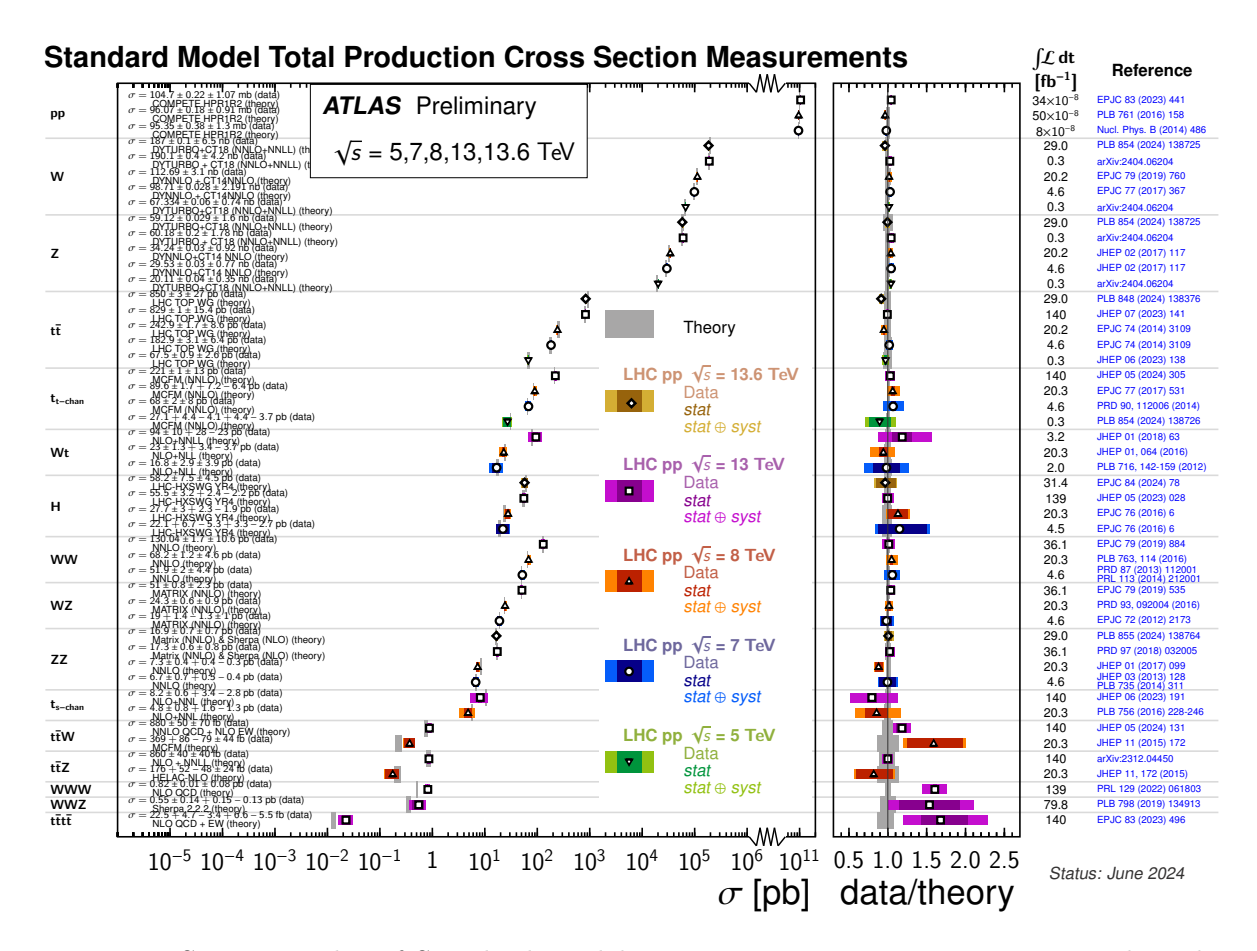


Figure 1.1: Summary plot of Standard Model cross section measurements compared to the corresponding theory uncertainty. The right panel shows the comparison to the corresponding theory uncertainties. The theory uncertainties are shown by gray whereas the experimental uncertainties are shown in different colors corresponding to different center of mass energies \sqrt{s} . Figure taken from ref. [25]

experimental measurements and theoretical calculations. As the experiments provide more precise measurements and have been successful in reducing their uncertainties, it is paramount to likewise increase the precision of theoretical calculations to fully exploit the experimental data. Indeed fully-differential calculations at fixed-order in perturbation theory have reached N³LO accuracy for simple processes [23, 24].

In figure 1.1, various measurements of Standard Model cross section by the ATLAS collaboration are shown. The cross sections in the lower part of the plot correspond to rather complicated processes. They are not only difficult to calculate but also hard to measure. Thus, both, theory and experimental uncertainties are rather large. In order to make sense of a measurement both uncertainties should be of a similar size. Otherwise it is impossible to tell whether there is a deviation from the SM prediction or the measurement is just not precise enough. In the upper half of the plot, some of the processes are measured to extremely high precision such that there is no visible uncertainty. The theory prediction, on the hand, is still visible and more precise predictions are needed.

Coming back to the Higgs boson as the youngest SM particle, precise measurements of its properties are essential to establish its role in the SM. So far the four main production mechanisms

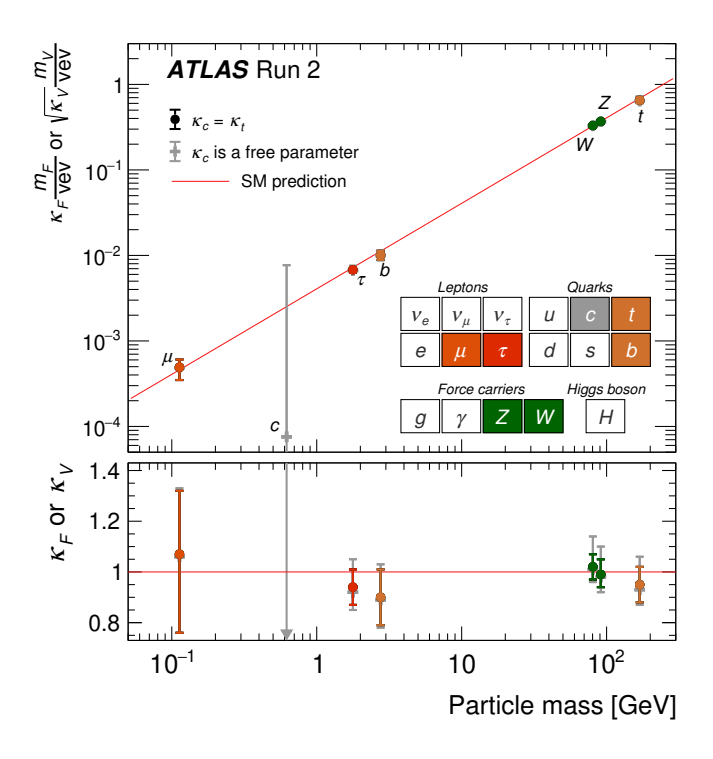


Figure 1.2: Summary of Higgs couplings measurements by the ATLAS collaboration. The red diagonal line corresponds to the Standard Model prediction of the couplings. Figure taken from ref. [30]

– gluon fusion, vector boson fusion, Higgsstrahlung, and top-quark pair associated production – have been observed experimentally [11,12,26–28] and the Higgs boson mass has been measured to high precision [29]

$$m_H = 125.20 \pm 0.11 \, \mathrm{GeV}.$$

The couplings of the Higgs boson to other particles are precisely predicted in the SM and are proportional to the particle mass. Figure 1.2 shows the status of the Higgs coupling measurements by the ATLAS collaboration [30]. In this figure, we can see that all coupling measurements are consistent with the SM prediction within the uncertainties. However, some of the couplings have not been measured yet or have large uncertainties.

In the SM, the couplings of the Higgs boson to fermions, i.e. the Yukawa couplings, y_F , are given by $y_F^{\rm SM} \equiv m_F/v$, where v denotes the Higgs vacuum expectation value. This implies that the measurement of the Yukawa couplings to the heavy fermions is within the reach of the LHC. In fact, the couplings for the top quark, bottom quark, and τ lepton have already been measured [30,31] and are also shown in figure 1.2. The bottom-quark Yukawa coupling y_b is particularly interesting as some BSM models, such as the two Higgs doublet model or the minimally supersymmetric SM, predict an enhanced bottom-Yukawa coupling relative to its SM value [32,33].

Higgs Production via Quark Annihilation

The bottom Yukawa coupling has been measured in $H \to b\bar{b}$ decays [26,34], which is challenging as the identification of the b-quarks requires b-tagging. Here a specific property of b-quarks is exploited: b-quarks have a relatively long lifetime and travel within in the detector before they decay. This produces a secondary vertex which is displaced from the vertex of the actual collision and can be reconstructed. This method combined with multivariate analysis techniques allows for efficient b-jet identification. However, processes featuring b-jets – or really any color-charged final state – often come with multiple jets and the measurement is still very challenging. First measurements of the charm Yukawa y_c in $H \to c\bar{c}$ decays have also been achieved [35, 36] but present an even greater challenge [37]. Therefore an alternative approach to measure the heavy-quark Yukawa couplings is of great interest.

Of course, the Higgs boson can also be produced via quark Yukawa interactions where the corresponding Yukawa coupling could – in principle – also be measured. However, a direct measurement of Higgs production in association with a $b\bar{b}$ pair seems hopeless [38]. An alternative approach is to study the Higgs transverse momentum spectrum for quark initiated Higgs production $(q\bar{q} \to H)$. This allows for a discrimination of gluon and quark induced channels in the initial state [39] as the radiation pattern for different initial states yield different shapes for the transverse momentum spectrum of the recoiling Higgs boson. Moreover, the different quark channels also exhibit different shapes due to the underlying quark parton distribution functions (PDFs)¹. The shape of the spectrum is thus sensitive to the quark-channel which can be used to fit the quark Yukawa couplings from the initial state [40,41]. With sufficient statistics, it might even be possible to obtain constraints on the strange Yukawa coupling.

In refs. [42, 43], ATLAS and CMS have demonstrated that it is already possible with existing data to obtain meaningful constraints on y_c and y_b from just the shape of the Higgs q_T spectrum. The corresponding illustration from the ATLAS collaboration is given in figure 1.3. To fully exploit this possibility, precise predictions of the q_T spectrum for both gluon fusion and quark annihilation are essential. At small $q_T \ll m_H$, logarithms of q_T/m_H grow large and spoil the convergence of the perturbative series. These logarithms need to be resummed to all orders to arrive at a sensible prediction. Currently, a N³LL'+N³LO resummed prediction exists for the Higgs q_T spectrum in gluon fusion [44], which was used in ref. [42], and predictions of similar accuracy also exist for the Drell-Yan process [45–49]. However, no prediction of similar accuracy exists for $q\bar{q} \to H$, which so far has only been resummed to NNLL+NNLO accuracy [50,51]. Parts of this thesis are dedicated to providing an analogous prediction for the quark-induced processes.

Event generators

High precision predictions are essential for the success of the experimental program at the LHC. However, the experimentally measured final states rarely correspond directly to the predicted distribution. In reality, the final states of the hard interaction hadronize and form collimated sprays of particles (jets) before they are detected. Comparing these measurements to a prediction at parton-level requires complicated – if at all possible – unfolding of detector effects as well as decay and shower processes [52]. Event generators simulate the full process from the hard interaction to final states that can be detected at colliders and therefore provide a realistic

¹PDFs describe the probability to find a parton (a gluon or quark) with a given momentum fraction of its parent's hadron momentum.

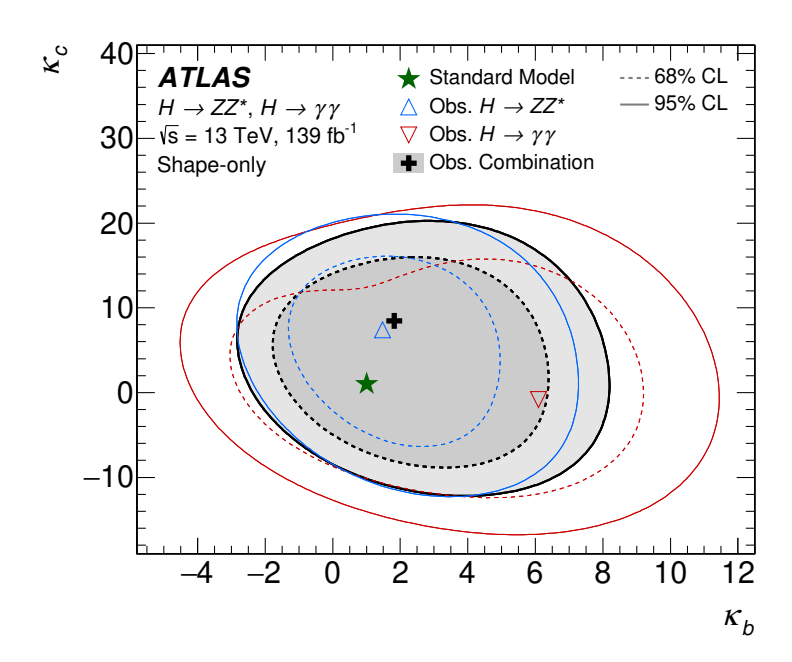


Figure 1.3: Coupling modifiers. The so-called coupling modifiers κ_c and κ_b are given by $\kappa_q = y_q/y_q^{\rm SM}$ where y_q is the measured value of the coupling and $y_q^{\rm SM}$ is the SM prediction. We therefore expect $\kappa_q = 1$ in the Standard Model. Figure taken from ref. [42]

picture of what is happening in a particle collision. Partons originating from a hadron collision emit high energetic quarks and gluons which keep emitting more radiation. An exact description of these emissions is in principle possible but a calculation would be intractable. These particles eventually hadronize in a non-perturbative process and form jets. Consequently, hadronization cannot be described by the methods of perturbation theory. The evolution from a single parton to a jet is modeled by parton showers which provide an approximate description of the underlying partonic processes. Event generators thus provide an important bridge between high precision calculations of the underlying hard processes and the final states measured at experiments.

Factorization and sub-leading power effects

In high energy physics, we often use factorization as a tool to factorize physics at different scales. For instance, if we have a high scale Q and low scale m with $m \ll Q$, the cross section can be written as

$$\sigma(m,Q) = H(Q,\mu)F(m,\mu) + \mathcal{O}\left(\frac{m}{Q}\right), \tag{1.1}$$

where we introduced an additional scale μ in order to factorize the cross section. The scale dependence between the functions $H(Q,\mu)$ and $F(m,\mu)$ has to cancel such that the cross section is independent of μ . Now, all physics at the high scale is captured by $H(Q,\mu)$ and physics at the low scale is described by $F(m,\mu)$. In general the cross section $\sigma(m,Q)$ can contain large logarithms of m/Q which spoil the convergence of the perturbative series. Factorization is the first step towards resumming these logarithms which then restores the convergence of the cross section and yields a meaningful prediction.

Chapter 1 – Introduction

The first term in the sum of eq. (1.1) is referred to as leading power whereas the corrections of $m/Q \ll 1$ are suppressed due to the small size of m relative to Q. Usually it is sufficient to include the leading power contribution. However, with this unprecedented amount of precision data provided by the LHC increasingly precise predictions are needed and often sub-leading power effects can no longer be ignored. Unfortunately, calculations at sub-leading power are often tedious and include some undesired features such as endpoint divergences. These divergences arise at the level of the cross section and have to be regulated and canceled carefully. In this thesis, we will often consider heavy-quark effects which are in fact subleading: to good approximation quarks can be treated as massless particles in high energy collision where a typical energy scale is $Q \approx 100 \, \text{GeV}$ while the bottom-quark mass is roughly $m_b = 5 \, \text{GeV}$. However, when considering the transverse momentum spectrum for quark initiated Higgs production, we will see that quark mass effects become relevant at this level of precision and should in fact be included.

Hadronization

So far, we have mostly elaborated on the bigger picture: short-comings of our underlying theory, the Standard Model. However there are of course other puzzles in particle physics which might not question our understanding of the underlying theory but also affect our understanding of nature. A prominent example is hadronization – the process describing how color charged partons (gluons and quarks) from high energy collisions form color neutral bound-states. These bound-states are called hadrons. The most famous hadrons are protons and neutrons that together with electrons form atoms and, thus, the matter that we encounter in our every day lives. The Standard Model provides us with a description of quark and gluon interactions which is referred to as Quantum Chromodynamnics (QCD). The strong coupling constant q determines the strength of the interactions between quarks and gluons. In contrast to the name the coupling constant is in fact not constant but evolves with the energy scale of the considered process. At low energies around 100 MeV the coupling constant diverges and the coupling becomes infinitely strong. This phenomenon is called confinement and leads to the hadronization of quarks and gluons. Hence, we know that hadronization is happening but a fundamental understanding of how quarks and gluons are fragmenting into hadrons cannot be gained from perturbative calculations within the Standard Model. There exist different approaches of hadronization models but an understanding from first principles remains elusive [53].

On the way to gain a better understanding of the fragmentation process heavy-quarks like charm and bottom quarks can play a vital role. For light quark fragmentation, we have multiple light hadrons after the fragmentation process but it is unclear which hadron contains the parent quark. This is illustrated in figure 1.4a where the gray blob represents the hadronization and the orange ellipses represent light hadrons. These additional hadrons originate from QCD radiation that the parent light quark emitted during the fragmentation process. The heavy quark fragmentation process is shown in figure 1.4b. In this case, there will also be additional QCD radiation which eventually fragments into light hadrons. However, the heavy-quark exists through the whole fragmentation process and will fragment into a heavy hadron which can be identified. Further, the mass of the heavy quark provides a perturbative scale on the otherwise non-perturbative dynamics of hadronization. For these reasons, heavy quarks are ideal to study the hadronization process. In this thesis, we will use the framework of transverse-momentum distribution for heavy quarks for the first time.

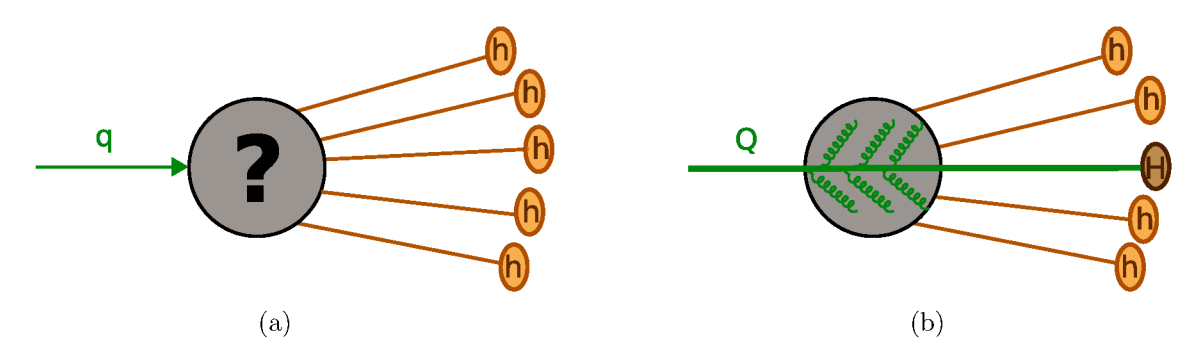


Figure 1.4: Illustration of light (a) and heavy (b) quark fragmentation. In the light quark case it is not possible to identify the hadron containing the parent quark. In the heavy quark case on the other hand, the quark exists throughout the full fragmentation process and fragments into a heavy hadron which can be identified.

Outline

This thesis is structured as follows. Chapter 2 gives a brief overview of the theoretical foundations of this thesis beginning with a review of QCD. We also discuss the main features and important properties of Higgs boson production at colliders including a discussion of soft and collinear limits of QCD radiation. Next, we give a short introduction to effective field theories where we focus on Soft-Collinear Effective field theory (SCET). We also discuss the factorization and resummation of processes at colliders focusing on the transverse momentum as an observable. In chapter 3, we present a new state-of-the-art prediction for the transverse momentum spectrum of quark initiated Higgs production at three-loop order in resummed perturbation theory matched to an approximate N³LO prediction. We introduce a decorrelation method to achieve a sensible approximation at this high order. Further, the standard procedure for matching the resummed and fixed-order contributions leads to unphysically large uncertainties –especially for the $b\bar{b} \to H$ channel. To mitigate this issue, we employ a modified matching procedure which is discussed in detail. Chapter 4 provides the first steps towards an NNLO+PS prediction for the $q\bar{q} \to H$ process using transverse resolution variables. In chapter 5, we consider bottom-mass effects in the transverse momentum spectrum for Higgs production via gluon fusion. These mass-effects appear at next-to-leading power and, so far, have only been considered for the form factor with just a Higgs boson in the final state. The emitted gluon introduces an additional scale, the transverse momentum, making it a three-scale problem with $m_b \ll m_H$, where m_b is the bottom mass and m_H is the Higgs mass. As a result, we need to consider different regimes and derive a factorization formula for each case. A major challenge in this chapter is the subtle cancellation of endpoint divergences between the soft and collinear sectors. In chapter 6, we present the first study of heavy-quark transverse momentum dependent (TMD) fragmentation functions (FFs). We also calculated all TMD parton distribution functions for the production of heavy quarks from polarized gluons within the nucleon. Moreover, we use these results to make phenomenological predictions for cross sections in e^+e^- collisions and semi-inclusive deep inelastic scattering, which are relevant for existing B-factories and the future EIC, respectively. In chapter 7, we calculate all TMD FFs involving heavy quarks and the associated TMD matrix element in heavy-quark effective theory to next-to-leading order in the strong coupling. We conclude in chapter 8.

Chapter 2

Theoretical Framework

In this chapter, we present the theoretical foundations necessary to follow the topics discussed in this thesis. We begin with a brief overview of Quantum Chromodynamics (QCD) in section 2.1. QCD is the fundamental theory describing the strong interaction, which plays a central role in the production and dynamics of hadronic processes. We then discuss Higgs boson production at hadron colliders in section 2.2, highlighting the key production mechanisms and taking a first look at the production cross section. In sections 2.3 and 2.4, we introduce effective field theories, focusing on the Heavy Quark Effective Theory (HQET) and Soft-Collinear Effective Theory (SCET), which provide powerful tools for handling multi-scale problems in QCD. Building on these concepts, we explore factorization and resummation techniques in section 2.5, which allow for the systematic separation of short- and long-distance physics and the resummation of large logarithms. In section 2.6, we examine transverse momentum distributions, which are important for describing the kinematics of particles produced in hadronic collisions or partons fragmenting into hadrons.

2.1 Basics of QCD

Quantum Chromodynamics (QCD) [54–59] is the quantum field theory describing strong interactions. It is based on the non-abelian $SU(N_c)$ gauge group where $N_c = 3$ is the number of colors. The degrees of freedom of this theory are spin-1/2 fermions called *quarks* and massless spin-1 bosons called *gluons*. Quarks are described by Dirac fields ψ_f^i which transform under the fundamental representation of SU(3)

$$\psi_f^i(x) \to \psi_f^{\prime i}(x) = \sum_j^{N_c} U_{ij} \psi_f^j(x) \quad \text{with} \quad U \in SU(3).$$
 (2.1)

The subscript f indicates the flavor of the quark which can take the values up, down, charm, strange, bottom or top. For brevity, we will from now on suppress the indices of the fundamental representation and write $\psi_f(x) \to U\psi_f(x)$. Gluons, on the other hand, are described by a vector field A^a_μ and transform under the adjoint representation of SU(3)

$$A_{\mu}(x) \equiv A_{\mu}^{a}(x)T^{a} \to A_{\mu}'(x) = A_{\mu}^{a}(x)UT^{a}U^{\dagger},$$
 (2.2)

where we left the sum over adjoint color indices a implicit. The matrices T^a are the generators of the SU(3) group in the fundamental representation. The generators fulfill the following relations

$$[T^a, T^b] = if^{abc}T^c, \quad Tr(T^aT^b) = T_F\delta_{ab} = \frac{1}{2}\delta_{ab}, \tag{2.3}$$

where f^{abc} is the so-called structure constant of the corresponding Lie algebra. The quadratic Casimir operators of the fundamental (C_F) and adjoint (C_A) representations are given by

$$T^a T^a = C_F \mathbf{1}, \quad f^{acd} f^{bcd} = C_A \delta^{ab}. \tag{2.4}$$

For SU(3), we have $N_c = 3$ and thus

$$C_F = \frac{N_c^2 - 1}{2N_c} = \frac{4}{3}, \quad C_A = N_c = 3.$$
 (2.5)

The QCD Lagrangian is constructed by demanding its invariance under local gauge transformations U(x) of eqs. (2.1) and (2.2)

$$\psi_f(x) \to \psi_f'(x) = U(x)\psi_f(x),$$
(2.6)

$$A_{\mu}(x) \to A'_{\mu}(x) = U(x)[A_{\mu}(x) + \frac{i}{g}\partial_{\mu}]U^{\dagger}(x),$$
 (2.7)

where g is the coupling parameter. Given these transformation properties, we define the covariant derivatives for the fundamental and adjoint representations as

$$D_{\mu} = \partial_{\mu} - igA_{\mu}(x), \tag{2.8}$$

$$D^{ab}_{\mu} = \partial_{\mu} \delta^{ab} + g f^{abc} A^{c}_{\mu}(x). \tag{2.9}$$

With these definitions, the QCD Lagrangian takes the form

$$\mathcal{L}_{\text{QCD}} = \sum_{f} \bar{\psi}_{f} (i \not \!\!\!D - m_{f}) \psi_{f} - \frac{1}{4} G_{\mu\nu}^{a} G^{a \mu\nu} + \mathcal{L}_{\text{gauge-fix}} + \mathcal{L}_{\text{ghost}}, \qquad (2.10)$$

The first term is the QCD quark term where sum runs over the quark flavor f. The second term describes the gluon kinematics with the gluon field strength tensor

$$G_{\mu\nu}^{a} = \partial_{\mu}A_{\nu}^{a}(x) - \partial_{\nu}A_{\mu}^{a}(x) + gf^{abc}A_{\mu}^{b}(x)A_{\nu}^{c}(x). \tag{2.11}$$

The remaining two terms in eq. (2.10) are related to gauge invariance: In the path integral formalism, the generating functional for the theory involves integrating over all possible configurations of the gluon fields. In the path integral over A^a_μ , there are many different configurations of A^a_μ that only differ by gauge transformation and, thus, leave the path integral unchanged. This leads to divergences in the path integral because of overcounting non-physical degrees of freedom. This issue can be resolved by adding a gauge fixing term to Lagrangian which explicitly breaks gauge invariance. The Faddeev-Popov procedure [60] involves choosing a gauge condition to fix the redundant degrees of freedom and introducing a correction term to account for the overcounting of configurations. This term is given in terms of anti-commuting spin-0 fields c^a called ghosts. The gauge-fixing and and the ghost term in the QCD Lagrangians are given by

$$\mathcal{L}_{\text{ghost}} = \bar{c}^a(i\partial^\mu)(iD_\mu^{ab})c^b, \quad \mathcal{L}_{\text{gauge-fix}} = \frac{1}{2\xi}(i\partial^\mu A_\mu^a)(i\partial^\nu A_\nu^a). \tag{2.12}$$

The parameters of QCD are given by the coupling constant g and the quark masses m_f which are given in table 2.1 [29]. The quark masses obey a strong hierarchy where the top quark is by far the heaviest. In fact, the top quark is too heavy to contribute to the dynamics at typical production energies at the LHC. We will, therefore, use $n_f = 5$ as the active number of flavors

quark flavor	mass	charge
up	$2.16 \pm 0.07\mathrm{MeV}$	$+\frac{2}{3}$
down	$4.70 \pm 0.07\mathrm{MeV}$	$-\frac{1}{3}$
strange	$93.5 \pm 0.8 \mathrm{MeV}$	$-\frac{1}{3}$
charm	$1.2730 \pm 0.0046 \mathrm{GeV}$	$+\frac{2}{3}$
bottom	$4.183\pm0.007\mathrm{GeV}$	$-\frac{1}{3}$
top	$172.57\pm0.29\mathrm{GeV}$	$+\frac{2}{3}$

Table 2.1: Quark flavors and their masses and charges. The charge is given in units of the elementary charge e.

in this thesis. The other quark masses are often neglected in perturbative QCD calculations. However, in this thesis, we are interested in heavy quark effects in factorization and resummation and therefore often count bottom and charm quarks as massive.

As QCD is a renormalizable theory the coupling g as well as the quark masses have to be renormalized. In this thesis we employ the modified minimal subtraction ($\overline{\text{MS}}$) scheme. In this scheme, ultra-violet (UV) divergences are regulated using dimensional regularization, i.e. the calculations are carried out in $d=4-2\epsilon$ spacetime dimensions [61]. The strong coupling $\alpha_s=g^2/(4\pi)$ picks up an explicit dependence on the renormalization scale μ . In the $\overline{\text{MS}}$ scheme, we have

$$\alpha_s = \mu^{2\epsilon} \alpha_s(\mu) Z_{\alpha_s}(\epsilon, \mu), \tag{2.13}$$

where $Z_{\alpha_s}(\epsilon, \mu)$ is the $\overline{\rm MS}$ renormalization factor

$$Z_{\alpha_s}(\epsilon, \mu) = \frac{e^{\epsilon \gamma_E}}{(4\pi)^{\epsilon}} \left[1 - \frac{\alpha_s(\mu)}{4\pi} \frac{\beta_0}{\epsilon} + \mathcal{O}(\alpha_s^2) \right]. \tag{2.14}$$

The prefactor $e^{\epsilon \gamma_E}/(4\pi)^{\epsilon}$ is precisely the difference between the $\overline{\rm MS}$ scheme and "regular" minimal subtraction (MS) where the prefactor is simply 1. The so-called *bare coupling* (non-renormalized) on left hand side of eq. (2.13) is independent of the renormalization scale. By taking the μ derivative, we find

$$\mu \frac{\mathrm{d}\alpha_s(\mu)}{\mathrm{d}\mu} = \alpha_s(\mu) \left[-2\epsilon - Z_{\alpha_s}^{-1}(\mu)\mu \frac{\mathrm{d}Z_{\alpha_s}(\mu)}{\mathrm{d}\mu} \right]$$
 (2.15)

Solving the above equation order by order, we find the β -function [62,63]

$$\mu \frac{\mathrm{d}\alpha_s(\mu)}{\mathrm{d}\mu} \equiv \beta[\alpha_s(\mu)] = -2\epsilon\alpha_s(\mu) - 2\alpha_s(\mu) \sum_{n=0}^{\infty} \beta_n \left(\frac{\alpha_s(\mu)}{4\pi}\right)^{n+1}, \tag{2.16}$$

which describes the dependence of $\alpha_s(Q)$ on a physical scale $Q \sim \mu$. The coefficients β_n can be calculated perturbatively and are known up to five loops [58, 59, 64–73]. The first term is given by

$$\beta_0 = \frac{11}{3}C_A - \frac{4}{3}T_F n_f. \tag{2.17}$$

The leading order solution to eq. (2.16) is given by

$$\alpha_s(\mu) = \frac{\alpha_s(\mu_0)}{1 + \alpha_s(\mu_0) \frac{\beta_0}{2\pi} \log \frac{\mu}{\mu_0}},$$
(2.18)

which is known as the running coupling. In the above equation $\alpha_s(\mu_0)$ is a value at reference scale μ_0 that has to be extracted from experiments. This is usually done at $\mu_0 = m_Z$, the mass of the Z boson, with the current world average being $\alpha_s(m_Z) = 0.1180(9)$ [29]. For $n_f \leq 16$, β_0 is positive and $\alpha_s(\mu)$ decreases for large values of μ . This behavior is called asymptotic freedom and describes the phenomenon that quarks and gluons can be treated as free particles at sufficiently large energies due to the small coupling. On the other hand, the coupling $\alpha_s(\mu)$ becomes large for small values of μ and diverges as μ approaches the so-called Landau-pole $\Lambda_{\rm OCD}$. At one loop it is given by

$$\Lambda_{\rm QCD}^{(1)} = \mu_0 \exp\left[-\frac{2\pi}{\beta_0 \alpha_s(\mu_0)}\right] \approx 100 \,\text{MeV}. \tag{2.19}$$

At this scale, the perturbative description of QCD breaks down, and quarks and gluons can no longer be treated as free particles. Instead, they form color-neutral bound states, a phenomenon known as (color) confinement. These bound states, called hadrons, consist either of a quark and an antiquark, forming a meson, or three quarks or antiquarks, forming a baryon. In principle there are also more exotic states such as tetra- and pentaquarks. However, we will not consider these states in this thesis. In experiments, free quarks and gluons are never observed. Instead, high-energy collisions produce collimated sprays of hadrons known as jets. The observation of these jets is consistent with the assumption that they originate from a primary parton [74]. Despite strong empirical evidence for confinement, its precise mechanism within QCD remains unkown. While phenomenological models such as the Lund string model [75] and the cluster model [76] provide ive descriptions of hadronization, a rigorous derivation from first principles is still unknown.

In QFT, all parameters in the Lagrangian have to be renormalized which leads us to the renormalization of the quark mass. This works completely analogous to the renormalization of the coupling and we can write

$$m = m(\mu)Z_m(\mu), \tag{2.20}$$

with the $\overline{\rm MS}$ mass renormalization factor

$$Z_m(\mu) = 1 - \frac{\alpha_s(\mu)}{4\pi} 3C_F + \mathcal{O}(\alpha_s^2). \tag{2.21}$$

Taking the μ derivative, we obtain

$$\mu \frac{\mathrm{d}m(\mu)}{\mathrm{d}\mu} = m(\mu) \left[-Z_m^{-1}(\mu)\mu \frac{\mathrm{d}Z_m(\mu)}{\mathrm{d}\mu} \right] \equiv m(\mu)\gamma_m(\mu), \tag{2.22}$$

where

$$\gamma_m(\mu) = \sum_{n=0}^{\infty} \gamma_{m,n} \left(\frac{\alpha_s(\mu)}{4\pi} \right)^{n+1}, \qquad (2.23)$$

is the mass anomalous dimension which governs the μ dependence of the quark mass just like the β -function for the coupling. The mass anomalous dimension is known up to five loops [77–83]. The renormalized quark mass at next-to-leading order is given by

$$m(\mu) = m(\mu_0) \left[1 - \frac{\alpha_s(\mu_0)}{4\pi} \gamma_{m,0} \log \frac{\mu_0}{\mu} \right],$$
 (2.24)

with $\gamma_{m,0} = -6C_F$. The reference scale μ_0 for the quark masses is given by their respective pole mass $\mu_0 = m_f$. An overview of anomalous dimensions is given in section B.1. Equations like eqs. (2.16) and (2.24) that describe the scale dependence of a renormalized parameter or –more generally– of a physical observable are called *renormalization group equations* (RGEs). As we will see in section 2.5, these RGEs are essential to resum large logarithms and thereby restore the convergence of the perturbative series.

2.2 Higgs production at hadron colliders

A large portion of this thesis is dedicated to providing high-precision predictions for the Higgs transverse momentum spectrum. In this section, we give a brief overview of the main Higgs production mechanisms and take a first look at structure of infra-red (IR) divergences.

Since the discovery of the Higgs boson in 2012 by the ATLAS and CMS experiments at the LHC [11,12], precise measurements of its properties has been one of the key goals of the LHC physics program. The mechanism of electroweak symmetry breaking [13–18] not only explains how the electroweak gauge bosons acquire mass but also provides a framework in which the Higgs couplings to other particles are uniquely predicted within the Standard Model. Consequently, high-precision measurements of these couplings serve as stringent tests of the Standard Model and offer a sensitive probe for potential new physics.

A key element is the Higgs coupling to fermions, which is described by the Yukawa interaction. This interaction is introduced into the Lagrangian as

$$\mathcal{L}_{\text{yuk}} = -y_f \,\bar{\psi} \,\phi \,\psi + \text{h.c.}, \quad y_f \sim \frac{m_f}{v},$$
 (2.25)

where ψ represents the fermion field, ϕ denotes the scalar Higgs field, m_f is the fermion mass, and v is the vacuum expectation value of the Higgs field. The relation $y_f \sim m_f/v$ contains the prediction that heavier fermions couple more strongly to the Higgs boson. Therefore, precision measurements of these Yukawa couplings provide vital information on the mechanism by which particles acquire mass.

2.2.1 Higgs production channels at hadron colliders

The dominant Higgs production channels in proton collisions are shown in figures 2.1 and 2.2, where the initial state partons originate from the colliding protons. We can group the Higgs production mechanisms in two classes: In the first class, the Higgs boson is produced in a via quark interactions, i.e. involving a coupling to quarks and, thus, featuring a Yukawa coupling. These processes are shown in figure 2.1. Gluon fusion (figure 2.1a) is the dominant production mechanism for the Higgs boson at hadron colliders like the LHC despite it only appearing at $\mathcal{O}(\alpha_s^2)$. Since gluons are massless they cannot couple directly to the Higgs boson and the interaction is mediated by a loop of heavy quarks. The top-quark is by far the heaviest elementary particle and the Yukawa coupling being proportional to the fermion mass compensates the

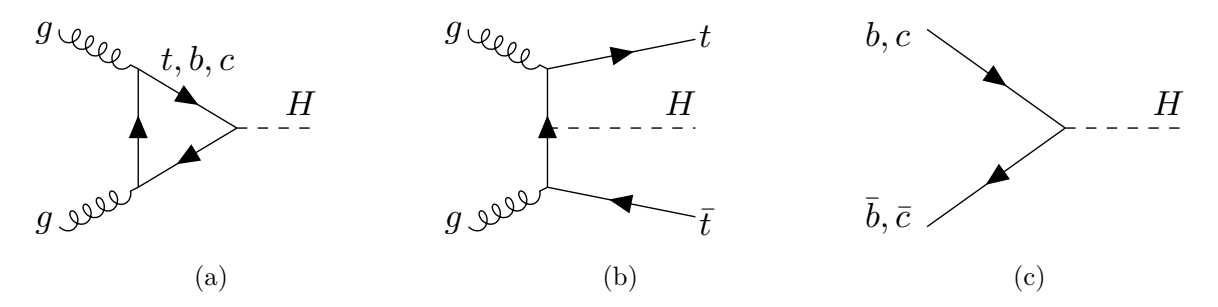


Figure 2.1: Higgs production channels involving a direct coupling to fermions: gluon fusion (left), associated production (ttH) (middle) and quark initiated production ($q\bar{q}H$) (right).

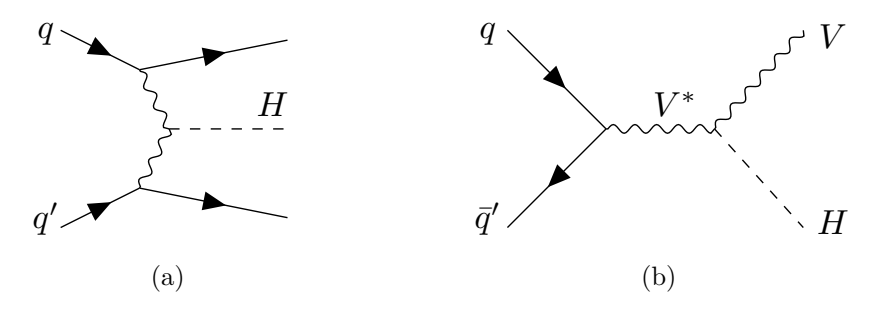


Figure 2.2: Higgs production channels involving direct coupling to vector bosons where V = W, Z: vector boson fusion (left) and Higgs strahlung (right).

formal suppression. As the Higgs coupling to the top-quark is approximately 40 times larger than to the next heaviest quark (bottom), usually only the top-quark is considered in gluon fusion. However, with the increasing precision of experimental measurements subleading-power effects become increasingly important and we will consider b-mass effects in gluon fusion in chapter 5.

Figure 2.1b shows Higgs production in association with a $t\bar{t}$ pair. Here the initial state gluons interact to produce a $t\bar{t}$ pair and the Higgs boson is radiated off one of the top quarks.

In quark initiated Higgs production two quarks directly annihilate into a Higgs boson. This process is shown in figure 2.1c. Note that top-quarks are not considered constituents of the proton and can therefore not participate as an initial state particle in this and other production channels. The dominant contribution, thus, comes from the bottom-quark. Figure 2.1c is the leading-order diagram in the *five-flavor scheme* where only the top-quark is considered heavy and the other five quarks are considered to be light. In contrast, there is also the four-flavor scheme, where both top and bottom-quark are considered to be heavy. In this case, the bottom quark would not participate in the quark initiated diagram either. We will discuss quark initiated Higgs production in detail in chapter 3.

Figure 2.2 shows the second class of diagrams. Here the Higgs boson is produced in an interaction with vector bosons. In vector boson fusion (figure 2.2a) two quarks from colliding protons each emit a vector boson (W or Z) which then fuse to produce a Higgs boson. In Higgsstrahlung, which is shown in figure 2.2b, a quark and an anti-quark produce a vector boson which then radiates off a Higgs boson. In this thesis, we are mostly interested in the quark Yukawa couplings and will therefore focus on class of production mechanisms that features a direct coupling to quarks. Table 2.2 provides a summary of the production cross sections for the processes discussed above.

channel	cross section	Ref.
Gluon fusion	48.61 pb	[84]
Vector boson fusion	$3.77\mathrm{pb}$	[84]
WH	$1.36\mathrm{pb}$	[84]
ZH	$0.88\mathrm{pb}$	[84]
t ar t H	$0.51\mathrm{pb}$	[84]
$bar{b}H$	$0.49\mathrm{pb}$	[85]

Table 2.2: Cross sections for key production mechanisms of a Higgs boson at the LHC for $\sqrt{s} = 13 \,\text{TeV}$ and $m_H = 125.09 \,\text{GeV}$.

Higgs cross section

As we are considering Higgs production in proton collisions we have no control over the initial state particles or their energies. Instead, the probability to find a parton i with a given momentum fraction x of the proton's momentum is described by parton distribution functions (PDFs). These objects are intrinsically non-perturbative and have to be extracted from experiments. Another important property is that PDFs are universal among processes. A process at hadron colliders, such as Higgs production at the LHC, involves a perturbative scale, e.g. $\mu = m_H = 125 \,\text{GeV}$. Then the cross section can be written in a factorized way using the collinear factorization theorem [86]

$$\sigma(pp \to X) = \sum_{i,j} \int_0^1 dx_a \int_0^1 dx_b f_i(x_a, \mu_F) f_j(x_b, \mu_F) \hat{\sigma}_{ij \to X}(x_a P_a, x_b P_b, \mu_R, \mu_F) + \mathcal{O}\left(\frac{\Lambda_{\text{QCD}}}{Q}\right),$$
(2.26)

stating that the production cross section for a state X in a proton collision with proton momenta P_a and P_b is given in terms of PDFs, $f_i(x, \mu_F)$, and the partonic cross section $\hat{\sigma}_{ij\to X}$. Here i and j are the type of the parton and $x_{i,j}$ are their respective momentum fractions inside the parent hadron. In the above equation all non-pertubative dynamics are captured by the PDFs. The partonic cross section, on the other hand, can be calculated perturbatively. Both PDFs and the partonic cross section, depend on the factorization scale μ_F which separates physics at different scales. The partonic cross section has an additional dependence on the renormalization scale μ_R . Eq. (2.26) is valid up to so-called higher-twist corrections of $\Lambda_{\rm QCD}/Q$ where Q is the hard scale of the process. For Higgs production we can take $Q = m_H$.

Coming back to the Higgs production mechanisms shown in figures 2.2 and 2.1, we want to focus on the most inclusive channels meaning processes with one Higgs boson as the only final state particle. This leaves gluon fusion and quark initiated production. Then the leading-order partonic cross section is given by

$$\hat{\sigma}_{ij\to H}^{(0)} = \frac{1}{2\hat{s}} \int d\phi_H \delta^4(p_i + p_j - p_H) |\mathcal{M}^{(0)}|^2, \qquad (2.27)$$

where $\hat{s} = (p_i + p_j)^2$ is the partonic center of mass energy squared and $\mathcal{M}^{(0)}$ is the matrix element of the Born process. To keep the notation compact, we assume that $|\mathcal{M}^{(0)}|^2$ is already averaged over spin and color of initial state particles. We integrate over the phase space $d\phi_H$ of the final state particle where the δ -function enforces momentum conservation.

In this thesis, we are interested in transverse momentum distributions where the final-state particle, in our example, the Higgs boson recoils against initial state radiation. Let us for now

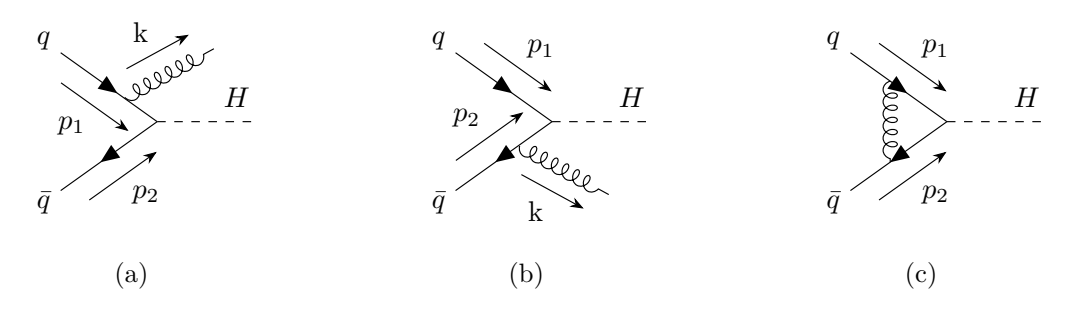


Figure 2.3: Next-to-leading order correction to quark initiated Higgs production

consider quark initiated Higgs production where we attach an extra gluon to one of the initial state quarks as shown in figures 2.3a and 2.3b. This real radiation contributes another quark propagator to the matrix element where for massless quarks the denominator is proportional to $(p_i - k)^2 = -2p_i \cdot k$ with i = 1, 2. This propagator diverges for $p_i \cdot k \to 0$. We distinguish two different limits: in the soft limit the gluon has low energy and we have $k^{\mu} \ll Q$. In this limit, both denominators are small as $p_1 \cdot k \to 0$ and $p_2 \cdot k \to 0$ and the matrix element diverges. In the collinear limit, the emitted gluon need not have low energy, but is closely aligned with its parent quark and either $p_1 \cdot k \to 0$ or $p_2 \cdot k \to 0$. In general, soft and collinear singularities are referred to as infra-red divergences. We write the scalar products as

$$(p_i - k)^2 = \frac{k_T^2}{(1 - z_i)},\tag{2.28}$$

where $k_T^2 = -k_\perp^2$ is the Euclidean transverse momentum and z can be interpreted as the momentum fraction of the parent quark i.

The cross section in the soft limit is given in terms of the leading-order cross section times a divergent integral over k_T and z

$$\hat{\sigma}_{q\bar{q}}^{\text{soft}}(p_1, p_2) = \hat{\sigma}_{q\bar{q}}^{(0)}(p_1, p_2) \times \text{div.}$$
 (2.29)

Divergences from the soft limit fully cancel in physical cross sections against poles arising from virtual gluon exchanged shown in figure 2.3c. The reason for this is that real and virtual gluons cannot be distinguished as $k \to 0$.

For the collinear limit, we consider the gluon to be aligned with the incoming quark carrying momentum p_1 . Then the cross section is given by

$$\hat{\sigma}_{q\bar{q}}^{p_1\text{-coll}}(p_1, p_2) \sim \int_0^\infty \frac{\mathrm{d}k_T^2}{k_T^2} \int_0^1 \mathrm{d}z_1 \frac{1 + z_1^2}{1 - z_1} \hat{\sigma}_{q\bar{q}}^{(0)}(z_1 p_1, p_2). \tag{2.30}$$

The singularity for $k_T \to 0$ and $z_1 \to 1$ corresponds to a soft gluon emission. This is already captured by the soft contribution and needs to be subtracted, yielding

$$\hat{\sigma}_{q\bar{q}}^{p_1\text{-coll}}(p_1, p_2) \sim \int_0^\infty \frac{\mathrm{d}k_T^2}{k_T^2} \int_0^1 \mathrm{d}z_1 P_{qq}(z_1) \hat{\sigma}_{q\bar{q}}^{(0)}(z_1 p_1, p_2). \tag{2.31}$$

The P_{qq} is a splitting function

$$P_{qq}(z) = C_F \left[\frac{1+z^2}{1-z} \right]_+,$$
 (2.32)

where the plus distribution regulates the divergence at z=1. An overview over plus distributions is given in Appendix C. The leftover divergence is purely collinear and stays uncanceled. However, the partonic cross section is not physical observable. We still need to include the PDFs and integrate over their momentum fractions to arrive at the hadronic cross section. This allows us to absorb the collinear divergences into renormalized PDFs. The scale evolution of the PDFs is given by the Dokshitzer-Gribov-Lipatov-Altarelli-Parisi (DGLAP) equations [87–89]. At leading order they are given by

$$\mu \frac{\mathrm{d}}{\mathrm{d}\mu} f_q(z,\mu) = \frac{\alpha_s}{2\pi} \int_x^1 \frac{\mathrm{d}z}{z} \left[2P_{qq} \left[\alpha_s(\mu), z \right] f_q \left(\frac{x}{z}, \mu \right) + 2P_{qg} \left[\alpha_s(\mu), z \right] f_g \left(\frac{x}{z}, \mu \right) \right],$$

$$\mu \frac{\mathrm{d}}{\mathrm{d}\mu} f_g(z,\mu) = \frac{\alpha_s}{2\pi} \int_x^1 \frac{\mathrm{d}z}{z} \left[2P_{gg} \left[\alpha_s(\mu), z \right] f_g \left(\frac{x}{z}, \mu \right) + 2\sum_g P_{gq} \left[\alpha_s(\mu), z \right] f_q \left(\frac{x}{z}, \mu \right) \right], \quad (2.33)$$

where the sum runs over all quark flavors. The splitting functions are know up to three loops [90,91] with partial results available at four loops [92–96].

As PDFs are universal across processes, they can therefore be extracted at one experiment at a scale μ_0 and used universally. However, as they depend on the energy scale, they must be evolved to the correct energy scale Q by solving the differential equations in eq. (2.33)

2.3 Effective field theory

Effective field theory (EFT) is a powerful framework for tackling multiscale problems. It enables the systematic separation of physics at different energy scales, e.g. a low scale q and a high scale Q with $q \ll Q$. This separation can be implemented directly in physical observables, such as cross sections, by performing a power expansion in a dimensionless power-counting parameter $\lambda = (q/Q)^a$ where $\lambda \ll 1$ and a > 0, however, typically a = 1. The expansion can then be truncated at any desired order: the leading term is called the *leading-power* contribution, and higher-order terms are referred to as *subleading-power* corrections.

There two different types of EFTs: in bottom-up EFTs, the EFT is constructed without assuming any knowledge of the underlying high energy theory. In this approach the couplings are not known and have to be extracted from the experiment. A prominent example is the Standard Model effective field theory (SMEFT) which extends the Standard Model (SM) by higher dimensional operators to capture effects of physics beyond the SM. These higher dimensional operators respect SM symmetries.

For top-down EFTs, the high energy theory is known, but they simplify the study of low-energy properties. Here, interactions in the low-energy degrees of freedom not already included in the EFT Lagrangian are described by writing down operators allowed by symmetries of the full theory. The coefficients of these operators are determined through a *matching* procedure where we compare scattering amplitudes of some representative processes computed in both full theory and the EFT. Since the EFT and full theory agree in the infrared, the matching procedure fixes once for all the coefficients that account for the mismatch of the two theories in the UV region. Once the coefficients are fixed, we can use the EFT as standalone theory.

The general approach to set up an EFT is the following

- 1. Identify the low-energy degrees of freedom at the low scale q.
- 2. Write down all possible operators \mathcal{O}_i consistent with the symmetries of the full theory up to the desired order in λ .

- 3. Determine the so-called Wilson coefficients C_i in $\mathcal{L}_{EFT} = \sum_i C_i \mathcal{O}_i$. For top-down theories this archived by performing a matching calculation, for bottom-up theories the coefficients have to be extracted from the experiment.
- 4. Calculate the desired observables in the EFT.

In this thesis, we work with two top-down theories: Heavy-Quark Effective Theory (HQET) [97–100] and Soft-Collinear Effective Theory (SCET) [101–106] which will be reviewed in the following sections.

Heavy-Quark Effective Theory

This section follows the review on HQET from ref. [19]. For a detailed discussions see e.g. ref. [107]. Heavy quark physics is a prime example for the application of EFTs. The mass of the heavy quark m_Q provides a natural separation of scales with $m_Q \gg \Lambda_{\rm QCD}$. Here, physics at the scale m_Q is high energetic whereas physics at the scale $\Lambda_{\rm QCD}$ describes low energetic hardonic effects. In HQET, we consider a heavy quark Q with four-momentum

$$p_Q^{\mu} = m_Q v^{\mu} + k^{\mu}, \tag{2.34}$$

with the velocity of the heavy quark v and $v^2 = 1$. The momentum k^{μ} denotes fluctuations due to interactions with soft (low-energetic) degrees of freedom and scales as $k^{\mu} \sim \Lambda_{\rm QCD}$. The heavy quark field can then be written as

$$\psi_Q(x) = e^{-im_Q v \cdot x} \left[h_v(x) + H_v(x) \right],$$
(2.35)

where $h_v(x)$ are the large and $H_v(x)$ are the small components. The $h_v(x)$ are implemented as Dirac spinors satisfying the projection relations

$$P_{\pm} \equiv \frac{1 \pm \psi}{2}$$
, $P_{+}h_{v} = h_{v}$, $P_{-}h_{v} = 0$, $\bar{h}_{v}P_{+} = \bar{h}_{v}$, $\bar{h}_{v}P_{-} = 0$. (2.36)

The field $H_v(x)$ is suppressed by $1/m_Q$ compared to $h_v(x)$ and describes off-shell fluctuations of the heavy quark field at the scale m_Q . Then the tree-level matching of the massive QCD quark field onto h_v at $\mu \sim m$ reads:

$$\psi_Q(x) = e^{-\mathrm{i}mv \cdot x} h_v(x) \left[1 + \mathcal{O}\left(\frac{1}{m}\right) \right]. \tag{2.37}$$

Inserting this yields the leading-order HQET Lagrangian

$$\mathcal{L} = \bar{h}_v(iv \cdot D)h_v + \mathcal{L}_{light} + \mathcal{O}\left(\frac{1}{m_Q}\right), \qquad (2.38)$$

where $\mathcal{L}_{\text{light}}$ is a copy of the QCD Lagrangian with n_{ℓ} massless quark flavors.

The spin degrees of freedom of the heavy-quark can be explicitly decoupled from the light dynamics at leading power in 1/m by performing a field redefinition involving static Wilson lines $Y_v(x)$ [103, 108],

$$h_v(x) = Y_v(x) h_v^{(0)}(x), \qquad Y_v(x) = P\left[\exp\left(ig \int_0^\infty ds \, v \cdot A(x+vs)\right)\right].$$
 (2.39)

In this way, the heavy-quark Lagrangian becomes that of a free theory,

$$\mathcal{L}^{(0)} = \bar{h}_v^{(0)} (iv \cdot \partial) h_v^{(0)} \tag{2.40}$$

and $Y_v(x)$ takes $h_v(x)$ place in all external operators where it serves as a source of soft gluons. We will use HQET and in particular bHQET – its application to boosted heavy quarks– in chapter 6 to study heavy-quark fragmentation functions.

2.4 Soft-Collinear Effective Theory

SCET is a top-down EFT describing dynamics of soft and collinear degrees of freedom associated with energetic particles particles participating in a high energy collision at a hard scale $Q \gg \Lambda_{\rm QCD}$. Soft particles carry less energy with $p_s^0 \ll Q$ and exhibit isotropic scaling. Collinear particles, on the other hand, are more energetic $p_c^0 \sim Q$. See the discussion above eq. (2.28). Similar to HQET, we will integrate out off-shell modes but not entire degrees of freedom.

This review is based on ref. [109] where we use the label momentum formalism developed in refs. [101–104]. One can also perform a multipole expansion in position space [105, 106], see ref. [110] for a review.

When describing soft and collinear particles, it is convenient to work in light-cone coordinates where we decompose four-vectors in terms of in terms of lightlike vectors n^{μ} , \bar{n}^{μ} . These vectors need to fulfill the following relations:

$$n^2 = 0, \qquad \bar{n}^2 = 0, \qquad n \cdot \bar{n} = 2.$$
 (2.41)

A typical choice is

$$n^{\mu} = (1, 0, 0, 1), \qquad \bar{n}^{\mu} = (1, 0, 0, -1).$$
 (2.42)

Note that there is some freedom in the choice of the light-cone vectors n and \bar{n} : they only requirement is that eq. (2.41) is obeyed. This freedom leads to symmetry of SCET referred to as reparametrization invariance (RPI) which guarantees that observables remain unchanged under the transformations summarized in table 2.3. With the vectors n and \bar{n} , we can now write four-momenta as

$$p^{\mu} = n \cdot p \, \frac{\bar{n}^{\mu}}{2} + \bar{n} \cdot p \, \frac{n^{\mu}}{2} + p_{\perp}^{\mu} \equiv (p^{+}, p^{-}, p_{\perp}) \,, \tag{2.43}$$

with

$$p^- \equiv \bar{n} \cdot p, \quad p^+ \equiv n \cdot p. \tag{2.44}$$

We always take transverse vectors with subscript \perp to be Minkowskian, $p_{\perp}^2 \equiv p_{\perp} \cdot p_{\perp} < 0$, and denote their magnitude by $p_T = \sqrt{-p_{\perp}^2}$. Then the invariant mass is given by

$$p^2 = p^- p^+ + p_\perp^2. (2.45)$$

We can also define the metric and antisymmetric tensor in transverse space as

$$g_{\perp}^{\mu\nu} \equiv g^{\mu\nu} - \frac{n^{\mu}\bar{n}^{\nu}}{2} - \frac{\bar{n}^{\mu}n^{\nu}}{2}, \qquad \epsilon_{\perp}^{\mu\nu} \equiv \epsilon^{\mu\nu\rho\sigma} \frac{\bar{n}_{\rho}n_{\sigma}}{2}. \tag{2.46}$$

Our convention for the antisymmetric tensor is $\epsilon^{0123}=+1$.

To identify the relevant degrees of freedom, let us consider a high energetic collision with two incoming particle beams, one in n and one in \bar{n} direction. The hard interaction takes place at a scale Q. Then n-collinear and \bar{n} -collinear particles exhibit the momentum scaling

$$p_{nc}^{\mu} = (p^+, p^-, p_\perp) \sim Q(\lambda^2, 1, \lambda), \qquad p_{\bar{n}c}^{\mu} \sim Q(1, \lambda^2, \lambda),$$
 (2.47)

with the power-counting parameter $\lambda \ll 1$. Collinear to a directions refers to the fact that a *n*-collinear particle travels near to the *n*-direction but not exactly along that direction. In

RPI-I	RPI-II	RPI-III
$n^{\mu} \rightarrow n^{\mu} + \Delta^{\mu}_{\perp}, \ \Delta_{\perp} \sim \lambda$	$n^{\mu} \rightarrow n^{\mu}$	$n^{\mu} \rightarrow e^{\alpha} n^{\mu}, \ \alpha \sim 1$
$\bar{n}^{\mu} ightarrow \bar{n}^{\mu}$	$\bar{n}^{\mu} \rightarrow \bar{n}^{\mu} + \epsilon_{\perp}^{\mu}, \; \epsilon_{\perp} \sim 1$	$\bar{n}^{\mu} \to e^{-\alpha} \bar{n}^{\mu}$

Table 2.3: Summary of reparametrization invariance. Type I and II are infinitesimal transformations that require $n \cdot \Delta_{\perp} = \bar{n} \cdot \Delta_{\perp} = 0$ and $n \cdot \epsilon_{\perp} = \bar{n} \cdot \epsilon_{\perp} = 0$ and type III is a finite transformation. The scaling for Δ_{\perp} , ϵ_{\perp} and α follow from requiring that the collinear scaling $(\lambda^2, 1, \lambda)$ stays unchanged on these transformations.

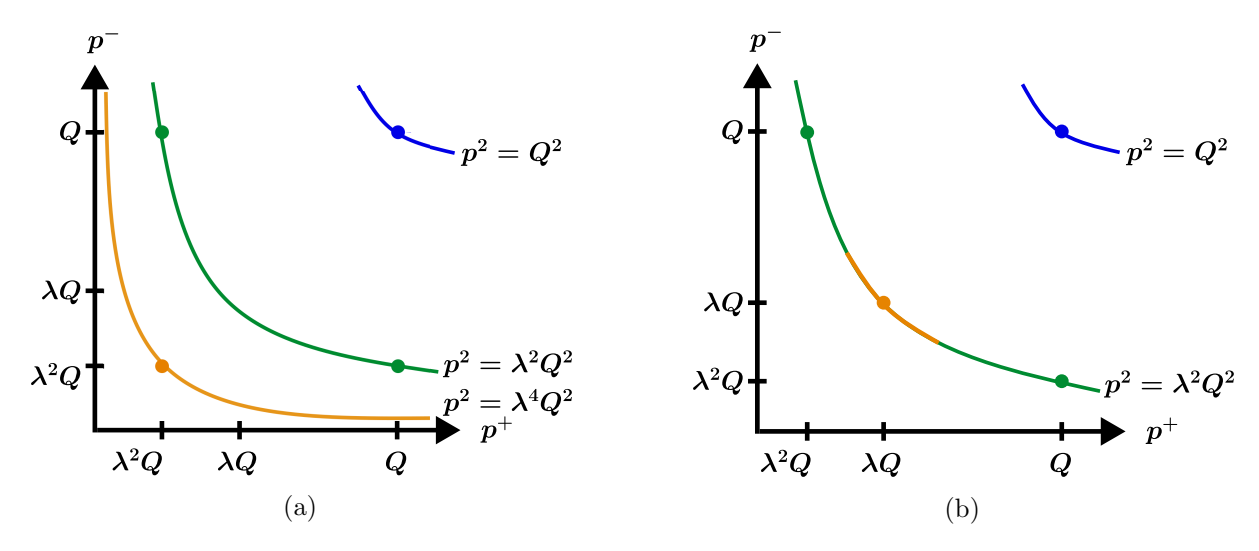


Figure 2.4: Modes for SCET_I-like (a) and SCET_{II}-like setups. The different modes are separated by their virtuality. Hard modes (blue) will be integrated out in the theory. Collinear modes are shown in green and soft and ultra-soft modes in orange.

addition to collinear modes, there can also be soft and ultra soft modes with the momentum scalings

$$p_s^{\mu} \sim Q(\lambda, \lambda, \lambda), \qquad p_{us}^{\mu} \sim Q(\lambda^2, \lambda^2, \lambda^2).$$
 (2.48)

The parametric scaling of soft modes is either larger or smaller as the p^{\pm} components of collinear modes. Thus, soft and collinear modes can only interact via the \perp component. On the other, ultra-soft modes can directly interact with the p^{\pm} of $n(\bar{n})$ -collinear modes. Ultra-soft and soft modes lead to different effective theories referred to as SCET_I and SCET_{II}, respectively. Their relevant modes are illustrated in figure 2.4. SCET_I is commonly used for measurements which are sensitive to the \pm momenta, whereas SCET_{II} is used for oberservables with a dependence on the transverse momentum. Finally, there are Glauber modes,

$$p_G^{\mu} \sim Q(\lambda^2, \lambda^2, \lambda). \tag{2.49}$$

These modes are off-shell and can therefore not radiate into the final state. The contribution from these modes for sufficiently inclusive processes, such as the ones considered here, cancels to all orders or is perturbatively suppressed, we will not consider them in this thesis.

2.4.1 The SCET_I Lagrangian

We will start with deriving the SCET_I Lagrangian to leading power by expanding the QCD Lagrangian in the power-counting parameter λ . To do so, we start by expanding the Dirac Spinors for particles, u(p), and anti-particles, v(p), with n-collinear momentum p. Recall that the large momentum component for n-collinear momenta is given by $p^- \equiv p_3 + p_0 \ll p^+ \equiv p_3 - p_0$. Then we can write the Dirac spinors as

$$u(p) = \frac{\sqrt{2p_0}}{2} \begin{pmatrix} \mathcal{U} \\ \frac{\vec{\sigma} \cdot \vec{p}}{p_0} \mathcal{U} \end{pmatrix} = \frac{\sqrt{p^-}}{2} \begin{pmatrix} \mathcal{U} \\ \sigma_3 \mathcal{U} \end{pmatrix} + \mathcal{O}(\lambda)$$

$$v(p) = \frac{\sqrt{2p_0}}{2} \begin{pmatrix} \mathcal{V} \\ \frac{\vec{\sigma} \cdot \vec{p}}{p_0} \mathcal{V} \end{pmatrix} = \frac{\sqrt{p^-}}{2} \begin{pmatrix} \mathcal{V} \\ \sigma_3 \mathcal{V} \end{pmatrix} + \mathcal{O}(\lambda)$$
(2.50)

by introducing lightcone momenta and expanding in λ . We define

$$u_n = \frac{\sqrt{p^-}}{2} \begin{pmatrix} \mathcal{U} \\ \sigma_3 \mathcal{U} \end{pmatrix}, \qquad v_n = \frac{\sqrt{p^-}}{2} \begin{pmatrix} \mathcal{V} \\ \sigma_3 \mathcal{V} \end{pmatrix}.$$
 (2.51)

Here \mathcal{U} and \mathcal{V} are either (1 0) or (0 1). For our purpose, it is also useful to define the projection operators

$$P_n = \frac{\cancel{n}\cancel{n}}{4} = \frac{1}{2} \begin{pmatrix} \mathbf{1} & \sigma_3 \\ \sigma_3 & \mathbf{1} \end{pmatrix}, \qquad P_{\bar{n}} = \frac{\cancel{n}\cancel{n}}{4} = \frac{1}{2} \begin{pmatrix} \mathbf{1} & -\sigma_3 \\ -\sigma_3 & \mathbf{1} \end{pmatrix}, \tag{2.52}$$

with $P_n + P_{\bar{n}} = 1$. These operators act on our collinear spinors as

$$P_n u_n = u_n, \qquad P_n v_n = v_n, \qquad P_{\bar{n}} v_n = 0, \qquad P_{\bar{n}} u_n = 0.$$
 (2.53)

In the next step, we split the quark field in two components

$$\psi = P_n \psi + P_{\bar{n}} \psi = \hat{\xi}_n + \varphi_{\bar{n}}. \tag{2.54}$$

From the definition of P_n and $P_{\bar{n}}$, we can derive the following relations

$$\eta \hat{\xi}_n = 0, \quad P_n \hat{\xi} = \hat{\xi}, \quad \vec{\eta} \varphi_{\bar{n}} = 0, \quad P_{\bar{n}} \varphi_{\bar{n}} = \varphi_{\bar{n}}.$$
(2.55)

We can now insert eq. (2.54) in the massless QCD lagrangian

$$\mathcal{L}_{QCD} = \bar{\psi} i \not \!\! D \psi
= (\bar{\hat{\xi}}_n + \bar{\varphi}_{\bar{n}}) \left(\frac{\not \!\! n}{2} i n \cdot D + \frac{\not \!\! n}{2} i \bar{n} \cdot D + i \not \!\! D_{\perp} \right) (\hat{\xi}_n + \varphi_{\bar{n}})
= \bar{\hat{\xi}}_n \frac{\not \!\! n}{2} i n \cdot D \hat{\xi}_n + \bar{\varphi}_{\bar{n}} i \not \!\! D_{\perp} \hat{\xi}_n + \bar{\hat{\xi}}_n i \not \!\! D_{\perp} \varphi_{\bar{n}} + \bar{\varphi}_{\bar{n}} \frac{\not \!\! n}{2} i \bar{n} \cdot D \varphi_{\bar{n}}$$
(2.56)

The field $\varphi_{\bar{n}}$ only contributes at subleading power and can therefore be integrated out. This is achieved by imposing the equations of motion yielding

$$\frac{\delta \mathcal{L}}{\delta \varphi_{\bar{n}}} = 0 \quad \Rightarrow \quad \varphi_{\bar{n}} = \frac{1}{\mathrm{i}\bar{n} \cdot D} \mathrm{i} \not D_{\perp} \frac{\bar{n}}{2} \hat{\xi}. \tag{2.57}$$

Inserting this in eq. (2.56), two terms cancel and we can write the leading power Lagragian for the $\hat{\xi}_n$ field as

$$\mathcal{L} = \bar{\hat{\xi}}_n \left(in \cdot D + i \not \!\! D_\perp \frac{1}{i\bar{n} \cdot D} i \not \!\! D_\perp \right) \frac{\not \!\! n}{2} \hat{\xi}_n. \tag{2.58}$$

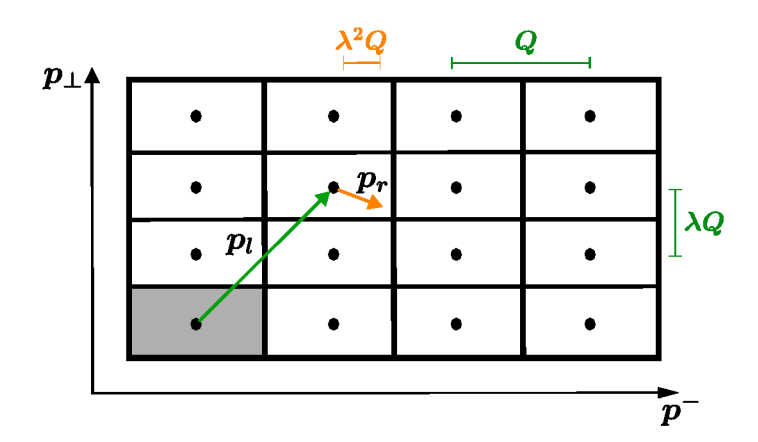


Figure 2.5: Illustration of the grid interpretation of the label momentum.

To derive the leading-power quark Lagrangian, we still need to expand the covariant derivative $D^{\mu} = \partial^{\mu} - igA^{\mu}$.

We start assigning a scaling to ∂^{μ} . This can be done by multipole expanding the quark field $\hat{\xi}_n$. The Fourier conjugate of our quark field is given by

$$\tilde{\xi}_n(p) = \int d^4x e^{ip \cdot x} \hat{\xi}_n(x). \tag{2.59}$$

We can split n-collinear momentum p_n in a large label momentum and a small residual momenta

$$p_n^{\mu} = p_l^{\mu} + p_r^{\mu}, \tag{2.60}$$

with the scaling

$$p_l^{\mu} = (0, 1, \lambda), \qquad p_r^{\mu} = (\lambda^2, \lambda^2, \lambda^2).$$
 (2.61)

Then an integral over a collinear momentum can be written as

$$\int d^4p \to \sum \int d^4p_r, \tag{2.62}$$

where we interpret p_l as a discrete point in the $p^- \times p_\perp$ grid, allowing us to rewrite the integral as a discrete sum. The residual momentum defines a location within the boxes. This is illustrated in figure 2.5. Note that $p_l = 0$ is not included in the sum defining the $\xi_n(x)$ field. In fact, $p_l = 0$ corresponds to an ultrasoft soft mode and needs to be excluded to avoid double counting. This mode is referred to as zero-bin and represented by the gray shading in figure 2.5. This allows us to write

$$\hat{\xi}_n(x) = \sum_{p_l \neq 0} \int d^4 p_r e^{-ip \cdot x} \tilde{\xi}_n(p) = \sum_{p_l \neq 0} \int d^4 p_r e^{-ip_l \cdot x} e^{-ip_r \cdot x} \tilde{\xi}_{n,p_l}(p_r) = \sum_{p_l \neq 0} e^{-ip_l \cdot x} \xi_{n,p_l}(x), \quad (2.63)$$

where in the last step we introduced the notation for quark field with label momentum p_l

$$\xi_{n,p_l} = \int d^4 p_r e^{-ip_r \cdot x} \tilde{\xi}_{n,p_l}(p_r). \tag{2.64}$$

At this point it is useful the define the label operator

$$\mathcal{P}^{\mu}\xi_{n,m}(x) \equiv p_l \xi_{n,m}(x), \tag{2.65}$$

which picks out the label momentum p_l . Recalling the scaling of p_l in eq. (2.61), we find

$$n \cdot \mathcal{P} = 0, \qquad \bar{\mathcal{P}} \equiv \bar{n} \cdot \mathcal{P} \sim p_l^- \sim \mathcal{O}(\lambda^0), \qquad \mathcal{P}_{\perp}^{\mu} \sim p_{l,\perp}^{\mu} \sim \mathcal{O}(\lambda).$$
 (2.66)

Now, we can rewrite our collinear quark field as

$$\hat{\xi}_n(x) = \sum_{p_l \neq 0} e^{-ip_l \cdot x} \xi_{n,p_l}(x) = \sum_{p_l \neq 0} e^{-i\mathcal{P} \cdot x} \xi_{n,p_l}(x) = e^{-i\mathcal{P} \cdot x} \xi_n(x).$$
 (2.67)

Then the derivative ∂^{μ} acts on the collinear quark field as

$$i\partial^{\mu}\hat{\xi}_{n}(x) = i\partial^{\mu}e^{-i\mathcal{P}\cdot x}\xi_{n}(x) = e^{-i\mathcal{P}\cdot x}(\mathcal{P}^{\mu} + i\partial^{\mu})\xi_{n}(x), \tag{2.68}$$

where the label operator picks out the large components and ∂^{μ} has ultra-soft scaling. For the full SCET_I Lagrangian, we must include contributions from both *n*-collinear and ultrasoft gluons. An *n*-collinear gluon field scales as $A_n \sim p_n \sim (\lambda^2, 1, \lambda)$ while an ultra-soft gluon field scales as $A_{us} \sim p_{us} \sim (\lambda^2, \lambda^2, \lambda^2)$. We can therefore write

$$A^{\mu} = \hat{A}_{n}^{\mu} + A_{us}^{\mu} + \text{p.c.}, \tag{2.69}$$

where "p.c." stands for power corrections which can be ignored at leading order. We proceed with the collinear gluon field analogous to the collinear quark field and write

$$\hat{A}_{n}^{\mu}(x) = \sum_{q_{l} \neq 0} e^{-iq_{l} \cdot x} A_{n,q_{l}}^{\mu} = e^{-i\mathcal{P} \cdot x} A_{n}^{\mu}(x), \qquad (2.70)$$

where

$$A_n^{\mu}(x) = \sum_{q_l \neq 0} A_{n,q_l}^{\mu}.$$
 (2.71)

This allows to write the collinear quark Lagrangian as

$$\mathcal{L} = e^{-i\mathcal{P}\cdot x}\bar{\xi}_n \left(in \cdot D + i\not D_{\perp} \frac{1}{i\bar{n} \cdot D} i\not D_{\perp} \right) \frac{\not n}{2} \xi_n$$
 (2.72)

and with the covariant derivative

$$D^{\mu} = \partial^{\mu} - i\mathcal{P} - igA^{\mu}. \tag{2.73}$$

Now, that we assigned a scaling to all fields and derivatives, we can expand the covariant derivative in our power counting parameter λ

$$in \cdot D = in \cdot \partial + gn \cdot A_n + gn \cdot A_{us} \qquad \sim \mathcal{O}(\lambda^2),$$

$$i\bar{n} \cdot D = \bar{\mathcal{P}} + g\bar{n} \cdot A_n + \mathcal{O}(\lambda) = i\bar{n} \cdot D_n + \mathcal{O}(\lambda) \qquad \sim \mathcal{O}(\lambda^0),$$

$$iD_{\perp} = \mathcal{P}_{\perp}^{\mu} + g\bar{n} \cdot A_n + \mathcal{O}(\lambda^2) = iD_{n\perp} + \mathcal{O}(\lambda^2) \qquad \sim \mathcal{O}(\lambda). \qquad (2.74)$$

Finally, we have all ingredients to write down the leading power collinear quark Lagrangian

$$\mathcal{L}_{n\xi}^{(0)} = \bar{\xi}_n \left(in \cdot D + i \not \!\!D_{n\perp} \frac{1}{i\bar{n} \cdot D_n} i \not \!\!D_{n\perp} \right) \frac{\vec{n}}{2} \xi_n, \tag{2.75}$$

where we omitted the overall factor of $e^{-i\mathcal{P}\cdot x}$. In order to derive the Lagrangian for collinear and ultra-soft gluons, we start with the gluonic part of the QCD Lagrangian

$$\mathcal{L} = -\frac{1}{2} \operatorname{Tr} \{ G^{\mu\nu} G_{\mu\nu} \} + \frac{1}{\xi} \operatorname{Tr} \{ (i\partial_{\mu} A^{\mu})^{2} \} + 2 \operatorname{Tr} \{ \bar{c} i \partial_{\mu} i D^{\mu} c \}, \tag{2.76}$$

where ξ is the gauge-fixing parameter. In the next step, we expand the covariant derivative for collinear gluons

$$i\mathcal{D}^{\mu} = \frac{n^{\mu}}{2}(\bar{\mathcal{P}} + g\bar{n}\cdot A_n) + (\mathcal{P}^{\mu}_{\perp} + gA^{\mu}_{\perp,n}) + \frac{\bar{n}^{\mu}}{2}(in\cdot\partial + gn\cdot A_n + gn\cdot A_{us})$$
(2.77)

and ultra-soft gluons

$$i\mathcal{D}_{us} = \frac{n^{\mu}}{2}\bar{\mathcal{P}} + \mathcal{P}_{\perp}^{\mu} + \frac{\bar{n}^{\mu}}{2}(in \cdot \partial + gn \cdot A_{us})$$
(2.78)

where we kept the leading terms only. Then the leading-order collinear gluon Lagrangian is given by

$$\mathcal{L}_{ng}^{(0)} = \frac{1}{2g^2} \operatorname{Tr}\{[i\mathcal{D}^{\mu}, i\mathcal{D}^{\mu}]^2\} + \frac{1}{\xi_c} \operatorname{Tr}\{[i\mathcal{D}_{us}^{\mu}, A_{n\mu}]^2\} + 2 \operatorname{Tr}\{\bar{c}_n[i\mathcal{D}_{\mu}^{us}, [i\mathcal{D}^{\mu}, c_n]]\},$$
(2.79)

with the collinear gauge-fixing parameter ξ_c . At leading power, ultra-soft quarks and gluons are simply described by the QCD Lagrangian

$$\mathcal{L}_{us}^{(0)} = \bar{\psi}_{us} i \not\!\!D_{us} \psi_{us} - \frac{1}{2} \operatorname{Tr} \{ G_{us}^{\mu\nu} G_{\mu\nu}^{us} \} + \frac{1}{\tau_{us}} \operatorname{Tr} \{ (i\partial_{\mu} A_{us}^{\mu})^{2} \} + 2 \operatorname{Tr} \{ \bar{c}_{us} i \partial_{\mu} i D_{us}^{\mu} c_{us} \}$$
 (2.80)

where the fields and covariant derivatives satisfy ultra-soft scaling and $D_{us}^{\mu} = \partial^{\mu} - igA_{us}$. We introduce the ultra-soft gauge-fixing parameter τ_{us} in the above equation. Finally, we can write down the full SCET_I Lagrangian which is given by

$$\mathcal{L}^{(0)} = \mathcal{L}_{n\xi}^{(0)} + \mathcal{L}_{ng}^{(0)} + \mathcal{L}_{us}^{(0)}. \tag{2.81}$$

The corresponding Feyman rules are given in figures 2.6 and 2.7. The extension of this result to multiple collinear sector is straightforward. We simply add sum over all distinct n_i -collinear modes

$$\mathcal{L}_{SCET_{I}}^{(0)} = \sum_{n} \left(\mathcal{L}_{n\xi}^{(0)} + \mathcal{L}_{ng}^{(0)} \right) + \mathcal{L}_{us}^{(0)}.$$
 (2.82)

Two collinear modes n_i and n_j are only distinct if they fulfill

$$n_i \cdot n_j \gg \lambda^2 \quad \text{for} \quad i \neq j.$$
 (2.83)

2.4.2 Symmetries of SCET

In this section, we want to discuss the symmetries of SCET which are a powerful tool to constrain operators in the effective theory. We already mentioned RPI as a manifestation of Lorentz symmetry that is explicitly broken by the choice of light-cone coordinates below eq. (2.42). In particular, RPI-III ensures that for arbitrary four-vectors A^{μ} and B^{μ} only the following combinations can appear

$$\frac{n \cdot A}{n \cdot B} = \frac{A^+}{B^+}, \qquad \frac{\bar{n} \cdot A}{\bar{n} \cdot B} = \frac{A^-}{B^-}, \qquad (n \cdot A)(\bar{n} \cdot B) = A^+ B^-, \qquad A_\perp \cdot B_\perp. \tag{2.84}$$

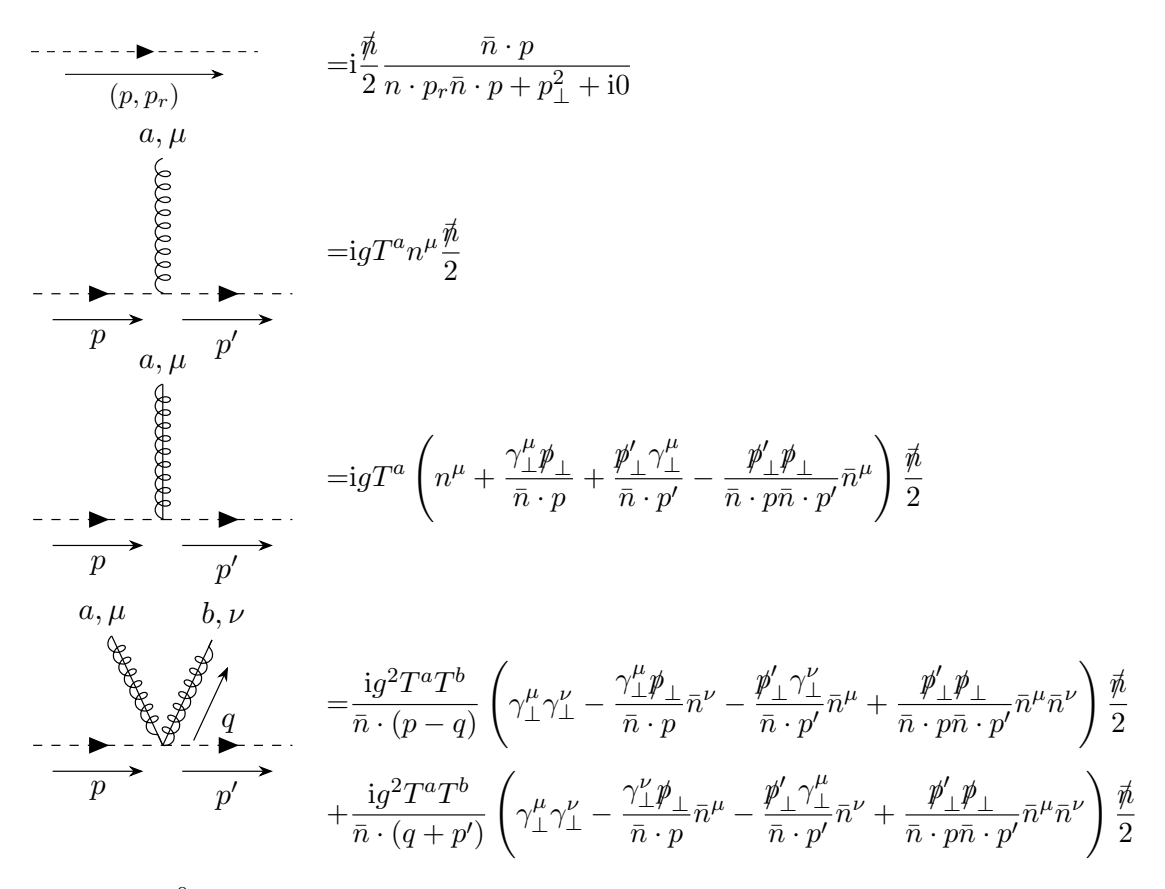


Figure 2.6: $\mathcal{O}(\lambda^0)$ Feynman rules. Collinear quarks are represented by the dashed fermion line, collinear gluons are springs with a line and soft gluons are regular springs.

Another important symmetry of SCET is gauge invariance. As the QCD fields split into collinear and ultrasoft fields ξ_n and ξ_{us} , they also require distinct gauge transformations U_c and U_{us} with independent gauge-fixing parameters ξ_c and τ_{us} [102–104]

$$U_n = \exp\left[i\alpha_n^a(x)T^a\right], \qquad U_{us} = \exp\left[i\alpha_{us}^a(x)T^a\right]. \tag{2.85}$$

In SCET, it is particularly important that the gauge transformation does not change the scaling of the field. Otherwise they would no longer be described by the EFT. Thus, the gauge transformations must follow the scalings

$$i\partial^{\mu}U_{n}(x) \sim Q(\lambda^{2}, 1, \lambda)U_{n}(x), \qquad i\partial^{\mu}U_{us}(x) \sim Q(\lambda^{2}, \lambda^{2}, \lambda^{2})U_{us}(x).$$
 (2.86)

The collinear gauge transformation can be implemented using a Fourier transform as $\psi(x) \to U(x)\psi(x)$ is equivalent to $\tilde{\psi}(p) \to \int \mathrm{d}q \tilde{U}(p-q)\tilde{\psi}(q)$ which includes a convolution over label momenta. Then the collinear gauge transformations are given by

$$\xi_{n,p}(x) \to U_{n,p-q}(x)\xi_{n,q}(x),$$

$$A_{n,p}^{\mu}(x) \to U_{n,p-q}(x) \left[gA_{n,q-q'}^{\mu}(x) + \delta_{q,q'} \frac{i}{g} \mathcal{D}_{us}^{\mu} \right] U_{n,q'}^{\dagger}(x), \tag{2.87}$$

$$\begin{array}{c} \underbrace{a,\mu}_{\text{SERVINGENERAL STREET}} & b,\nu \\ \hline (p,p_r) & = \frac{-\mathrm{i}\delta^{ab}}{n\cdot p_r\bar{n}\cdot p + p_\perp^2 + \mathrm{i}0} \left[g_{\mu\nu} - \left(1 - \frac{1}{\xi_c}\right)\frac{p_\mu p_\nu}{n\cdot p_r\bar{n}\cdot p + p_\perp^2}\right] \\ \\ a,\mu \\ b,\nu & c,\rho \\ \hline equation & p' \\ \hline p & p' \\ \hline a,\mu & b,\nu \\ c,\rho & d,\sigma \\ \hline equation & d,\sigma \\ \hline c,\rho & d,\sigma \\ \hline equation & d,\sigma \\ equation & d$$

Figure 2.7: $\mathcal{O}(\lambda^0)$ Feynman rules of collinear gluons interacting with ultra-soft gluons. Collinear gluons are springs with a line and ultra-soft gluons are regular springs. The interactions of collinear and ultra-soft quarks among themselves are given by standard QCD Feynman rules with the understanding the gluons have collinear or ultra-soft scaling.

where we left the sum over label momenta implicit. Ultra-soft fields do not transform under collinear gauge transformations to preserve their scaling

$$\psi_{us}(x) \to \psi_{us}(x), \qquad A^{\mu}(x)_{us} \to A^{\mu}_{us}(x).$$
 (2.88)

Further, ultra-soft fields transform under ultra-soft gauge transformations just like standard QCD fields transform under a gauge transformation

$$\psi_{us}(x) \to U_{us}(x)\psi_{us}(x), \qquad A^{\mu}_{us}(x) \to U_{us}(x) \left[A^{\mu}_{us}(x) + \frac{\mathrm{i}}{g} \partial^{\mu} \right] U^{\dagger}_{us}(x).$$
 (2.89)

Collinear fields, on the other hand, transform covariantly under ultra-soft gauge transformation with A_{us} treated as a background field

$$\xi_n(x) \to U_{us}(x)\xi_n(x),$$

$$A_n^{\mu}(x) \to U_{us}(x)A_n^{\mu}(x)U_{us}^{\dagger}(x).$$
(2.90)

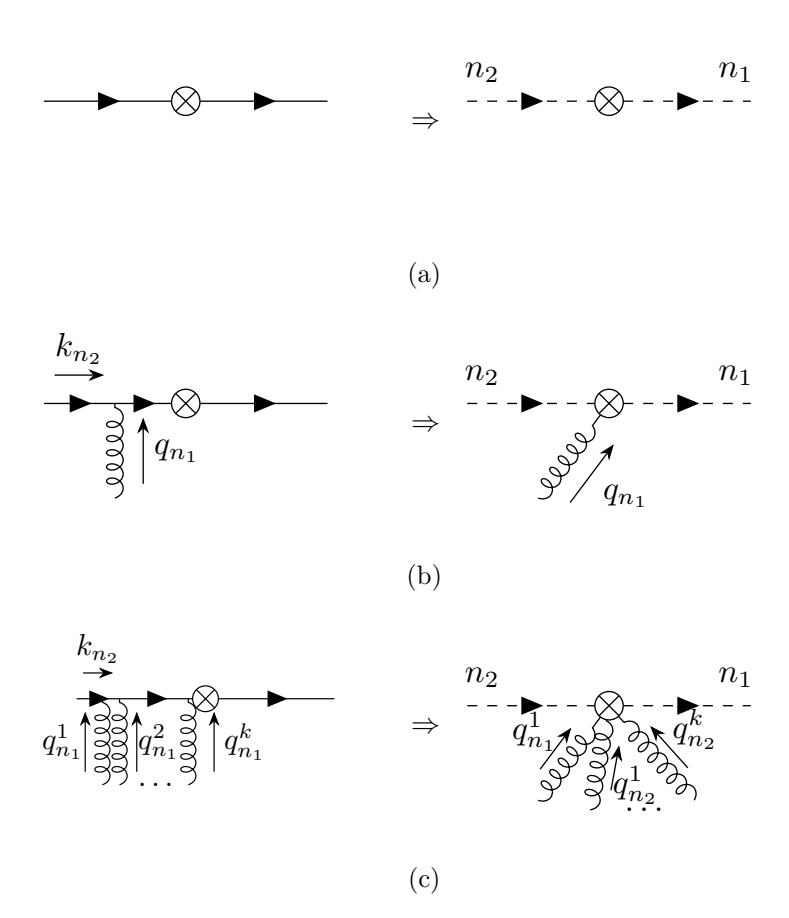


Figure 2.8: Emergence of the collinear Wilson line. (a) Tree-level matching of dijet operator onto SCET. (b) Attachment of an n_1 -collinear gluon to an n_2 collinear quark. (c) Attachment of multiple n_1 -collinear gluons to an n_2 collinear quark.

2.4.3 Collinear Wilson lines

Let us consider of two distinct collinear sectors that are cuopled through the QCD current

$$J_{\rm QCD} = \bar{\psi} \Gamma \psi. \tag{2.91}$$

At tree-level, this is matched onto

$$J_{\text{SCET}} = \bar{\xi}_{n_1} \Gamma \xi_{n_2}, \tag{2.92}$$

where n_1 and n_2 represent the different collinear sectors as shown in figure 2.8a. Next, we want to attach gluons to figure 2.8a: The attachment of n_i -collinear gluons to n_i -collinear quarks is described by the SCET Lagrangian in eq. (2.75). Additionally, we can consider scenarios shown in figures 2.8b and 2.8c where we attach one (or multiple) n_1 -collinear gluon(s) to the n_2 -collinear quark. This diagram cannot be described by the SCET Lagrangian in eq. (2.75) and require new operators beyond eq. (2.92) The matrix element is given by

$$A_{n_1}^{\mu a} \bar{\xi}_{n_1} \Gamma \frac{i(\not q + \not k_{n_2})}{(q + k_{n_2})^2} ig T^a \gamma^{\mu} \xi_{n_2} = \bar{\xi}_{n_1} \Gamma \left(\frac{-g \bar{n}_1 \cdot A_{n_1}}{\bar{n}_1 \cdot q} \right) \xi_{n_2} + \mathcal{O}(\lambda), \tag{2.93}$$

where we expanded the gluon field and all momenta in λ and used that $\psi_i^2 = 0$ and $\psi_i \xi_{n_i} = 0$. Note that the quark propagator is off-shell with

$$(k_{n_2} + q)^2 = 2k_{n_2} \cdot q = (\bar{n}_2 \cdot k_{n_2})(\bar{n}_1 \cdot q_{n_1}) \frac{n_1 \cdot n_2}{2} \gg \lambda^2, \tag{2.94}$$

because $n_2 \cdot n_2 \gg \lambda^2$ and hence must be integrated out. Its effects are captured in an effective operator. Additionally, it is important to highlight that the result with the attached gluon in eq. (2.93) is not power-suppressed but instead contributes at leading order in λ .

We can now go one step further and study multiple gluon attachments shown in figure 2.8c where each attached gluon contributes an off-shell propagator and needs to be integrated out. Summing over all emissions, we can write the SCET current as

$$J_{\text{SCET}} = \bar{\xi}_{n_1} \Gamma W_{n_1} \xi_{n_2}, \tag{2.95}$$

where an *n-collinear Wilson line* in momentum space is defined as

$$W_n = \sum_{k=0} \sum_{\text{perms.}} \frac{(-g)^k}{k!} \left[\frac{\bar{n} \cdot A_n(q_1) \cdots \bar{n} \cdot A_n(q_k)}{(\bar{n} \cdot q_1) \cdots (\bar{n} \cdot \sum_{i=1}^k q_k)} \right]. \tag{2.96}$$

Since we must consider diagrams with crossed gluon lines, we need to include a sum over the permutations of the momenta $\{q_1, \dots q_k\}$. In position space, the *n*-collinear Wilson line is given by

$$W_n(x) = \operatorname{P} \exp \left[ig \int_{-\infty}^0 ds \, \bar{n} \cdot A_n(x + \bar{n}s) \right], \qquad (2.97)$$

with the path-ordering operator P. It can also be convenient to write the Wilson line in a more compact notation using the label operator

$$W_n(x) = \sum_{\text{perms}} \exp\left[\frac{-g}{\bar{n} \cdot \mathcal{P}} \bar{n} \cdot A_n(x)\right]. \tag{2.98}$$

Considering n_1 -collinear gluon attachments to an n_2 -collinear gluon line yields new operators which can be summed up via the replacement

$$W_{n_2} \to W_{n_1} W_{n_2} W_{n_1}^{\dagger},$$
 (2.99)

and vice versa. Returning to the SCET current in eq. (2.95), we can of course also have n_1 -collinear attachments to the n_2 -collinear quark line, yielding

$$J_{\text{SCET}} = \bar{\xi}_{n_1} W_{n_2}^{\dagger} \Gamma W_{n_1} \xi_{n_2}. \tag{2.100}$$

At this point, the Wilson lines appear to the in the wrong order. However, so far we have only considered multiple gluon attachments to a quark line. We can of course also have n_1 -collinear gluon attachments to an n_2 -collinear gluon line and vice versa. Taking all possible $\mathcal{O}(g^2)$ diagrams into account, we find the

$$J_{\text{SCET}} = (\bar{\xi}_{n_1} W_{n_1}) \Gamma(W_{n_2}^{\dagger} \xi_{n_2}) \tag{2.101}$$

with the correct order of Wilson lines. In fact, we can replace all occurrences of the field $\bar{n} \cdot A_n$ by the Wilson line W_n : Using the equation of motion of the Wilson line

$$i\bar{n} \cdot D_n W_n = (\bar{\mathcal{P}} + g\bar{n} \cdot A_n) W_n = 0, \qquad (2.102)$$

allows to write the action of $i\bar{n} \cdot D_n$ and some operator as

$$i\bar{n} \cdot D_n(W_n \mathcal{O}) = (\bar{\mathcal{P}} + g\bar{n} \cdot A_n)W_n \mathcal{O} = [(\bar{\mathcal{P}} + g\bar{n} \cdot A_n)W_n]\mathcal{O} + W_n \bar{\mathcal{P}}\mathcal{O} = W_n \bar{\mathcal{P}}\mathcal{O}. \tag{2.103}$$

This allows to write the collinear quark Lagrangian as

$$\mathcal{L}_{n\xi}^{(0)} = \bar{\xi}_n \left(in \cdot D + i \not \!\! D_{n\perp} W_n^{\dagger} \frac{1}{\bar{\mathcal{P}}} W_n i \not \!\! D_{n\perp} \right) \frac{\not \!\! n}{2} \xi_n. \tag{2.104}$$

An important outcome of writing the Lagrangian $\mathcal{L}_{n\xi}^{(0)}$ in this way is that it is explicitly local at and below the scale $Q\lambda$ because of absence of inverse derivative operators, whereas the non-locality only appears at the short distance scale Q. Note that collinear Wilson lines transform under gauge transformations as

collinear:
$$W_{n,p}(x) \to U_{n,p-q}(x) W_{n,q}(x),$$

ultra-soft: $W_{n,p}(x) \to U_{us}(x) W_{n,q}(x) U_{us}^{\dagger}.$ (2.105)

This transformation behavior exactly cancels the transformation behavior of the collinear gauge fields, guaranteeing that eq. (2.101) is gauge invariant.

2.4.4 Ultra-soft factorization

In the current form of the SCET Lagrangian, the ultra soft gluon still interacts with the collinear fields and prevents a full factorization of the collinear and ultra-soft sectors. Now, consider QCD graphs analogous to figure 2.8 where we attach ultra-soft gluons to either n_1 or n_2 collinear quarks. In this case, the numerator involves $n_2 \cdot A_{us} \sim \lambda^2$ which, though power suppressed, is compensated by the scaling of the quark propagator, $(k_{n_2} + q)^2 = (\bar{n}_2 \cdot k_n 2)(n_2 \cdot q) \sim \lambda^2$, yielding a contribution at leading power. Summing over all possible graphs yields

$$Y_n(x) = P \exp \left[ig \int_{-\infty}^0 ds \, n \cdot A_{us}(x + ns) \right], \qquad (2.106)$$

which describes the emission of an ultra-soft gluon from a collinear quark. Note that the above equation is only valid for incoming collinear particles. For outgoing particles the integral runs over $s \in [0, \infty]$. An ultra-soft emission of a collinear gluon is given by the adjoint representation $\mathcal{Y}_n(x)$ where we replace $A_\mu = A_\mu^a T^a \to A_\mu^a (-\mathrm{i} f^{abc})$.

The ultra-soft Wilson satisfies the following relations

$$in \cdot DY_n = 0, \qquad Y_n Y_n^{\dagger} = \mathbf{1}. \tag{2.107}$$

We can now perform the Bauer-Pirjol-Stewart (BPS) field redefinition [103]

$$\xi_n(x) = Y_n(x)\xi_n^{(0)}(x), \qquad A_n^{\mu} = Y_n(x)A_n^{(0)\mu}(x)Y_n^{\dagger}(x), \qquad c_n^{\mu} = Y_n(x)c_n^{(0)\mu}(x)Y_n^{\dagger}(x).$$
 (2.108)

As Y_n commutes with the label operator, the collinear Wilson line tranforms as

$$W_n(x) \to Y_n(x)W_n^{(0)}(x)Y_n^{\dagger}(x),$$
 (2.109)

where $W_n^{(0)}$ is built from $A_n^{(0)}$. The above equation is analogous to eq. (2.99). We have now explicitly removed all ultra-soft interactions and the remain fields $\xi_n^{(0)}$, $A_n^{(0)}$ and $c_n^{(0)}$ completely decouple and we can write our collinear quark Langrangian as

$$\mathcal{L}_{n\xi}^{(0)} = \bar{\xi}_{n,p}^{(0)} \left[i n \cdot \partial + g n \cdot A_{n,q}^{(0)} + \left(\mathcal{P}_{n\perp} + g \mathcal{A}_{n,q,\perp}^{(0)} \right) W_n^{(0)\dagger} \frac{1}{\bar{\mathcal{P}}} W_n^{(0)} (\mathcal{P}_{n\perp} + g \mathcal{A}_{n,q,\perp}^{(0)}) \right] \frac{\rlap{/}n}{2} \xi_{n,p}^{(0)}, \quad (2.110)$$

which is completely independent of the ultra-soft gluon field. It is easy to show that the same happens for the full leading-order collinear Lagrangian $\mathcal{L}_n^{(0)}$ and the ultra-soft gluon field decouples completely at Lagrangian level

$$\mathcal{L}_{n}^{(0)}[\xi_{n}, A_{n}^{\mu}, c_{n}, n \cdot A_{us}] = \mathcal{L}_{n}^{(0)}[\xi_{n}^{(0)}, A_{n}^{(0), \mu}, c_{n}^{(0)}, 0]. \tag{2.111}$$

The interactions with the ultra-soft gluon field, however, have not disappeared. They simply moved from the Lagrangian into the currents. Let us, for example, consider the SCET current in eq. (2.101)

$$J_{\text{SCET}} = (\bar{\xi}_{n_2} W_{n_2}) \Gamma(W_{n_1}^{\dagger} \xi_{n_1})$$

= $\bar{\xi}_{n_2}^{(0)} W_{n_2}^{(0)} Y_{n_2}^{\dagger} \Gamma Y_{n_1} W_{n_1}^{(0) \dagger} \xi_{n_1}^{(0)}.$ (2.112)

Now, the ultra-soft and n_1 - and n_2 -collinear sectors are fully factorized.

Operator building blocks

At this point it is convenient to define gauge invariant operator building blocks. The $SCET_I$ building blocks are given by the "quark jet field"

$$\chi_n \equiv W_n^{\dagger} \xi_n, \tag{2.113}$$

and the "gluon jet field"

$$\mathcal{B}_{n,\perp}^{\mu} \equiv \frac{1}{g} \left[\frac{1}{\bar{n} \cdot \mathcal{P}} W_n^{\dagger} \left[i\bar{n} \cdot D_n, D_{n,\perp}^{\mu} \right] W_n \right]. \tag{2.114}$$

The two degrees of freedom in the above equation can be interepreted as the physical gluon polarizations. A complete basis of operators to build collinear operators to all orders in λ is given by [111]

$$\xi_n, \qquad \mathcal{B}^{\mu}_{n,\perp}, \qquad \mathcal{P}^{\mu}_{n,\perp}.$$
 (2.115)

All other operators can be expressed in terms of these objects and we can write the SCET current as

$$J_{\text{SCET}} = \bar{\chi}_{n_2} Y_{n_2}^{\dagger} \Gamma Y_{n_1} \chi_{n_1}. \tag{2.116}$$

2.4.5 SCET_{II} and rapidity divergences

In SCET_{II}, soft and collinear modes which share the same virtuality $p_s^2 = p_n^2 = \lambda^2 Q^2$ contribute to the measurement. The interaction of soft gluons with collinear particles puts the resulting particle off the mass-shell

$$p = p_n + p_s \sim Q(\lambda, 1, \lambda). \tag{2.117}$$

These off-shell particles need to be integrated out. This gives rise to the soft Wilson line

$$S_n(x) = \operatorname{P} \exp \left[ig \int_{-\infty}^0 ds \, n \cdot A_s(x + ns) \right]$$
$$= \sum_{\text{perms}} \exp \left[\frac{-g}{n \cdot \mathcal{P}} n \cdot A_s(x) \right]. \tag{2.118}$$

The soft Wilson line appears in currents to ensure gauge invariance under soft gauge transformations. The adjoint soft Wilson line is given by

$$T^a \mathcal{S}_n^{ab} = S_n T^b S_n^{\dagger}. \tag{2.119}$$

SCET_{II} can be constructed by a subsequent matching [112]

$$QCD \to SCET_I \to SCET_{II}.$$
 (2.120)

First, we match QCD onto SCET_I with a power-counting parameter $\sqrt{\lambda}$. Then we have hard-collinear and ultra-soft modes which scale as $p_{hc} \sim Q(\lambda, 1, \sqrt{\lambda})$ and $p_{us} \sim Q(\lambda, \lambda, \lambda)$, respectively. Next, we perform the BPS field redefinition. In the last step, we match onto SCET_{II} by lowering the virtuality of the collinear modes and taking $Y_n \to S_n$

$$p_{hc} \sim Q(\lambda, 1, \sqrt{\lambda}) \rightarrow p_n \sim Q(\lambda^2, 1, \lambda),$$

 $p_{us} \sim Q(\lambda, \lambda, \lambda) \rightarrow p_s \sim Q(\lambda, \lambda, \lambda).$ (2.121)

As soft and collinear modes have the same virtuality, they live on the same trajectory in figure 2.4 and are only separated by their rapidity $y = \log(p^-/p^+)/2$. This separation explicitly breaks boost invariance and introduces divergences when $p^-/p^+ \to 0$ and $p^-/p^+ \to \infty$ [113–117]. These rapidity divergences arise from an overlap of the collinear and soft integrals. A typical rapidity divergent integral has the from

$$\mathcal{I}_n = \int_0^\infty \frac{\mathrm{d}k^-}{k^-} R(k, \eta), \qquad (2.122)$$

where $R(k,\eta)$ is the regulator function. The resulting integrals cannot be regulated using dimensional regularization and require a rapidity regulator which allows to distinguish the different modes. Since the full theory is free of rapidity divergences, they have to cancel when combining soft and collinear sectors. There is a variety of regulators that have been used in the literature such as the η -regulator [113,118,119], hard cutoffs [115,120–122], the δ -regulator [123], tilting Wilson lines off the lightcone [124], the analytic regulator [125–127], the exponential regulator [128] or the pure rapidity regulator [129]. In this thesis we employ the η -regulator and the pure rapidity regulator where the latter is particularly well suited for next-to-leading power calculations.

The η -regulator regulates the k^z momentum of emissions by modifying the Wilson Lines to

$$W_n(x) = \sum_{\text{perms}} \exp\left[\frac{-g}{\bar{n} \cdot \mathcal{P}} \frac{w^2 |2\mathcal{P}^z|^{-\eta}}{\nu^{-\eta}} \bar{n} \cdot A_n(x)\right],$$

$$S_n(x) = \sum_{\text{perms}} \exp\left[\frac{-g}{n \cdot \mathcal{P}} \frac{w |2\mathcal{P}^z|^{-\frac{\eta}{2}}}{\nu^{-\frac{\eta}{2}}} n \cdot A_s(x)\right],$$
(2.123)

where we introduced the rapidity regularization scale ν . Similarly to the ϵ -poles from dimensional regularization, the rapidity divergences will appear in the from of η poles after integrating and expanding in η . We also inserted a book-keeping parameter w, which will be set to 1 in the end. It ensures that the regulated Wilson lines are independent of ν

$$\nu \frac{\mathrm{d}w(\nu)}{\mathrm{d}\nu} = -\frac{\eta}{2}w(\nu),\tag{2.124}$$

analogously to the QCD β -function in eq. (2.16). The regulator function for the η -regulator is given by

$$R(k,\eta) = w^2 \left| \frac{2k^z}{\nu} \right|^{-\eta} = w^2 \left| \frac{k^- - k^+}{\nu} \right|^{-\eta}.$$
 (2.125)

In the *n*-collinear limit, the k^- dominates and we can write

$$R_n(k,\eta) = w^2 \left| \frac{k^-}{\nu} \right|^{-\eta}$$
 (2.126)

The \bar{n} -collinear limit yields the same result with $k^- \to k^+$. In the soft limit, the regulator is homogeneous in λ and will not be expanded.

The pure rapidity regulator is similar to the but instead of the momentum k^z it regulates the rapidity y_k of the momentum k^{μ} . The regulator function is then given by

$$R_Y(k,\eta) = w^2 v^{\eta} \left| \frac{k^-}{k^+} \right|^{-\frac{\eta}{2}}.$$
 (2.127)

The rapidity scale v is dimensionless but apart from that analogous to the scale v. An important feature of the pure rapidity regulator is that it renders typical soft integrals scaleless as we will see when considering b-quark effects in gluon fusion later in this thesis.



Figure 2.9: Higgs production via gluon fusion (left) and quark annihilation (right) with one additional emission.

2.5 Factorization and resummation

2.5.1 Resummation of large logarithms

In this thesis, we are interested in the transverse momentum spectra of final state particles produced in hadron collisions. Let us consider a Higgs boson that is produced at the LHC, either via gluon fusion or quark-antiquark annihilation. At Born-level the Higgs boson is produced at rest, such that $q_T = 0$, resulting in a trivial q_T spectrum. We therefore need at least one emission the Higgs boson can recoil against to pick up a transverse momentum as illustrated in figure 2.9. Most Higgs bosons are produced at small q_T . Hence, we are most interested in the cross section for $q_T \ll Q = m_H$. In general the cross section will contain large logarithms of the form

$$\log \frac{q_T}{Q} = \log \frac{q_T}{\mu} + \log \frac{\mu}{Q},\tag{2.128}$$

where the additional scale μ has been introduced in order to split up the logarithm which allows to separate the high and the low scale. Let us consider a toy example where the cross section can then be written in a factorized way as

$$\sigma(q_T, Q) = H(Q, \mu) F(q_T, \mu) + \mathcal{O}\left(\frac{q_T^2}{Q^2}\right).$$
 (2.129)

Here, $H(Q, \mu)$ is the hard function capturing all physics at the hard scale whereas $F(q_T, \mu)$ describes the dynamics at the low scale q_T . Each power of strong coupling comes with a large logarithm –to a possibly different power. This leads to a complete break down of the perturbative series for small values of q_T . More precisely, the cross section involves $\delta(q_T)$ distributions and logarithmic plus distributions $\lceil \log^n(q_T/Q)/Q \rceil_+$ in the $q_T \to 0$ limit.

In order to arrive at a meaningful prediction, these large logarithms must be resummed using the renormalization group equations (RGEs) of the factorized ingredients. The RGEs govern the μ dependence of the renormalized functions $H(Q, \mu)$ and $F(q_T, \mu)$. They read

$$\mu \frac{\mathrm{d}}{\mathrm{d}\mu} H(Q,\mu) = \gamma_H H(Q,\mu), \qquad \mu \frac{\mathrm{d}}{\mathrm{d}\mu} F(q_T,\mu) = \gamma_F F(q_T,\mu), \tag{2.130}$$

where $\gamma_{H,F}$ are the anomalous dimensions of the respective functions. Then, the all-order resummation is archived by evaluating $H(Q,\mu)$ and $F(q_T,\mu)$ at their canonical scales

$$\mu_H = Q, \qquad \mu_F = q_T, \tag{2.131}$$

which are chosen such that the logarithms are minimized at this scale. Next, $H(Q, \mu)$ and $F(q_T, \mu)$ are evolved to a common scale μ by solving the RGEs. The resummed cross section is

then given by

$$\sigma^{\text{res}}(q_T, Q) = H(Q, \mu_H) U_H(\mu_H, \mu) F(q_T, \mu_F) U_F(\mu_F, \mu). \tag{2.132}$$

The renormalization group evolution factors, also called evolution kernels, are given by

$$U_X(\mu_X, \mu) = \exp\left[\int_{\mu_X}^{\mu} \frac{\mathrm{d}\mu'}{\mu'} \gamma_X(\mu')\right],\tag{2.133}$$

with X = H, F. In particular, the functions $H(Q, \mu_H)$ and $F(q_T, \mu_F)$ are free of large logarithms at their respective canonical scale. The large logarithms are exponentiated in kernels which restores the convergence of the perturbative series. This procedure is referred to as resummation. The resummation generates a Sudakov peak in the cross section before it goes to 0 as $q_T \to 0$ which is illustrated in figure 2.10.

As the physical cross section does not depend on the scale μ

$$\mu \frac{\mathrm{d}}{\mathrm{d}\mu} \sigma(q_T, Q) = 0, \tag{2.134}$$

we can use RG consistency as a cross check

$$\gamma_H = -\gamma_F, \tag{2.135}$$

which in this toy example states that the anomalous dimensions must cancel.

Turning away from our toy example, the anomalous dimension of the hard function actually has a more complicated form

$$\gamma_H^i = 4\Gamma_{\text{cusp}}^i \left[\alpha_s(\mu)\right] \log \frac{Q}{\mu} + \gamma_H^i \left[\alpha_s(\mu)\right], \tag{2.136}$$

where the cusp anomalous dimension, Γ^i_{cusp} , is universal among processes and only depends on the color representation of the annihilating parton i. The non-cusp anomalous dimension, γ^i_H , on the other hand, is process dependent. We give the explicit expressions of the cusp and non-cusp anomalous dimensions in appendix B.1. The specific structure of the hard anomalous dimension containing a $\log Q/\mu$ allows for the resummation of Sudakov double-logarithms $\alpha^n_s \log^m(q_T/Q)$ with $m \leq 2n$. These logarithms arise in high-energy processes when there is an overlap of soft and collinear regions of phase space.

Next, we analyze the structure of a generic perturbative series. The standard, so-called fixed-order, counting counts powers of the strong coupling α_s

$$\sigma(q_T) \sim 1 + \frac{\alpha_s}{4\pi} \left[c_{12} \log^2 \frac{q_T}{Q} + c_{11} \log \frac{q_T}{Q} + c_{10} \right] \qquad \text{NLO}$$

$$+ \left(\frac{\alpha_s}{4\pi} \right)^2 \left[c_{24} \log^4 \frac{q_T}{Q} + c_{23} \log^3 \frac{q_T}{Q} + c_{22} \log^2 \frac{q_T}{Q} + \dots \right] \qquad \text{NNLO}$$

$$+ \left(\frac{\alpha_s}{4\pi} \right)^3 \left[c_{36} \log^6 \frac{q_T}{Q} + c_{35} \log^5 \frac{q_T}{Q} + c_{34} \log^4 \frac{q_T}{Q} + \dots \right] \qquad \text{N}^3 \text{LO} \qquad (2.137)$$

$$\text{LL} \qquad \text{NLL} \qquad \text{NNLL}$$

However, for small values of q_T terms scaling as $\alpha_s^n \log^m(q_T/Q) \gtrsim 1$ are no longer suppressed. Hence, we need to adapt our counting to capture the leading logarithmic terms where we count

	Boundary	Anomalous dimensions		FO matching
Order	conditions	$\gamma_i \text{ (noncusp)}$	$\Gamma_{\rm cusp},\beta$	(nonsingular)
LL	1	-	1-loop	-
NLL	1	1-loop	2-loop	-
NLL' (+NLO)	α_s	1-loop	2-loop	α_s
NNLL (+NLO)	α_s	2-loop	3-loop	α_s
NNLL' (+NNLO)	α_s^2	2-loop	3-loop	α_s^2
$N^3LL (+NNLO)$	α_s^2	3-loop	4-loop	α_s^2
$\overline{\mathrm{N^3LL'} \; (+\mathrm{N^3LO})}$	α_s^3	3-loop	4-loop	α_s^3
$N^4LL (+N^3LO)$	α_s^3	4-loop	5-loop	α_s^3

Table 2.4: Definition of resummation orders. The $(+N^nLO)$ in the order refers to whether or not the nonsingular $\mathcal{O}(\alpha_s^n)$ corrections in the last column are included.

columns instead of lines. The first column captures the the leading-logarithmic order (LL), the second column the next-to-leading-logarithmic order (NLL) and so forth.

In order to archive LL resummation, we only require the leading contribution of the cusp anomalous dimension as it is enhanced by a logarithm compared to the non-cusp contribution as well as the leading term of the QCD- β -function. Starting from NNLL, we also need to include the $\mathcal{O}(\alpha_s)$ contribution of the functions evaluated at there canonical scales, $H(Q, \mu_H)$ and $F(q_T, \mu_F)$. This contributions are referred to as boundary condition or boundary term. A summary of the ingredients needed for resummation up N⁴LL is given in table 2.4.

2.5.2 Matching to fixed order

The resummed cross section provides a meaningful for small values of q_T . In addition to the leading-power contributions, which can be resummed by making use of the factorization theorem in eq. (2.132), we also have to include the nonsingular power corrections of q_T^2/Q^2 in eq. (2.129) which become important for large values of q_T . To obtain a prediction that is valid across the entire q_T range, we add the resummed singular contributions and the fixed-order nonsingular terms. The resulting matched cross section is given by

$$\sigma(q_T, Q) = \sigma^{\text{res}}(q_T, Q) + \sigma^{\text{nons}}(q_T, Q)$$

$$= \sigma^{\text{res}}(q_T, Q) + \left[\sigma^{\text{FO}}(q_T, Q) - \sigma^{\text{sing}}(q_T, Q)\right]. \tag{2.138}$$

The first line is equivalent to eq. (2.129), using the all-order resummed result $\sigma^{\rm res}$ for the leading-power term. By the singular cross section, $\sigma^{\rm sing}(q_T,Q)$, we mean the fixed-order reexpansion of the resummed cross section where all terms are evaluated at the fixed-order scale $\mu_{\rm FO} \sim Q$. To avoid double counting, the overlap of the resummed and singular contributions has to be subtracted. The nonsingular cross section $\sigma^{\rm nons}(q_T,Q)$ is obtained as shown in the second line in eq. (2.138), i.e. by using eq. (2.129) at fixed order and subtracting the fixed-order singular terms from the full fixed-order result, where both are evaluated at common fixed-order scales $\mu_{\rm FO}$. For small $q_T \ll m_H$, the nonsingular terms are a small power correction and it is sufficient to include them at fixed order despite the fact that the singular terms are resummed there. For the nonsingular to be indeed power suppressed it is essential that $\sigma^{\rm FO}$ and $\sigma^{\rm sing}$ are evaluated at the same fixed order, such that $\sigma^{\rm sing}$ exactly contains and cancels the singular terms of $\sigma^{\rm FO}$.

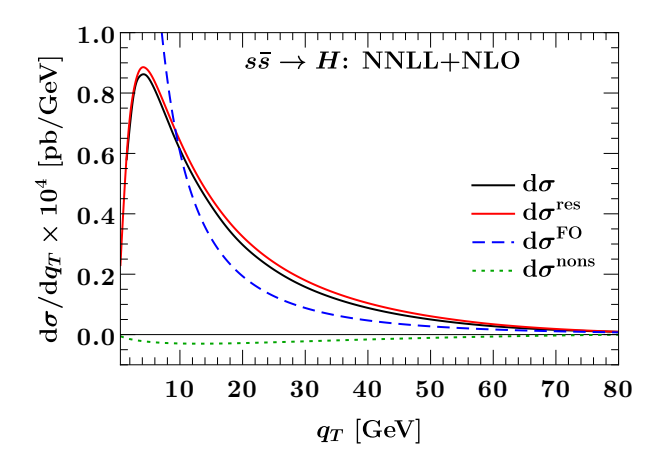


Figure 2.10: Matched cross section for quark initiated Higgs production at NNLL+NLO.

If this is cancellation is correctly taken care of the NⁿLL accuracy of the resummed result is preserved in the low q_T region.

On the other hand, as q_T approaches $q_T \sim Q$, the distinction between singular and nonsingular becomes arbitrary and only the full fixed-order result in $\sigma^{\rm FO}$ is physically meaningful. To recover the correct $\sigma^{\rm FO}$ in this limit, $\sigma^{\rm res}(\mu_{\rm res})$ and $\sigma^{\rm sing}(\mu_{\rm FO})$ must cancel each other in eq. (2.138). We require this cancellation to be exact with no leftover higher-order terms in α_s , because for $q_T \sim Q$ the resummed terms are unphysical and typically become numerically much larger than the actual physical result given by $\sigma^{\rm FO}$. This requires the turning off of the resummation in $\sigma^{\rm res}(\mu_{\rm res})$ – in so doing, one guarantees that the result becomes equal to the fixed-order $\sigma^{\rm sing}(\mu_{\rm FO})$ and preserves the fixed-order N^mLO accuracy of the matched result. Considering the first line of eq. (2.138), this implies that for $q_T \sim m_H$ there are typically large numerical cancellations between the singular and nonsingular contributions.

In summary, in order to have a consistent description of the cross section for all values of q_T , the terms in eq. (2.138) are required to satisfy two conditions: firstly, $\sigma^{\rm sing}$ and $\sigma^{\rm FO}$ must be evaluated at the same fixed order; secondly, $\sigma^{\rm sing}$ and $\sigma^{\rm res}$ must become equal in the limit where the resummation in $\sigma^{\rm res}$ is turned off.

The most natural way to turn off the resummation in $\sigma^{\rm res}(\mu_{\rm res})$ is to set all boundary scales to the common fixed-order scales $\mu_{\rm FO}$, i.e. in our notation $\mu_{\rm res} = \mu_{\rm FO}$. The second condition above thus requires $\sigma^{\rm res}(\mu_{\rm res} = \mu_{\rm FO}) = \sigma^{\rm sing}(\mu_{\rm FO})$. In order for the first condition above to be fulfilled it is necessary that for a given resummation order nonsingular matching corrections of the corresponding order are included. Namely, the α_s order of the boundary conditions in the resummed result must match the α_s order of the full and nonsingular results, which are the orders shown in the last column of table 2.4. The accuracy of the matched result is then given by $N^n LL + N^m LO$.

Figure 2.10 shows the matched cross section for quark initiated Higgs production where we chose the $s\bar{s}\to H$ channel for illustrative purposes. The full-fixed order cross section is shown in dashed blue and diverges for $q_T\lesssim 15\,\mathrm{GeV}$. The non-singular (dotted green) is power suppressed and indeed goes to 0 for $q_T\to 0$. The resummed shown in red has Sudakov peak at $q_T\sim 5\,\mathrm{GeV}$ before turning to zero. Finally, the matched cross section in equal to resummed at the very beginning of the spectrum. At the peak the matched slightly differs from the resummed which is due to non-singular contribution that are included. At large values of q_T , the matched becomes

equal to the full fixed-order prediction.

2.5.3 Factorization and resummation for q_T spectra

In this thesis, we focus on resummed transverse momentum (q_T) spectra of color singlet processes which are dominated by soft and collinear radiation. The color-singlet finial state particle recoils against soft and collinear initial state radiation and picks up a transverse momentum. Studying the q_T spectra at experiments allows to extract more information from the experimental data—such as the shape of the spectrum—as e.g. a total cross section would. The relevant theory framework to describe this is provided by SCET_{II} with the power-counting parameter $\lambda = q_T/Q$. The factorization of the leading-power q_T spectrum was first established by Collins, Soper and Sterman [130–132], and was further elaborated upon and extended in refs. [124,133,134]. Here, we employ the framework of SCET, in which q_T factorization was formulated in refs. [113,119, 128,135], and which is equivalent to the modern formulation in ref. [124].

The factorized form for the transverse momentum spectrum, often also referred to as transverse momentum dependent (TMD) factorization is given by

$$\frac{\mathrm{d}\sigma^{\mathrm{sing}}}{\mathrm{d}Y\mathrm{d}^2\vec{q}_T} = \sum_{a,b} H_{ab}(Q^2;\mu)[B_a \otimes B_b \otimes S_{ab}](x_a, x_b, \vec{q}_T; \mu), \qquad (2.139)$$

where the kinematic quantities $\omega_{a,b}$ and $x_{a,b}$ are given by

$$\omega_a = Qe^{+Y}, \quad \omega_b = Qe^{-Y} \quad \text{and} \quad x_{a,b} = \frac{\omega_{a,b}}{E_{cm}}.$$
 (2.140)

Physically, x_i is the longitudinal momentum fraction of the parton i and ω_i is the large lightcone momentum component of the parton in the lab frame.

The process dependence is encoded in the hard function $H_{ab}(Q^2, \mu)$. It describes the underlying hard interaction producing the color singlet particle via $ab \to X$ where the sum runs over the available parton channels a, b.

The factor $[B_a \otimes B_b \otimes S_{ab}]$ describes physics at the low scale $\mu \sim q_T$. The beam function B_i describes a collinear parton i with transverse momentum \vec{k}_i and longitudinal momentum ω_i originatizing from a proton with collinear momentum $P_n^{\mu} = P_n^- n^{\mu}/2$. In SCET, the bare quark and gluon beam functions are defined as proton matrix elements of collinear fields

$$B_{q}\left(\frac{\omega}{P_{n}^{-}},\vec{k}\right) = \theta(\omega)\frac{1}{2}\sum_{\text{spin}}\langle p_{n}|\bar{\chi}_{q,n}(0)[\delta(\omega-\bar{\mathcal{P}})\delta^{2}(\vec{k}-\vec{\mathcal{P}}_{\perp})\frac{\vec{n}}{2}\chi_{q,n}(0)]|p_{n}\rangle,$$

$$B_{g}^{\mu\nu}\left(\frac{\omega}{P_{n}^{-}},\vec{k}\right) = \theta(\omega)\omega\frac{1}{2}\sum_{\text{spin}}\langle p_{n}|\mathcal{B}_{n,\perp}^{\mu}(x)[\delta(\omega-\bar{\mathcal{P}})\delta^{2}(\vec{k}-\vec{\mathcal{P}}_{\perp})\mathcal{B}_{n,\perp}^{\nu}(0)]|p_{n}\rangle, \tag{2.141}$$

where the gluon beam function has a non-trivial polarized contribution $\propto k_g^{\mu} k_g^{\nu}/k_g^2 - g_{\perp}^{\mu\nu}/2$ due to the vectorial nature of the measurements [136]. We suppressed the Lorentz indices in eq. (2.139) for brevity.

The the soft function S_{ab} describes soft radiation with total transverse momentum \vec{k}_s . It is given in terms of a vacuum expectation value of Wilson lines

$$S_{qq}(\vec{k}) = \frac{1}{N_c} \langle 0 | \operatorname{Tr} \{ \bar{T}[S_{\bar{n}}^{\dagger}(x) S_n(x)] \delta^2(\vec{k} - \vec{\mathcal{P}}_{\perp}) T[S_{\bar{n}}^{\dagger}(0) S_n(0)] \}$$

$$S_{gg}(\vec{k}) = \frac{1}{N_c^2 - 1} \langle 0 | \operatorname{Tr} \{ \bar{T}[S_{\bar{n}}^{\dagger}(x) S_n(x)] \delta^2(\vec{k} - \vec{\mathcal{P}}_{\perp}) T[S_{\bar{n}}^{\dagger}(0) S_n(0)] \}.$$
(2.142)

Note that the soft function is specific to color singlet processes.

Momentum conservation in the transverse plane implies that the sum of \vec{k}_a , \vec{k}_b , \vec{k}_s must be equal to the measured final state transverse momentum \vec{q}_T , leading to the convolution structure in of the factor $[B_a \otimes B_b \otimes S_{ab}]$

$$[B_a \otimes B_b \otimes S_{ab}](x_a, x_b, \vec{q}_T; \mu) \equiv \int d^2 \vec{k}_a d^2 \vec{k}_b d^2 \vec{k}_s \, \delta^2(\vec{q}_T - \vec{k}_a - \vec{k}_b - \vec{k}_s)$$

$$\times B_a(x_a, \vec{k}_a; \mu, \nu/\omega_a) \, B_b(x_b, \vec{k}_b; \mu, \nu/\omega_b) \, S_{ab}(\vec{k}_s; \mu, \nu) \,.$$
(2.143)

The functions in eq. (2.143) are universal objects in \vec{q}_T factorization, independent of the details of the hard process. The above equation can be futher simplified by applying azimuthal symmetry: the soft functions in eq. (2.142) and the quark beam function B_q are azimuthally symmetric. Thus their Fourier transform only depends on the magnitude of $b_T \equiv |\vec{b}_T|$. The gluon beam function can be split in two orthogonal contributions, $k_g^{\mu} k_g^{\nu}/k_g^2$ and $g_{\perp}^{\mu\nu}/2$. The coefficients of these contributions again only depend on b_T in Fourier space. Then eq. (2.143) simplifies to

$$[B_a \otimes B_b \otimes S_{ab}](x_a, x_b, \vec{q}_T; \mu)$$

$$= \frac{1}{2\pi} \int_0^\infty db_T b_T J_0(b_T q_T) \tilde{B}_a(x_a, b_T; \mu, \nu/\omega_a) \, \tilde{B}_b(x_b, b_T; \mu, \nu/\omega_b) \, \tilde{S}_{ab}(b_T; \mu, \nu) , \qquad (2.144)$$

where J_0 is the zeroth Bessel function of the first kind.

Renormalization of beam and soft functions

In this section, we will discuss briefly the renormalization of the hard, beam and soft functions. For more details we refer to refs. [137, 138]. The hard function is renormalized as

$$H^{\text{bare}}(Q) = Z_H(Q, \mu) H(Q, \mu)$$
(2.145)

with the counterterm Z_H . The RGE and the running of the hard function were already discussed in section 2.5.1.

As we are working in SCET_{II}, there will be rapidity divergences arising from on overlap of soft and collinear regions that need to be regulated. This is denoted by the additional dependence on the rapidity scale ν of beam and soft functions in eq. (2.143). The scale ν is analogous to the Collins-Soper scale ζ used in ref. [130]. For the q_T spectrum, we employ the exponential regulator from ref. [128]. Up to two loops it yields the same results as the η regulator used in refs. [113,119]. The rapidity divergences are sensitive to q_T and therefore renormalized in a convolution. Note that RGEs for gluon and quark beam and soft functions have the same structure. We will therefore omit the q and g indices.

The bare functions are renormalized as

$$B^{\text{bare}}(\omega, \vec{p}_T) = \int d^2 \vec{k}_T Z_B(\vec{p}_T - \vec{k}_T, \omega, \mu, \nu) B(\omega, \vec{k}_T, \mu, \nu)$$
(2.146)

$$S^{\text{bare}}(\vec{p}_T) = \int d^2 \vec{k}_T Z_S(\vec{p}_T - \vec{k}_T, \omega, \mu, \nu) S(\vec{k}_T, \mu, \nu)$$
 (2.147)

where Z_X again denote the counterterms. The RGEs are given by

$$\mu \frac{\mathrm{d}}{\mathrm{d}\mu} B(\omega, \vec{p}_T, \mu, \nu) = \gamma_B(\omega, \mu, \nu) B(\omega, \vec{p}_T, \mu, \nu)$$
 (2.148)

$$\mu \frac{\mathrm{d}}{\mathrm{d}\mu} S(\vec{p}_T, \mu, \nu) = \gamma_S(\mu, \nu) S(\vec{p}_T, \mu, \nu). \tag{2.149}$$

The μ -anomalous dimensions of beam and soft functions have the all-order form

$$\gamma_B(\omega, \mu, \nu) = 2\Gamma_{\text{cusp}} \left[\alpha_s(\mu) \right] \log \frac{\nu}{\omega} + \gamma_B \left[\alpha_s(\mu) \right], \tag{2.150}$$

$$\gamma_S(\mu, \nu) = 4\Gamma_{\text{cusp}} \left[\alpha_s(\mu) \right] \log \frac{\mu}{\nu} + \gamma_S \left[\alpha_s(\mu) \right]. \tag{2.151}$$

The μ independence of the physical cross section is given by the RG consistency relation

$$\gamma_H(\alpha_s) + 2\gamma_B(\alpha_s) + \gamma_S(\alpha_s) = 0, \qquad (2.152)$$

where $\gamma_H(\alpha_s)$ is the noncusp anomalous dimension of the hard function. The rapidity RGEs are given in terms of convolutions in \vec{k}_T

$$\nu \frac{\mathrm{d}}{\mathrm{d}\nu} B(\omega, \vec{p}_T, \mu, \nu) = \int \mathrm{d}^2 \vec{k}_T \, \gamma_{\nu, B}(\vec{p}_T - \vec{k}_T, \mu, \nu) B(\omega, \vec{k}_T, \mu, \nu), \qquad (2.153)$$

$$\nu \frac{\mathrm{d}}{\mathrm{d}\nu} S(\vec{p}_T, \mu, \nu) = \int \mathrm{d}^2 \vec{k}_T \, \gamma_{\nu, S}(\vec{p}_T - \vec{k}_T, \mu, \nu) S(\vec{p}_T, \mu, \nu). \tag{2.154}$$

Just as for the resummation scale μ , the cross section has to be independent of the rapidity scale ν . This argument implies that there is only one rapidity anomalous dimension that we take to be

$$\gamma_{\nu}(\vec{p}_T, \mu) \equiv \gamma_{\nu,S}(\vec{p}_T, \mu) = -2\gamma_{\nu,B}(\vec{p}_T, \mu).$$
 (2.155)

At this point is more convenient switch to b_T space where it is easy to see that the μ and ν RGEs from a coupled system of equations

$$\mu \frac{\mathrm{d}}{\mathrm{d}\mu} \tilde{B}(\omega, b_T, \mu, \nu) = \tilde{\gamma}_B(\omega, \mu, \nu) \tilde{B}(\omega, b_T, \mu, \nu), \qquad \mu \frac{\mathrm{d}}{\mathrm{d}\mu} \tilde{S}(b_T, \mu, \nu) = \tilde{\gamma}_S(\mu, \nu) \tilde{S}(b_T, \mu, \nu),$$

$$\nu \frac{\mathrm{d}}{\mathrm{d}\nu} \tilde{B}(\omega, b_T, \mu, \nu) = -\frac{1}{2} \tilde{\gamma}_{\nu}(b_T, \mu) \tilde{B}(\omega, b_T, \mu, \nu), \qquad \nu \frac{\mathrm{d}}{\mathrm{d}\nu} \tilde{S}(b_T, \mu, \nu) = \tilde{\gamma}_{\nu}(b_T, \mu) \tilde{S}(b_T, \mu, \nu).$$

$$(2.156)$$

We can take the μ and ν derivatives of the soft RGEs to relate the anomalous dimensions yielding

$$\mu \frac{\mathrm{d}}{\mathrm{d}\mu} \gamma_{\nu}(b_T, \mu) = \nu \frac{\mathrm{d}}{\mathrm{d}\nu} \gamma_S(\mu, \nu) = -4\Gamma_{\mathrm{cusp}} [\alpha_s(\mu)], \qquad (2.157)$$

where we used the fact that the μ and ν derivates of the soft function commute. The above equation also serves as RGE for $\gamma_{\nu}(b_T, \mu)$ which needs to be resummed itself if the rapidity evolution takes place at a scale $\mu \gg \mu_0 \sim 1/b_T$.

Canonical scales and resummation

The canonical scales for hard, beam and soft functions in q_T space are given by

virtuality:
$$\mu_H \sim Q$$
, $\mu_B \sim q_T$, $\mu_S \sim q_T$, $\mu_0 \sim q_T$
rapidity: $\nu_B \sim Q$, $\nu_S \sim q_T$. (2.158)

Due to the vectorial structure of \vec{q}_T , the resummation in q_T is very challenging [139]. As shown in ref. [137], the exact solution for the RG evolution in \vec{q}_T space in terms of distributions is equivalent to this canonical solution in b_T space modulo different conventions for the boundary conditions. Since the latter is much easier to obtain, we also use it here, as is often done. The

resummed singular \vec{q}_T spectrum, $d\sigma^{\rm res}$, is then obtained as the inverse Fourier transform of the canonically resummed b_T space result, $d\tilde{\sigma}^{\rm res}(\vec{b}_T)$,

$$\frac{\mathrm{d}\sigma^{\mathrm{res}}}{\mathrm{d}Y\mathrm{d}^2\vec{q}_T} = \int \frac{\mathrm{d}^2\vec{b}_T}{(2\pi)^2} \, e^{-\mathrm{i}\vec{b}_T\cdot\vec{q}_T} \quad \frac{\mathrm{d}\tilde{\sigma}^{\mathrm{res}}(\vec{b}_T)}{\mathrm{d}Y\mathrm{d}^2\vec{b}_T} \, .$$

The canonical boundary scales in b_T space are given by

$$\mu_H = Q, \quad \mu_B = b_0/b_T, \quad \mu_S = b_0/b_T, \quad \mu_0 = b_0/b_T,$$

$$\nu_B = Q, \quad \nu_S = b_0/b_T, \qquad (2.159)$$

where we choose the convention $b_0 \equiv 2e^{-\gamma_E} \approx 1.12291$. We can now evaluate the functions in the factorization theorem at their canonical scales and use the RGEs in eq. (2.153) to evolve them to common scales μ and ν . The resummed cross section is then given by

$$\frac{\mathrm{d}\sigma^{\mathrm{res}}}{\mathrm{d}Y\mathrm{d}^{2}\vec{q}_{T}} = \int \frac{\mathrm{d}^{2}\vec{b}_{T}}{(2\pi)^{2}} e^{-\mathrm{i}\vec{b}_{T}\cdot\vec{q}_{T}} H_{ab}(Q^{2},\mu_{H})\tilde{B}_{a}(\omega_{a},b_{T},\mu_{B},\nu_{B})\tilde{B}_{b}(\omega_{b},b_{T},\mu_{B},\nu_{B})\tilde{S}(b_{T},\mu_{S},\nu_{S})$$

$$\times \exp\left[\int_{\mu_{H}}^{\mu} \frac{\mathrm{d}\mu'}{\mu'} \gamma_{H}(Q,\mu') + 2\int_{\mu_{B}}^{\mu} \frac{\mathrm{d}\mu'}{\mu'} \gamma_{B}(\omega,\mu',\nu_{B}) + \int_{\mu_{S}}^{\mu} \frac{\mathrm{d}\mu'}{\mu'} \gamma_{S}(\mu',\nu_{S})\right]$$

$$\times \exp\left\{\log\frac{\nu_{B}}{\nu_{S}} \left[\int_{\mu_{0}}^{\mu} \frac{\mathrm{d}\mu'}{\mu'} \gamma_{\nu}(b_{T},\mu')\right]\right\}.$$
(2.160)

Here the first line contains the fixed-order boundary conditions of the hard beam and soft functions where each of them is evaluated at their canonical scales. The second line describes the evolution from the canonical scales μ_X to a common scale μ where all large logarithms of μ_H/μ_B and μ_H/μ_S are being resummed. The last line governs the rapidity evolution which resums logarithms of ν_B/ν_S including the evolution of the rapidity anomalous dimension from μ_0 to μ . The relevant anomalous dimensions are given in appendix B.1. Eq. (2.160) is the main result of this section and will be used to obtain the q_T spectrum for quark initiated Higgs production in chapter 3.

2.5.4 Factorization of N-jettiness

The resummation of the transverse momentum q_T plays an important role when measuring color singlet processes. In these processes, the hadronic radiation is not measured directly; rather, it is reconstructed from the recoil of the color-singlet state which could for example be a Higgs boson. Event shape observables take a different approach and aim to describe the geometry of the final-state particles after the event. A famous example of these kinds of observables is the N-jettiness observable [140]. It describes how well a final is described by an event with N hard jets. N-jettiness is most often defined is as

$$\mathcal{T}_N = \sum_i \min_m \left\{ \frac{2q_m \cdot p_i}{Q_m} \right\} \,, \tag{2.161}$$

where the sum runs over the four-momenta of all colored particles p_i^{μ} , the minimization over $m = \{a, b, 1, ..., N\}$ runs over all beam and jet reference momenta q_m^{μ} , and the factors Q_m are normalization factors. Here, a, b denote the incoming beams and 1, ..., N the N jets. To make this more accessible, let us consider the example of \mathcal{T}_0

$$\mathcal{T}_0 = \sum_{i} \min \left\{ \frac{2q_a \cdot p_i}{Q_a}, \frac{2q_b \cdot p_i}{Q_b} \right\} , \qquad (2.162)$$

which is an appropriate variable to describe color-singlet production processes, since they do not feature a hard jet in the final state. The reference vectors q_a and q_b are aligned with the beam axis. There are two possible choices for the normalization factor [141,142]: either $Q_{a,b} = Q$ or $Q_{a,b} = Qe^{\pm Y}$ where Y is the rapidity. If the scalar product of the beam reference momentum and a colored particle $q_a \cdot p_i$ is small, the particle is closely aligned with the beam axis. If this is true for all colored particles, the final state looks like a 0-jet event and the 0-jettiness is small, $\mathcal{T}_0 \to 0$.

The definition in eq. (2.161) uses an invariant mass-like measure and follows a SCET-I type factorization. The factorization formula reads [140]

$$\frac{\mathrm{d}\sigma_{\kappa}}{\mathrm{d}Q\mathrm{d}Y\mathrm{d}\mathcal{T}_{N}} = \sum_{i,j} \operatorname{tr} \hat{H}_{ij}(Q^{2},\mu) \prod_{J=1}^{N} \int \mathrm{d}s_{J} \int \mathrm{d}t_{a} \, \mathrm{d}t_{b} \, B_{i}(t_{a},x_{a},\mu) \, B_{j}(t_{b},x_{b},\mu)
\times \hat{S}_{N}^{ij} \left(\mathcal{T}_{N} - \frac{t_{a}}{Q_{a}} - \frac{t_{b}}{Q_{b}} - \sum_{J} \frac{s_{J}}{Q_{J}}, \{q_{m}\}, \mu \right) J_{J}(s_{J},\mu) + \mathcal{O}\left(\frac{\mathcal{T}_{N}}{Q}\right), \qquad (2.163)$$

where the soft function \hat{S} and the hard function \hat{H} are matrices in color space and tr denotes a trace in color space. The inclusive beam $B_{i,j}$ and jet J functions describe collinear radiation emitted from the initial and final state, respectively. Further, s_J is the invariant mass of the radiation within the jet and $t_{a,b}$ are the total virtualities of the colliding partons.

In general, the cross section in eq. (2.163) will contain large logarithms of \mathcal{T}_N/Q which need to be resummed. To do so the the hard, beam, jet and soft functions have to be computed at their canonical scales [140]

$$\mu_H \sim Q, \qquad \mu_B \sim \sqrt{T_N}Q, \qquad \mu_J \sim \sqrt{T_N}Q, \qquad \mu_S \sim T_NQ.$$
 (2.164)

In the second step, we use the RGEs to evolve them to a common scale μ . The renormalization group evolution of the beam function is governed by [140,143]

$$\mu \frac{\mathrm{d}}{\mathrm{d}\mu} B_i(t_i, x_i, \mu) = \int \mathrm{d}t_i' \, \gamma_B^i(t_i - t_i', \mu) \, B_i(t_i', x_i, \mu) , \qquad (2.165)$$

with the anomalous dimension

$$\gamma_B^i(t,\mu) = -2\Gamma_{\text{cusp}}^i(\alpha_s)\mathcal{L}_0(t,\mu) + \gamma_B^i(\alpha_s)\delta(t). \qquad (2.166)$$

The evolution of the beam function is well known [144–146], but we refrain from giving the explicit solution of this equation in this thesis and refer to ref. [143] for details. The jet function's renormalization group equation reads [140, 143]

$$\mu \frac{\mathrm{d}}{\mathrm{d}\mu} J_J(s_J, \mu) = \int \mathrm{d}s'_J \gamma_B^i \left(s_J - s'_J, \mu \right) J_J(s'_J, \mu) , \qquad (2.167)$$

where in fact $\gamma_J^i(t,\mu) = \gamma_B^i(t,\mu)$ to all orders in perturbation theory [143]. Finally, the RGE of the soft function is given by [141,143]

$$\mu \frac{\mathrm{d}}{\mathrm{d}\mu} S(k,\mu) = \int \mathrm{d}k' \, \gamma_S^i \left(k - k', \mu\right) S\left(k', \mu\right) \,, \tag{2.168}$$

with

$$\gamma_S^i(k,\mu) = 4\Gamma_{\text{cusp}}^i(\alpha_s)\mathcal{L}_0(k,\mu) + \gamma_S^i(\alpha_s)\delta(k). \qquad (2.169)$$

The soft function $S(k,\mu)$ is the hemisphere soft function for incoming Wilson lines which is defined by measuring $k = \sum_i \{k_i^+, k_i^-\}$ on all soft emissions k_i . In chapter 4, we will use \mathcal{T}_1 with a generalized measure as a jet resolution variable.

2.6 Transverse Momentum Distributions

In the previous section, we discussed factorization of transverse momentum distributions at length. In this section, we want to look at this topic from a different angle by using transverse momentum distributions (TMDs) and their factorization theorems. In large parts of this thesis, we are considering processes at hadron colliders. In section 2.2, we established that the exact initial state in hadron collisions is not fully determined, since protons are composite objects. Instead, we rely on collinear PDFs to describe the probability of finding a parton of type a carrying a momentum fraction x_a in a colliding proton. However, collinear PDFs only describe the dependence on the longitudinal momentum and therefore only provide a one dimensional picture. In the framework of transverse momentum dependent distributions the parton distributions pick up an additional dependence on the transverse momentum of the parton which allows for a three dimensional description of the motion of quarks and gluons inside the nucleon.

The final state counterparts of TMD PDF are TMD fragmentation functions (FFs). Collinear fragmentation functions describe the probability of parton to hadronize into a specific hadron. They depend on the longitudinal momentum fraction z_H that the hadron retains from its parent parton. TMD FFs describe the transverse momentum that the hadron picks up by recoiling against other fragmentation products, including the full quantum correlations with the quark polarization, which provides a three-dimensional picture of the fragmentation cascade. Thus, TMD factorizing provides a rigorous field-theoretic framework in which hadronization can be studied in detail. Corresponding all-order factorization theorems have been established in ref. [147]. The TMD dynamics of light quarks and gluons are a well-established field of experimental study [148–158], phenomenological analysis (see e.g. refs. [159–162]), and progress towards first-principle calculations using lattice field-theory [163–169]. For a recent overview, see ref. [170].

In this section, we aim to give a brief overview of TMDs. We start by considering factorization at hadron colliders in terms of TMD PDFs in section 2.6.1. In sections 2.6.2 and 2.6.3, we discuss the leading TMD PDFs and FFs that are relevant to this thesis. In section 2.6.4, we give a brief overview of TMD cross sections. This section in part follows ref. [170]. Parts of sections 2.6.2 and 2.6.3 follow the introductory sections of ref. [3].

2.6.1 TMD factorization at hadron colliders

As an illustrative example we start with the collinear factorization theorem for the Higgs production cross section from section 2.2. In this section, we are particularly interested in the transverse momentum spectrum. For large values of q_T , we can write as

$$\frac{\mathrm{d}\sigma}{\mathrm{d}Y\mathrm{d}^2\vec{q}_T} = \sum_{i,j} \int_0^1 \mathrm{d}x_a \int_0^1 \mathrm{d}x_b f_i(x_a) f_j(x_b) \frac{\mathrm{d}\hat{\sigma}_{ij}(x_a, x_b)}{\mathrm{d}Y\mathrm{d}^2\vec{q}_T} \left[1 + \mathcal{O}\left(\frac{\Lambda_{\mathrm{QCD}}^2}{q_T^2}, \frac{\Lambda_{\mathrm{QCD}}^2}{Q^2}\right) \right], \quad (2.170)$$

where we omitted the dependence on the factorization scale for brevity. Just as in the previous sections, x_a and x_b are longitudinal momentum fractions and $\hat{\sigma}$ is the partonic cross section. For small values of q_T , it becomes apparent that we need a different description of the cross section. For $\Lambda_{\rm QCD} \lesssim q_T \ll Q$, the parton distributions describing the incoming partons need an additional dependence on the transverse momentum. This leads to the TMD version of the

factorization theorem

$$\frac{d\sigma}{dYd^{2}\vec{q}_{T}} = \sum_{ij} H_{ij}(Q^{2}, \mu) \int d^{2}\vec{k}_{a}d^{2}\vec{k}_{b} \,\delta^{(2)}(\vec{q}_{T} - \vec{k}_{a} - \vec{k}_{b}) \,f_{i}(x_{a}, \vec{k}_{a}, \mu, \zeta_{a}) \,f_{j}(x_{b}, , \vec{k}_{b}, \mu, \zeta_{b})$$

$$\times \left[1 + \mathcal{O}\left(\frac{q_{T}^{2}}{Q^{2}}, \frac{\Lambda_{\text{QCD}}^{2}}{Q^{2}}\right) \right] , \qquad (2.171)$$

where $H_{ij}(Q^2, \mu)$ is the process dependent hard function. Now, the densities describing the incoming partons not only depend on the longitudinal momentum fraction but also on the transverse components of the incoming partons. They are referred to as transverse momentum dependent PDFs (TMD PDFs). As TMD PDFs suffer from endpoint divergences which need to be regulated, they pick up an additional dependence on the Collins-Soper scales $\zeta_{a,b}$ [130, 131] which are given by

$$\zeta_a = x_a^2 M_N^2 e^{2Y_A}, \qquad \zeta_b = x_b^2 M_N^2 e^{2Y_B}.$$
(2.172)

Here M_N is the nucleon mass and $Y_{A,B}$ are the nucleon rapidities. Their product yields the mass invariant mass of the hard process

$$\zeta_a \zeta_b = Q^4. \tag{2.173}$$

We denote the quantities related to nucleon with the subscripts A, B whereas everything related to partons carries the subscripts a, b. It is understood that the parton a originates from the nucleon A.

In practice, we will often work with the Fourier transformed TMD PDFs which is given by

$$f_i(x, \vec{b}_T, \mu, \zeta) = \int d^2 \vec{k}_T e^{-i\vec{b}_T \cdot \vec{k}_T} f_i(x, \vec{k}_T, \mu, \zeta).$$
 (2.174)

Then the TMD cross section reads

$$\frac{d\sigma}{dYd^{2}\vec{q}_{T}} = \sum_{ij} H_{ij}(Q^{2}, \mu) \int \frac{d^{2}\vec{b}_{T}}{(2\pi)^{2}} e^{i\vec{b}_{T} \cdot \vec{q}_{T}} f_{i}(x_{a}, \vec{b}_{T}, \mu, \zeta_{a}) f_{j}(x_{b}, \vec{b}_{T}, \mu, \zeta_{b}). \tag{2.175}$$

The above equation closely resembles the factorized cross-section given in eq. (2.139). Indeed, they are equivalent ways of writing the same cross section where the soft and beam functions were combined to the TMD PDF

$$f_i(x, \vec{b}_T, \mu, \zeta) = B_i(x, \vec{b}_T, \mu, \nu / \sqrt{\zeta}) \sqrt{S_i(b_T, \mu, \nu)}.$$
 (2.176)

The hard function, $H_{ij}(Q^2, \mu)$, is identical in both descriptions. We traded the rapidity evolution scale ν for the Collins-Soper scale ζ . For TMD PDFs, the rapidity evolution is governed by the rapidity anomalous dimension, known as the Collins-Soper kernel. For details on TMD evolution see e.g. ref. [170].

2.6.2 Leading quark TMD PDFs

In the previous section, we discussed TMD cross section for Higgs production in terms of the unpolarized TMD PDFs $f = f_1$. The unpolarized TMD PDF which describes an unpolarized parton originating from an unpolarized nucleon. In this section, we will extend our discussion to

possibly polarized quarks and nucleons. There exists of course also gluon TMD PDFs. However, in this thesis, we are interested in heavy-quark effects and will therefore focus on quark TMDs. The nucleon has momentum

$$P_N^{\mu} = P_N^{-} \frac{n^{\mu}}{2} + \frac{M_N^2}{P_N^{-}} \frac{\bar{n}^{\mu}}{2} \,, \tag{2.177}$$

with $P_N^- \gg P_N^+ = M_N^2/P_N^-$ in the rest frame of the hard scattering. Note that we take the large component of the hadron (nucleon) momentum to be along the n^{μ} direction to make this section self contained, but the case of an \bar{n} -collinear incoming hadron follows from $n^{\mu} \leftrightarrow \bar{n}^{\mu}$.

The bare TMD quark-quark correlator between forward nucleon states that describes this process is

$$\Phi^{\beta\beta'}(x,b_{\perp}) = \int \frac{\mathrm{d}b^{+}}{4\pi} e^{-\mathrm{i}b^{+}(xP_{N}^{-})/2} \langle N | \bar{\psi}_{Q}^{\beta'}(b) W(b) W^{\dagger}(0) \psi_{Q}^{\beta}(0) | N \rangle, \qquad (2.178)$$

where x is the lightcone momentum fraction carried by the heavy quark and $b \equiv (0, b^+, b_\perp)$ is the Fourier conjugate of the transverse momentum k_T . Recall that we are using the notation $b_T = \sqrt{-b_\perp^2}$. Further, we have suppressed the rapidity regulator, the soft factor, and transverse gauge links at infinity in the above equation for simplicity. The Wilson line W(x) is defined as an anti-path ordered exponential of gauge fields extending to positive infinity along the lightcone direction \bar{n}^μ ,

$$W(x) = \bar{P}\left[\exp\left(-ig\int_0^\infty ds\,\bar{n}\cdot A(x+\bar{n}s)\right)\right]. \tag{2.179}$$

The Wilson lines only depend on the direction of \bar{n}^{μ} and are thus invariant under $\bar{n}^{\mu} \mapsto e^{\alpha} \bar{n}^{\mu}$. This also applies to the full correlator and is a manifestation of type-III reparameterization invariance discussed in section 2.4.

For the explicit perturbative calculations it can also be useful to define the momentum-space version of the above correlator,

$$\Phi^{\beta\beta'}(x,k_{\perp}) = \int \frac{\mathrm{d}^2 b_{\perp}}{(2\pi)^2} e^{-\mathrm{i}k_{\perp} \cdot b_{\perp}} \Phi^{\beta\beta'}(x,b_{\perp}). \tag{2.180}$$

The spin decomposition of eq. (2.180) in terms of scalar TMD PDFs is well known [171, 172],

$$\Phi(x > 0, k_{\perp}) = \left\{ f_{1}(x, k_{T}) - f_{1T}^{\perp}(x, k_{T}) \frac{\epsilon_{\perp}^{\rho\sigma} k_{\perp \rho} S_{\perp \sigma}}{M_{N}} + g_{1L}(x, k_{T}) S_{L} \gamma_{5} - g_{1T}^{\perp}(x, k_{T}) \frac{k_{\perp} \cdot S_{\perp}}{M_{N}} \gamma_{5} \right. \\
+ h_{1T}(x, k_{T}) \gamma_{5} \mathcal{L}_{\perp} + h_{1L}^{\perp}(x, k_{T}) S_{L} \gamma_{5} \frac{\not k_{\perp}}{M_{N}} - h_{1T}^{\perp}(x, k_{T}) \frac{k_{\perp} \cdot S_{\perp}}{M_{N}^{2}} \gamma_{5} \not k_{\perp} \\
+ i h_{1}^{\perp}(x, k_{T}) \frac{\not k_{\perp}}{M_{N}} + \left(\text{higher twist} \right) \right\} \frac{\not h}{4}, \qquad (2.181)$$

where S_L is the longitudinal nucleon polarization in the Trento frame [173] and S_{\perp} is the transverse nucleon polarization. The TMD PDFs can be obtained by tracing the correlator against suitable Dirac structures, also called projectors. The different TMD PDFs correspond to different quark and nucleon polarizations

• The unpolarized TMD PDF $f_1(x, k_T)$ describes an unpolarized quark within an unpolarized hadron, similar to the unpolarized collinear PDF.

- The helicity TMD PDF g_{1L} describes a longitudinally polarized quark inside a longitudinally polarized hadron which is similar to the collinear helicity PDF.
- The transversity TMD PDF h_{1T} describes a transversely polarized quark inside a transversely polarized hadron which corresponds to the TMD case of the collinear transversity PDF.

The remaining five distributions do not have collinear counterparts and only appear when the transverse momentum is measured.

- The Sivers function $f_{1T}^{\perp}(x, k_T)$ [174] describes an unpolarized quark inside a transversely polarized hadron.
- The worm-gear T, g_{1T}^{\perp} , [175] and L, h_{1L}^{\perp} , [176] describe a longitudinally polarized quark inside a transversely polarized hadron and vice versa.
- The Bœr-Mulders function h_1 describes a transversely polarized quark within an unpolarized hadron [177].
- Finally, there is the pretzelosity function, h_{1T}^{\perp} , which contributes to the TMD distribution of a transversely polarized quark inside a transversely polarized hadron in addition to the helicity TMD PDF [178].

The Sivers function as well as the Bœr-Mulders function are time-reversal odd. For LHC physics, only the unpolarized TMD PDF and Bœr-Mulders function are relevant as the protons at the LHC are unpolarized. However, there are other experiments using polarized proton beams such as the future Electron-Ion Collider (EIC) [179]. In fact, precision TMD measurements are part of its key physics targets.

2.6.3 TMD fragmentation functions

Besides PDFs, there are also fragmentation function which can be seen as the "final-state counterpart" to PDFs. Fragmentation describes the process of partons produced in a high-energy collision forming color-neutral bound states, hadrons. A collinear fragmentation function (FF) $D_i^h(z_H)$ describes the probability of an initial parton i to fragment into the hadron h where z_H is the fraction of the partons longitudinal momentum retained by the hardon. Similar to PDFs, there is also a transverse momentum description of FFs, TMD FFs. These are of particular interest when studying hadronization process as they allow for a three dimensional picture of the hadronization cascade (in contrast to collinear FFs which only provide a one dimensional picture).

In position space, the TMD quark-quark correlator describing this fragmentation process is defined as

$$\Delta_{h/q}^{\beta\beta'}(z_H, b_\perp) = \frac{1}{2z_H N_c} \int \frac{\mathrm{d}b^+}{4\pi} e^{\mathrm{i}b^+(P_H^-/z_H)/2} \times \operatorname{Tr} \sum_{X} \left\langle 0 \left| W^{\dagger}(b) \psi_Q^{\beta}(b) \right| HX \right\rangle \left\langle HX \left| \bar{\psi}_Q^{\beta'}(0) W(0) \right| 0 \right\rangle, \tag{2.182}$$

where β, β' are the open spin indices of the quark fields, Tr denotes a trace over fundamental color indices, and $b \equiv (0, b^+, b_\perp)$. The hadron momentum is given by

$$P_H = P_H^{-} \frac{n^{\mu}}{2} + P_H^{+} \frac{\bar{n}^{\mu}}{2}, \tag{2.183}$$

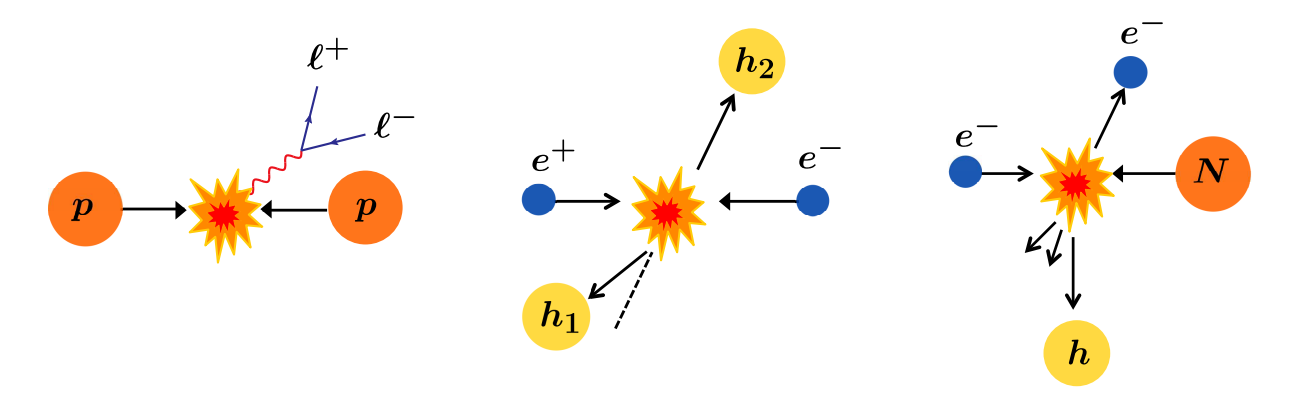


Figure 2.11: Illustration of TMD processes at colliders: Drell-Yan (left), di-hadron production in e^+e^- collisions (middle) and SIDIS (right). Figure adapted from ref. [170]

where $P_H \ll P_H^+ = M_H^2/P_H^-$ with the hadron mass M_H is boosted in the frame of the hard scattering and by definition $P_{H,\perp} = 0$, coinciding with the "hadron frame" for fragmentation [147]. We have kept a sum over the possible hadron helicities h_H , which are not experimentally resolved, implicit in the constrained sum over states, i.e.,

$$\oint_{X} |HX\rangle\langle HX| \equiv \oint_{X} \sum_{h_h} |H, h_H; X\rangle\langle H, h_H; X|.$$
(2.184)

The Wilson line W(x) was defined in eq. (2.179). As for the TMD PDF, we have suppressed the rapidity regulator, the soft factor, and transverse gauge links at infinity in eq. (2.182).

There are eight leading-power quark TMD FFs, which are defined by tracing the correlator against a suitable Dirac structure. Just like TMD PDFs, the leading TMD fragmentation functions have been proven to be universal between processes [180], i.e., they are independent of whether the Wilson line points to the future $(e^+e^- \to \text{hadrons})$ or the past (SIDIS).

In this thesis, we want to restrict ourselves to unpolarized hadrons which leaves two TMD FFs. The unpolarized TMD FF $(D_{1H/Q})$ encodes the total rate for producing an unpolarized hadron from an unpolarized quark, while the Collins TMD FF $(H_{1H/Q}^{\perp(1)})$ describes the strength of the correlation between the quark's transverse polarization and the direction of the hadron transverse momentum. They are defined in position space as¹

$$D_{1H/q}(z_H, b_T) = \text{tr}\left[\frac{\rlap{/}n}{2} \Delta_{H/q}(z_H, b_\perp)\right],$$

$$H_{1H/q}^{\perp(1)}(z_H, b_T) = \text{tr}\left[\frac{\rlap{/}n}{2} \frac{\rlap{/}b_\perp}{M_H b_T^2} \Delta_{H/q}(z_H, b_\perp)\right],$$
(2.185)

where tr denotes a trace over spin indices.

2.6.4 TMD processes at colliders

As already hinted above, TMDs are universal between processes. In this section, we want to briefly discuss the processes most relevant to this thesis which are illustrated in figure 2.11. In

¹Our conventions for Fourier transforms and the spin decomposition of TMD correlators follow ref. [172]. Note the superscript (1) on the b_T -space Collins function indicating a b_T derivative that arises from integrating a term k_{\perp} in the momentum-space correlator by parts, and that is specifically required due to the conventional normalization to the hadron mass [181].

section 2.6.1, we already discussed TMD cross section for processes at hadron colliders such as Tevatron or the LHC. The standard example for TMD cross sections at hadron collinsions is usually the Drell-Yan process

$$p + p \to \ell^+ + \ell^- + X,$$
 (2.186)

where two protons p collide and produce at lepton pair $\ell^+\ell^-$. Additional final-state particles including remnants of the proton are denoted by X. The Drell-Yan process is shown in left panel of figure 2.11. The underlying hard scattering process is described by a quark-anti-quark pair producing the lepton pair via a virtual photon or Z-boson. Schematically, the cross section can be written as

$$\frac{\mathrm{d}\sigma_{pp\to\ell^+\ell^-+X}}{\mathrm{d}Y\mathrm{d}Q\mathrm{d}^2\vec{q}_T} = = \hat{\sigma}_{q\bar{q}\to\ell^+\ell^-} \otimes f_q \otimes f_{\bar{q}},\tag{2.187}$$

where the first convolutions is in the longitudinal momentum fraction and the second convolution is the both, the transverse and the longitudinal momentum fraction. The hard part is given by $\hat{\sigma}_{q\bar{q}\to\ell^+\ell^-}$ and f_q and $f_{\bar{q}}$ are TMD PDFs.

The cross section for quark initiated Higgs production has the same form as eq. (2.187). The cross section only differ by the process dependent hard function. For gluon fusion, the TMD cross section again has a similar structure. However, since the process is gluon induced, we need gluon TMD PDFs.

So far we only considered cross section containing TMD PDFs but of course there are also other processes containing TMD FFs such as semi-inclusive deep inelastic scattering (SIDIS). In traditional DIS, an electron (or a different lepton) scatters off a nucleon via the exchange of a virtual photon. SIDIS extends this to not only detecting the electron in the final state but also at least one hadron,

$$\ell + N \to \ell' + h + X,\tag{2.188}$$

where ℓ and ℓ' are the initial and final leptons, N is the nucleon, h is the identified hadron and X are undetected remnants of the nucleon. This process is illustrated in the right panel of figure 2.11. SIDIS is particularly well suited to study TMD PDFs and FFs as provides direct access to both the intrinsic transverse momentum of partons and the correlations between spin and momentum. The SIDIS cross section can be written in terms of a hard scattering part, $\hat{\sigma}_{\ell q \to \ell' q'}$, a TMD PDF, f_q , and a TMD FF, $D_{h/q'}$:

$$\frac{\mathrm{d}\sigma_{\ell N \to \ell' h X}}{\mathrm{d}x \,\mathrm{d}y \,\mathrm{d}z \,\mathrm{d}^2 \vec{P}_T} = \hat{\sigma}_{\ell q \to \ell' q'} \otimes f_q \otimes D_{h/q'}. \tag{2.189}$$

The finial state quark, q', fragments into the detected hadron after participating in the hard interaction. Here x is the Bjorken scaling variable, y is the fraction of initial lepton's energy transferred to the nucleon, z is the momentum fraction of the finial state quark, q', retained by the identified hadron and \vec{P}_T is the hadron's transverse momentum. With the future EIC, there is a modern SIDIS experiment with polarized beams which will provide more detailed information on the respective TMDs and the 3D hadron structure.

Finally, there is also di-hadron production in e^+e^- collision which is the first process where TMD factorization was proven [130], which is illustrated in the central panel of figure 2.11. Here, two leptons annihilate and produce a quark-anti-quark. The quarks then fragment into a di-hadron

$Chapter\ 2-Theoretical\ Framework$

pair. At leading order, the two hadrons would be exactly back-to-back. However, in practice there is additional radiation X which spoils this behavior. The cross section for this process is given in terms of a hard contribution and two fragmentation functions [131]

$$\frac{\mathrm{d}\sigma_{e^+e^-\to h_1h_2}}{\mathrm{d}\cos\theta\,\mathrm{d}\phi\,\mathrm{d}z_1\,\mathrm{d}z_2\,\mathrm{d}^2\vec{P}_{1,T}} = \hat{\sigma}_{e^+e^-\to qq'} \otimes D_{h_1/q} \otimes D_{h_2/q'}. \tag{2.190}$$

where $\cos \theta$ and ϕ are the spherical coordinates of hadron h_2 , z_1 and z_2 are the lightcone momentum fractions of the two hadrons, and $\vec{P}_{1,T}$ is the transverse momentum of hadron h_1 .

Chapter 3

The q_T spectrum in Higgs Production via Quark Annihilation

In this chapter, we present a new state-of-the-art prediction for the transverse momentum spectrum of a Higgs boson produced via the annihilation of heavy quarks (s, c, b) in proton-proton collisions. Our finial result is a prediction at three-loop order in resummed perturbation theory (N^3LL') matched to full fixed-order results at approximate N^3LO (aN 3LO).

This chapter is based on ref. [2] reflecting the author's contribution. Compared to ref. [2], we included analytic leading-order calculation in the main part of this chapter. Additionally, we included the gluon fusion contribution in figure 3.17 and adapted the discussion of this figure.

3.1 Motivation

We have already established that precise measurements of the Higgs boson's properties are essential to understand its role in the SM. Further, we need equally precise theoretical predictions to exploit the full potential of the high precision data that is taken at the LHC. In this thesis we focus on the Yukawa couplings for bottom, charm and strange quarks. The bottom-quark Yukawa coupling is of particular interest, as certain BSM models, such as the Two Higgs Doublet Model or the Minimally Supersymmetric Standard Model (MSSM), predict an enhanced bottom-quark Yukawa coupling relative to its SM value [32, 33].

The bottom and charm Yukawa couplings have been measured from $H \to b\bar{b}$ and $H \to c\bar{c}$ decays, respectively [26, 34–36]. These measurements are rather challenging due to the required jet tagging and the huge multi-jet background. An alternative for the measurement of quark Yukawa couplings is therefore of great interest. A promising approach is to measure the Yukawa couplings from a fit to the Higgs transverse momentum spectrum which is sensitive to the quark flavor [40,41]. Indeed, ATLAS and CMS have already demonstrated that they can constrain y_b and y_c from their shape only [42,43].

In this chapter, we present a new state-of-the-art prediction for the q_T spectrum of Higgs production via quark annihilation $q\bar{q}\to H$, where we consider bottom, charm, and strange quarks for the incoming quarks. Of these, bottom-quark annihilation is by far the dominant process since the b is the heaviest, followed by charm and then strange annihilation. Precise predictions for the $q\bar{q}\to H$ process are important, since it can in principle provide direct sensitivity to the quark Yukawa couplings from the production process. In addition, while the

cross section for bottom-quark annihilation is significantly smaller than that of gluon fusion, these are often grouped together in experimental analyses, since they have very similar acceptances and are a priori hard to distinguish experimentally.

For these reasons, $q\bar{q} \to H$ production, in particular bottom-quark annihilation, has received much attention in the past, see e.g. refs. [32, 50, 51, 182–198]. The $q\bar{q}H$ form factor and hard function have been computed up to four loops [199, 200], the total inclusive $b\bar{b} \to H$ cross section to N³LO [201, 202], and $b\bar{b} \to H$ +jet to NNLO₁ [203] (the subscript 1 on the order counting indicates that it is relative to the H+1-parton cross section).

In ref. [2], we computed the resummed q_T spectrum for $q\bar{q} \to H$ at N³LL' order matched to fixed NNLO and approximate N³LO.¹ We use soft-collinear effective theory (SCET) [102–105, 204] to resum the logarithms of q_T/m_H . We work in the limit $m_q \ll q_T$, where we only keep the Yukawa coupling of the annihilating quarks and otherwise take them to be massless. For $b\bar{b} \to H$, this is commonly referred to as the five-flavour scheme. Finite-mass effects become relevant for $m_q \sim q_T$ and are thus necessary for a complete description of the small- q_T region, especially for $b\bar{b} \to H$ [50,205]. Their full treatment in the resummed q_T spectrum was worked out in ref. [205] and is quite involved. We therefore focus here on the massless limit and leave the inclusion of finite-mass effects in the resummed spectrum to future work.

This chapter is organized as follows. We explain how the resummed results were obtained in section 3.2, where we also discuss the general procedure for matching the resummed and fixed-order calculations using profile scales. In section 3.3, we discuss our implementation of the fixed-order results and the matching to them in some detail. It transpires that the numerical size of the nonsingular fixed-order corrections depends strongly on the incoming quark flavour. In particular, they are substantially larger for $b\bar{b} \to H$ than what is commonly found to be the case for gluon-fusion or Drell-Yan production. This requires additional care in the matching and some refinements to the usual estimation of the matching uncertainties based on profile-scale variations. Furthermore, we discuss the matching to approximate N³LO, i.e., to approximate $\mathcal{O}(\alpha_s^3)$. For this purpose, we introduce a general strategy to decorrelate the singular and nonsingular contributions at large q_T , generalizing a method recently introduced in ref. [206]. This allows us to construct an approximation of the missing $\mathcal{O}(\alpha_s^3)$ nonsingular contributions and a corresponding approximate full NNLO₁ result that incorporates the exact $\mathcal{O}(\alpha_s^3)$ singular contributions, which are necessary for a consistent matching to the N³LL' result. We present our numerical results for the resummed q_T spectrum and its perturbative uncertainties in section 3.4 and provide a summary in section 3.5.

3.2 Resummed prediction

We consider the cross section for an on-shell Higgs boson differential in the Higgs rapidity Y and Higgs transverse momentum \vec{q}_T . Recalling the factorization theorem discussed in section 2.5.3, we can write singular cross section as

$$\frac{\mathrm{d}\sigma^{\mathrm{sing}}}{\mathrm{d}Y\mathrm{d}^2\vec{q}_T} = \sum_{a,b} H_{ab}(m_H^2;\mu)[B_a \otimes B_b \otimes S_{ab}](x_a, x_b, \vec{q}_T; \mu), \qquad (3.1)$$

¹We note that, at $\mathcal{O}(\alpha_s^3)$, contributions to the subprocess $qg \to Hq$ may appear which do not feature a Yukawa coupling y_q but instead proceed via a top-quark loop. These are usually considered to be part of the gluon-fusion process, and hence we do not include them here, instead setting $y_t = 0$. The approximate inclusion of these effects in the heavy-top limit has been found to have a sub-percent level effect on y_b [203].

where the kinematic quantities $\omega_{a,b}$ and $x_{a,b}$ are given by

$$\omega_a = m_H e^{+Y}, \quad \omega_b = m_H e^{-Y} \quad \text{and} \quad x_{a,b} = \frac{\omega_{a,b}}{E_{cm}}.$$
 (3.2)

The process dependence is encoded in the hard function $H_{ab}(m_H^2, \mu)$. It describes the underlying hard interaction producing the Higgs boson via $ab \to H$, with the available partonic channels being $ab = \{q\bar{q}, \bar{q}q\}$. At leading order, $H^{(0)}$ corresponds to the partonic Born squared matrix element, while at higher orders it includes the finite virtual corrections to the Born process. To perform all-order resummation, each function is first evaluated at its own natural boundary scale(s): μ_H , (μ_B, ν_B) and (μ_S, ν_S) . By choosing appropriate values for the boundary scales close to their canonical values (see section 3.2.1), each function is free of large logarithms and can therefore be evaluated in fixed-order perturbation theory. Next, all functions are evolved from their respective boundary conditions to a common arbitary point (μ, ν) by solving their coupled system of renormalization group equations (RGEs). For details on the resummation procedure, we refer to section 2.5.3.

For the resummation at N³LL' we require the N³LO boundary conditions for the hard function [199, 207], and the beam and soft functions [208–212]. We also need the 3-loop noncusp virtuality [143, 208, 210, 213, 214] and rapidity anomalous dimensions [208, 209, 215], as well as the 4-loop cusp anomalous dimension Γ_{cusp} [90, 216–219] and QCD β function [66–69].

3.2.1 Canonical scales and resummation in b_T space

The canonical boundary scales in b_T space are given by

virtuality:
$$\mu_H = m_H$$
, $\mu_B = b_0/b_T$, $\mu_S = b_0/b_T$, $\mu_f = b_0/b_T$, $\mu_0 = b_0/b_T$, rapidity: $\nu_B = m_H$, $\nu_S = b_0/b_T$, (3.3)

where $b_0 \equiv 2e^{-\gamma_E} \approx 1.12291$. Here, μ_H , (μ_B, ν_B) , and (μ_S, ν_S) are the boundary scales for the hard, beam, and soft functions, and μ_f is the scale at which the PDFs inside the beam functions are evaluated. The rapidity anomalous dimension must also be resummed and μ_0 is its associated boundary scale. When the functions in eq. (3.1) are evolved from these scales, the evolution resums all canonical b_T -space logarithms $\ln^n[(b_0/b_T)/m_H]$.

As shown in ref. [137], the exact solution for the RG evolution in \vec{q}_T space in terms of distributions is equivalent to this canonical solution in b_T space modulo different conventions for the boundary conditions. Since the latter is much easier to obtain, we also use it here, as is often done. The resummed singular \vec{q}_T spectrum, $d\sigma^{res}$, is then obtained as the inverse Fourier transform of the canonically resummed b_T space result, $d\tilde{\sigma}^{res}(\vec{b}_T)$,

$$\frac{\mathrm{d}\sigma^{\mathrm{res}}}{\mathrm{d}Y\mathrm{d}^{2}\vec{q}_{T}} = \int \mathrm{d}^{2}\vec{b}_{T} \, e^{\mathrm{i}\,\vec{q}_{T}\cdot\vec{b}_{T}} \, \frac{\mathrm{d}\tilde{\sigma}^{\mathrm{res}}(\vec{b}_{T})}{\mathrm{d}Y} = 2\pi \int \mathrm{d}b_{T} \, b_{T} J_{0}(b_{T}q_{T}) \, \frac{\mathrm{d}\tilde{\sigma}^{\mathrm{res}}(\vec{b}_{T})}{\mathrm{d}Y} \,. \tag{3.4}$$

With the canonical scales in eq. (3.3), the strong coupling and the PDFs inside the beam functions are evaluated at $\alpha_s(b_0/b_T)$, which means the beam and soft functions and rapidity anomalous dimension become sensitive to nonperturbative effects for $1/b_T \lesssim \Lambda_{\rm QCD}$. To perform the Fourier transform in eq. (3.4), we must therefore choose a prescription to avoid such nonperturbative scales.

The traditional approach is to perform a global replacement of b_T everywhere in the b_T -space cross section by a function $b^*(b_T)$, which asymptotes to some fixed perturbative scale $b_{\text{max}} \lesssim 1/\Lambda_{\text{QCD}}$

for $1/b_T \to 0$, while away from this limit it becomes b_T . An important drawback of this global b^* prescription is that it leads to much larger than necessary distortions of the b_T -space cross section. This can be avoided by applying this replacement only to the canonical scale choices [220], which suffices to avoid nonperturbative scales. More precisely, following ref. [49], we use the μ_* prescription

$$\mu_X = \mu_* (b_0/b_T, \mu_X^{\min}) \text{ with } \mu_*(x, y) = \sqrt{x^2 + y^2},$$
 (3.5)

where μ_X stands for any of μ_S , μ_B , μ_0 , μ_f . In principle any function $\mu_*(x,y)$ can be used which satisfies $\mu_*(x \to 0, y) \to y$ and $\mu_*(x \gg y, y) \to x$. Under these conditions, all scales approach their chosen minimum value μ_X^{\min} for $1/b_T \to 0$, while approaching their canonical values away from this limit, as desired. Note that one advantage of this prescription is that we have the option to choose different μ_X^{\min} values for different scales, which we will make use of for μ_f .

3.2.2 Profile scales and matching to fixed order

Recalling the discussion in section 2.5.2, the resummed prediction is only appropriate for small values of $q_T \ll m_H$. For $q_T \sim m_H$ the cross section is given by the fixed-order contribution. In order to have description that is valid for all values of q_T , we need to combine both contributions resulting in the matched cross section

$$d\sigma = d\sigma^{\text{res}}(\mu_{\text{res}}) + d\sigma^{\text{nons}}(\mu_{\text{FO}})$$

$$= d\sigma^{\text{res}}(\mu_{\text{res}}) + \left[dd\sigma^{\text{FO}}(\mu_{\text{FO}}) - d\sigma^{\text{sing}}(\mu_{\text{FO}}) \right]. \tag{3.6}$$

Now, for small values of q_T the nonsingular terms $d\sigma^{\rm nons}(\mu_{\rm FO})$ are small and the resummed dominates. For $q_T \sim m_H$, the cross section is given in terms of the fixed-order contribution as $d\sigma^{\rm res}(\mu_{\rm res}) - d\sigma^{\rm sing}(\mu_{\rm FO})$ cancels in this limit. In practice, we want to turn off the resummation smoothly, such that the difference $d\sigma^{\rm res}(\mu_{\rm res}) - d\sigma^{\rm sing}(\mu_{\rm FO})$ vanishes equally smoothly as $q_T \rightarrow m_H$. This is conveniently achieved by using profile scales [221, 222], which provide a smooth transition for $\mu_{\rm res}$ from canonical resummation scales to the common fixed-order scales. Here we use hybrid profile scales $\mu_X(b_T,q_T)$ [220], which depend on both b_T and q_T and undergo a smooth transition from their canonical b_T -dependence in eq. (3.5) to the b_T -independent $\mu_{\rm FO}$, with the transition happening as a function of q_T ,

$$\mu_X(b_T, q_T) = \mu_* \left(b_0 / b_T, \mu_X^{\min} \right) \quad \text{for} \quad q_T \ll m_H ,$$

$$\mu_X(b_T, q_T) \to \mu_{FO} \qquad \text{for} \quad q_T \to m_H . \tag{3.7}$$

We choose the central scales as

$$\mu_{H} = \nu_{B} = \mu_{FO} = m_{H} ,$$

$$\mu_{X} = m_{H} f_{run} \left[\frac{q_{T}}{m_{H}}, \frac{1}{m_{H}} \mu_{*} \left(\frac{b_{0}}{b_{T}}, \mu_{X}^{min} \right) \right] \quad \text{for} \quad \mu_{X} \in \{\mu_{B}, \mu_{S}, \nu_{S}, \mu_{f}\} ,$$

$$\mu_{0} = \mu_{*} \left(\frac{b_{0}}{b_{T}}, \mu_{0}^{min} \right) , \tag{3.8}$$

where $f_{\rm run}$ is the hybrid profile function given by [220]

$$f_{\text{run}}(x,y) = 1 + g_{\text{run}}(x)(y-1),$$
 (3.9)

where $g_{\text{run}}(x)$ determines the transition as a function of $x = q_T/m_H$,

$$g_{\text{run}}(x) = \begin{cases} 1 & 0 < x \le x_1, \\ 1 - \frac{(x - x_1)^2}{(x_2 - x_1)(x_3 - x_1)} & x_1 < x \le x_2, \\ \frac{(x - x_3)^2}{(x_3 - x_1)(x_3 - x_2)} & x_2 < x \le x_3, \\ 0 & x_3 \le x, \end{cases}$$
(3.10)

with the transition points x_i with $i \in \{1, 2, 3\}$. The parameters x_1 and x_3 determine the start and the end of the transition and $x_2 = (x_1 + x_3)/2$ corresponds to the turning point. As a result the scales are canonical for $q_T \le x_1 m_H$ and the resummation is fully turned off for $q_T > x_3 m_H$. The values are usually chosen such that the transition begins somewhere in the resummation region and is finished by the time the singular and the nonsingular contributions are of the same size and exhibit sizeable numerical cancellations. We will use $[x_1, x_2, x_3] = [0.1, 0.45, 0.8]$ as our central values as explained in section 3.3.2.

For the $\mu_X^{\rm min}$ nonperturbative cutoffs we use

$$\mu_B^{\min} = \mu_S^{\min} = \mu_0^{\min} = 1 \text{ GeV}, \qquad \nu_S^{\min} = 0.$$
(3.11)

We can set $\nu_S^{\min}=0$ because ν_S never appears as argument of α_s or the PDFs. For μ_f^{\min} we pick the larger of the PDF's Q_0 value or a value based on the quark mass m_q used by the PDF set as threshold for the corresponding heavy-quark PDF. This choice of μ_f^{\min} avoids running into numerical noise below the scale where the heavy-quark PDFs vanish and where the results are in any case not particularly meaningful without the proper inclusion of finite-mass effects, which is beyond our scope here. For the MSHT20nnlo PDF set we use, this amounts to taking $\mu_f^{\min}=Q_0=1.0\,\mathrm{GeV}$ for $s\bar{s}\to H$, $\mu_f^{\min}=m_c=1.4\,\mathrm{GeV}$ for $c\bar{c}\to H$ and $\mu_f^{\min}=5.0\,\mathrm{GeV}$ for $b\bar{b}\to H$. The latter is chosen slightly above the actual bottom-quark mass threshold $m_b=4.75\,\mathrm{GeV}$ to avoid numerical instabilities.

In the fixed-order limit, we can identify $\mu_{FO} \equiv \mu_R$ with the usual renormalization scale for α_s and $\mu_f \equiv \mu_F$ with the usual factorization scale at which the PDFs are evaluated. Our central choices above correspond to $\mu_R = \mu_F = m_H$.

3.2.3 Perturbative uncertainties

To estimate the perturbative uncertainties, we vary the profile scales around their central values given in section 3.2.2. Following refs. [49, 138, 223], we identify several different sources of uncertainty, which are considered as independent and are estimated from different suitable types of variations. The profile scales are varied as follows:

$$\mu_{H} = \mu_{FO} = 2^{w_{FO}} m_{H},
\nu_{B} = \mu_{FO} f_{\text{vary}}^{v_{\nu_{B}}} \left(\frac{q_{T}}{m_{H}}\right),
\mu_{X} = \mu_{FO} f_{\text{vary}}^{v_{\mu_{X}}} \left(\frac{q_{T}}{m_{H}}\right) f_{\text{run}} \left[\frac{q_{T}}{m_{H}}, \frac{1}{m_{H}} \mu_{*} \left(\frac{b_{0}}{b_{T}}, \frac{\mu_{X}^{\text{min}}}{2^{w_{FO}} f_{\text{vary}}^{v_{\mu_{X}}}}\right)\right] \quad \text{for} \quad \mu_{X} \in \{\mu_{B}, \mu_{S}, \nu_{S}\},
\mu_{f} = 2^{w_{F}} m_{H} f_{\text{run}} \left[\frac{q_{T}}{m_{H}}, \frac{1}{m_{H}} \mu_{*} \left(\frac{b_{0}}{b_{T}}, \frac{\mu_{f}^{\text{min}}}{2^{w_{F}}}\right)\right],
\mu_{0} = \mu_{*} \left(\frac{b_{0}}{b_{T}}, \mu_{0}^{\text{min}}\right).$$
(3.12)

To estimate an uncertainty associated with the resummation Δ_{res} , the beam and soft scales are varied, where the exponents v_{μ_B} , v_{ν_B} , v_{μ_S} , and v_{ν_S} are taken to be $v_i = \{-1, 0, +1\}$ with the central scales corresponding to $v_i = 0$. The function

$$f_{\text{vary}}(x) = \begin{cases} 2(1 - x^2/x_3^2) & 0 \le x \le x_3/2, \\ 1 - 2(1 - x/x_3)^2 & x_3/2 < x \le x_3, \\ 1 & x_3 \le x, \end{cases}$$
(3.13)

with $x \equiv q_T/m_H$ controls the size of the variations, ranging from a factor of 2 for x = 0 to 1 for $x \geq x_3$, where x_3 is the same as for $f_{\text{run}}(x)$. This source of uncertainty is thus turned off for $q_T \geq x_3 m_H$ just as the resummation itself is turned off. To estimate the resulting resummation uncertainty Δ_{res} we perform 36 variations of suitable combinations of the v_i and take their maximum envelope. For details, we refer the reader to ref. [138].

For the fixed-order uncertainty $\Delta_{\rm FO}$, we vary $\mu_{\rm FO}$ by a factor of 2 by taking $w_{\rm FO}=\{-1,0,+1\}$ everywhere. Note that $\Delta_{\rm FO}$ is not defined to be the uncertainty in the fixed-order limit but is rather meant to estimate a common uncertainty due to missing fixed-order contributions at any q_T . It therefore contributes to both the singular and nonsingular pieces. In the resummed singular it amounts to an overall variation of the boundary scales such that the resummed logarithms are unchanged, which is why one can interpret it as a fixed-order uncertainty. Furthermore, we estimate a separate uncertainty Δ_{μ_f} related to the DGLAP running of the PDFs, for which we vary the PDF scale μ_f by taking $w_F = \{-1,0,+1\}$ (where $w_F = 0$ is the central value). In the nonsingular and full fixed-order cross sections, this corresponds to taking $\mu_f \equiv \mu_F = 2^{w_F} m_H$. The resulting $\Delta_{\rm FO}$ and Δ_{μ_f} are then given by the maximum envelope of the respective variations. We obtain the total perturbative uncertainty by adding the individual uncertainties in quadrature,

$$\Delta_{\text{total}} = \sqrt{\Delta_{\text{FO}}^2 + \Delta_{\text{res}}^2 + \Delta_{\mu_f}^2 + \Delta_{\text{match}}^2}.$$
 (3.14)

The matching uncertainty Δ_{match} will be discussed in section 3.3.2.

Note that in the fixed-order limit, we do not use an envelope of μ_R and μ_F variations as is commonly done. Instead, we estimate separate uncertainties Δ_{FO} and Δ_{μ_f} which are added in quadrature. By separating these two uncertainties in the resummation limit, we essentially have no choice but to do the same also at fixed order. This is not problematic, but is in fact a perfectly sensible choice for the fixed-order prediction – here, as in the resummation, the two variations probe two conceptually different sources of uncertainty.

3.3 Fixed-order contributions

In this section, we discuss several aspects specific to the $q\bar{q}\to H$ process we are interested in. In section 3.3.1, we describe our implementation and validation of the fixed-order calculation for the $q\bar{q}\to H+j$ process from which we obtain the nonsingular corrections. In section 3.3.2, we discuss how we choose the transition points for the profile function in eq. (3.10), and detail the procedure to estimate the associated matching uncertainty, which is particularly delicate for $b\bar{b}\to H$. In section 3.3.3, we describe a general strategy to decorrelate the singular and nonsingular contributions. Based on this, we construct in section 3.3.4 a suitable approximation for the fixed $\mathcal{O}(\alpha_s^3)$ corrections to the nonsingular and full cross sections.

As discussed in section 2.5.2, the nonsingular corrections are obtained at fixed order by taking

$$\frac{\mathrm{d}\sigma^{\mathrm{nons}}}{\mathrm{d}q_T} = \frac{\mathrm{d}\sigma^{\mathrm{FO}}}{\mathrm{d}q_T} - \frac{\mathrm{d}\sigma^{\mathrm{sing}}}{\mathrm{d}q_T}, \qquad (3.15)$$

where $d\sigma^{\rm sing}$ is obtained directly in momentum space from the fixed-order expansion of the factorization theorem in eq. (3.1). Since $d\sigma^{\rm nons}$ is power suppressed, we only need it for $q_T > 0$. Hence, to evaluate $d\sigma^{\rm FO}$ we require the fixed-order calculation for the q_T spectrum in $q\bar{q} \to H + j$. At N³LL' we need $d\sigma^{\rm FO}$ at $\mathcal{O}(\alpha_s^3)$ corresponding to the $q\bar{q} \to H + j$ calculation at NNLO₁.

3.3.1 LO_1 and NLO_1

Analytic LO₁ calculation

We consider the production of an on-shell Higgs boson, measuring its rapidity Y and the magnitude of its transverse momentum $q_T^2 = |\vec{q}_T|^2$. The underlying partonic process is

$$a(p_a) + b(p_b) \to H(q) + X(k_1,)$$
 (3.16)

where a and b are incoming partons and X denotes additional QCD radiation. Following ref. [129], the cross section can be written as

$$\frac{d\sigma}{dYdq_T^2} = \int_0^1 d\zeta_a d\zeta_b \frac{f_a(\zeta_a) f_b(\zeta_b)}{2\zeta_a \zeta_b E_{cm}^2} \int \left(\prod_i \frac{d^d k_i}{(2\pi)^d} (2\pi) \delta_+(k_i^2) \right) \int \frac{d^d q}{(2\pi)^d} |\mathcal{M}(p_a, p_b; \{k_i\}, q)|^2 \\
\times (2\pi) \delta(q^2 - m_H^2) (2\pi)^d \delta^{(d)}(p_a + p_b - k - q) \delta\left(Y - \frac{1}{2} \ln \frac{q^-}{q^+}\right) \delta(q_T^2 - |\vec{k}_T|^2) . \quad (3.17)$$

Here, $k = \sum_i k_i$ denotes the total outgoing hadronic momentum, and in particular, $\vec{k}_T = \sum_i \vec{k}_{i,T}$ is the vectorial sum of the transverse momenta of all emissions. Moreover, the incoming momenta are given by

$$p_a^{\mu} = \zeta_a E_{\rm cm} \frac{n^{\mu}}{2} , \qquad p_b^{\mu} = \zeta_b E_{\rm cm} \frac{\bar{n}^{\mu}}{2} .$$
 (3.18)

The δ -functions in eq. (3.17) set the Higgs boson on-shell and measure its rapidity, fixing the incoming momentum fractions to be

$$\zeta_a(k) = \frac{1}{E_{\rm cm}} \left(k^- + e^{+Y} \sqrt{m_H^2 + k_T^2} \right), \quad \zeta_b(k) = \frac{1}{E_{\rm cm}} \left(k^+ + e^{-Y} \sqrt{m_H^2 + k_T^2} \right), \quad (3.19)$$

and allowing us to simplify eq. (3.17) to

$$\frac{d\sigma}{dYdq_T^2} = \int \left(\prod_i \frac{d^d k_i}{(2\pi)^d} (2\pi) \delta_+(k_i^2) \right) \frac{\pi}{\zeta_a \zeta_b E_{cm}^4} f_a(\zeta_a) f_b(\zeta_b) A(Y; \{k_i\}) \delta(q_T^2 - |\vec{k}_T|^2) . \tag{3.20}$$

where $A(Y; \{k_i\})$ denotes the squared matrix-element

$$A(Y; \{k_i\}) \equiv |\mathcal{M}(p_a, p_b, \{k_i\}, q = p_a + p_b - k)|^2.$$
(3.21)

For reference, we start with the LO₀ cross section, i.e. the cross-section for the Born process $q\bar{q} \to H$ without any QCD radiation, which can be seen in figure 3.1a. Since there is no extra emission, the Higgs has no transverse momentum and the cross section is proportional to $\delta(q_T^2)$. Following from eq. (3.20) we obtain

$$\frac{d\sigma^{(0)}}{dYdq_T^2} = \frac{\pi}{x_a x_b E_{cm}^4} f_a(x_a) f_b(x_b) A^{(0)}(Y) \delta(q_T^2), \qquad (3.22)$$

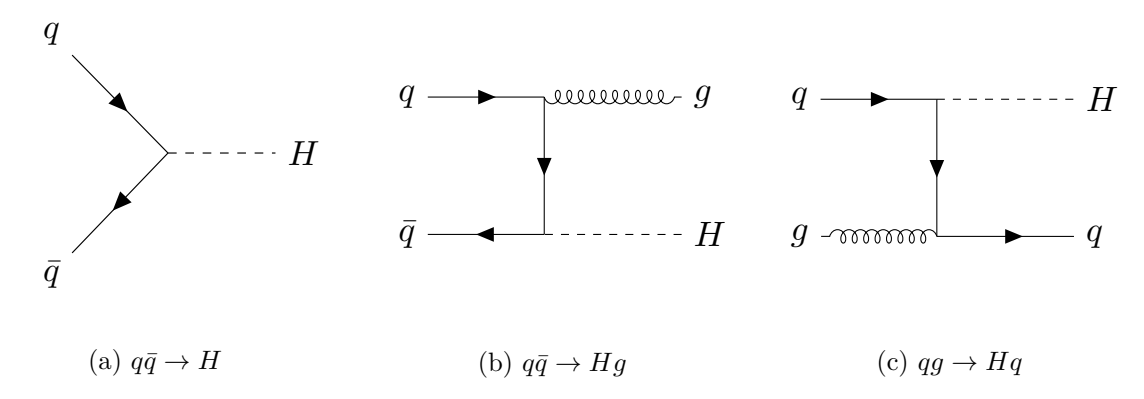


Figure 3.1: (a): Born process, (b) and (c): Feynman diagrams contributing to LO₁

where

$$x_a = \frac{m_H e^Y}{E_{\rm cm}}, \quad x_b = \frac{m_H e^{-Y}}{E_{\rm cm}},$$
 (3.23)

and the squared matrix element is given by

$$A^{(0)}(Y) = \frac{m_q^2 x_a x_b E_{\rm cm}^2}{2v^2 N_c}, \qquad (3.24)$$

For convenience we also define the partonic Born cross section $\hat{\sigma}^{(0)}$ through

$$\frac{\mathrm{d}\sigma^{(0)}}{\mathrm{d}Y\mathrm{d}q_T^2} = \int \mathrm{d}x_a \,\mathrm{d}x_b \,\hat{\sigma}^{(0)}\delta(x_a x_b E_{\mathrm{cm}}^2 - m_H^2) \,\delta\left[Y - \frac{1}{2}\ln\left(\frac{x_a}{x_b}\right)\right] \delta(q_T^2),\tag{3.25}$$

yielding

$$\hat{\sigma}^{(0)} = \frac{\pi m_q^2}{2v^2 N_c}. (3.26)$$

At LO₁, we have one QCD emission so the boson will have a finite transverse momentum. From eq. (3.20) we obtain

$$\frac{\mathrm{d}\sigma^{(1)}}{\mathrm{d}Y\mathrm{d}q_{T}^{2}} = \int \frac{\mathrm{d}^{d}k}{(2\pi)^{d}} (2\pi)\delta_{+}(k^{2}) \frac{\pi}{\zeta_{a}\zeta_{b}E_{\mathrm{cm}}^{4}} f_{a}(\zeta_{a}) f_{b}(\zeta_{b}) A^{(1)}(Y;k) \delta(q_{T}^{2} - |\vec{k}_{T}|^{2})$$

$$= \frac{q_{T}^{-2\epsilon}}{(4\pi)^{2-\epsilon}\Gamma(1-\epsilon)} \int_{0}^{\infty} \frac{\mathrm{d}k^{-}}{k^{-}} \frac{\pi}{\zeta_{a}\zeta_{b}E_{\mathrm{cm}}^{4}} f_{a}(\zeta_{a}) f_{b}(\zeta_{b}) A^{(1)}(Y;k) \Big|_{k^{+}=q_{T}^{2}/k^{-}}. \tag{3.27}$$

The type of diagrams contributing to the squared matrix element can be seen in figures 3.1b and 3.1c. We decompose $A^{(1)}(Y;k) \equiv \sum_{a,b=q,\bar{q},g} A^{(1)}_{ab}$ into its contributing channels

$$\begin{split} A_{q\bar{q}}(k^-,q_T^2,Y) &= A_{\bar{q}q}(k^-,q_T^2,Y) = \alpha_s C_F \frac{4\pi m_b^2}{N_c v^2} \left(\frac{s_{ab}^2 + m_H^4}{s_{ak}s_{bk}} \right), \\ A_{gq}(k^-,q_T^2,Y) &= A_{g\bar{q}}(k^-,q_T^2,Y) = \alpha_s C_F \frac{4\pi m_q^2}{(N_c^2 - 1)v^2} \left(\frac{s_{bk}^2 + m_H^4}{-s_{ab}s_{ak}} \right), \\ A_{qg}(k^-,q_T^2,Y) &= A_{\bar{q}g}(k^-,q_T^2,Y) = \alpha_s C_F \frac{4\pi m_q^2}{(N_c^2 - 1)v^2} \left(\frac{s_{ak}^2 + m_H^4}{-s_{ab}s_{bk}} \right), \end{split} \tag{3.28}$$

where the s_{ab} , s_{ak} and s_{bk} are kinematic invariants that can be written in terms of k^- , q_T^2 and Y as

$$s_{ab} \equiv 2p_a \cdot p_b = m_H^2 + 2q_T^2 + (k^+ e^Y + k^- e^{-Y}) \sqrt{m_H^2 + q_T^2},$$

$$s_{ak} \equiv -2p_a \cdot k = -q_T^2 - k^+ e^{+Y} \sqrt{m_H^2 + q_T^2},$$

$$s_{bk} \equiv -2p_b \cdot k = -q_T^2 - k^- e^{-Y} \sqrt{m_H^2 + q_T^2},$$
(3.29)

with $k^+ = q_T^2/k^-$. The limits of the k^- integral are found by constraining the PDF argument to be between zero and one, yielding

$$k_{\min}^{-} = \frac{q_T^2}{E_{\text{cm}}} - e^{-Y} \sqrt{q_T^2 + m_H^2},$$

$$k_{\max}^{-} = E_{\text{cm}} - e^{+Y} \sqrt{q_T^2 + m_H^2}.$$
(3.30)

We implemented the analytic expression of the LO₁cross section (eq. (3.27)) in the C++ library SCETLIB [224] to obtain our phenomenological predictions.

Numerical NLO₁ contribution using GENEVA

For the NLO₁ calculation, we use a parton-level Monte Carlo calculation, which we have implemented in the Geneva event generator [225, 226] using FKS subtractions [227]. We have used the virtual matrix elements in analytic form, which were calculated in ref. [228] and implemented in the Geneva code in ref. [229]. The tree-level double-real emission matrix elements are obtained from the OpenLoops library [230]. Note that often only the $b\bar{b} \to H$ process is considered. We therefore performed several internal cross checks to also ensure the correct implementation of $c\bar{c} \to H + j$ and $s\bar{s} \to H + j$. At LO₁, we also checked the implementation against our analytic implementation in SCETLIB.

A powerful cross check of the fixed-order calculation is provided by the cancellation of all singular terms in the $q_T \to 0$ limit in eq. (3.15). This is shown for both the $\mathcal{O}(\alpha_s)$ and $\mathcal{O}(\alpha_s^2)$ corrections in figure 3.2. In both cases, the full (blue) and singular (red) results become essentially equal for small q_T , and the nonsingular (green) given by their difference exhibits the expected power suppression. Note that these plots show $|\mathrm{d}\sigma/\mathrm{d}\log_{10}q_T|$ on a log-log scale, for which an $\mathcal{O}(q_T^2/m_H^2)$ power suppression corresponds to a line with an asymptotic slope of -2 for $q_T \to 0$. This is clearly seen at $\mathcal{O}(\alpha_s)$. At $\mathcal{O}(\alpha_s^2)$ this is less apparent due to the limited Monte-Carlo integration precision at very small q_T and because the nonsingular contribution contains powers of logarithms $\ln^n(q_T^2/m_H^2)$ up to $n \leq 3$, which weaken the power suppression and effectively delay the strictly quadratic scaling to smaller q_T . We nevertheless observe a clear power suppression from around 30 GeV down to a few GeV until the numerical precision becomes insufficient to actually resolve the small but nonzero value of the nonsingular. Note that once this happens, the result for the nonsingular should fluctuate around and be consistent with zero within the statistical uncertainties. This is confirmed in figure 3.3, which shows the nonsingular from figure 3.2 but on a linear y axis and including the sign.

For completeness, here we provide the analogous plots for $c\bar{c} \to H$ and $s\bar{s} \to H$ on a logarithmic scale in figure 3.4 and on a linear scale in figure 3.5. In both cases we observe the expected power suppression of the nonsingular similar to $b\bar{b} \to H$, which provides an important validation of our implementation of the LO₁ and NLO₁ fixed-order results.

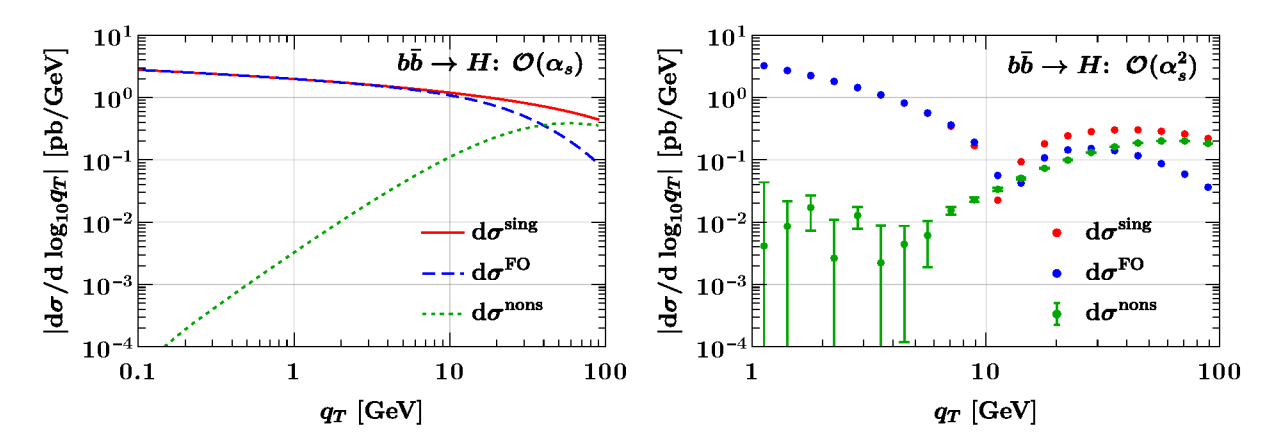


Figure 3.2: Singular (solid red), full (dashed blue), and nonsingular (dotted green) contributions for $b\bar{b} \to H$ at fixed $\mathcal{O}(\alpha_s)$ (left) and $\mathcal{O}(\alpha_s^2)$ (right). The nonsingular exhibit the expected quadratic power suppression for $q_T \to 0$.

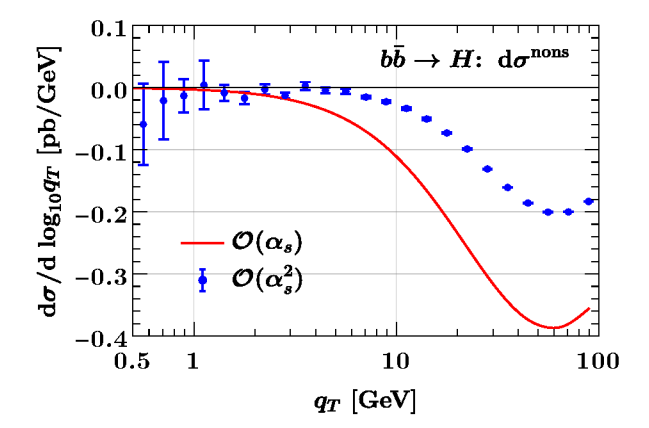


Figure 3.3: Nonsingular contributions at $\mathcal{O}(\alpha_s)$ (red) and $\mathcal{O}(\alpha_s^2)$ for $b\bar{b} \to H$ on a linear scale, corresponding respectively to the green curves and points in figure 3.2.

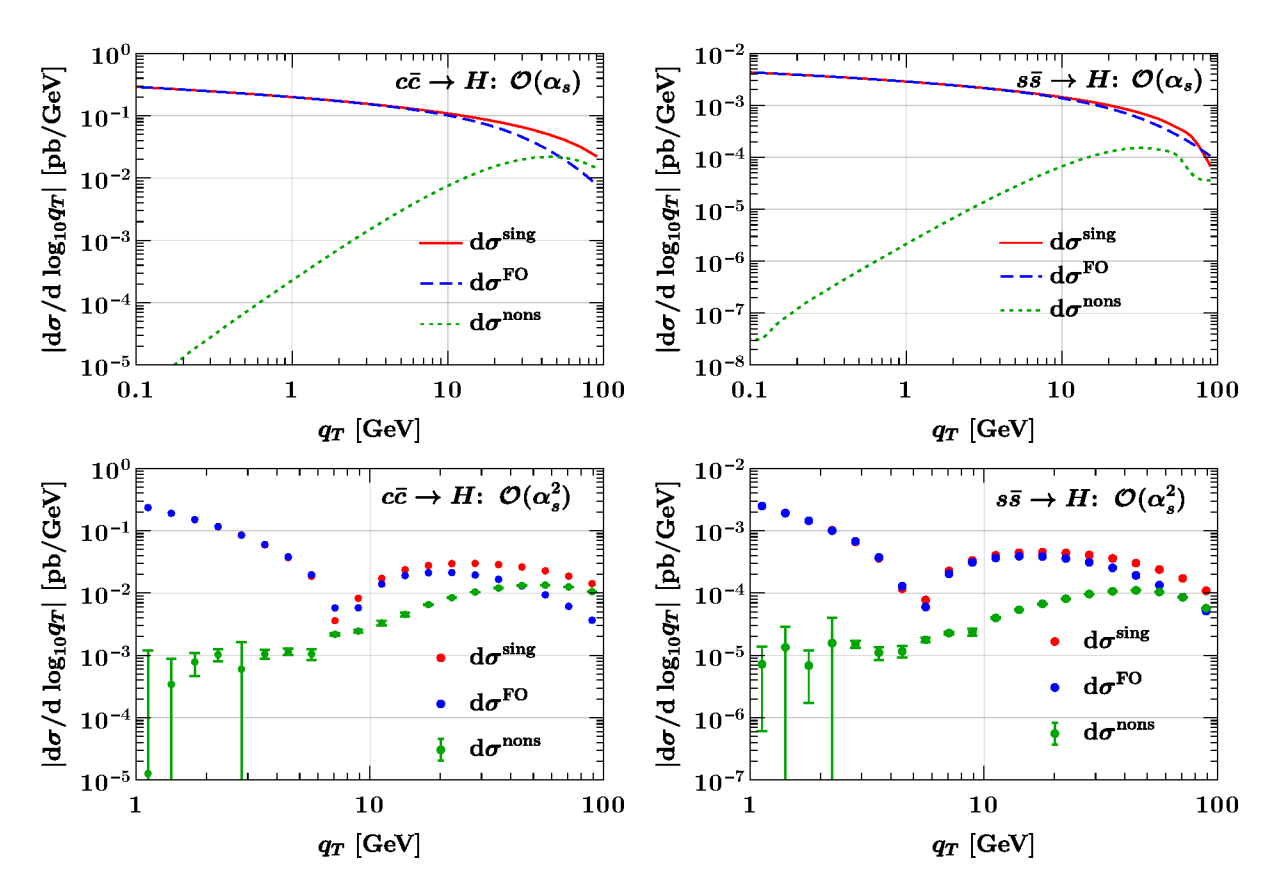


Figure 3.4: Singular (solid red), full (dashed blue), and nonsingular (dotted green) contributions for $c\bar{c} \to H$ (left) and $s\bar{s} \to H$ (right) at fixed $\mathcal{O}(\alpha_s)$ (top) and $\mathcal{O}(\alpha_s^2)$ (bottom).

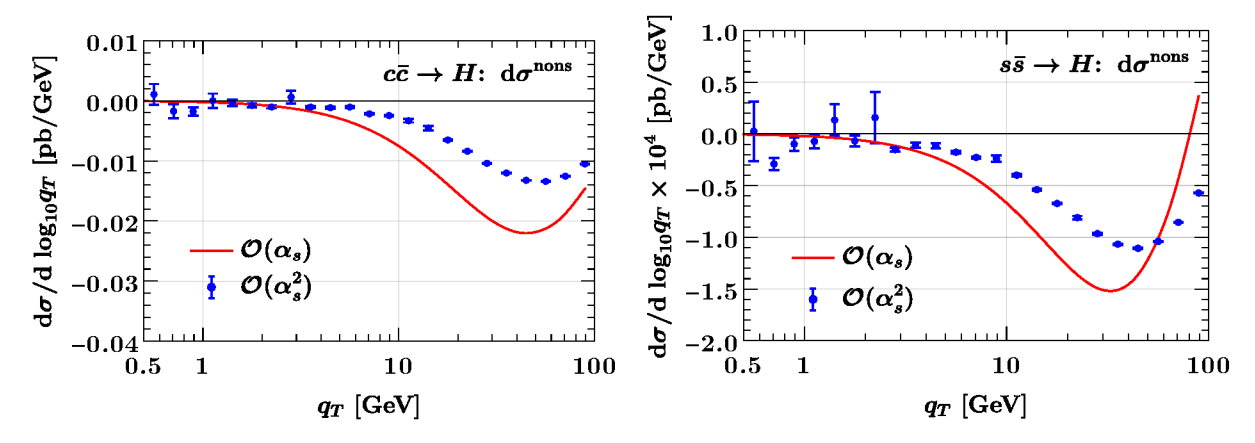


Figure 3.5: Nonsingular contributions at $\mathcal{O}(\alpha_s)$ (red) and $\mathcal{O}(\alpha_s^2)$ (blue) for $c\bar{c} \to H$ (left) and $s\bar{s} \to H$ (right), corresponding respectively to the green curves and points in figure 3.4.

$NNLO_1$

A calculation for $b\bar{b} \to H + j$ has been achieved at NNLO₁ in ref. [203] using N-jettiness subtractions [231, 232]. This calculation uses a cut on the jet- $p_T \geq 30\,\text{GeV}$, which gives an unbiased result for the q_T spectrum only for $q_T \geq 60\,\text{GeV}$. The jet- p_T cut limits the size of residual power corrections in the N-jettiness slicing parameter, which scale with the inverse of the smallest kinematic scale in the process. It would require substantial high-performance computing resources to perform the full NNLO₁ calculation without a jet cut down to much smaller q_T (this is also what experience has shown in case of Drell-Yan [48]). On the other hand, the spectrum at small q_T is entirely dominated by the resummed singular contributions, while the $\mathcal{O}(\alpha_s^3)$ nonsingular corrections only give a very small correction: this does not justify the computational cost and associated carbon footprint. In addition, we also need the NNLO₁ calculations for charm and strange production, which are not presently available. Therefore, we find it more prudent to construct an approximate NNLO₁ calculation, described in section 3.3.4, that is suitable for our purposes and which is designed to give good agreement with the known result for $b\bar{b} \to H + j$ at $q_T \geq 60\,\text{GeV}$.

$y_t y_q$ interference contributions

Starting at $\mathcal{O}(\alpha_s^3)$ there are contributions, e.g. to the subprocess $qg \to Hq$, that do not feature a light-quark Yukawa coupling y_q but instead proceed via the Higgs being emitted from a closed top-quark loop proportional to y_t . Effectively, these contributions amount to an interference between real-emission corrections to the $q\bar{q} \to H$ and $gg \to H$ Born processes proportional to y_ty_q . Due to their different coupling structure, they form a gauge-invariant subset and can be considered separately from the leading y_q^2 contributions discussed here. The corresponding y_t^2 contributions to the partonic subprocess $qq' \to Hqq'$ with light-quark final states are part of the double-real corrections to the gluon-fusion process.

At leading power in q_T , the $y_t y_q$ interference contributions are not present to all orders in α_s , because the structure of the leading-power result is determined by the Born process and the $q\bar{q} \to H$ and $gg \to H$ Born processes cannot interfere with each other due to their different initial states. In other words, their respective leading-power factorization theorems cannot interfere. This is in contrast to the $gg \to H$ process, which does receive leading-power $y_t y_q$ contributions, from the interference of closed top and light-quark triangle diagrams at Born level which we consider in chapter 5. As a result, these interference contributions do not enter at any order in the resummed predictions. Instead, they are purely nonsingular and only enter via matching to the full $\mathcal{O}(\alpha_s^3)$ results at large q_T . Since our primary focus here is on the $q\bar{q} \to H$ channel and its leading-power resummation at small q_T , we do not include the $y_t y_q$ interference contributions, as is also often done in the literature (see e.g. ref. [203]). If desired for phenomenological studies, these terms can be obtained from a separate fixed NLO₂ calculation [192, 233] and can simply be added to our results.

3.3.2 Estimation of the matching uncertainties

Naïvely, one might expect the $q\bar{q} \to H$ process to share many features in its numerical behavior with the Drell-Yan process. Indeed, both are quark-initiated at Born level and produce a single heavy color-singlet state in the s channel. Therefore, both cross sections have the form of eq. (3.1) and contain the same beam and soft functions. The only difference in the process dependent hard function and one would expect rather similar results for these processes. Nevertheless, inspecting

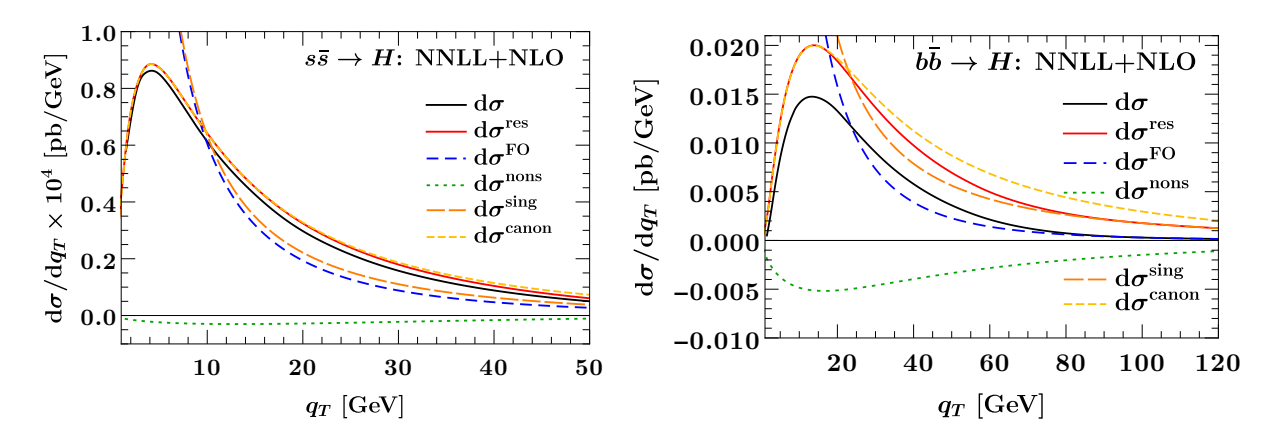


Figure 3.6: Different contributions entering the matching procedure for $s\bar{s} \to H$ (left) and $b\bar{b} \to H$ (right) at NNLL+NLO. The final matched result $d\sigma$ (solid black) is the sum of the nominal resummed $d\sigma^{\rm res}$ (solid red) and the nonsingular $d\sigma^{\rm nons}$ (dashed green). The fixed-order result $d\sigma^{\rm FO}$ (dashed blue) is the sum of the fixed-order singular $d\sigma^{\rm sing}$ (long-dashed orange) and $d\sigma^{\rm nons}$ (dashed green). Here, the canonically resummed result is denoted as $d\sigma^{\rm canon}$ (short-dashed yellow). The nominal resummed $d\sigma^{\rm res}$ transitions from $d\sigma^{\rm canon}$ at small q_T to $d\sigma^{\rm sing}$ at large q_T .

figure 3.6, we see that this is not quite the case. The figure shows the various contributions entering in the matching procedure for both $s\bar{s}\to H$ and $b\bar{b}\to H$. It shows that the numerical importance of the different contributions strongly depends on the incoming flavour. The $s\bar{s}$ channel indeed behaves very similar to Drell-Yan (see e.g. ref. [138]): it exhibits a very small nonsingular contribution $d\sigma^{\rm nons}$ (dotted green), such that the final matched result (solid black) is almost the same as the nominal resummed result $d\sigma^{\rm res}$ (solid red). Furthermore, the transition of $d\sigma^{\rm res}$, using profile scales, from the canonically resummed result $d\sigma^{\rm canon}$ (short-dashed yellow) at small q_T towards the fixed-order singular $d\sigma^{\rm sing}$ (long-dashed orange) at large q_T is very gentle. The $b\bar{b}$ channel instead features a much larger nonsingular contribution, and the transition that $d\sigma^{\rm res}$ has to undergo from canonical resummation to fixed-order singular is very pronounced. The result of this is a much increased sensitivity to the precise choice of the transition points x_i compared to the Drell-Yan case.

This difference between the channels can be understood from the very different size of the quark PDFs involved. At lowest order, the nonsingular receives contributions from two different flavour channels, namely $q\bar{q}\to Hg$ and $gq\to Hq$ (which includes $g\bar{q}\to H\bar{q}$ for the sake of this discussion). In Drell-Yan, these two channels have opposite sign and similar size (see e.g. ref. [129]), and thus partially cancel each other, leading to the relatively small nonsingular corrections typical for that process. The same also happens for $s\bar{s}\to H$. For $b\bar{b}\to H$, however, the very small b-quark PDF suppresses the $b\bar{b}$ -induced contributions. This has two effects leading to the observed behaviour: first, the nonsingular is dominated by the gluon-induced channels leading to smaller cancellations. This is compounded by the fact that the leading (NLL) contributions in the resummed are also $b\bar{b}$ induced and numerically suppressed. Both of these effects numerically enhance the nonsingular. The second effect furthermore causes a larger difference between (canonically) resummed and fixed-order singular. From this discussion one would expect the $c\bar{c}\to H$ process (not shown in figure 3.6) to exhibit behaviour intermediate between $s\bar{s}\to H$ and $b\bar{b}\to H$, which is indeed the case.

The stronger sensitivity to the (ultimately arbitrary) choice of transition points in $b\bar{b} \to H$

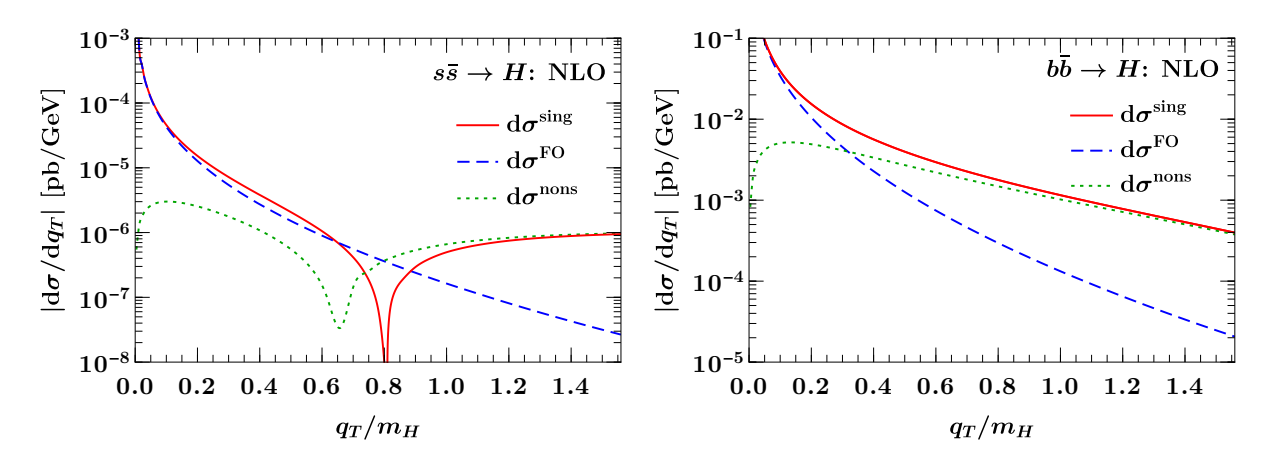


Figure 3.7: Singular (solid red), full (dashed blue), and nonsingular (dotted green) contributions at fixed $\mathcal{O}(\alpha_s)$ as a function of q_T/m_H for $s\bar{s} \to H$ (left) and $b\bar{b} \to H$ (right).

requires us to take greater care in choosing the transition points and in estimating the associated matching uncertainty. Usually, the start and endpoints of the transition, x_1 and x_3 (see section 3.2.2) are chosen based on examining the relative sizes of the singular and nonsingular pieces as a function of q_T , as shown in figure 3.7 for $s\bar{s} \to H$ (left) and $b\bar{b} \to H$ (right). The rather different behaviour of the channels is seen again here. The $s\bar{s} \to H$ channel again looks very similar to Drell-Yan, with the nonsingular becoming important only at relatively large $q_T/m_H \gtrsim 0.8$, such that a typical choice for the transition points would be $x_1 = 0.3$, $x_3 = 0.9$, $x_2 = (x_1 + x_3)/2 = 0.6$ [49,138]. In contrast, for $b\bar{b} \to H$ the nonsingular becomes important much earlier. Based on this plot, one might take sensible central values of $x_1 = 0.2$, $x_3 = 0.7$, and $x_2 = (x_1 + x_3)/2 = 0.45$.

The matching uncertainty Δ_{match} is related to the ambiguity in these choices. The standard method to estimate it is to vary x_1 and x_3 , typically by ± 0.1 , with x_2 given by $(x_1 + x_3)/2$ for any given variation. The resulting variations for $b\bar{b} \to H$ are shown in figure 3.8. We first note that this standard method leads by construction to a one-sided uncertainty above the central x_3 and below the central x_1 , because varying x_3 up or x_1 down can only change the cross section in one direction. In practical applications, e.g. when propagating the $x_{1,3}$ variations in a fit, this is a rather undesirable feature. Furthermore, varying x_1 and x_3 up (long-dashed green) produces an unreasonably large uncertainty. The reason for this large variation, as evident from the left plot, is precisely due to the rather large difference between the canonically resummed and fixed-order results already discussed, between which the transition must interpolate.

We therefore adopt a somewhat different approach to estimate the matching uncertainty. We first fix x_1 to its lowest and x_3 to its highest reasonable value, e.g. to their respective minimum and maximum values one would consider in the previous approach (which are $x_1 = 0.1$ and $x_3 = 0.8$ in our example). We then vary the point x_2 to estimate the matching uncertainty. Conceptually, this effectively varies whether the transition happens earlier or later within the maximal window in which the transition should occur. Here, we take $x_2 = (x_1 + x_3)/2 = 0.45$ as our central value and vary it within the range [0.2, 0.6]. Note that the size of this range is twice that of the x_1 and x_3 variations, so the total amount of variation is preserved. The resulting variations are shown in figure 3.9.

We begin by observing that this method avoids the undesired one-sided uncertainties, although the uncertainty is still somewhat asymmetric at any given q_T . This is practically unavoidable,

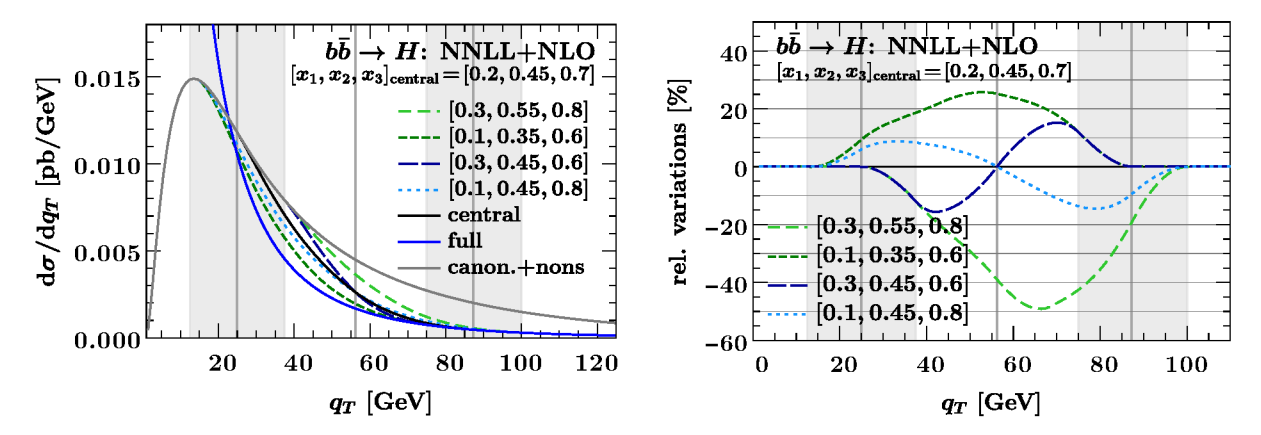


Figure 3.8: Standard variation of the transition points x_1 and x_3 for $b\bar{b} \to H$ at NNLL+NLO. The absolute variation in the spectrum is shown on the left, and the relative variation with respect to the central result is shown on the right. The vertical lines indicate the central values $[x_1, x_2, x_3] = [0.2, 0.45, 0.7]$, and the grey bands the variations of x_1 and x_3 by ± 0.1 , where always $x_2 = (x_1 + x_3)/2$.

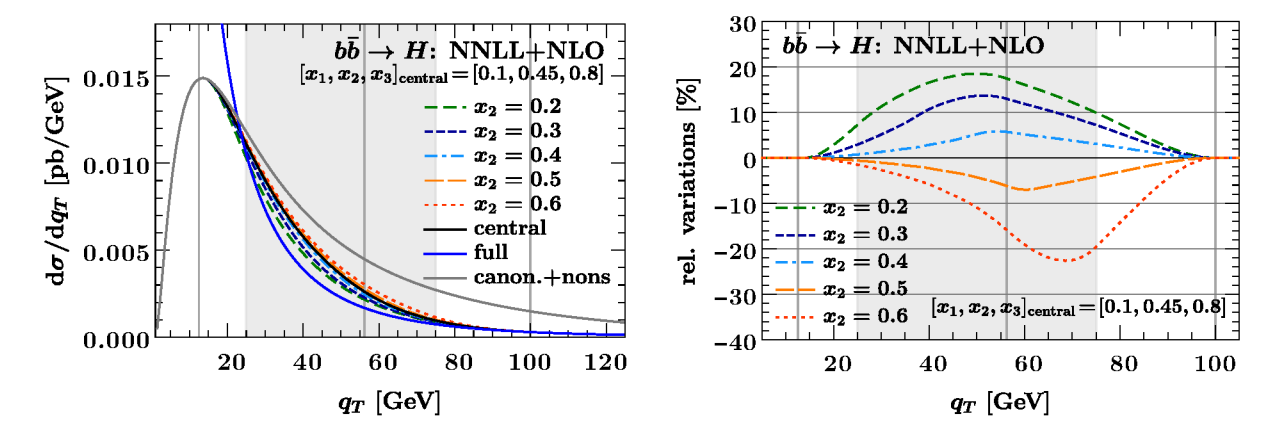


Figure 3.9: New variation of the transition point x_2 for $b\bar{b} \to H$ at NNLL+NLO. The absolute variation in the spectrum is shown on the left, and the relative variation with respect to the central result is shown on the right. The vertical lines indicate the central values $[x_1, x_2, x_3] = [0.1, 0.45, 0.8]$, where x_1 and x_3 are fixed to their respective minimum and maximum values used in figure 3.8. The grey band shows the variation in x_2 from 0.2 to 0.6.

since it is inherent to the nature of the matching uncertainty. We can, however, choose the x_2 range of variation such that the maximum up and down variations in the cross section are of similar size, which is why we vary it further down than up. Furthermore, the x_2 variation yields a much more reasonable size for the matching uncertainty. Finally, this method has the added benefit that the matching uncertainty is now parametrized by a single variable. This makes it much easier to propagate in practice, as it avoids having to take envelopes of different parameter variations.

For our final numerical results, the matching uncertainty Δ_{match} is still obtained as the maximum of the absolute impact of varying x_2 down to 0.2 and up to 0.6. However, this is now just for ease of presentation and not a requirement. Since $s\bar{s} \to H$ and $c\bar{c} \to H$ are less sensitive to the precise transition, we will use the same central values and x_2 variations for simplicity.

3.3.3 Decorrelation of singular and nonsingular contributions

As discussed in section 3.3.1, we wish to construct an approximate result for $d\sigma^{FO}$ at NNLO₁, which we can consistently match to $d\sigma^{res}$ at N³LL'. This requires that the NNLO₁ cross section contains the correct singular terms $d\sigma^{sing}$, which are part of the N³LL' result. We must therefore approximate the remaining nonsingular part of the full NNLO₁. However, at large q_T there is a strong cancellation between singular and nonsingular. Thus, the two pieces are strongly correlated and only the full fixed-order result is meaningful for large values of q_T . Hence, at large q_T we should do the opposite and approximate the full result, considering the nonsingular as a derived quantity given by the difference of full and singular. To satisfy these competing requirements, we introduce a general method to decorrelate the singular and nonsingular contributions, which we will then use in the next subsection to construct the actual approximation.

The basic idea behind the decorrelation of the singular and nonsingular contributions at large q_T involves shifting a correlated piece between the two [206],

$$d\sigma^{FO}(q_T) = d\sigma^{sing}(q_T) + d\sigma^{nons}(q_T)$$

$$= \underbrace{d\sigma^{sing}(q_T) + d\sigma^{corr}(q_T)}_{d\tilde{\sigma}^{sing}} + \underbrace{d\sigma^{nons}(q_T) - d\sigma^{corr}(q_T)}_{d\tilde{\sigma}^{nons}} \equiv d\tilde{\sigma}^{sing}(q_T) + d\tilde{\sigma}^{nons}(q_T),$$
(3.31)

where here and below we use the notation $d\sigma(q_T) \equiv d\sigma/dq_T$ to make the q_T dependence explicit. We call $d\tilde{\sigma}^{\rm sing}(q_T)$ and $d\tilde{\sigma}^{\rm nons}(q_T)$ the decorrelated singular and nonsingular contributions. The correlated piece $d\sigma^{\rm corr}(q_T)$ is as of yet unspecified.

To achieve the desired decorrelation, we require the decorrelated nonsingular to become equal to the full fixed-order result toward large q_T , and as a consequence the decorrelated singular to vanish,

$$d\tilde{\sigma}^{\text{nons}}(q_T \to m_H) \to d\sigma^{\text{FO}}(q_T), \qquad d\tilde{\sigma}^{\text{sing}}(q_T \to m_H) \to 0.$$
 (3.32)

This guarantees that no cancellations occur between them. At the same time, the decorrelated nonsingular must remain power suppressed for $q_T \ll m_H$, such that the decorrelated singular still contains all singular terms,

$$\frac{\mathrm{d}\tilde{\sigma}^{\mathrm{nons}}(q_T)}{\mathrm{d}\sigma^{\mathrm{sing}}(q_T)} \sim \mathcal{O}\left(\frac{q_T^2}{m_H^2}\right), \qquad \mathrm{d}\tilde{\sigma}^{\mathrm{sing}}(q_T) = \mathrm{d}\sigma^{\mathrm{sing}}(q_T) \left[1 + \mathcal{O}\left(\frac{q_T^2}{m_H^2}\right)\right]. \tag{3.33}$$

These two conditions are equivalent to the following two conditions on $d\sigma^{corr}(q_T)$,

$$d\sigma^{\rm corr}(q_T \to m_H) \to -d\sigma^{\rm sing}(q_T), \qquad \frac{d\sigma^{\rm corr}(q_T)}{d\sigma^{\rm sing}(q_T)} \sim \mathcal{O}\left(\frac{q_T^2}{m_H^2}\right).$$
 (3.34)

The easiest way to satisfy these conditions might be simply to take $d\sigma^{corr}(q_T)$ to be a constant, $d\sigma^{corr}(q_T) = -d\sigma^{sing}(m_H)$. This is equivalent to what was used in ref. [206], where the analogous decorrelation was used in a similar context. In that particular case, the phase space was strictly bounded to the equivalent of $q_T \leq m_H$. In contrast, this is no longer possible in our case: the phase space does not have such a strict boundary, and the decorrelation condition in eq. (3.31) must hold not only at the single point $q_T = m_H$ but for any $q_T \gtrsim m_H$. In other words, we require not only that $d\tilde{\sigma}^{sing}(q_T)$ crosses through 0 at $q_T = m_H$, but also that it remains zero for any larger q_T . Furthermore, a constant value for $d\sigma^{corr}(q_T)$ only corresponds to a linear power suppression of $\mathcal{O}(q_T/m_H)$. To obtain the correct quadratic power suppression of $\mathcal{O}(q_T^2/m_H^2)$, the correct extension of ref. [206] to our case is to take $d\sigma^{corr}/dq_T^2$ to be a constant.

To achieve this, let us denote $s(q_T) \equiv d\sigma/dq_T^2$ and choose $d\sigma^{corr}(q_T)$ more generally such that

$$s^{\rm corr}(q_T) = -s^{\rm sing}(q_T)$$
 for $q_T \sim m_H$,
 $s^{\rm corr}(q_T) = -s^{\rm sing}(\kappa m_H) = {\rm const.}$ for $q_T \ll m_H$. (3.35)

That is, $s^{\text{corr}}(q_T)$ is given by $-s^{\text{sing}}(q_T)$ at large q_T and freezes to a constant $-s^{\text{sing}}(\kappa m_H)$ at small q_T , where $\kappa \sim 1$ is a constant of our choice. To make this a smooth transition, we can reuse our profile functions and take

$$s^{\text{corr}}(q_T) = -s^{\text{sing}}[\tilde{q}_T(q_T)], \qquad (3.36)$$

where $\tilde{q}_T(q_T)$ is a function of q_T that transitions from κm_H to q_T ,

$$\tilde{q}_T(q_T) = \kappa m_H g_{\text{run}}(q_T/m_H) + q_T[1 - g_{\text{run}}(q_T/m_H)],$$
(3.37)

and $g_{\text{run}}(q_T)$ is defined as in eq. (3.10). For simplicity, we will use the same transition points [0.1, 0.45, 0.8] which we use for turning off the resummation (see section 3.2.2). Using eq. (3.36), we arrive at our final choice for $d\sigma^{\text{corr}}(q_T)$,

$$d\sigma^{\text{corr}}(q_T) = -2q_T s^{\text{sing}}[\tilde{q}_T(q_T)] = -\frac{q_T}{\tilde{q}_T(q_T)} d\sigma^{\text{sing}}[\tilde{q}_T(q_T)]. \tag{3.38}$$

In figure 3.10, we study the decorrelation procedure at NLO₁, where the fixed-order result is fully known. The left panel of the figure shows the correlated piece $d\sigma^{corr}(q_T)$ for different choices of κ alongside $-d\sigma^{sing}(q_T)$. For $q_T \geq x_3 m_H = 100 \,\text{GeV}$, $d\sigma^{corr}(q_T)$ exactly equals $-d\sigma^{sing}(q_T)$, while going to lower q_T it starts to deviate and eventually turn around and vanish linearly for $q_T \to 0$ as required by eq. (3.38). The correlated contribution itself depends strongly on the choice of κ , which determines where it effectively freezes out and turns around toward 0. Note also that by construction this dependence cancels exactly, such that the full result at this order is independent of κ . The actual choice of κ could in principle influence our NNLO₁ approximation, but essentially does not do so, as we shall see in the following subsection.

The right panel of figure 3.10 shows both the original, correlated singular (solid grey) and nonsingular (dotted grey) as well as the decorrelated singular (solid red) and nonsingular (dotted green) for $\kappa = 0.6$. Since they each sum to the fixed-order result (dashed blue), the correlated terms clearly exhibit a large cancellation for large $q_T \sim m_H$. In contrast, the decorrelated

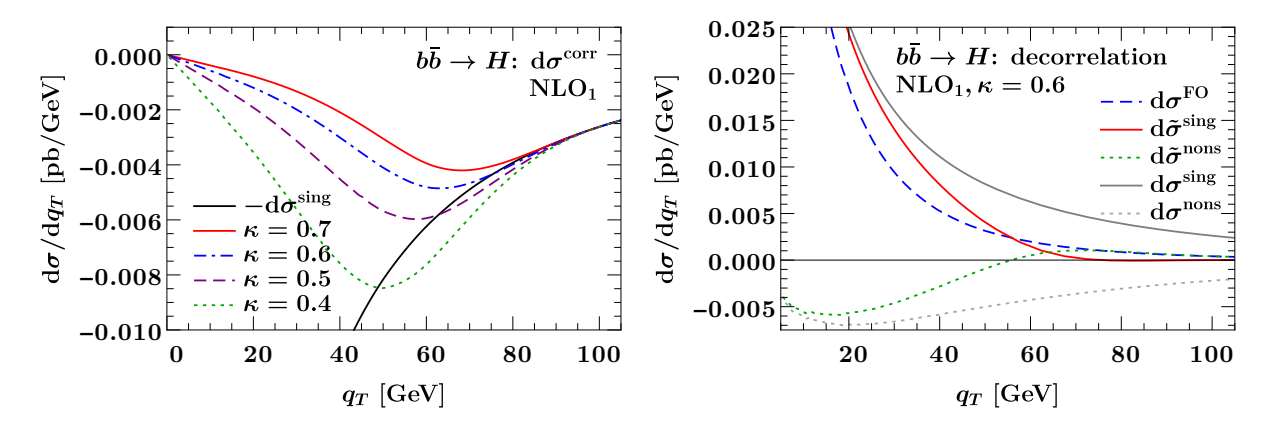


Figure 3.10: Decorrelation of singular and nonsingular at NLO₁. Left: Correlated contribution for different choices of κ (coloured lines) and its large- q_T asymptotic value $-\mathrm{d}\sigma^{\mathrm{sing}}$ (black). Right: Decorrelated singular (solid red), full, (dashed blue), and decorrelated nonsingular (dotted green) for $\kappa = 0.6$ at fixed NLO₁. The original, correlated singular and nonsingular are shown by the dotted and solid grey lines.

singular goes to zero for $q_T \sim m_H$, while the decorrelated nonsingular (dotted green) becomes equal to the full fixed order. This confirms that the decorrelation works as expected, and that $d\tilde{\sigma}^{\text{nons}}$ and $d\tilde{\sigma}^{\text{sing}}$ no longer exhibit strong cancellations. We will therefore use $\kappa = 0.6$ for $b\bar{b} \to H$. Since the strong cancellations between singular and nonsingular occur successively later for $c\bar{c} \to H$ and $s\bar{s} \to H$, as we saw in section 3.3.2, we will use higher values $\kappa = 0.7$ for $c\bar{c} \to H$ and $\kappa = 0.8$ for $s\bar{s} \to H$.

3.3.4 Approximate NNLO₁

Using the decorrelation method explained in the previous section, we are now in a position to construct an approximate $NNLO_1$ result as

$$d\sigma^{FO}(q_T) = d\tilde{\sigma}^{sing}(q_T) + d\tilde{\sigma}^{nons}(q_T) = d\sigma^{sing}(q_T) + d\sigma^{corr}(q_T; \kappa) + d\tilde{\sigma}^{nons}(q_T; \kappa), \quad (3.39)$$

where we made the dependence on κ in the last two terms explicit. We now need to approximate the unknown $\mathcal{O}(\alpha_s^3)$ contribution of $d\tilde{\sigma}^{\text{nons}}(q_T)$. To do so, we decompose $d\tilde{\sigma}^{\text{nons}}$ at the fixed scale $\mu_R = \mu_F = m_H$ in terms of perturbative coefficients $\tilde{c}_i(q_T)$,

$$d\tilde{\sigma}^{\text{nons}}(q_T) = |y_b(m_H)|^2 \left[\alpha_s(m_H) \,\tilde{c}_1(q_T) + \alpha_s^2(m_H) \,\tilde{c}_2(q_T) + \alpha_s^3(m_H) \,\tilde{c}_3(q_T) \right], \tag{3.40}$$

where $\tilde{c}_1(q_T)$ and $\tilde{c}_2(q_T)$ are known, and our goal is to approximate $\tilde{c}_3(q_T)$. To get the correct power of logarithms for $\tilde{c}_3(q_T)$, we perform a Padé-like approximation

$$\tilde{c}_3^{\text{approx}}(q_T) = K \frac{[\tilde{c}_2(q_T)]^2}{\tilde{c}_1(q_T)},$$
(3.41)

where we use the constant factor K to rescale this result such that its overall size agrees with ref. [203]. When using this approximation in eq. (3.39), we refer to the result as aNNLO₁. To determine an appropriate value for K, we consider the ratio of our approximate $\mathcal{O}(\alpha_s^3)$ coefficient to the exact result shown on the right in figure 3.11. The exact $\mathcal{O}(\alpha_s^3)$ coefficient is obtained by subtracting NNLO₁-NLO₁, where we can read off the ratio NNLO₁/NLO₁ from

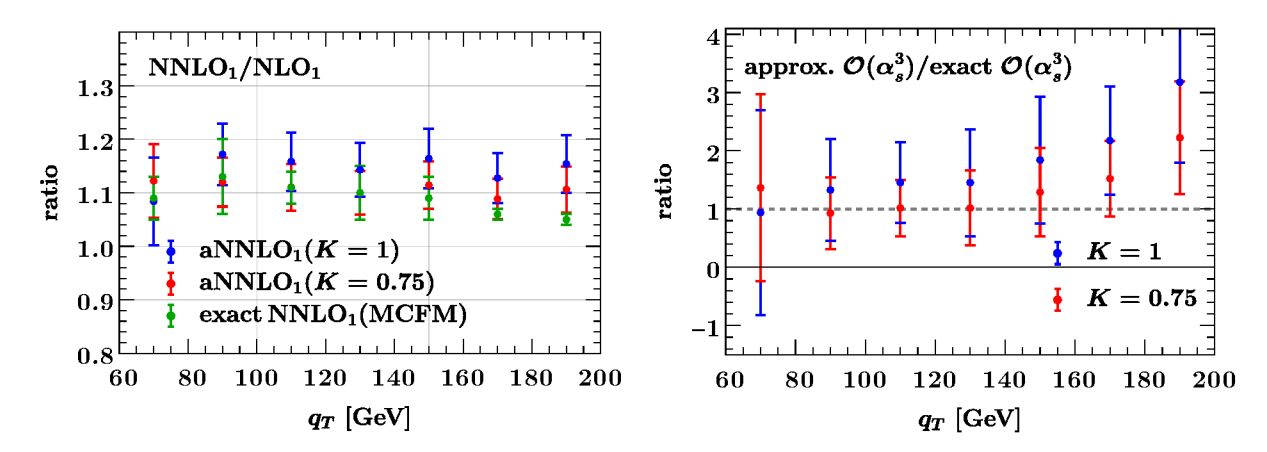


Figure 3.11: Comparison of the exact NNLO₁ results from ref. [203] at large q_T to our approximation. Left: Ratio of NNLO₁/NLO₁ for the exact result (green) and the approximate result with K=1 (blue) and K=0.75 (red). Right: Ratio of the approximate and exact $\mathcal{O}(\alpha_s^3)$ contribution for K=1 (blue) and K=0.75 (red). The uncertainties in all cases correspond to the scale variations.

the results shown in ref. [203]. As already mentioned, ref. [203] uses a cut on the leading jet $p_T \geq 30\,\mathrm{GeV}$, so we can only use their results for $q_T \geq 60\,\mathrm{GeV}$. For this purpose we use the same inputs as ref. [203], i.e., $\mu_F = m_H/2$ and the CT14nnlo PDF set. To extract a value for K, we perform a simple χ^2 fit to this ratio as a function of K, requiring that the ratio is unity. Since the kinematic region we are interested in is $q_T \lesssim m_H$, we use the first four points for $q_T \in [60, 140]\,\mathrm{GeV}$. Note that in this region the ratio is well approximated by a constant, which shows that the approximation in eq. (3.41) captures the q_T dependence well. We find K = 0.75, which we will use as our default value. We refrain from including an uncertainty on K, since it would be negligible compared to the nominal perturbative uncertainties.

The left panel of figure 3.11 shows the ratio NNLO₁/NLO₁ for the exact NNLO₁ result from ref. [203] (green) as well as for our approximate aNNLO₁ for K=1 (blue) and our default K=0.75 (red). The uncertainties correspond to varying μ_R and μ_F by a factor of 2. For our default K, we find very good agreement in the region of interest $q_T \lesssim m_H$ between our approximation and the exact results.

We then use the same value of K also at lower values of q_T as well as for the $s\bar{s} \to H$ and $c\bar{c} \to H$ channels and our default PDF set. That is, we effectively use our approximation to extrapolate the exact results from ref. [203] to lower q_T and the other channels and PDF.

The coefficients $\tilde{c}_i(q_T)$ depend on the choice of κ . For the exact coefficients, the κ dependence exactly cancels between the last two terms in eq. (3.39). However, when using the approximate $\tilde{c}_3^{\text{approx}}(q_T)$, the κ dependence will no longer cancel exactly. The residual κ dependence of the aNNLO₁ result is shown in the left panel of figure 3.12. Happily, we find that the approximate result is practically independent of the value of κ . In the right panel of figure 3.12, we illustrate the decomposition of the approximated full result for our default choice $\kappa = 0.6$ into the decorrelated singular and nonsingular pieces.

To obtain the correct scale dependence for the approximated result, we re-expand $\alpha_s(m_H)$ and

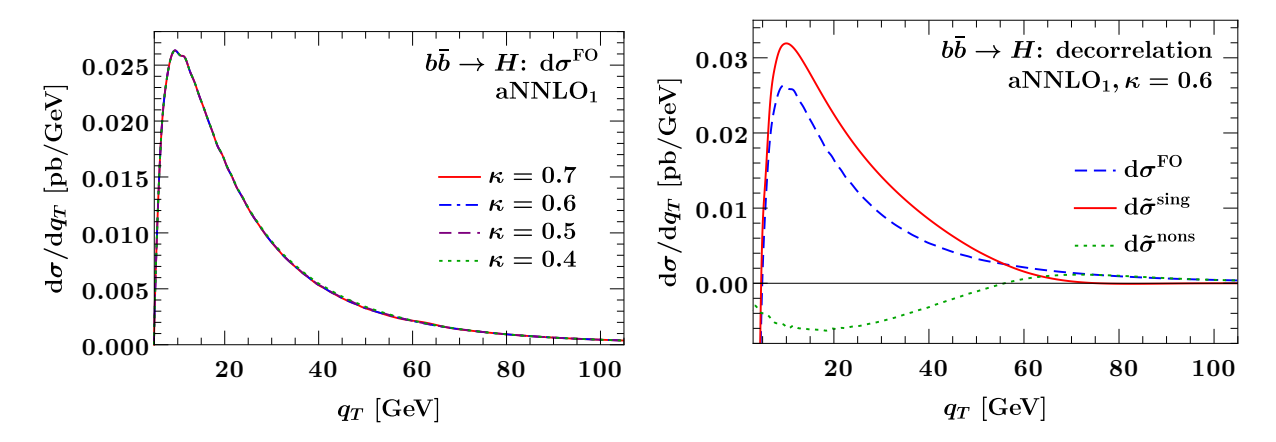


Figure 3.12: Decorrelation at aNNLO₁. Left: The resulting full fixed-order order cross section for different values of κ . Right: Decorrelated singular (solid red), full (dashed blue), and decorrelated nonsingular (dotted green) for $\kappa = 0.6$.

 $y_b(m_H)$ in terms of $\alpha_s(\mu_R)$, which yields

$$\frac{d\tilde{\sigma}^{\text{nons}}}{dq_T} = |y_b(\mu_R)|^2 \left\{ \alpha_s(\mu_R) \, \tilde{c}_1(q_T) + \alpha_s^2(\mu_R) \left[\tilde{c}_2(q_T) + \frac{\tilde{c}_1}{2\pi} (\beta_0 - \gamma_0) \ln \frac{\mu_R}{m_H} \right] \right. \\
+ \alpha_s^3(\mu_R) \left[\tilde{c}_3(q_T) + \left[\frac{\tilde{c}_1(q_T)}{8\pi^2} (\beta_1 - \gamma_1) + \frac{\tilde{c}_2(q_T)}{2\pi} (2\beta_0 - \gamma_0) \right] \ln \frac{\mu_R}{m_H} \right. \\
+ \left. \frac{\tilde{c}_1(q_T)}{8\pi^2} (2\beta_0^2 - 3\beta_0 \gamma_0 + \gamma_0^2) \ln^2 \frac{\mu_R}{m_H} \right] \right\}, \tag{3.42}$$

where β_n and γ_n are the relevant coefficients of the QCD beta function and the Yukawa anomalous dimension which are given in appendix B.1. The μ_R dependence in the approximated result is therefore exact, and we are able to vary μ_R without further approximation.

For the μ_F dependence, for simplicity we perform the approximation for $\tilde{c}_3(q_T)$ in eq. (3.41) in terms of $\tilde{c}_1(q_T)$ and $\tilde{c}_2(q_T)$ at any given μ_F , using the same rescaling factor K as for the central μ_F choice. This means we will only have an approximate μ_F dependence at $\mathcal{O}(\alpha_s^3)$ that only approximately cancels up to higher $\mathcal{O}(\alpha_s^4)$ terms. This will lead to slightly larger μ_F variations compared to the exact $\mathcal{O}(\alpha_s^3)$ μ_F dependence, which we can simply consider as an additional uncertainty due to the approximation.

3.4 The q_T spectrum at N³LL'+aN³LO

In this section, we present our numerical result for the $q\bar{q} \to H$ q_T spectrum. We use $E_{\rm cm}=13\,{\rm TeV},\ m_H=125\,{\rm GeV}$, and the MSHT20nnlo PDF set [234] with $\alpha_s(m_Z)=0.118$. We assess the impact of changing the PDF set in appendix D. For the Yukawa coupling we evolve $\overline{m}_q(\mu_q)$ to $\mu_{\rm FO}$ where $\mu_{b,c}=\overline{m}_{b,c}$ for the bottom and charm quarks and $\mu_s=2\,{\rm GeV}$ for the strange quark. The input $\overline{\rm MS}$ quark masses are $\overline{m}_b(\overline{m}_b)=4.18\,{\rm GeV},\ \overline{m}_c(\overline{m}_c)=1.27\,{\rm GeV}$, and $\overline{m}_s(2\,{\rm GeV})=93.4\,{\rm MeV}$ [19], and we use $v=246.22\,{\rm GeV}$ for the Higgs vev to convert the masses into Yukawa couplings. Our scale choices are described in sections 3.2.1 and 3.2.2. All our numerical results for the resummed and fixed-order singular contributions are obtained with SCETLIB [224]. The full fixed-order results are obtained as discussed in sections 3.3.1 and 3.3.4. For the aNNLO₁ result we use the parameter K=0.75.

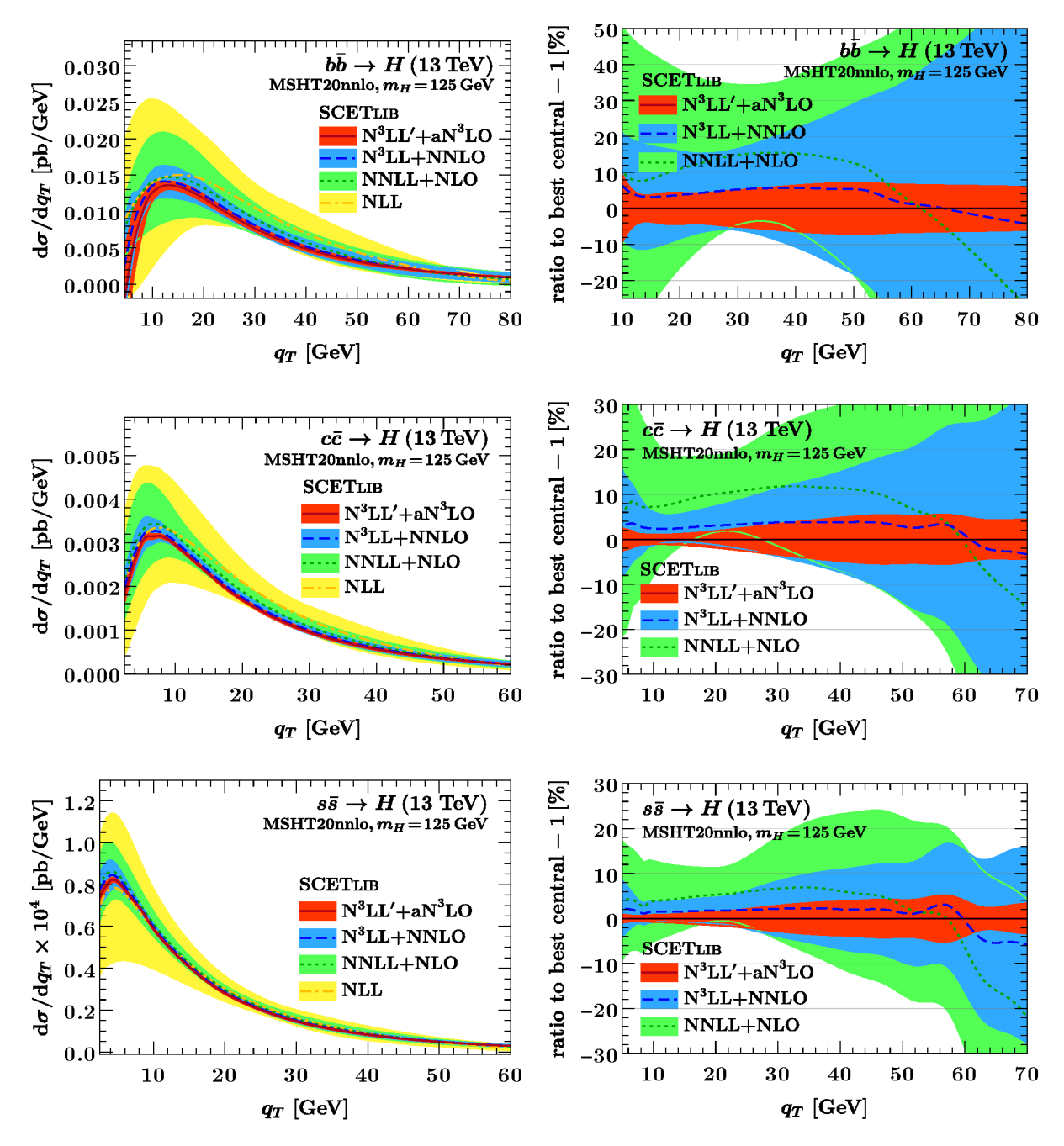


Figure 3.13: Resummed q_T spectrum up to N³LL'+aN³LO for $b\bar{b} \to H$ (top row), $c\bar{c} \to H$ (middle row), and $s\bar{s} \to H$ (bottom row). The results for the spectrum are shown on the left. The results normalized relative to the best central value at N³LL'+aN³LO are shown on the right.

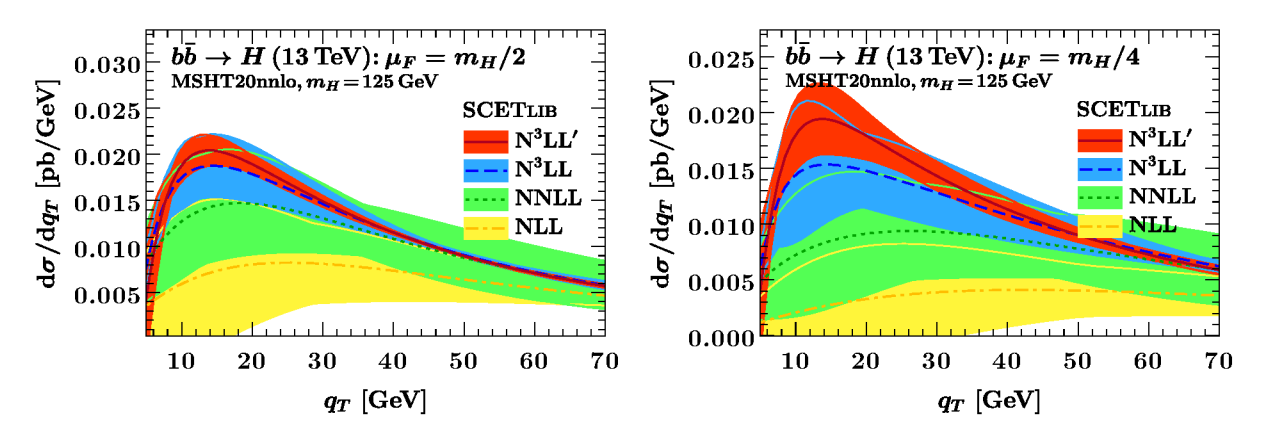


Figure 3.14: The purely resummed result for $b\bar{b} \to H$ at different orders for different values of μ_F .

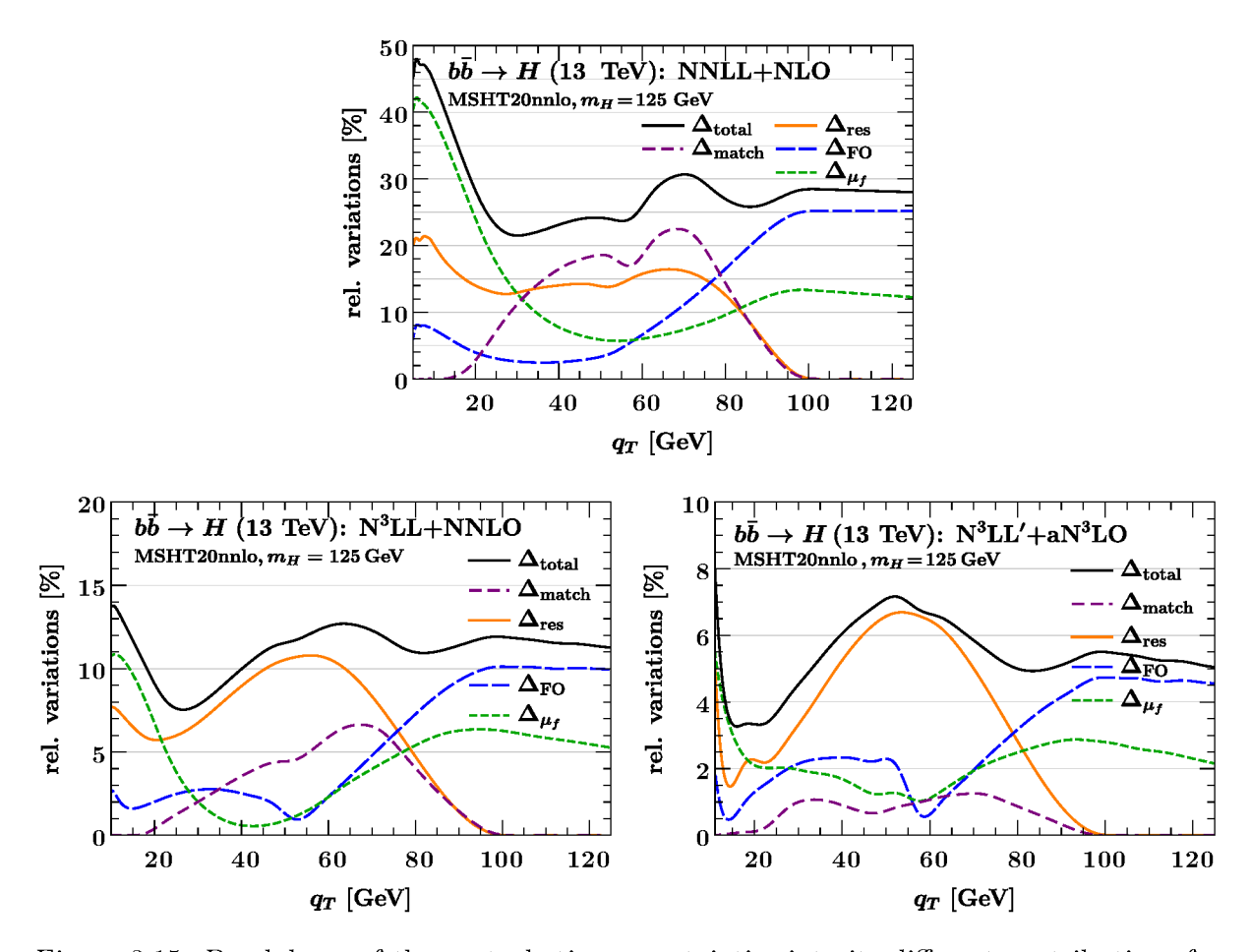


Figure 3.15: Breakdown of the perturbative uncertainties into its different contributions for $b\bar{b} \to H$ at NNLL+NLO (top), N³LL+NNLO (bottom left), and N³LL'+aN³LO (bottom right). Note the different scales on the vertical axes for each plot.

In figure 3.13, we show the resummed q_T spectrum for $b\bar{b} \to H$ (top), $c\bar{c} \to H$ (middle) and $s\bar{s} \to H$ (bottom) at different resummation orders up to the highest N³LL'+aN³LO. The bands show the perturbative uncertainty estimate as discussed in section 3.2.3. We observe excellent perturbative convergence for all channels, with reduced uncertainties at each higher order. The perturbative uncertainties increase in general from $s\bar{s} \to H$, to $c\bar{c} \to H$, to $b\bar{b} \to H$. Comparing the ratio plots for $s\bar{s} \to H$ and $b\bar{b} \to H$ it is evident that the relative uncertainties for $b\bar{b} \to H$ at a given order are of similar size as those for $s\bar{s}\to H$ at one lower order. As already mentioned in section 3.3.2, the main difference between the channels is the relative size of the PDF luminosities. Since for $bb \to H$, the bb Born channel is numerically suppressed by the small b-quark PDFs, the gluon-induced PDF channels which start at one higher order play a much more prominent role. This explains the observed pattern of uncertainties for the different cases. We also want to point that plot showing the $bb \to H q_T$ spectrum in figure 3.13 is only shown for $q_T > 5 \,\text{GeV}$. With the bottom mass $m_b = 4.18\,\mathrm{GeV}$ our assumption of $m_q \ll q_T$ and therefore our factorization theorem are no longer valid for $q_T \lesssim 5 \,\text{GeV}$ and we would have to include proper mass effects. In fact, we can already see for $q_T \approx 7 \,\text{GeV}$ that highest-order prediction is no longer included in the lower uncertainty bands which indicated that the subleading-power mass effects should be included at this order. For the $c\bar{c} \to H$ and $s\bar{s} \to H$ channels this is less of a problem due to the lighter quark masses.

Our default choice for the PDF scale μ_f corresponds to taking $\mu_F = m_H$ in the fixed-order limit. Fixed-order predictions for $b\bar{b} \to H$ traditionally use a lower scale of $\mu_F = m_H/2$ or $\mu_F = m_H/4$, so one might wonder whether the uncertainties for $b\bar{b} \to H$ might be reduced by choosing a lower central value for μ_F . For completeness, we therefore also give results for $b\bar{b} \to H$ at these lower values for the central factorization scale. We implement this by taking $w_F = -1$ or $w_F = -2$ as central choice in eq. (3.12). Figure 3.14 shows the convergence of the resummed contribution to the q_T spectrum at NLL (yellow), NNLL (green), N³LL (blue), and N³LL' (red) for $\mu_F = m_H/2$ (left) and $\mu_F = m_H/4$ (right). While the convergence pattern of subsequent orders is acceptable in all cases, both the corrections and perturbative uncertainties are somewhat larger for $\mu_F = m_H/2$ than for $\mu_F = m_H$, and substantially larger for $\mu_F = m_H/4$. In our context these lower choices are therefore clearly less preferable.

A detailed breakdown of the uncertainty estimate for $bb \to H$ is shown in figure 3.15. The Δ_{μ_f} uncertainty (short-dashed green) dominates up to $q_T \lesssim 20\,\text{GeV}$ before tending to a constant for $q_T \gtrsim 80\,\text{GeV}$. At NNLL+NLO the matching uncertainty Δ_{match} (long-dashed purple) is largest for $30\,\text{GeV} \lesssim q_T \lesssim 80\,\text{GeV}$ and vanishes outside of the transition region as it should. At higher orders, the resummation uncertainty Δ_{res} (solid orange) dominates in this region before going to zero as the resummation is turned off toward large q_T . As one might expect, at the same time the fixed-order uncertainty Δ_{FO} (dashed blue) increases and becomes the dominant uncertainty in the fixed-order region.

In figure 3.16, we show the impact of the individual uncertainties for $c\bar{c} \to H$ and $s\bar{s} \to H$. In general, they display a behaviour very similar to $b\bar{b} \to H$. The main difference between the processes is the size of the resummation and the matching uncertainty. The matching uncertainty is slightly smaller for $b\bar{b} \to H$; this is to be expected, since we chose our transition points in section 3.3.2 for this specific case. On the other hand, $\Delta_{\rm res}$ is smaller for $c\bar{c} \to H$ and $s\bar{s} \to H$. The total uncertainty for $s\bar{s} \to H$ is therefore dominated by $\Delta_{\rm match}$ for 30 GeV $\lesssim q_T \lesssim$ 70 GeV. For $c\bar{c} \to H$, $\Delta_{\rm match}$ has the largest impact at N³LL+NNLO whereas at N³LL'+aN³LO $\Delta_{\rm res}$ contributes the most. The fixed-order uncertainty starts to dominate the total uncertainty slightly earlier than for $b\bar{b} \to H$ as the other contributions are in general smaller.

In figure 3.17, we compare the normalized q_T spectra for $s\bar{s} \to H$ (red), $c\bar{c} \to H$ (blue), and

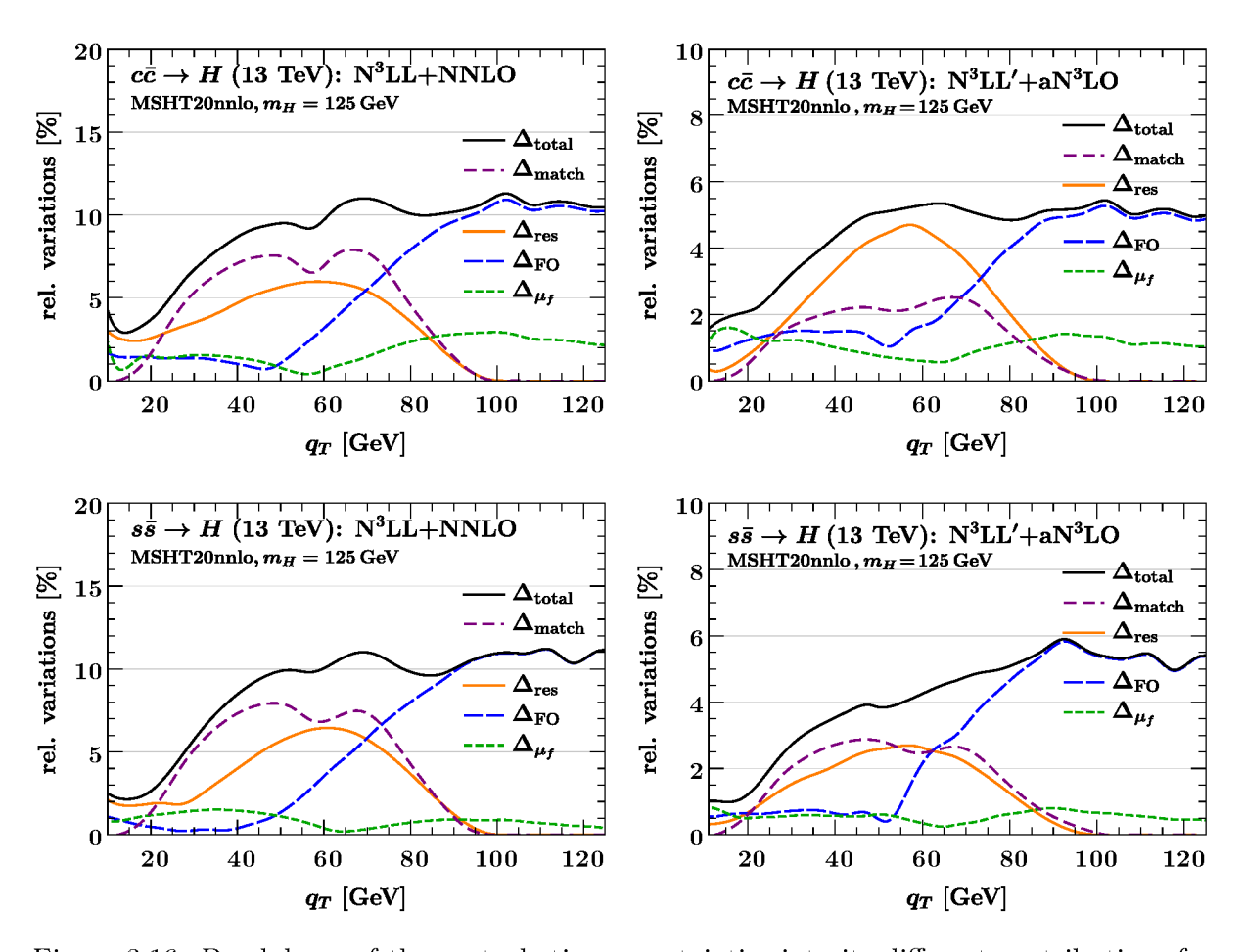


Figure 3.16: Breakdown of the perturbative uncertainties into its different contributions for $c\bar{c} \to H$ (left) and $s\bar{s} \to H$ (right) at N³LL+NNLO (top) and N³LL'+aN³LO (bottom).

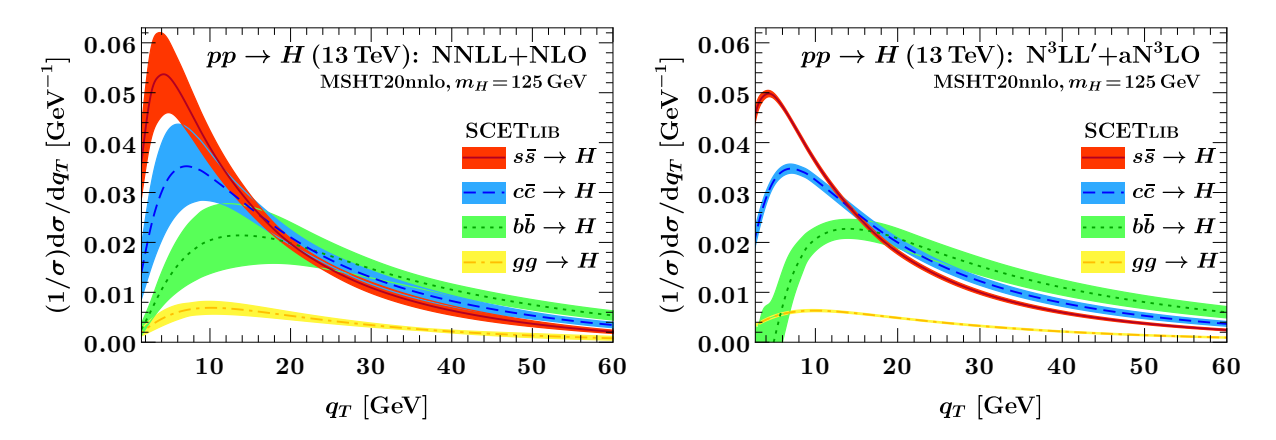


Figure 3.17: Comparison of the normalized q_T spectrum for $s\bar{s} \to H$, $c\bar{c} \to H$, $bb \to H$ and $gg \to H$ at NNLL+NLO (left) and N³LL'+aN³LO (right). The $gg \to H$ channel is only included at N³LL'+NLO

 $b\bar{b} \to H$ (green). We also included the gluon fusion contribution $(gg \to H)$ in yellow. The left panel shows the spectra at NNLL+NLO, where one can already see that the spectra of the channels exhibit different shapes. At this order however the uncertainties largely overlap in the peak region. The right panel shows the spectra at N³LL'+aN³LO. Here, the uncertainties are significantly smaller and we can clearly distinguish the channels by their different shapes in q_T . Just as before the plot is only shown for $q_T > 5 \,\text{GeV}$. Below this value of q_T bottom-mass effects become relevant and our factorization theorem is no longer valid. A prediction for $q_T < 5 \,\text{GeV}$ would therefore not be reliable. The gluon fusion prediction exhibits a slightly different shape with a much broader peak and be clearly distinguished in both plots. This difference in the shape is due to the different color factors in the Wilson coefficient of the hard function. The quark induced channels come with a C_F whereas the gluon induced contribution comes with a C_A instead. We want to point out that the gluon fusion contribution looks much smaller then the quark initiated channels. This is due to the normalization.

Our predictions could therefore be used to improve the determination of quark Yukawa coupling from the shape of the measured Higgs q_T spectrum – such an analysis has already been performed in refs. [42, 43], using measurements in the $H \to ZZ^* \to 4\ell$ and $H \to \gamma\gamma$ decay channels.

3.5 Summary and Outlook

In this chapter, we have studied the transverse momentum spectrum of the Higgs boson produced in heavy quark annihilation, $q\bar{q} \to H$ with q = s, c, b. This is an interesting process, as it has the potential to constrain the Yukawa couplings of charm, bottom, and possibly strange quarks. We have used soft-collinear effective theory to resum large logarithms of q_T/m_H up to N³LL' order and matched these results to fixed-order calculations. For $b\bar{b} \to H$ and to a lesser extent $c\bar{c} \to H$, the large size of the nonsingular terms requires extra care in the matching procedure and the estimation of matching uncertainties. Accordingly, we introduced some refinements to the standard method when using profile-scale variations, which could also be useful in other contexts. It consists of fixing the extreme profile function transition points and varying instead the central point over a wider range. This leads to an uncertainty estimate without one-sided

uncertainties, and which in our case avoids being overly conservative.

We have constructed an approximation of the q_T spectrum at fixed $\mathcal{O}(\alpha_s^3)$, which we have used to extrapolate from existing NNLO₁ results for $b\bar{b} \to H + j$ for $q_T \ge 60\,\text{GeV}$ to smaller q_T and other flavour channels. This is based on introducing a decorrelation procedure to ensure the correct cancellation between singular and nonsingular terms at scales $q_T \sim m_H$, and then approximating the $\mathcal{O}(\alpha_s^3)$ nonsingular piece. This allows us to achieve a final accuracy of N³LL'+aN³LO for the q_T spectrum. Our results display good convergence properties from order to order, and constitute the highest available accuracy for these processes. As we have seen in figure 3.17, at the highest available order the uncertainties are significantly reduced, such that the different flavour channels are clearly distinguishable by their different shapes in q_T . Our predictions could therefore be used to improve the determination of Higgs Yukawa couplings from the Higgs q_T spectrum as carried out in refs. [42,43].

Our treatment of the $q\bar{q} \to H$ process in this work has neglected finite quark-mass effects, which are relevant for $q_T \sim m_q$ and are thus an important consideration especially for $bb \to H$. The inclusion of these terms in the resummation formalism has been derived for the Drell-Yan process in ref. [205], and the extension to our case would be relatively straightforward. It would also be interesting to investigate in more detail the impact of the resummation of time-like logarithms in the $q\bar{q}H$ hard function on the resummed q_T spectrum, as it has been shown to have a nontrivial impact on the inclusive $b\bar{b} \to H$ cross section [207]. Further, we used scale variation to estimate our uncertainties. These uncertainties often fail to capture the next higher order, i.e. they underestimate the uncertainties at the given perturbative order. More importantly, scale variations do not contain any information about the correlations between different uncertainties. These correlation are important for experimental analysis. A promising method that fully captures the correlations of different sources of uncertainties are theory nuisance parameters (TNPs) [235]. It would be interesting to see how the uncertainties change if we use TNPs instead of scale variations. Finally, we have only considered the q_T spectrum for inclusive Higgs production here. Experimentally required cuts on the Higgs decay products induce fiducial power corrections [138,236], which were found to be important in case of $gg \to H$ production [44]. It would thus be interesting to investigate their importance also in case of $q\bar{q} \to H$. These topics, however, are beyond the scope of this thesis.

Chapter 4

Resumming transverse observables in GENEVA

In the previous chapter, we presented a new high-precision prediction for the transverse momentum spectrum of quark initiated Higgs production. However, in practice the experimental data looks quite different from the analytically calculated spectrum. Often, the final-state particles cannot be detected directly and can only be reconstructed from their decay products. Event generators are important tools in particle physics as they simulate the full evolution of a collision. This includes the hard interaction process as well as hadronization, parton showers and decays to the color-neutral hadrons which are detected. In this chapter, we present the full implementation of the $q\bar{q}\to H$ process in the event generator Geneva [225, 226]. We choose the transverse momentum q_T and 1-jettiness as resolution variables to distinguish events with zero, one or two and more jets which we resum to NNLL' and NLL' accuracy. This presents a first step towards NNLO+PS in Geneva for the $q\bar{q}\to H$ process and is –to our knowledge– the first time that the generalized 1-jettiness variable is resummed beyond leading logarithmic order.

This chapter is based ref. [6] reflecting the author's contribution. Compared to ref. [6], we shortened section 4.3 and give preliminary results of the q_T and \mathcal{T}_1 spectra. Additionally, we extended the discussion section 4.4.1.

4.1 Motivation

The state-of-the-art for predictions matched to parton shower generators is currently next-to-next-to-leading order (NNLO+PS). Two main approaches exist to achieve this accuracy [237,238], while a third, rather different approach, is currently under active development [239]

An interesting question relevant to the construction of NNLO+PS generators concerns the choice of resolution variables, which partition the phase space into jet bins of differing multiplicity. These resolution variables must be resummed to high logarithmic accuracies. While many choices are in principle possible, the predictions for exclusive observables will depend on this choice, naturally introducing a source of systematic uncertainty. A natural way to gauge the size of this uncertainty would be to compare the predictions of generators constructed using the same method but different resolution variables. In addition, the availability of higher-accuracy parton shower algorithms [240–243] means that one may wish to explore novel variable choices to ensure the preservation of the shower accuracy in matching.

In this chapter, we implement a new combination of resolution variables in the Geneva approach. The original formulation of GENEVA [225] used the zero- and one-jettiness [140] to separate the phase space into zero, one and two or more jet bins. Here zero- and one-jettiness take care of the separation between 0/1- and 1/2- jet bins respectively, and indeed many electroweak processes have since been examined in this context [226, 229, 244–248]. The jettiness variable has the advantage of considerable simplicity, admitting a simple factorization structure in SCET-I which faciliates resummation [141,249]. The factorization of N-jettiness was discussed in section 2.5.4. However, the fact that the usual definition of the jettiness involves an invariant mass-like measure complicates the matching to commonly employed parton shower algorithms, which tend to be ordered in transverse momentum. An alternative formulation using the colour-singlet transverse momentum q_T to separate the 0/1-jet bins was studied in Ref. [250], with q_T resummation at N³LL provided by the RadISH formalism [251,252]. The 1/2-jet separation variable remained, however, the one-jettiness. In Ref. [253], a generator for W^+W^- production was constructed using the hardest and second-hardest jet transverse momenta as variables and SCET-based resummation [223, 254]. With these choices, the need for truncated showering techniques [255] in Geneva could be overcome.

The new class of generators we initiate in this work uses transverse observables to separate all jet bins, as in Ref. [253]. We use q_T as the primary resolution variable, though exploiting analytic SCET-II resummation provided by SCETLIB [224] rather than the RadISH approach previously taken. As a secondary resolution variable, we choose a generalization of the one-jettiness which uses a transverse momentum-like measure. Though the definition of this observable was introduced in the original N-jettiness paper over 14 years ago [140], to our knowledge this is the first time that its resummation has been accomplished beyond leading logarithmic order. ¹ The observable is interesting not merely because it facilitates matching for color-singlet production in association with additional jets. The work we present here takes a very first step in this direction, achieving resummation at NLL'.

As a case study, we consider the production of a Higgs boson through bottom-quark annihilation $b\bar{b} \to H$. The q_T resummation for this process was discussed in detail in the previous chapter. An NNLO+PS generator for the $b\bar{b}H$ process was constructed in Ref. [257] using the MiNNLOPS formalism. As detailed in e.g. Ref. [40], measurements of the Higgs boson q_T spectrum could be used in conjunction with precision theory predictions for $b\bar{b}H$ to extract a value for the bottom Yukawa coupling y_b . Generalizations to other color-singlet processes are in principle straightforward.

The rest of this chapter is arranged as follows. In section 4.2, we provide a brief overview of the Geneva method. In section 4.3 we briefly review the definition of the generalized jettiness. We present NNLL'+NLO results for the q_T spectrum and NLL'+NLO results for the \mathcal{T}_1 spectrum for $b\bar{b}H$ in section 4.4 which present the first steps towards an NNLO+PS prediction with these resolution variables and summarize our results in section 4.5.

4.2 The GENEVA method

The GENEVA method [225, 237] relies on defining infra-red (IR) safe events at a specific perturbative order, which are obtained from both fixed-order and resummed calculations. This is achieved by converting IR-divergent final states with M partons into IR-finite final states with

¹We note that a similar generalization of the jettiness has more recently been proposed in Ref. [256].

N partonic jets, where $M \geq N$, ensuring that the divergences cancel on an event-by-event basis. This conversion is performed using an N-jet resolution variable r_N which divides the phase space into regions with different numbers of resolved emissions: Φ_0 where there is no additional jet, Φ_1 with one jet and Φ_2 with two or more jets in the final state. Then, the 0-jet cross section contains all 0-jet events and all events with $r_0 < r_0^{\rm cut}$, i.e. where the additional jet is unresolved. The differential cross section with no extra emission is given by

$$\frac{d\sigma_0^{\text{MC}}}{d\Phi_0}(r_0^{\text{cut}}) = \frac{d\sigma^{\text{NNLL'}}}{d\Phi_0} - \frac{d\sigma^{\text{NNLL'}}}{d\Phi_0} \bigg|_{\text{NNLO}_0} + (B_0 + V_0 + W_0)(\Phi_0) + \int \frac{d\Phi_1}{d\Phi_0}(B_1 + V_1)(\Phi_1)\theta[r_0(\Phi_1) < r_0^{\text{cut}}] + \int \frac{d\Phi_2}{d\Phi_0}B_2(\Phi_2)\theta[r_0(\Phi_2) < r_0^{\text{cut}}], \tag{4.1}$$

where $d\sigma^{\text{NNLL'}}$ is the resummed cross section at NNLL' and $d\sigma^{\text{NNLL'}}|_{\text{NNLO}_0}$ is its fixed-order expansion. B_M contains the tree-level contributions with M partons in the final state, V_M the M-parton one-loop contributions and W_0 the two-loop contribution. We also introduced the short-hand notation

$$\frac{\mathrm{d}\Phi_M}{\mathrm{d}\Phi_N} = \mathrm{d}\Phi_M \delta[\Phi_N - \Phi_N(\Phi_M)],\tag{4.2}$$

which indicates an integration over the part of the Φ_M phase space that can be reached from a Φ_N point. The differential cross sections with one additional jet has two contributions: the one above r_0^{cut}

$$\frac{d\sigma_{1}^{\text{MC}}}{d\Phi_{1}}(r_{0} > r_{0}^{\text{cut}}; r_{1}^{\text{cut}}) = \left\{ \frac{\sigma^{\text{NNLL'}}}{d\Phi_{0}dr_{0}} \mathcal{P}(\Phi_{1}) - \left[\frac{d\sigma^{\text{NNLL'}}}{d\Phi_{0}dr_{0}} \mathcal{P}(\Phi_{1}) \right]_{\text{NLO}_{1}} + (B_{1} + V_{1}^{C})(\Phi_{1}) \right\} \\
\times U_{1}(\Phi_{1}, r_{1}^{\text{cut}})\theta(r_{0} > r_{0}^{\text{cut}}) \\
+ \int \left[\frac{d\Phi_{2}}{d\Phi_{1}^{r}} B_{2}(\Phi_{2})\theta(r_{0}(\Phi_{2}) > r_{0}^{\text{cut}})\theta(r_{1} < r_{1}^{\text{cut}}) \\
- \frac{d\Phi_{2}}{d\Phi_{1}^{C}} C_{2}(\Phi_{2})\theta(r_{0} > r_{0}^{\text{cut}}) \right] \\
- B_{1}(\Phi_{1})U_{1}^{(1)}(\Phi_{1}, r_{1}^{\text{cut}})\theta(r_{0} > r_{0}^{\text{cut}}), \tag{4.3}$$

and the nonsingular terms below r_0^{cut} which arises from non-projectable configurations

$$\frac{\mathrm{d}\sigma_1^{\mathrm{MC}}}{\mathrm{d}\Phi_1}(r_0 \le r_0^{\mathrm{cut}}; r_1^{\mathrm{cut}}) = (B_1 + V_1)(\Phi_1)\overline{\Theta}_{\mathrm{map}}^{\mathrm{FKS}}(\Phi_1)\theta(r_0 < r_0^{\mathrm{cut}}). \tag{4.4}$$

Similarly, the cross section for two or more jets is given by

$$\frac{d\sigma_{\geq 2}^{MC}}{d\Phi_{2}}(r_{0} > r_{0}^{cut}; r_{1} > r_{1}^{cut}) = \left\{ \frac{\sigma^{NNLL'}}{d\Phi_{0}dr_{0}} \mathcal{P}(\Phi_{1}) - \left[\frac{d\sigma^{NNLL'}}{d\Phi_{0}dr_{0}} \mathcal{P}(\Phi_{1}) \right]_{NLO_{1}} + (B_{1} + V_{1}^{C})(\Phi_{1}) \right\} \\
\times U_{1}'(\Phi_{1}, r_{1})\theta(r_{0} > r_{0}^{cut}) \Big|_{\Phi_{1} = \Phi_{1}^{r}(\Phi_{2})} \mathcal{P}(\Phi_{2})\theta(r_{1} > r_{1}^{cut}) \\
+ \left\{ B_{2}(\Phi_{2})[1 - \Theta^{r}(\Phi_{2})\theta(r_{1} < r_{1}^{cut})] \right. \\
\left. - B_{1}(\Phi_{1}^{r})U_{1}^{(1)} '(\Phi_{1}^{r}, r_{1})\mathcal{P}(\Phi_{2})\theta(r_{1} < r_{1}^{cut}) \right\} \\
\times \theta(r_{0}(\Phi_{2}) > r_{0}^{cut}), \tag{4.5}$$

and

$$\frac{d\sigma_{\geq 2}^{MC}}{d\Phi_2}(r_0 > r_0^{\text{cut}}; r_1 \leq r_1^{\text{cut}}) = B_2(\Phi_2)\overline{\Theta}_{\text{map}}^{\text{r}}(\Phi_2)\theta(r_1 < r_1^{\text{cut}})\theta(r_0(\Phi_2) > r_0^{\text{cut}}). \tag{4.6}$$

In the above equations, $U_1(\Phi_1, r_1^{\text{cut}})$ denotes the NLL Sudakov factor that resums r_1^{cut} and $U_1(\Phi_1, r_1^{\text{cut}})'$ is its derivative with respect to r_1^{cut} . The terms $U_1^{(1)}(\Phi_1, r_1^{\text{cut}})$ and $U_1^{(1)}(\Phi_1, r_1^{\text{cut}})$ denote their respective $\mathcal{O}(\alpha_s)$ expansion.

The projection

$$\frac{\mathrm{d}\Phi_2}{\mathrm{d}\Phi_1^r} \equiv \mathrm{d}\Phi_2 \delta[\Phi_1 - \Phi_1^r(\Phi_2)]\Theta^r(\Phi_2),\tag{4.7}$$

is used to generate $1 \to 2$ events, where $\Theta^r(\Phi_2)$ defines the region of Φ_2 that can be projected onto the Φ_1 via the map $\Phi_1^r(\Phi_2)$. The mapping is constructed in such a way that it preserves the value of r_0

$$r_0(\Phi_1^r(\Phi_2)) = r_0(\Phi_2), \tag{4.8}$$

which crucial to ensure the cancellation of the singular r_0 dependence on an event-by-event basis in eqs. (4.3) and (4.5). The V_1^C term is given by

$$V_1^C = V_1(\Phi_1) + \int \frac{d\Phi_2}{d\Phi_1^C} C_2(\Phi_2), \tag{4.9}$$

where C_2 acts as a standard NLO subtraction that reproduces the singular behaviour of B_2 . We need to extend the dependence of the resummed cross section from an N-jet to an N + 1-jet phase space. This can be achieved by using a normalized splitting function

$$\int \frac{\mathrm{d}\Phi_{N+1}}{\mathrm{d}\Phi_N \mathrm{d}r_N} \mathcal{P}(\Phi_{N+1}) = 1. \tag{4.10}$$

The differential dependence on Φ_{N+1} is included in terms of r_N and two other variables. These could, for example, be an energy fraction z and an azimuthal angle φ .

Additionally, we are using an extension of the GENEVA method, developed in [253], which provides better control over the resummation of variable r_1 . Using an NLL Sudakov factor in eqs. (4.3) and (4.5) does not account for all singular terms in the $r_1 \to 0$ limit. This can be solved by upgrading the resummation accuracy of r_1 to NLL'. Then the 0-jet exclusive, 1-jet exclusive and 2-jet differential cross sections are given by

$$\begin{split} \frac{\mathrm{d}\sigma_{0}^{\mathrm{MC}}}{\mathrm{d}\Phi_{0}}(r_{0}^{\mathrm{cut}}) &= \frac{\mathrm{d}\sigma^{\mathrm{NNLL'_{r_{0}}}}}{\mathrm{d}\Phi_{0}}(r_{0}^{\mathrm{cut}}) - \frac{\mathrm{d}\sigma^{\mathrm{NNLL'_{r_{0}}}}}{\mathrm{d}\Phi_{0}}(r_{0}^{\mathrm{cut}}) \bigg|_{\mathrm{NLO_{0}}} + \frac{\mathrm{d}\sigma^{\mathrm{NLO_{0}}}}{\mathrm{d}\Phi_{0}}(r_{0}^{\mathrm{cut}}) \\ &= \left\{ \left[\frac{\mathrm{d}\sigma^{\mathrm{NNLL'_{r_{0}}}}}{\mathrm{d}\Phi_{0}\mathrm{d}r_{0}} - \frac{\mathrm{d}\sigma^{\mathrm{NNLL'_{r_{0}}}}}{\mathrm{d}\Phi_{0}\mathrm{d}r_{0}} \bigg|_{\mathrm{NLO_{1}}} \right] \mathcal{P}_{0\to 1}(\Phi_{1})U_{1}(\Phi_{1}) \\ &+ \frac{\mathrm{d}\sigma^{\mathrm{NLO_{1}}}}{\mathrm{d}\Phi_{1}}(r_{1}^{\mathrm{cut}}) + \frac{\mathrm{d}\sigma^{\mathrm{NLL'_{r_{1}}}}}{\mathrm{d}\Phi_{1}}(r_{1}^{\mathrm{cut}}) - \frac{\mathrm{d}\sigma^{\mathrm{NLL'_{r_{1}}}}}{\mathrm{d}\Phi_{1}}(r_{1}^{\mathrm{cut}}) \bigg|_{\mathrm{NLO_{1}}} \right\} \theta(r_{0} > r_{0}^{\mathrm{cut}}) \\ &+ \frac{\mathrm{d}\sigma^{\mathrm{LO_{1}}}_{\mathrm{nonproj}}}{\mathrm{d}\Phi_{1}} \\ &\frac{\mathrm{d}\sigma^{\mathrm{MC}}_{\geq 2}}{\mathrm{d}\Phi_{2}} = \left\{ \left[\frac{\mathrm{d}\sigma^{\mathrm{NNLL'_{r_{0}}}}}{\mathrm{d}\Phi_{0}\mathrm{d}r_{0}} - \frac{\mathrm{d}\sigma^{\mathrm{NNLL'_{r_{0}}}}}{\mathrm{d}\Phi_{1}\mathrm{d}r_{1}} \bigg|_{\mathrm{NLO_{1}}} \right] \mathcal{P}_{0\to 1}(\Phi_{1})U_{1}'(\Phi_{1}, r_{1})\mathcal{P}_{1\to 2}(\Phi_{2}) \\ &+ \frac{\mathrm{d}\sigma^{\mathrm{LO_{2}}}}{\mathrm{d}\Phi_{2}} + \left[\frac{\mathrm{d}\sigma^{\mathrm{NLL'_{r_{1}}}}}{\mathrm{d}\Phi_{1}\mathrm{d}r_{1}} - \frac{\mathrm{d}\sigma^{\mathrm{NLL'_{r_{1}}}}}{\mathrm{d}\Phi_{1}\mathrm{d}r_{1}} \bigg|_{\mathrm{LO_{2}}} \right] \mathcal{P}_{1\to 2}(\Phi_{2}) \right\} \theta(r_{1} > r_{1}^{\mathrm{cut}})\theta(r_{0} > r_{0}^{\mathrm{cut}}) \\ &+ \frac{\mathrm{d}\sigma^{\mathrm{LO_{2}}}_{\mathrm{nonproj}}}{\mathrm{d}\Phi_{2}}\theta(r_{1} < r_{1}^{\mathrm{cut}})\theta(r_{0} > r_{0}^{\mathrm{cut}}), \tag{4.13} \end{split}$$

which reproduce the exact NNLL' spectrum for the r_0 resummation. We have also introduced the following short-hand notation

$$\frac{d\sigma^{\text{NLO}_0}}{d\Phi_0}(r_0^{\text{cut}}) = B_0(\Phi_0) + V_0(\Phi_0) + \int \frac{d\Phi_1}{df\Phi_0} B_1(\Phi_1)\theta(r_0 < r_0), \tag{4.14}$$

$$\frac{d\sigma^{\text{NLO}_1}}{d\Phi_2}(r_1^{\text{cut}}) = B_1(\Phi_1) + V_1(\Phi_1) + \int \frac{d\Phi_2}{df\Phi_1} B_2(\Phi_2)\theta(r_1 < r_1), \tag{4.15}$$

$$\frac{\mathrm{d}\sigma^{\mathrm{LO}_2}}{\mathrm{d}\Phi_2} = B_2(\Phi_2). \tag{4.16}$$

The contributions eqs. (4.4) and (4.6) which arise from the non-projectable configurations, are denoted by a subscript "nonproj".

In this chapter we use $r_0 = q_T$ where q_T is the transverse momentum of the Higgs boson, and $r_1 = \mathcal{T}_1$ is the 1-jettiness observable.

4.3 One-jettiness with generalized measures

In section 2.5.4, we discussed the definition of N-jettiness with an invariant mass-like measure. However, it was already pointed out in the original N-jettiness paper [140], that the definition in eq. (2.161) can be extended to use generic measures in each beam or jet region. Moreover, N-jettiness can be thought of not merely as an event-shape, but as a way to define an exclusive jet algorithm which partitions the phase space into two beam and N jet regions, to which emissions are assigned. The measure factors which are used to assign emissions to each region need not be identical to the value which the observable returns. In general, therefore, we must define separate distance measures $d_m(p_i)$ which, when minimal, assign an emission i to one of the N+2 regions m:

$$\mathcal{T}_{N}(\{\hat{n}_{m}\}) = \sum_{i} p_{T,i} \min \{d_{1}(p_{i}), \dots, d_{N}(p_{i}), d_{a}(p_{i}), d_{b}(p_{i})\}, \qquad (4.17)$$

and the resulting observable f_m which is returned by that emission once it falls into the region m,

$$\mathcal{T}^{(m)} = \sum_{i \in m} f_m(\eta_i, \phi_i) p_{T,i} , \qquad (4.18)$$

where η_i , ϕ_i and $p_{T,i}$ denote the pseudorapidity, azimuth and transverse momentum associated with i. The determination of the jet axes may be performed either by running an inclusive jet algorithm (e.g. anti- k_T) over the final state, or by a minimization of the N-jettiness over all possible axes,

$$\mathcal{T}_N = \min_{\hat{n}_1, \dots, \hat{n}_N} \mathcal{T}_N \left(\{ \hat{n}_m \} \right) . \tag{4.19}$$

The latter definition has the advantage of guaranteeing insensitivity to soft-recoil effects, whose correct treatment require the introduction of additional transverse momentum convolutions in the factorization formula. At one-loop, it is equivalent to using the winner-take-all (WTA) axis [258], in that the jet direction is determined solely by the 'hardest' emission.

This generalized definition of the N-jettiness has also been well-studied in the literature, and the choice of the measures has important consequences for the structure of the factorization. The XCone algorithm implements precisely the procedure described above to act as an exclusive jet algorithm, and in that context an number of different measure choices have been studied [259]. Ref. [260] completed the study of factorization types (i.e., all possible combinations of SCET-I/SCET-II measures for beams and jets) and provided the one-loop soft functions relevant for colour singlet production in association with a single jet. In addition, the N-subjettiness observable, introduced in ref. [261] as a way to study jet substructure, uses choices of the f_m which are transverse momentum-like by default.

In this work, we will make specific choices for both the d_m and f_m and use N=1, thus defining a generalized one-jettiness observable which we refer to as $\mathcal{T}_1^{p_T}$. Specifically, we choose the conical measure [259,262] for the region assignment, which (for isolated jets) clusters in a manner equivalent to the anti- k_T algorithm:

$$d_0(p_i) = 1, d_{m \ge 1}(p_i) = \frac{R_{im}^2}{R^2}.$$
 (4.20)

In the above equation, we have defined a single beam measure,

$$d_0(p_i) = \min\{d_a(p_i), d_b(p_i)\}, \tag{4.21}$$

and introduced the distance

$$R_{im} \equiv \sqrt{(\eta_i - \eta_m)^2 + (\phi_i - \phi_m)^2}$$
 (4.22)

and (constant) jet radius R. For the measurement itself, defining

$$\mathcal{T}_1 = \sum_{i} \begin{cases} p_{T,i} f_B(\eta_i), & \text{for } d_B(p_i) < d_J(p_i), \\ p_{T,i} f_J(\eta_i, \phi_i), & \text{for } d_J(p_i) < d_B(p_i), \end{cases}$$
(4.23)

we choose the boost-invariant generalization of broadening [260, 263] for the jet region,

$$f_J(\eta_i, \phi_i) = \sqrt{2 \cosh(\eta_i - \eta_J) - 2 \cos(\phi_i - \phi_J)}$$

$$\equiv \mathcal{R}_{i,J}$$
(4.24)

where the distance is measured with respect to the jet axis J, and the transverse energy for the beam region,

$$f_B(\eta_i) = 1. (4.25)$$

Both observables are of SCET-II type – the setup described above corresponds to one of the choices made in ref. [260], for which the one-loop soft function was calculated. It was shown in that work that the cross section then factorises as

$$\frac{\mathrm{d}\sigma_{\kappa}}{\mathrm{d}\Phi_{1}\mathrm{d}\mathcal{T}_{1}} = H_{\kappa}(\Phi_{1},\mu) \int \left(\prod_{n} \mathrm{d}k_{n}\right) S_{\kappa} \left(\mathcal{T}_{1} - \sum_{i} k_{i}, \{n_{m}\}, \{d_{m}\}, \mu, \frac{\nu}{\mu}\right) \times B_{\kappa_{a}} \left(k_{a}, x_{a}, \mu, \frac{\nu}{\omega_{a}}\right) B_{\kappa_{b}} \left(k_{b}, x_{b}, \mu, \frac{\nu}{\omega_{b}}\right) J_{\kappa_{j}} \left(k_{j}, \mu, \frac{\nu}{\omega_{j}}\right), \tag{4.26}$$

where the channel index $\kappa \equiv \{\kappa_a, \kappa_b, \kappa_j\}$ runs over all possible flavours of incoming and outgoing partons. The RGEs as well as the ingredients need to resum eq. (4.26) to NLL' accuracy are given in ref. [6].

4.4 Results

In this section, we present our numerical result for the $b\bar{b} \to H$ q_T and \mathcal{T}_1 spectra. We use $E_{\rm cm}=13\,{\rm TeV},\ m_H=125\,{\rm GeV}$. For our final resummed predictions, we use the MSHT20nnlo PDF set [234] with $\alpha_s(m_Z)=0.118$. For the validation we use CT14NNLO PDF set [264] with the same value of α_s . For the Yukawa coupling we evolve $\overline{m}_b(m_b)$ to $\mu_{\rm FO}$. The input $\overline{\rm MS}$ quark mass is given by are $\overline{m}_b(\overline{m}_b)=4.18\,{\rm GeV}$ [19], and we use $v=246.22\,{\rm GeV}$ for the Higgs vacuum expectation value to convert the masses into Yukawa couplings. The transverse momentum q_T as well as the 1-jettiness variable are resummed in SCETLIB which we linked to GENEVA.

4.4.1 Validation

We validate our implementation of $b\bar{b} \to H$ against implementation in MCFM [203]. For this comparison, we use $\mu_R = m_H$ and $\mu_F = m_H/4$. In figure 4.1, we show the NLO rapidity spectrum. The central values of the MCFM results are shown in green. Our fixed-order NLO implementation is shown in blue. This contribution was tested extensively for the use as the fixed-order prediction in ref. [2]. The resummed NLL'+NLO contributions are shown in red. As the rapidity distribution is an inclusive distributions, all three distribution have to agree. Indeed, in figure 4.1 we find good agreement between MCFM as well our fixed-order and resummed prediction. The error markers correspond to statistical uncertainties. On the right panel of figure 4.1, we show the deviations from the MCFM distribution in percent. In this plot the agreement of the different contributions is particularly apparent.

In figure 4.2, we compare our implementation of NNLL'+NNLO rapidity spectrum shown in blue against the NNLO spectrum provided by ref. [203] shown in red. We find good agreement across all bins.

4.4.2 Resummed q_T and \mathcal{T}_1 distributions

The q_T spectrum at NNLL'+NNLO accurary is shown in figure 4.3. In the right panel, we show the spectrum with \mathcal{T}_1 resummation (red) and without \mathcal{T}_1 resummation (blue). The left

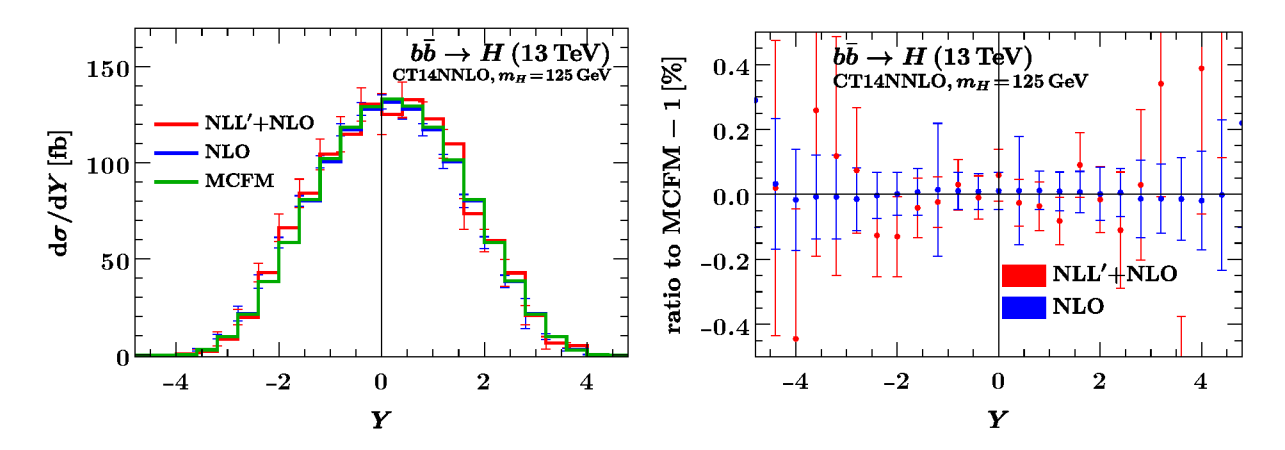


Figure 4.1: Comparison of rapidity distributions of the Higgs boson. The GENEVA predictions are shown in red (NLL'+NLO) and blue (NLO). The MCFM prediction is shown in green. The right panel shows the deviation from the MCFM distribution.

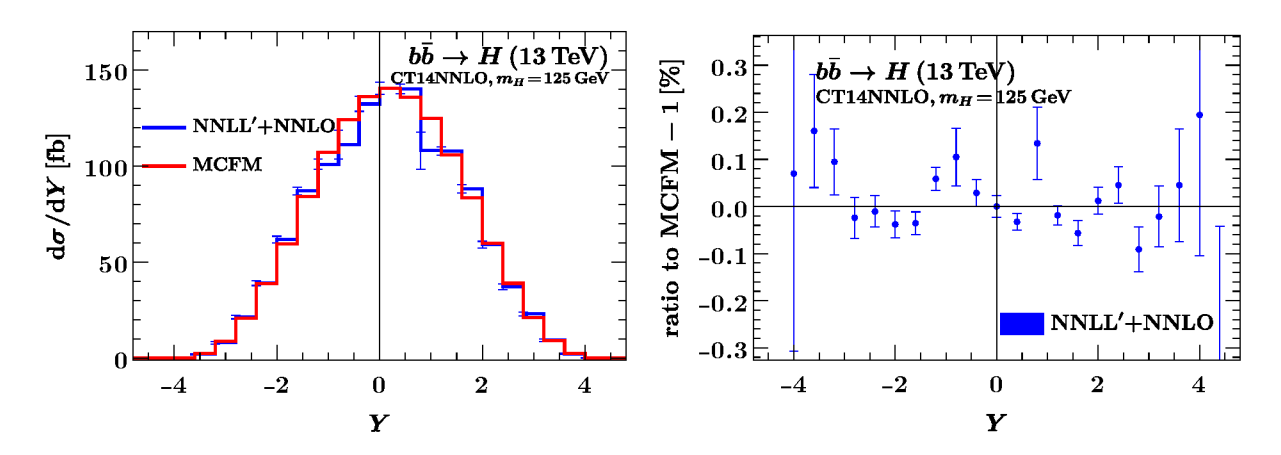


Figure 4.2: Comparison of rapidity distributions of the Higgs boson. The NNLL'+NNLO GENEVA prediction is shown in blue. The MCFM prediction is shown in red. The right panel shows the deviation from the MCFM distribution.

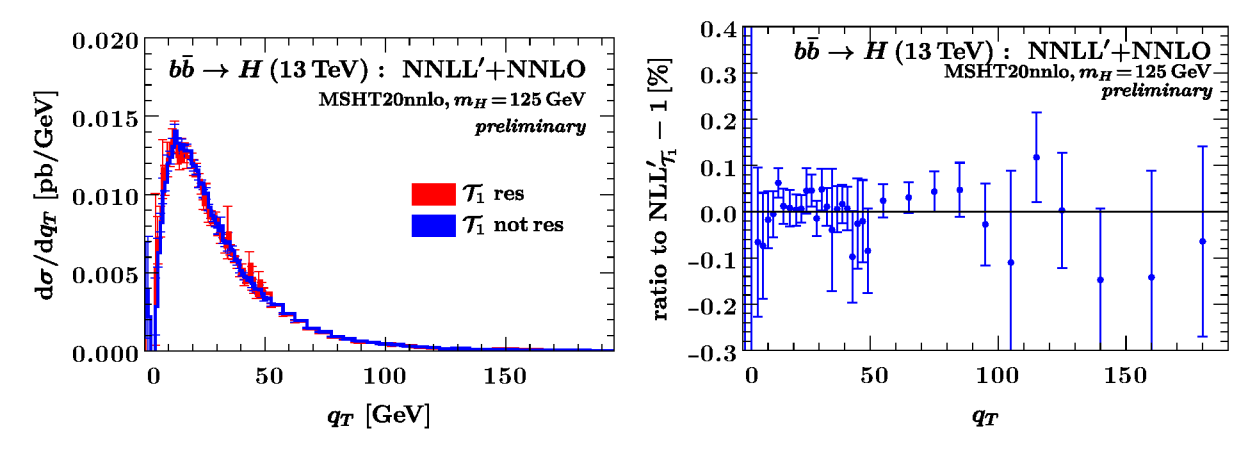


Figure 4.3: Resummed q_T spectrum at NNLL'+NNLO with and without \mathcal{T}_1 resummation.

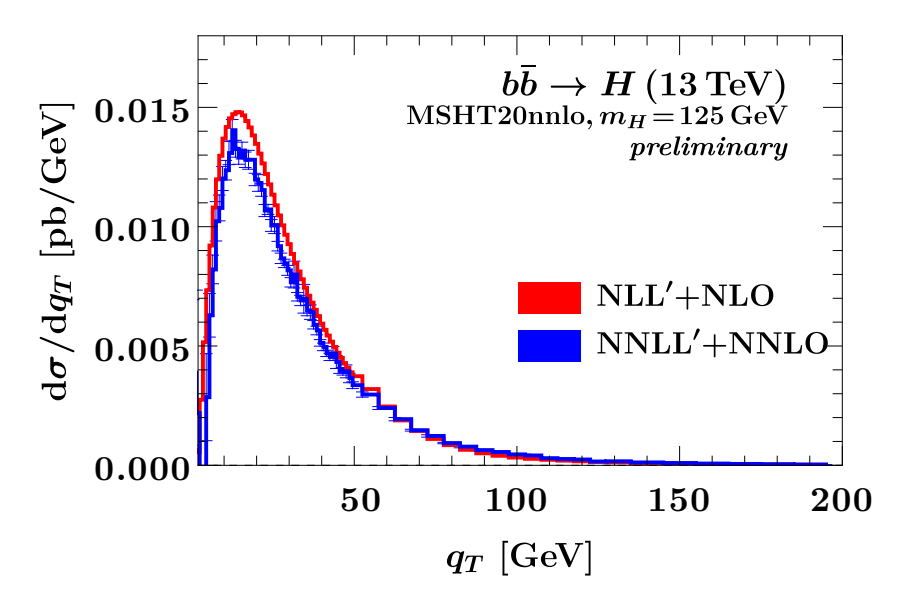


Figure 4.4: Resummed Higgs q_T spectrum at NNLL'+NNLO and NLL'+NLO.

panel shows the deviation from the \mathcal{T}_1 resummed spectrum. As expected, we find that the resummation of \mathcal{T}_1 does not affect the q_T spectrum. Figure 4.4 shows the Higgs q_T spectrum. The NNLL'+NNLO contribution is shown in blue and the NLL'+NLO contribution in red. The central values shown in this plot have been validate using the SCETLIB results from the previous chapter. A result including all uncertainties for both orders is currently under preparation. In figure 4.5, we show the \mathcal{T}_1 spectrum where the red curve shows the resummed contribution whereas the blue one does not include \mathcal{T}_1 resummation. We want to point the \mathcal{T}_1 resummation is only valid if \mathcal{T}_1 is smaller then any other scale. This is plot we chose $q_T^{\text{cut}} = 50 \,\text{GeV}$ to ensure that we have a hard jet in the final state. In the tail of the both contributions agree which is expected as there no large logarithms of \mathcal{T}_1 . For the fixed-order contribution we observe a very large first bin which indicates a divergence. The resummed contribution has a peak at around 30 GeV before smoothly going to zero. Figures 4.5 and 4.3 present the main results of this chapter.

4.5 Summary and Outlook

In this section, we presented first steps towards an NNLO+PS prediction for $q\bar{q} \to H$. We implemented a new set of resolution variables in Geneva , namely the transverse momentum q_T as 1-jet resolution variable and a generalization of 1-jettiness \mathcal{T}_1 with a transverse momentum-like measure as 2-jet resolution variable. This choice of resolution variables facilitates the matching to the shower as parton showers which tend to be ordered by the transverse momentum. Further, this is the first that a resummation beyond leading order is achieved for the 1-jettniness variable.

We validated our implementation of the resummed prediction using inclusive observables such as the total cross section and rapidity spectrum which are not sensitive to resummation. We found good agreement between our implementation and the NNLO rapidity spectrum from MCFM. We further checked that our transverse momentum spectrum is not affected by the \mathcal{T}_1 resummation.

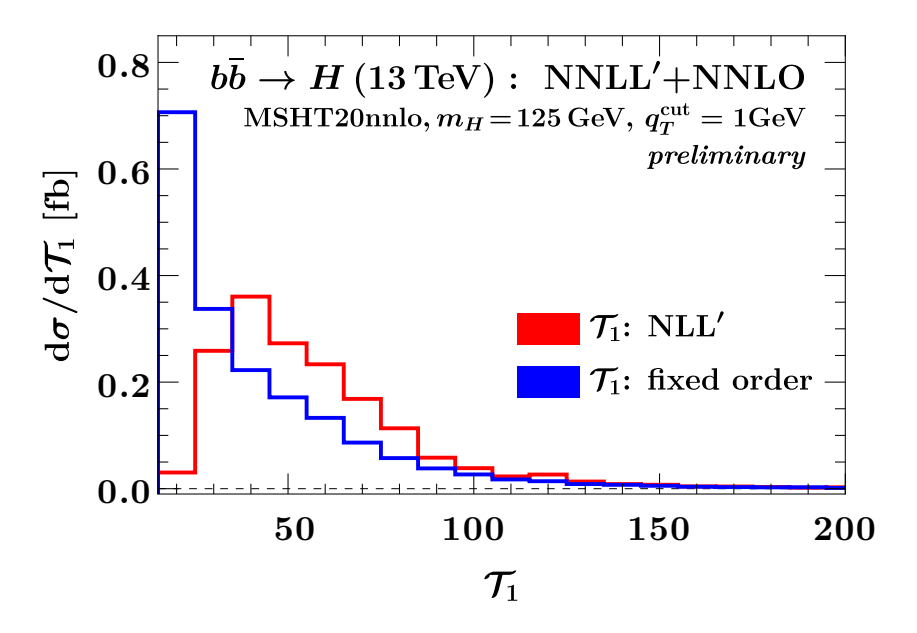


Figure 4.5: \mathcal{T}_1 spectrum at NLL'+NLO with and without \mathcal{T}_1 resummation.

Moreover, we saw that our resummed \mathcal{T}_1 prediction indeed resums large logarithms of \mathcal{T}_1 and restores the convergence of the spectrum.

The next step on the way towards an NNLO+PS prediction for this set of variables will be to implement the matching to the parton shower. However, this is beyond the scope of this thesis.

Chapter 5

Bottom Mass Effects in the Higgs Production via Gluon Fusion

In this chapter, we study finite b-mass effects in the Higgs q_T spectrum arising from the bottomloop in Higgs production via gluon fusion for the first time. In contrast to the cases of the $H \to \gamma \gamma$ decay or the $gg \to H$ form factor investigated previously at amplitude level, the nontrivial b-mass effects are also resolved by real emissions and have to be considered within the context of q_T factorization and resummation. We consider the various hierarchies between m_b and q_T and m_H , leading to different factorization setups.

This chapter is based on ref. [5] reflecting the author's contribution.

5.1 Motivation

In the last two chapters we discussed the q_T spectrum of quark initiated Higgs production in detail. One of our motivations for a new high-precision prediction was the measurement of the quark Yukawa couplings from fitting to the shape of the q_T spectrum of the Higgs boson which is sensitive to the initial states. This method was first suggested in refs. [39–41]. As we saw in chapter 3 shape of q_T spectrum is highly sensitive to the quark channel. The quark and gluon induced channels can also be well distinguished by there shape as their predictions come with different Casimir scaling, see figure 3.17. To allow a fit to the q_T spectrum it is particularly important that all contributions of the spectrum are known to sufficiently high orders. The full Higgs q_T spectrum in proton collisions reads

$$\frac{\mathrm{d}\sigma(pp\to H)}{\mathrm{d}q_T} = y_t^2 \frac{\mathrm{d}\sigma_{tt}}{\mathrm{d}q_T} + y_b^2 \frac{\mathrm{d}\sigma_{bb}}{\mathrm{d}q_T} + y_t y_b \frac{\mathrm{d}\sigma_{tb}}{\mathrm{d}q_T} + (y_b \to y_c), \tag{5.1}$$

where y_q denotes the respective quark Yukawa coupling. The first term describes the gluon fusion process and is diagrammatically shown in figure 5.1a. In this figure the top-quark loop was approximated by a contact operator as commonly done in the heavy top-quark limit. Recalling the production cross sections in table 2.2, we note that the gluon fusion process contributes the largest part to the Higgs production cross section. The q_T spectrum for gluon fusion was predicted to N³LL'+ N³LO in ref. [44]. The second term in eq. (5.1) denotes the b-quark initiated contribution that we discussed in detail in chapter 3 and is shown in figure 5.1b.

The focus of this chapter is the third contribution in eq. (5.1) which we refer to as the y_b - y_t interference term. Interference between different diagrams can only occur between diagrams

with the same initial and final states. This contribution is illustrated in figure 5.1c. Usually only the top contribution in gluon fusion is considered as the top is be far the heaviest quark. However, the contribution with the bottom-quark loop contributes up to $\mathcal{O}(5-10\%)$ to the gluon fusion cross section [265, 266]. Lighter quarks only make up a few percent of the cross section. In the cross section in eq. (5.1), these bottom-mass effects only appear at sub-leading power in $m_b/m_H \ll 1$. However, with the unprecedented amount of precision data obtained by the experiments at the LHC this contribution can no longer be ignored.

The amplitude of the related Higgs boson decay to two photons via a b-quark loop was studied a long time ago [267]. Both processes – the Higgs decay via two photons as well as Higgs production via gluon fusion – feature large logarithms of Q/m_b that need to be resummed. Here, the hard scale of the problem is given by $Q = m_H$ where m_H is the mass of the Higgs boson. The low scale is given by the bottom-quark mass $m_b \ll Q$. An all order resummation of these large logarithms to NLL was archived in refs. [267, 268] using the methods of perturbative QCD. This approach was extended in refs. [265, 266] The factorization and resummation of b-mass effects for the Higgs boson decay and production amplitudes in the context of SCET were first considered in refs. [269–271]. The renormalization and the treatment of endpoint divergences of the amplitude are still an active topic of research and were recently studied in ref. [272].

In this chapter, we study bottom-mass effects in the Higgs q_T spectrum using SCET for the first time. In comparison to the form factor calculation from refs. [269–271] the q_T measurement adds a third scale to the problem. To allow the Higgs boson to pick up a transverse momentum, we need to add an emission k that the Higgs boson can recoil against which is illustrated in figure 5.2b, where $\vec{k}_T = -\vec{q}_T$.

This chapter is organized as follows: in section 5.2, we discuss the leading-order contribution to this process (without the emission k) which is shown in figure 5.2a. We use this calculation as an illustrative example to introduce the notation and discuss the regularization of endpoint divergences. We want to point out that the results of this calculation are available in the literature and have been published in ref. [269]. In section 5.3, we write down bare factorization theorems that are valid in different kinematic regions. In section 5.4, we calculate the real emission diagrams corresponding to the diagrams shown in figure 5.2b, where we focus on the diagrams where the emission k has collinear scaling. In section 5.5 we summarize the rather subtle cancellation of endpoint divergences. We provide a summary of the main results in section 5.6.

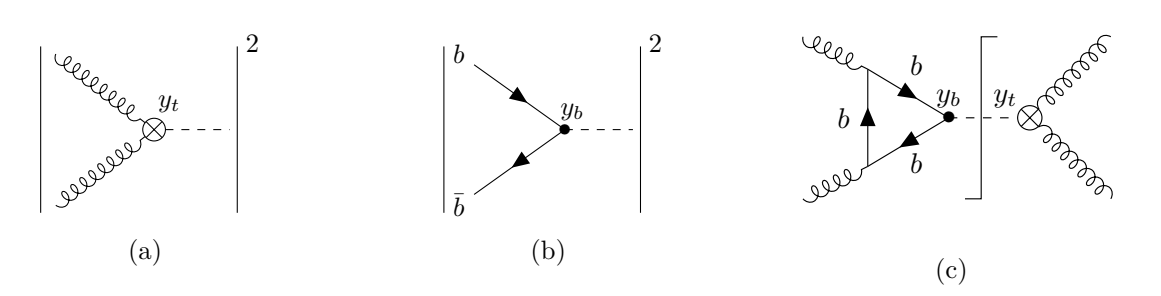


Figure 5.1: (a): Gluon fusion process, (b) quark initiated Higgs production and (c) y_b - y_t -interference contribution.

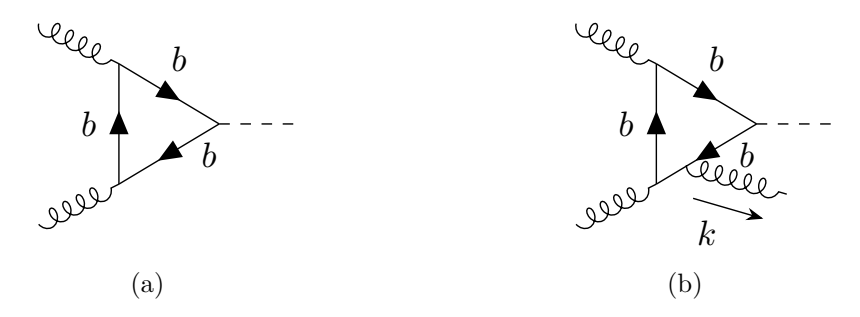


Figure 5.2: Illustration of Higgs production via gluon fusion via a bottom-quark loop. (a) Leading-order contribution. (b) Next-to-leading order contribution with an extra emission k. This diagram serves as an example for all possible gluon attachments to the leading order diagram.

5.2 Operator basis and calculation of the LO contribution

We want to start by calculating the amplitude for the leading-order gluon fusion diagram shown in figure 5.2a in SCET. To do so, we need consider the possible momentum scalings that can occur. In general, the loop momenta can scale as

$$n$$
-collinear: $p \sim m_H(\lambda^2, 1, \lambda)$
 \bar{n} -collinear: $p \sim m_H(1, \lambda^2, \lambda)$
hard: $p \sim m_H(1, 1, 1)$
soft: $p \sim m_H(\lambda, \lambda, \lambda)$, (5.2)

where our power-counting parameter is given by $\lambda = m_b/m_H$. The incoming gluons are n-and \bar{n} -collinear and scale as

$$p_1 \sim m_H(\lambda^2, 1, \lambda), \qquad p_2 \sim m_H(1, \lambda^2, \lambda).$$
 (5.3)

In fact, we can choose them to be exactly aligned with their respective lightcone momenta:

$$p_1^{\mu} = p_1^{-} \frac{n^{\mu}}{2}, \qquad p_2^{\mu} = p_2^{+} \frac{\bar{n}^{\mu}}{2},$$
 (5.4)

such that $p_1 = (0, p_1^-, 0)$ and $p_2 = (p_2^+, 0, 0)$. The Higgs boson is always produced in a hard interaction which we denote by \otimes . With these constraints, there are four possible scenarios which are diagrammatically shown in figure 5.4: One possibility is that all loop momenta have hard scaling. As commonly done in SCET they are integrated out and "shrunken to a point". This correponds to the first term in the sum in figure 5.4. We can also have two hard-collinear quark momenta producing the Higgs boson. Then the remaining quark line connecting the two gluons has soft scaling which is shown by second term in the sum. The last two terms correspond to a scenario where only one of the quark momenta involved in the production of the Higgs boson exhibits hard scaling. The remaining quark propagators then have n-collinear scaling (third term in the sum) or \bar{n} -collinear scaling which corresponds to the last term in figure 5.4. In practice, we only need to consider one of the collinear contributions as both contributions are related by symmetry. The soft and collinear contributions suffer from endpoint divergences. This is a common feature in SCET factorization theorems beyond leading power. We will regulate these divergences with rapidity regulators discussed in section 2.4.5.



Figure 5.3: Tree-level diagrams associated with the collinear operator \mathcal{O}_{bbg} (a) and the soft operator \mathcal{O}_{bbgq}^{ab} (b).

The relevant SCET operators at tree-level are shown in figure 5.3. For the definition of the building blocks we refer to section 2.4.4. The n-collinear operator is given by [269, 273]

$$\mathcal{O}_{bbg}^{a} = \bar{\chi}_{n,\omega_1} \frac{\rlap{/}{n}}{2} (g \mathcal{B}_{\bar{n},\perp})_{\bar{\omega}} T^a \chi_{n,\omega_2}, \tag{5.5}$$

where $\omega_{1,2}$ denote the large lightcone momenta of the collinear quarks and $\bar{\omega}$ denotes the gluon's large lightcone momentum. The sum of incoming + and - momenta has to add up to the Higgs + and - momenta. Hence, we have $\omega_1 + \omega_2 = q^- = m_H$ and $\bar{\omega} = q^+ = m_H$. The collinear Wilson coefficient is given by

$$C_{bbg} = \frac{1}{\omega_1} - \frac{1}{\omega_2},\tag{5.6}$$

which we can simply read off the Feynman rule in eq. (E.1). The soft operator is given by [269,273]

$$\mathcal{O}_{bbgg}^{ab}(\ell^{+}\ell^{-}) = \frac{1}{\ell^{+}\ell^{-}} [\bar{\psi}S_{n}\delta(\ell^{+} - n \cdot \mathcal{P}])[(g\mathcal{B}_{n\perp})_{q^{-}} T^{a} \frac{\bar{\psi}\psi}{4} S_{n}^{\dagger} S_{\bar{n}} (g\mathcal{B}_{\bar{n}\perp})_{q^{+}} T^{b}][S_{\bar{n}}^{\dagger}\psi\delta(\ell^{-} - \bar{n} \cdot \mathcal{P}]) + (n \leftrightarrow \bar{n}), \tag{5.7}$$

where we suppressed the +i0 in the $1/(\ell^+\ell^-)$ term for brevity. When calculating the soft diagram the imaginary part becomes relevant for the contour integral and needs to be reinstated. The Wilson coefficient for this operator is given by $C_{bbgg}^{(0)} = 1$ at this order. Note that we set the Yukawa coupling to 1 in both operators. It can trivially be included at any desired stage of the calculation.

In the following section, we calculate all relevant leading-order contributions. The relevant Feynman rules are given in appendix E.

5.2.1 Leading-order collinear contribution

The n-collinear leading-order diagram is shown in figure 5.5. We use massive SCET Feynman rules from ref. [109] and our Feynman rule for the effective vertex with the Higgs boson in eq. (E.1). Evaluating the trace, we find

$$\mathcal{M}_{c}^{\text{LO}} = -ig^{2}\delta_{ab} \int d\omega_{n}d\xi \int \frac{d^{d}\ell}{(2\pi)^{d}} C_{bbg}(\xi) \frac{m\mu^{2\epsilon}g_{\perp}^{\mu\nu}p_{1}^{-}}{(\ell^{2} - m^{2} + i0)\left[(\ell + p_{1})^{2} - m^{2} + i0\right]} \times \delta(\omega_{n} - p_{1}^{-})\delta(\xi\omega_{n} - \ell^{-} - p_{1}^{-})\delta(p_{2}^{+} - q^{+})\delta(\omega_{n} - q^{-}),$$
 (5.8)

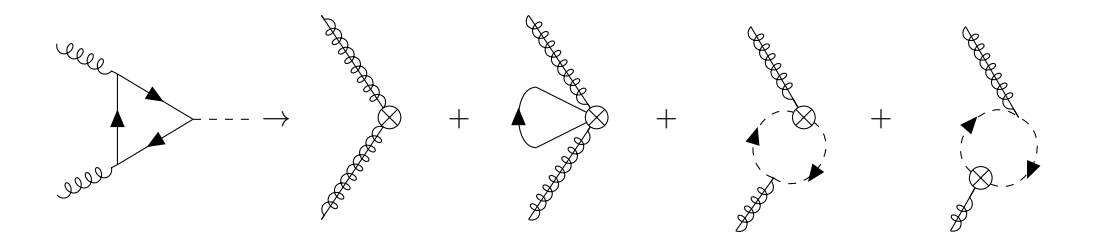


Figure 5.4: Decomposition of full QCD diagram in terms of hard, soft and n- and \bar{n} -collinear loop momenta. Springs with a line denote n_i -collinear gluons, dashed fermion lines n_i -collinear quarks, and solid fermion lines soft quarks. The hard interaction is denoted by \otimes .

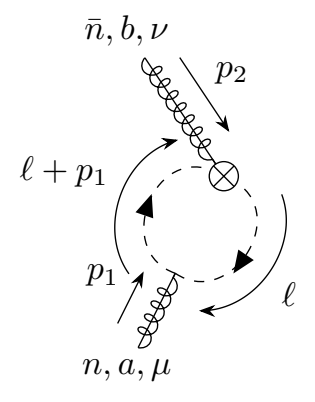


Figure 5.5: Leading-order n-collinear contribution.

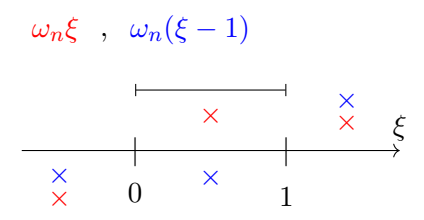


Figure 5.6: Pole analysis for the collinear leading-order contribution. This figure shows the sign of the factors that determine whether the pole will be in the upper or lower half of the complex plane. From this analysis we see that the two poles will only be on different sides and, therefore, give a nonzero contribution for $0 < \xi < 1$ which introduces a set of θ -functions for the ξ integral $\theta(\xi)\theta(1-\xi)$.

where q is the Higgs momentum. We also changed variables from $(\omega_1, \omega_1) \to (\omega_n, \xi)$ where $\omega_n = \omega_1 + \omega_2 = q^-$ and $\xi = -\omega_2/\omega_n$. In this notation the Wilson coefficient is given by

$$C_{bbg}(\xi) = \frac{1}{\xi} + \frac{1}{1 - \xi}.$$
 (5.9)

For simplicity, we will omit the δ -function constraining the overall + and - momenta. Throughout this calculation we assume transverse gluon polarization for the external gluons, i.e.

$$n^{\mu} = 0, \qquad n^{\nu} = 0, \qquad \bar{n}^{\mu} = 0, \qquad \bar{n}^{\nu} = 0.$$
 (5.10)

We also take the external gluons to be on shell, $p_1^2 = 0$ and $p_2^2 = 0$.

To evaluate the diagram in figure 5.5, we start by solving the ω_n and ℓ^- integrals that are fixed by δ -functions

$$\mathcal{M}_{c}^{\text{LO}} = \int d\xi \int \frac{d\ell^{+} d^{d-2}\ell_{\perp}}{(2\pi)^{d-1}} \frac{ig^{2}C_{bbg}(\xi)\omega_{n}\delta^{ab}m\mu^{2\epsilon}g_{\perp}^{\mu\nu}}{4\pi(\ell_{\perp}^{2} + \omega_{n}\xi\ell^{+} - m^{2} + i0)\left[\ell_{\perp}^{2} + \omega_{n}(\xi - 1)\ell^{+} - m^{2} + i0\right]}.$$
 (5.11)

The ξ integral will be divergent due to endpoint divergences. These divergences only cancel once the collinear and soft contributions are combined. We will regulate these divergences with two different regulators: the absolute value or η -regulator [113,118,119] and the pure rapidity regulator [129]. For the absolute value regulator it is sufficient to include the regulator just before integrating over ξ . The pure rapidity regulator, on the other hand, depends on ℓ^- and ℓ^+ and has to be included before performing the ℓ^+ integral. We start with the absolute value regulator in the next section.

Absolute value regulator

In the next step, we do the ℓ^+ integral by contours. Importantly, the signs of the poles in the complex plane depend on the sign of ξ . We only obtain a non-vanishing contour integral for values $0 < \xi < 1$. This is illustrated in figure 5.6. The resulting ℓ_{\perp} integral can be solved using standard formulæand we find

$$\mathcal{M}_c^{\text{LO}} = \int d\xi (-g^2) m \mu^{2\epsilon} (4\pi)^{\epsilon - 2} C_{bbg}(\xi) \delta^{ab} g_{\perp}^{\mu\nu} m^{-2\epsilon} \Gamma(\epsilon) \theta(\xi) \theta(1 - \xi). \tag{5.12}$$

Now, the only remaining integral is the endpoint divergent ξ integral. Recalling the definition of the Wilson coefficient in eq. (5.9), we see that the integral is singular in both limits. We also

note that the ξ dependence is fully given by $C_{bbg}(\xi)$ and the rest of the integral is independent of ξ . We regulate the integral in each limit with the absolute regulator and switch from the MS to the $\overline{\rm MS}$ scheme by shifting $\mu^2 \to e^{\gamma_E} \mu^2/(4\pi)$. Then the final result for the *n*-collinear contribution is given by

$$\mathcal{M}_{c}^{\text{LO}} = -\frac{g^{2}}{(4\pi)^{2}} \delta^{ab} g_{\perp}^{\mu\nu} e^{\epsilon\gamma_{E}} \mu^{2\epsilon} m^{1-2\epsilon} \Gamma(\epsilon) \int_{0}^{1} d\xi \left(\frac{1}{\xi} \left| \frac{\omega_{n} \xi}{\nu} \right|^{-\eta} + \frac{1}{1-\xi} \left| \frac{\omega_{n} (1-\xi)}{\nu} \right|^{-\eta} \right)$$

$$= \frac{g^{2}}{(4\pi)^{2}} \delta^{ab} g_{\perp}^{\mu\nu} e^{\epsilon\gamma_{E}} \mu^{2\epsilon} m^{1-2\epsilon} \left| \frac{\omega_{n}}{\nu} \right|^{\eta} \frac{2\Gamma(\epsilon)}{\eta}. \tag{5.13}$$

For this regulator, the \bar{n} -collinear diagram gives the same result as the n-collinear diagram. We therefore simply multiply our final result by a factor of 2

$$\mathcal{M}_{c}^{\mathrm{LO}} + \mathcal{M}_{\bar{c}}^{\mathrm{LO}} = \frac{g^{2}}{(4\pi)^{2}} T_{F} \delta^{ab} g_{\perp}^{\mu\nu} e^{\epsilon\gamma_{E}} \mu^{2\epsilon} m^{1-2\epsilon} \left| \frac{\omega_{n}}{\nu} \right|^{\eta} \frac{2\Gamma(\epsilon)}{\eta}, \tag{5.14}$$

where we made the color factor T_F explicit.

Pure rapidity regulator

For the pure rapidity regulator, the regulator has to be inserted before the ℓ^+ and ℓ^- integrals

$$\mathcal{M}_{c}^{\text{LO}} = -ig^{2}\delta_{ab} \int d\omega_{n} d\xi \int \frac{d^{d}\ell}{(2\pi)^{d}} C_{bbg}(\xi) \frac{m\mu^{2\epsilon}g_{\perp}^{\mu\nu}p_{1}^{-}\delta(\omega_{n} - p_{1}^{-})\delta(\xi\omega_{n} - \ell^{-} - p_{1}^{-})}{(\ell^{2} - m^{2} + i0)\left[(\ell + p_{1})^{2} - m^{2} + i0\right]} \left(\frac{\ell^{-} + i0}{\ell^{+} + i0}\right)^{-\frac{\eta}{2}}.$$
(5.15)

The ℓ^- integrals is again fixed by δ -functions

$$\mathcal{M}_{c \, p\eta}^{LO} = \int d\xi \int \frac{d\ell^{+} d^{d-2}\ell_{\perp}}{(2\pi)^{d-1}} \frac{ig^{2}C_{bbg}(\xi)\omega_{n}\delta^{ab}m\mu^{2\epsilon}g_{\perp}^{\mu\nu}[\omega_{n}(\xi-1)]^{-\frac{\eta}{2}}(\ell^{+}+i0)^{\frac{\eta}{2}}}{4\pi(\ell_{\perp}^{2}+\omega_{n}\xi\ell^{+}-m^{2}+i0)\left[\ell_{\perp}^{2}+\omega_{n}(\xi-1)\ell^{+}-m^{2}+i0\right]}, \quad (5.16)$$

where we kept the i0 in the ℓ^+ term. This term introduces a branch cut and the i0 moves the branch cut to the upper half-plane. However, by choosing the pole in the lower half-plane we can avoid this branch cut in the contour integral. The poles in the complex are the same as in our previous contour analysis shown in figure 5.6 and we find the same constraints on the ξ integral. Just as before, we can straightforwardly evaluate the ℓ_{\perp} integral and change to the $\overline{\rm MS}$ scheme in the same step. At this point we can simply evaluate the ξ integral and arrive at our finial expression for our n-collinear contribution using the pure rapidity regulator

$$\mathcal{M}_{c p \eta}^{\text{LO}} = -\frac{g^2}{(4\pi)^2} \delta^{ab} g_{\perp}^{\mu\nu} e^{\epsilon \gamma_E} \mu^{2\epsilon} m^{1-2\epsilon+\eta} \frac{\Gamma(\epsilon - \frac{\eta}{2})}{\Gamma(1 - \frac{\eta}{2})} \int_0^1 d\xi \left(\frac{1}{\xi} + \frac{1}{1 - \xi}\right) \left[\omega_n(\xi - 1)\right]^{-\frac{\eta}{2}} (\omega_n \xi)^{-\frac{\eta}{2}}$$

$$= -\frac{g^2}{(4\pi)^2} \delta^{ab} g_{\perp}^{\mu\nu} e^{\epsilon \gamma_E} \mu^{2\epsilon} m^{1-2\epsilon+\eta} (-\omega_n)^{-\eta} \frac{\Gamma(\epsilon - \frac{\eta}{2})\Gamma(-\frac{\eta}{2})^2}{\Gamma(1 - \frac{\eta}{2})\Gamma(-\eta)}$$
(5.17)

For \bar{n} -collinear contribution we have to replace $\eta \to -\eta$ this time,

$$\mathcal{M}_{\bar{c} \, p\eta}^{LO} = -\frac{g^2}{(4\pi)^2} \delta^{ab} g_{\perp}^{\mu\nu} e^{\epsilon \gamma_E} \mu^{2\epsilon} m^{1-2\epsilon-\eta} (-\omega_n)^{\eta} \frac{\Gamma(\epsilon + \frac{\eta}{2}) \Gamma(\frac{\eta}{2})^2}{\Gamma(1 + \frac{\eta}{2}) \Gamma(\eta)}$$
(5.18)

In the sum of the n- and \bar{n} -collinear contributions the endpoint divergences and the η -dependence cancel by definition,

$$\mathcal{M}_{c \, \mathrm{p}\eta}^{\mathrm{LO}} + \mathcal{M}_{\bar{c} \, \mathrm{p}\eta}^{\mathrm{LO}} = -\frac{g^2}{2\pi^2} T_F \delta^{ab} g_{\perp}^{\mu\nu} e^{\epsilon\gamma_E} \mu^{2\epsilon} m^{1-2\epsilon} \Gamma(\epsilon) \left[\psi^{(0)}(\epsilon) + \gamma_E + \log \frac{-\omega_n^2}{m^2} \right], \tag{5.19}$$

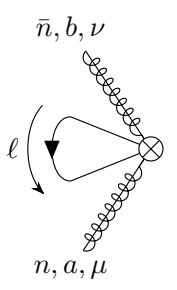


Figure 5.7: Leading-order soft contribution.

where $\psi^{(0)}$ is the polygamma function of order 0. For the pure rapidity regulator, there is a non-trivial zero-bin contribution for $\ell \to 0$ that needs to be subtracted. The zero bin yields exactly $-\mathcal{M}_{c\ pn}^{\mathrm{LO}}$ and we can simply include a factor of 2 in eq. (5.19) to account for it.

5.2.2 Soft LO₀

The soft leading-order diagram is shown in figure 5.7. Using SCET Feynman rules and our Feynman rule for the effective vertex with the Higgs boson in eq. (E.5) and evaluating the trace, we find

$$\mathcal{M}_{s} = \int \frac{\mathrm{d}^{d} \ell}{(2\pi)^{d}} \frac{1}{(\ell^{+} + \mathrm{i}0)(\ell^{-} - \mathrm{i}0)} \frac{-2\mathrm{i}g^{2}m\mu^{2\epsilon}\delta^{ab}g_{\perp}^{\mu\nu}}{\ell^{2} - m^{2} + \mathrm{i}0}$$
(5.20)

The $1/(\ell^+\ell^-)$ prefactor renders the contour analysis of the soft integral much more complicated then in the collinear case. At this point it is useful to change variables to $d\ell^+d\ell^- = 2d\ell_0d\ell_z$.

Absolute value regulator

As before, we only need to include the absolute value regulator before the divergent ℓ_z integral. We start with doing the ℓ_0 integral by contours.

$$\mathcal{M}_{s} = \int \frac{\mathrm{d}\ell_{0} \mathrm{d}\ell_{z} \mathrm{d}^{2-2\epsilon}\ell_{\perp}}{(2\pi)^{d}} \frac{-\mathrm{i}g^{2}\mu^{2\epsilon}m\delta^{ab}g_{\perp}^{\mu\nu}}{(\ell_{0} - \ell_{z} + \mathrm{i}0)(\ell_{0} + \ell_{z} - \mathrm{i}0)} \frac{1}{\ell_{\perp}^{2} + \ell_{0}^{2} - \ell_{z}^{2} - m^{2} + \mathrm{i}0}$$
(5.21)

In the contour analysis we find four poles in the complex ℓ_0 -plane

$$\ell_0^{1,2} = \pm \ell_z \mp i0, \qquad \ell_0^{3,4} = \pm \sqrt{\ell_z^2 - \ell_\perp^2 + m^2 - i0} = \pm \sqrt{\ell_z^2 - \ell_\perp^2 + m^2} \mp \frac{i0}{\sqrt{\ell_z^2 - \ell_\perp^2 + m^2}},$$
(5.22)

where $\ell_z^2 > \text{or} < \ell_\perp^2 - m^2$ determines the location of the pole in the complex ℓ_0 plane. Consequently, we need to consider the regions $\ell_z^2 > \text{and} < \ell_\perp^2 - m^2$ separately. Some calculational details as well as the full pole analysis is shown in appendix F.1. Using the residue theorem we find the

following results:

$$\mathcal{M}_{s}^{>} = g^{2} \mu^{2\epsilon} m \delta^{ab} g_{\perp}^{\mu\nu} \int_{\sqrt{\ell_{\perp}^{2} - m^{2}}}^{\infty} \frac{\mathrm{d}\ell_{z}}{2\pi} \int \frac{\mathrm{d}^{2-2\epsilon}\ell_{\perp}}{(2\pi)^{2-2\epsilon}} \frac{1}{\ell_{\perp}^{2} - m^{2}} \left[-\frac{1}{\ell_{z}} + \frac{1}{\sqrt{\ell_{z}^{2} - \ell_{\perp}^{2} + m^{2}}} \right],$$

$$\mathcal{M}_{s}^{<} = g^{2} \mu^{2\epsilon} m \delta^{ab} g_{\perp}^{\mu\nu} \int_{-\infty}^{\sqrt{\ell_{\perp}^{2} - m^{2}}} \frac{\mathrm{d}\ell_{z}}{2\pi} \int \frac{\mathrm{d}^{2-2\epsilon}\ell_{\perp}}{(2\pi)^{2-2\epsilon}} \frac{1}{\ell_{\perp}^{2} - m^{2}} \left[-\frac{1}{\ell_{z}} - \frac{1}{\sqrt{\ell_{z}^{2} - \ell_{\perp}^{2} + m^{2}}} \right]. \quad (5.23)$$

In the next step, we do the ℓ_z integral and introduce our rapidity regulator. We can already see in eq. (5.23) that the $1/\ell_z$ terms will combine to scaleless integral. For the second term we find

$$\mathcal{M}_{s}^{>} = g^{2} \mu^{2\epsilon} m \delta^{ab} g_{\perp}^{\mu\nu} \int \frac{\mathrm{d}^{2-2\epsilon} \ell_{\perp}}{(2\pi)^{2-2\epsilon}} \int_{\sqrt{\ell_{\perp}^{2}-m^{2}}}^{\infty} \frac{\mathrm{d} \ell_{z}}{2\pi} \frac{1}{\ell_{\perp}^{2}-m^{2}} \left| \frac{2\ell_{z}}{\nu} \right|^{-\eta} \frac{1}{\sqrt{\ell_{z}^{2}-\ell_{\perp}^{2}+m^{2}}}$$

$$= \frac{g^{2}}{2\pi} \mu^{2\epsilon} m \delta^{ab} g_{\perp}^{\mu\nu} \frac{|\nu|^{\eta}}{\eta} {}_{2} F_{1} \left(\frac{\eta}{2}, \eta; \frac{\eta+2}{2}; -1 \right) \int \frac{\mathrm{d}^{2-2\epsilon} \ell_{\perp}}{(2\pi)^{2-2\epsilon}} \frac{1}{(\ell_{\perp}^{2}-m^{2})^{1+\frac{\eta}{2}}}. \tag{5.24}$$

After the ℓ_z -integral the $\mathcal{M}_s^>$ and $\mathcal{M}_s^<$ are the same and we can simply multiply a factor of 2 to include the $\mathcal{M}_s^<$ contribution,

$$\mathcal{M}_{s} = \frac{g^{2}}{\pi} \mu^{2\epsilon} m \delta^{ab} g_{\perp}^{\mu\nu} \frac{|\nu|^{\eta}}{\eta} {}_{2} F_{1}(\frac{\eta}{2}, \eta; \frac{\eta + 2}{2}; -1) \int \frac{\mathrm{d}^{2-2\epsilon} \ell_{\perp}}{(2\pi)^{2-2\epsilon}} \frac{1}{(\ell_{\perp}^{2} - m^{2})^{1+\frac{\eta}{2}}}.$$
 (5.25)

The remaining ℓ_{\perp} integral is then given by standard integration formulas and yields

$$\mathcal{M}_s = -\frac{\mathrm{i}^{\eta} g^2}{4\pi^2} \delta^{ab} g_{\perp}^{\mu\nu} e^{\epsilon \gamma_E} \mu^{2\epsilon} m^{1-2\epsilon-\eta} \frac{|\nu|^{\eta}}{\eta} {}_2F_1\left(\frac{\eta}{2}, \eta; \frac{\eta+2}{2}; -1\right) \frac{\Gamma(\epsilon + \frac{\eta}{2})}{\Gamma(\frac{\eta}{2} + 1)},\tag{5.26}$$

where we shifted $\mu^2 \to e^{\gamma_E} \mu^2/(4\pi)$ corresponding to the $\overline{\rm MS}$ scheme.

Pure rapidity regulator

The soft contribution in eq. (5.20) can, of course, also be regulated with the pure rapidity regulator. In this case, we start by evaluating the ℓ_{\perp} -integral which can be straightforwardly done using known integral formulæ. The remaining integral is scaleless and the soft contribution using the pure rapidity regulator is zero.

5.2.3 Leading-order hard contribution

The leading-order hard contribution is given by the full QCD result minus the soft and collinear contributions. However, we can also get this contribution from evaluating the full QCD diagram for $p_1, p_2 \gg m$ which amounts to evaluating this diagram using the method of regions [274–276]. We start by taking the trace and expanding the full QCD diagram

$$\mathcal{M}_{h} = 2 \int \frac{\mathrm{d}^{d} \ell}{(2\pi)^{d}} \mathrm{Tr} \left\{ \frac{(-1)\mathrm{i}g T^{a} \gamma^{\mu} \mathrm{i}(l+m) \mathrm{i}g T^{b} \gamma^{\nu} \mathrm{i}(l+\not p_{2}+m) \mathrm{i}(l-\not p_{1}+m)}{(\ell^{2}-m^{2}+\mathrm{i}0)[(\ell+p_{2})^{2}-m^{2}+\mathrm{i}0][(\ell-p_{1})^{2}-m^{2}+\mathrm{i}0]} \right\}$$

$$= \int \frac{\mathrm{d}^{d} \ell}{(2\pi)^{d}} \frac{2\mathrm{i}g^{2} m \delta^{ab} [(2\ell^{2}+2p_{1}\cdot p_{2})g^{\mu\nu}-8\ell^{\mu}\ell^{\nu}]}{(\ell^{2}+\mathrm{i}0)[(\ell+p_{2})^{2}+\mathrm{i}0][(\ell-p_{1})^{2}+\mathrm{i}0]} + \mathcal{O}(m^{2}), \tag{5.27}$$

which has the form of a massless triangle. Note that there is also a contribution with reversed fermion flow. After integration, both contributions give the same result and we can simply calculate one diagram and multiply it with a factor of 2, which is already included in the equation above. Here, we evaluate the integral directly without switching to lightcone coordinates, yielding

$$\mathcal{M}_h = 2^{4\epsilon - 3} \pi^{\epsilon - \frac{1}{2}} g^2 m \delta^{ab} g_{\perp}^{\mu\nu} \frac{\csc(\pi \epsilon)}{\epsilon \Gamma(\frac{1}{2} - \epsilon)} (-\omega_n^2 - i0)^{-\epsilon} \left[\frac{2\epsilon^2}{2\epsilon^2 - 3\epsilon + 1} - \frac{\omega_n^2}{\omega_n^2 + i0} \right], \tag{5.28}$$

where we used that the incoming gluons can only have \perp polarization and $p_1^- = p_2^+ = \omega_n$. Details of the calculation are given in appendix F.2. For later convenience we expand the result and define

$$\mathcal{M}_{h} = \frac{g^{2}m\delta^{ab}g_{\perp}^{\mu\nu}}{8\pi^{2}} \left[-\frac{1}{\epsilon^{2}} + \frac{1}{\epsilon}\log\frac{-\omega_{n}^{2} - i0}{\mu^{2}} - \frac{1}{2}\log^{2}\frac{-\omega_{n}^{2} - i0}{\mu^{2}} + 2 + \frac{\pi^{2}}{12} \right]$$

$$= \frac{g^{2}m\delta^{ab}g_{\perp}^{\mu\nu}}{8\pi^{2}}C_{1}, \tag{5.29}$$

where C_1 is a hard Wilson coefficient that we will use in the NLO calculation.

5.2.4 Combine results

As illustrated in figure 5.4, the sum of individual contributions has to reproduce the full QCD amplitude. As the full QCD amplitude is free of endpoint divergences and ϵ -poles, all poles of the individual contributions have to cancel in the sum. Endpoint divergences are solely a feature of soft and collinear contributions. Hence, the sum of these contributions has to be free of endpoint divergences and independent of the regulator. We start by expanding our final results using the absolute value regulator for the soft and collinear terms in η and ϵ

$$\mathcal{M}_{c} + \mathcal{M}_{\bar{c}} = \frac{g^{2}m}{4\pi^{2}} g_{\perp}^{\mu\nu} T_{F} \delta^{ab} \left[\frac{2}{\epsilon \eta} + \frac{2}{\eta} \log \frac{\mu^{2}}{m^{2}} + \frac{1}{\epsilon} \log \frac{\nu^{2}}{\omega_{n}^{2}} + \log \frac{\nu^{2}}{\omega_{n}^{2}} \log \frac{\mu^{2}}{m^{2}} + \mathcal{O}(\eta, \epsilon) \right]$$

$$\mathcal{M}_{s} = \frac{g^{2}m}{4\pi^{2}} g_{\perp}^{\mu\nu} T_{F} \delta^{ab} \left[\frac{1}{\epsilon^{2}} - \frac{2}{\eta \epsilon} - \frac{2}{\eta} \log \frac{\mu^{2}}{m^{2}} - \frac{1}{\epsilon} \left(\log \frac{\nu^{2}}{\mu^{2}} - i\pi \right) + \frac{1}{2} \log \frac{\mu^{2}}{m^{2}} \left(\log \frac{\mu^{2}}{\nu^{2}} + \log \frac{m^{2}}{\nu^{2}} + 2i\pi \right) - \frac{\pi^{2}}{12} \right].$$

$$(5.30)$$

As expected, the endpoint divergences as well as the dependence on the rapidity scale ν cancel in the sum:

$$\mathcal{M}_c + \mathcal{M}_{\bar{c}} + \mathcal{M}_s = \frac{g^2 m}{4\pi^2} g_{\perp}^{\mu\nu} T_F \delta^{ab} \left[\frac{1}{\epsilon^2} - \frac{1}{\epsilon} \left(\log \frac{m_H^2}{\mu^2} - i\pi \right) - \log \frac{m^2}{\mu^2} \left(\log \frac{m\mu}{m_H^2} - i\pi \right) - \frac{\pi^2}{12} \right]. \tag{5.31}$$

Recalling that the soft contribution was scaleless using the pure rapidity regulator, the sum of the n- and \bar{n} -collinear contributions has to yield the same result as eq. (5.31). We find that this is indeed the case.

We can now add the hard contribution and find that also the ϵ -poles cancel and we arrive at a finite result.

$$\mathcal{M}_h + \mathcal{M}_c + \mathcal{M}_{\bar{c}} + \mathcal{M}_s = \frac{g^2 m \delta^{ab} g_{\perp}^{\mu\nu}}{4\pi^2} T_F \left[-\frac{1}{2} \left(\log \frac{m^2}{m_H^2} - i\pi \right)^2 + 2 \right].$$
 (5.32)

which agrees with the leading term in the full QCD result given in ref. [277].

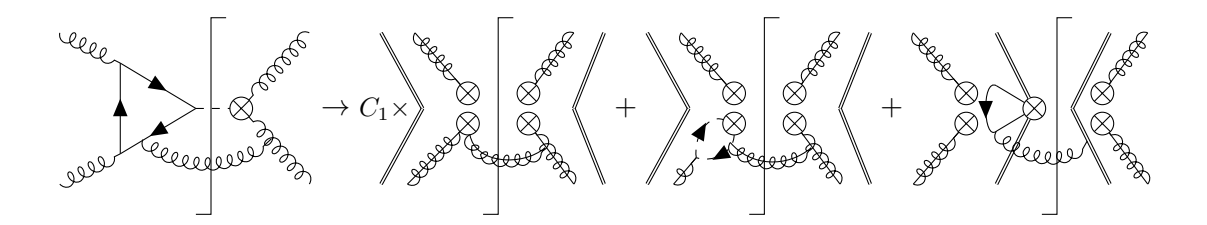


Figure 5.8: Decomposition of interference diagram in terms of hard, beam and soft functions. We only show example diagrams in each case. The springs with a solid line represent collinear gluons. Collinear gluons attached to \otimes represent a beam function. The solid double line represents a soft Wilson line where only soft gluons can attach.

5.3 Bare factorization theorems

We are now set up to think about the y_b - y_t -contribution to the Higgs q_T spectrum. While we just calculated a $2 \to 1$ amplitude, now we have a gluon crossing the cut. This is illustrated in figure 5.8. The first diagram shows the full QCD diagram which is then decomposed in terms of hard, collinear and soft contributions. Let us first focus on the right hand side of the cut which represents the top-quark loop that was integrated out. In the effective theory, this contribution is given in terms of leading-power beam and soft amplitudes. The left hand side of the cut shows the bottom-quark contributions. Similar to the leading-order diagram, we can write the this interference contribution in terms of next-to-leading-power (NLP) hard, beam and soft amplitudes. Once both sides are interfered, we will find new NLP beam and soft functions. In the first term in the sum the mass dependence is included in the Wilson coefficient C_1 that we defined in eq. (5.29). In the second and third terms in the sum the mass dependence is included in subleading-power beam and soft functions. Note that the diagrams in figure 5.8 symbolically stand for a full class of diagrams.

In order to pick up a transverse momentum, we need a singular emission $k_T = q_T$ that the Higgs boson can recoil against. This emission k_T adds a third scale to the problem. The masses, of course, follow the same scaling as before $m_b \ll m_H$ but the emission can have different scalings. Thus, we have to consider different kinematic regimes for our factorization theorems. These regimes are illustrated in figure 5.9. The hard scale $Q = m_H$ and the low scale m_b are always fixed. The hard-collinear scale is given by the intermediate scale $\sqrt{m_b Q}$.

5.3.1 Factorization theorem for $q_T \ll m_b \ll m_H$

We start by considering the kinematic region where the transverse momentum is smaller than any other scale $q_T \ll m_b \ll m_H$. This scenario is sketched in figure 5.9a. The bottom-quark mass, $m_b = 4.18\,\mathrm{GeV}$ [29] ($\overline{\mathrm{MS}}$ scheme), is already rather light. Thus, this kinematic region is only valid for the very beginning of the spectrum and is phenomenologically not particularly relevant. As m_b is much larger than the q_T , the bottom quark can be integrated out and we can describe this kinematic region using standard soft and beam function for $n_f = 4$ light flavors. The factorization theorem is given by

$$\frac{\mathrm{d}\sigma_{y_t y_b}}{\mathrm{d}q_T} = 2 \operatorname{Re} \left[C_{ggt}^*(m_H) C_{ggb}(m_b, m_H) \right] B_g(q_T) \otimes B_g(q_T) \otimes S_{gg}(q_T). \tag{5.33}$$

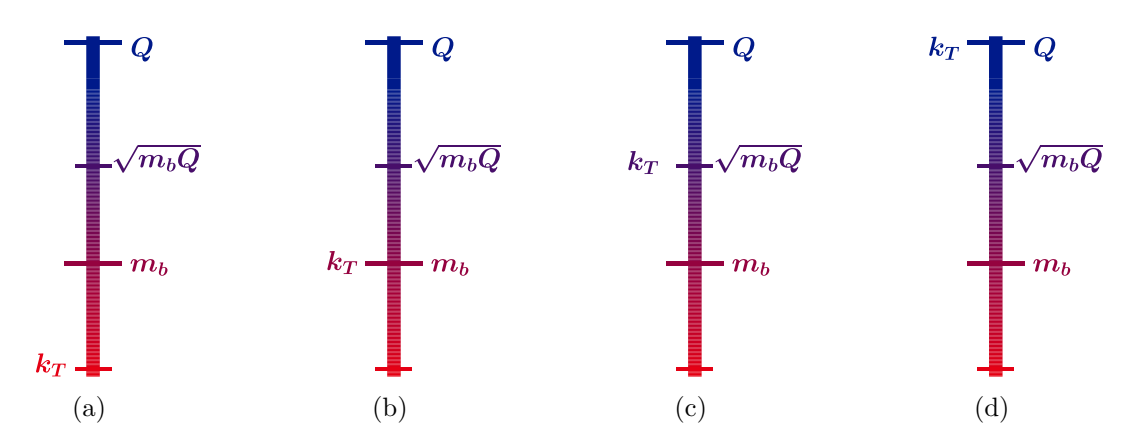


Figure 5.9: Illustration of different kinematic regimes with a hard scale $Q = m_H$, an intermediate scale $\sqrt{m_b Q}$ and a low scale m_b . The emission k_T can have different scalings.

In this factorization theorem the m_b and the q_T dependence nicely factorize. Here all emissions are described by leading-power beam and soft functions and the m_b -dependence is governed by the hard function. The hard function has two contributions: C_{ggt} is the Wilson coefficient that appears when integrating out the top quark and C_{ggb} is the Wilson coefficient from integrating out the bottom quark which is given in terms of the form factor for the Born process from ref. [271].

5.3.2 Factorization theorem for $q_T \sim m_b \ll m_H$

Next, we consider the regime where the transverse momentum is of the size of the bottom-quark mass corresponding to figure 5.9b. Phenomenologically, the regime is the most important one as the gluon fusion cross section peaks at roughly $q_T \approx 10 \,\text{GeV} \approx 2 m_b$. The all-order factorization theorem reads

$$\frac{\mathrm{d}\sigma_{y_t y_b}}{\mathrm{d}q_T} = H_{gg}(m) B_g(q_T) \otimes B_g(q_T) \otimes S_{gg}(q_T)
+ \int \mathrm{d}\xi H_{bbg}(\xi) \left[B_{n,\bar{\chi}\chi}(\xi, q_T, m, z) \otimes B_g(q_T) \otimes S_{gg}(q_T) \right]
+ B_g(q_T) \otimes B_{\bar{n},\bar{\chi}\chi}(\xi, q_T, m, z) \otimes S_{gg}(q_T) \right]
+ \int \mathrm{d}\ell^+ \mathrm{d}\ell^- H_{bbgg} \mathcal{J}(\ell^+) \mathcal{J}(\ell^-) B_g(q_T) \otimes B_g(q_T) \otimes S_{\bar{\psi}\psi}(\ell^+, \ell^-, q_T, m).$$
(5.34)

The next-to-leading power beam and soft functions are defined as

$$B_{n,\chi\bar{\chi}}(\xi,k_T,m,z=\frac{\omega}{P_N^-}) = \sum_{X} \langle N|\mathcal{B}_{\perp}^{a,\mu} \delta^2(k_{\perp} - P_{X,\perp})|X\rangle \langle X|\bar{\chi}_{n,\omega\xi} T^a \gamma_{\perp\mu} \chi_{n,\omega(1-\xi)}|N\rangle, \quad (5.35)$$

$$S_{\bar{\psi}\psi}(\ell^+, \ell^-, k_T, m) = \sum_{X} \frac{1}{N_c^2 - 1} \langle 0 | \mathcal{O}_s^{(0) ab} \delta^2(k_\perp - P_{X,\perp}) | X \rangle \langle X | \mathcal{O}_{s,\bar{\psi}\psi}^{ba} | 0 \rangle.$$
 (5.36)

The first term in both functions denotes the leading-power contribution where as the second term includes the NLP operators defined in eqs. (5.5) and (5.7). This factorization theorem in eq. (5.35) looks much more complicated than the previous one. In the following, we will go through the different contributions one by one and illustrate them using single-emission diagrams. The first term in the sum describes the scenario where all propagators in the loop are hard and

the mass dependence is fully encoded in the hard function $H_{gg}(m)$. Diagrammatically, we can write this contribution as

$$H_{gg}(m) B_g(q_T) \otimes B_g(q_T) \otimes S_{gg}(q_T) = C_1 \times \left[\begin{array}{c} & & & & \\ & & &$$

For convenience we only show the left hand side of the cut. The additional gluon is always understood to cross the cut and interfere with the leading-power contribution of the top quark. Here C_1 carries the subleading-power mass dependence whereas the emissions are described by leading-power soft and beam functions. Since there is no hard emission, C_1 is given by the leading-order hard contribution that we calculated in section 5.2.3. For the convolution of beam and soft functions there can only be one NLO contribution at this order and the other two functions contribute at leading order. The emission can be n or \bar{n} -collinear with the respective other beam function and the soft function contributing at leading order which is described by the first two terms in the sum of eq. (5.37). The emission can also have soft scaling, which is shown in the last term in the sum. In this case the two beam functions contribute at leading order.

Next we take a closer look a the second term in eq. (5.34) where the mass dependence is captured by either the n-or the \bar{n} -collinear beam function. This term is more complicated the first term we discussed as it suffers from endpoint divergences which appear in the ξ integral. Diagrammatically, we can write this term as

Here we have two contributions: In the first term in the sum, the emission comes from the subleading-power beam function which also governs the mass dependence. In second term, we have a virtual contribution to the subleading-power massive beam function, but the emission is given in terms of leading-power emissions.

Finally, we also want discuss the last term in the eq. (5.34) where the mass dependence is included in the soft function. Similar to eq. (5.38), we have a term where the emission originates from the subleading-power soft function and two terms with the leading-order massive soft function and leading-power emission from the beam functions

where the two jet functions $\mathcal{J}(\ell^+)\mathcal{J}(\ell^-)$ encode the effect of virtual and hard-collinear contributions. At our working order the jet functions are simply given by $\mathcal{J}(\ell^{\pm}) = 1$.

5.3.3 Factorization theorem for $m_b \ll q_T \ll m_H$ and $m_b \ll m_H \lesssim q_T$

Considering the kinematic regime where $m_b \ll q_T \ll m_H$ one could think that the factorization theorem has the form of a massless factorization theorem as $m_b \ll q_T$. However, this is not the case since there are still large logarithms of m_b that need to be resummed and, more importantly, subleading-power operators must still be included during the high-scale matching in order to pick up the correct mass suppression at the low scale where the bottom-quark loop is closed. A promising method to find the structure for this part of the cross section is to consider the two neighboring regimes and perform an interpolation, which will rely on the results of the thesis.

In the regime where q_T is of order of the hard scale, $m_b \ll m_H \lesssim q_T$, the logarithms of q_T/Q are no longer large and one could think that the full fixed order result which was originally calculated in ref. [278] is sufficient. However, the logarithms of m_b/Q are still large and require resummation and, as before, the subleading-power operators must be included during the high-scale matching. In order to pick up a transverse momentum of order Q the gluon crossing the cut must have hard scaling. Therefore, we cannot consider a diagram-level factorization in this regime. Instead, the factorization takes place at cross-section level and takes a PDF-like form.

A detailed discussion of these regimes as well as their factorization theorems are therefore beyond the scope of this thesis.

5.4 Collinear emission diagrams

In the leading-order calculation carried out in section 5.2, we separated the contributions by the scaling of the loop momenta which could be hard, soft or collinear. Now that we are considering real emission diagrams, we need to adjust this classification. Recalling the factorization theorems in eqs. (5.39) and (5.38), the emission can have soft or collinear scaling even if the loop momenta have e.g. soft scaling and vice versa. A substantial part of the NLO calculation will be to verify the cancellation of the endpoint divergences which we already encountered in section 5.2. We will see in this section that this cancellation is much more delicate at NLO. The endpoint divergences have to cancel point by point in k. This statement already hints towards a sensible classification: the sum of all diagrams with a collinear emission as well as the sum of all diagrams with a soft emission have to be individually η finite. Note that ϵ poles will only cancel once we combine the soft and collinear contributions with the contribution from the hard loop.

In this section, we will calculate all diagrams with a collinear emission as shown in figure 5.10. We introduce a color coding to clearly distinguish n-collinear and \bar{n} -collinear particles which are shown in green and magenta. The soft loop is shown as solid fermion line. As mentioned before that sum of all these diagrams has to be rapidity finite. We can, however, identify certain sub-classes which are rapidity finite on their own.

Before we start with the calculation of the diagrams in figure 5.10, we want to introduce a new variable $z \equiv \omega_n/p_1^- \in [0,1]$ which allows us to write the two external minus momenta as

$$p_1^- = \frac{\omega_n}{z}, \qquad k^- = \frac{\omega_n(1-z)}{z}.$$
 (5.40)

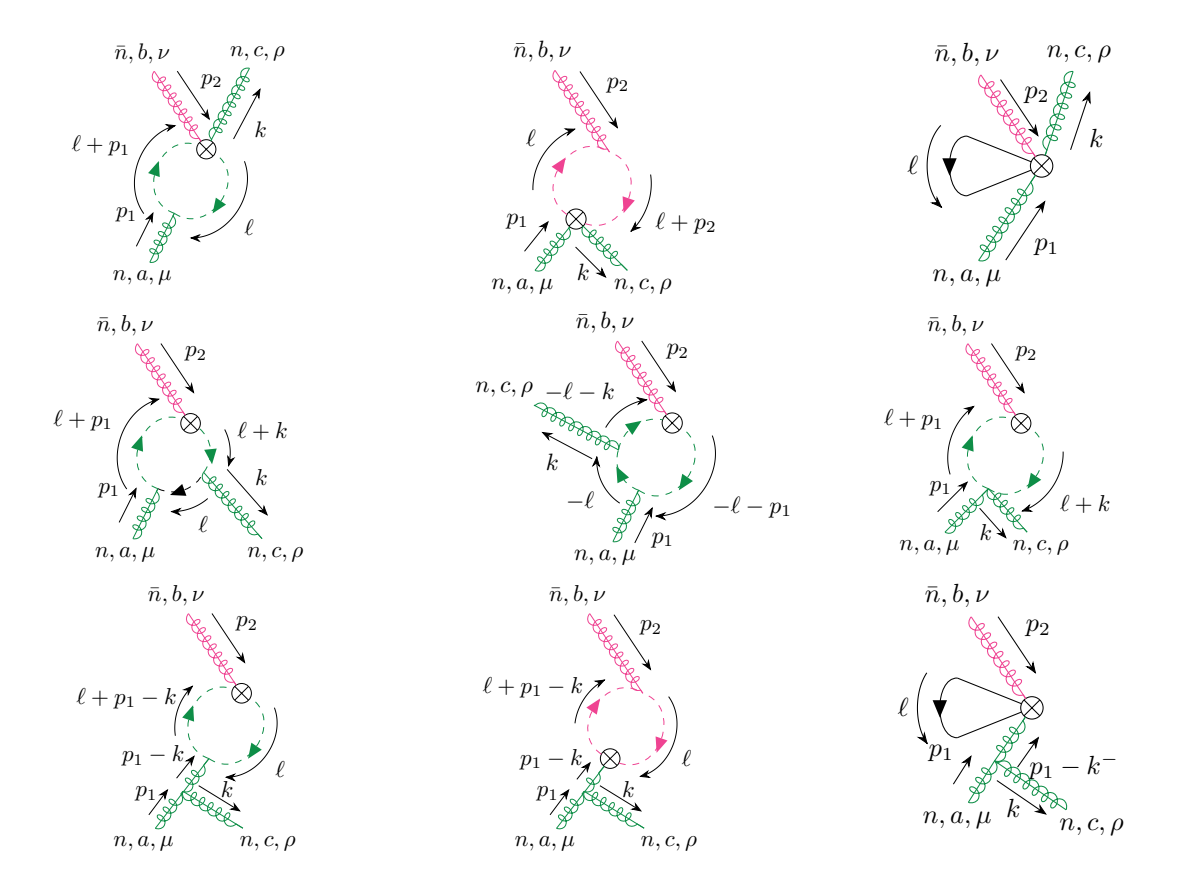


Figure 5.10: All diagrams where the emission k has collinear scaling. All particles with n (\bar{n})-collinear scaling are drawn in green (magenta). The sum of these diagrams is free of endpoint divergences.

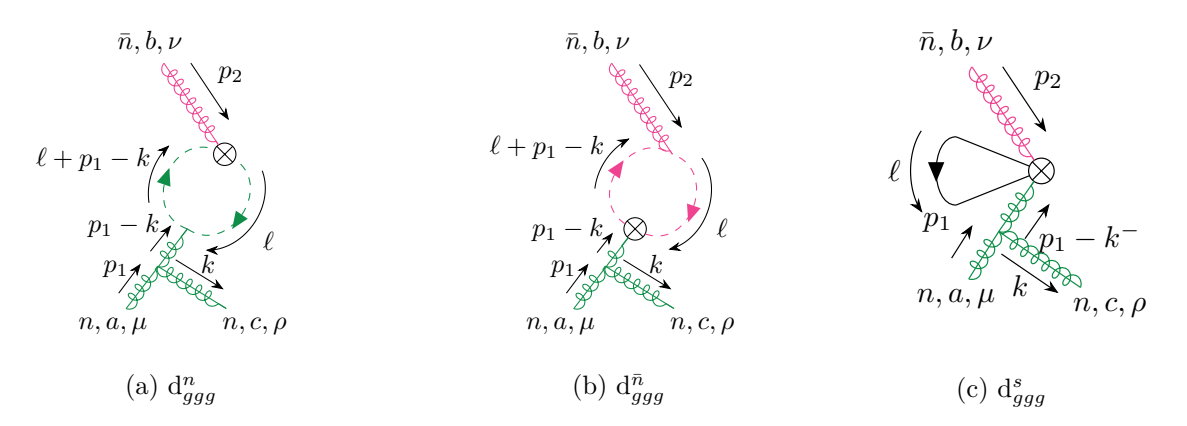


Figure 5.11: d_{ggg} -type diagrams: all diagrams where the collinear emission comes from the interaction of three collinear gluons.

We will also make use of the fact that our emission k is on-shell and replace $k^+ = -k_{\perp}^2/k^-$. As in section 5.2, ω_n denotes the overall minus momentum of the process which coincides with minus momentum of the Higgs boson. At NLO, we have

$$\omega_n = p_1^- - k^-. (5.41)$$

For the evaluation of the LO₁ diagram, we proceed just as in the LO₀ case: For the diagrams involving a collinear loop, we start by using the δ -function to perform the ℓ^- integral. Next, we do the ℓ^+ integral by contours. This constrains the ξ integral since the contour integral only has support in specific regions for ξ . After doing the contour integral we can use standard formulæ to solve the ℓ_{\perp} integral. In the last step, we evaluate the ξ integral which suffers from endpoint divergences and, thus, needs to be regulated. For the diagrams involving a soft loop, we can simply reuse the leading-order soft calculation as the loop is never affected by the additional collinear emission.

5.4.1 Triple-gluon-vertex emission diagrams

We start with the diagrams where the collinear emission comes from an interaction of three collinear gluons. This class of diagrams shown in figure 5.11 is very similar to the leading-order calculation as the collinear emission does not effect the loop.

We start with the contribution where the loop is n-collinear which is shown in figure 5.11a. The evaluation is completely analogous to the collinear LO calculation carried out in section 5.2.1. The result for this contribution can in fact be recovered from shifting $p_1 \to p_1 - k$ in eq. (5.8) and only contracting with the triple gluon vertex after all integrals are evaluated. We therefore

refrain from giving any calculational details. The result is given by

$$\mathcal{M}_{d_{ggg}^{n}} = \frac{f^{abc}g^{3}}{32\pi^{2}} \frac{me^{\epsilon\gamma_{E}}\mu^{2\epsilon}}{k_{\perp}^{2}\omega_{n}z} \left[2g_{\perp}^{\mu\nu}k_{\perp}^{\rho}\omega_{n}z(z-1) + g_{\perp}^{\mu\nu}\bar{n}^{\rho}k_{\perp}^{2}z^{2} + g_{\perp}^{\mu\nu}n^{\rho}\omega_{n}^{2}(1-z^{2}) \right. \\ \left. + 4g_{\perp}^{\nu\rho}k_{\perp}^{\mu}\omega_{n}z(1-z) + 4g_{\perp}^{\mu\rho}k_{\perp}^{\nu}\omega_{n}(z-1) + 4k_{\perp}^{\mu}k_{\perp}^{\nu}\bar{n}^{\rho}z(z-1) \right] \\ \times \left\{ \pi \log \left(1 + \frac{k_{\perp}^{2}}{2m(z-1)} + \frac{\sqrt{\frac{k_{\perp}^{2}}{1-z}}\sqrt{\frac{k_{\perp}^{2}}{1-z}} - 4m^{2}}{2m^{2}} \right) \right. \\ \left. + \pi \log \left(1 + \frac{k_{\perp}^{2}}{2m(z-1)} - \frac{\sqrt{\frac{k_{\perp}^{2}}{1-z}}\sqrt{\frac{k_{\perp}^{2}}{1-z}} - 4m^{2}}{2m^{2}} \right) \right. \\ \left. - \frac{\mathrm{i}}{16\pi^{2}}m^{-2\epsilon}\frac{\Gamma(\epsilon)}{\eta} \left| \frac{\nu}{\omega_{n}} \right|^{\eta} \right\}.$$
 (5.42)

Despite the similarity of the calculation the NLO result looks much more complicated. This is not only due to additional Lorentz structures but also due to the fact that the propagator in the loop features non-vanishing k^+ and k_{\perp} terms in the denominator.

Next, we consider diagram $d_{ggg}^{\bar{n}}$ which is shown in figure 5.11b. Here, the loop is \bar{n} -collinear and the gluon is emitted from the n-collinear gluon which affect the loop. The gluon emission puts the gluon participating in the hard interaction off-shell. The Feynman rule in eq. (E.3) was derived for on-shell gluons. We thus need to make a slight modification and replace $\not n \to \not n + \not p_{1,\perp}/p_1^-$ before evaluating the integral. In fact, we need to do the same replacement in the soft Feynman rule in eq. (E.5) when evaluating the d_{ggg}^s diagram (figure 5.11c). Evaluating these integrals in analogy to the leading-order calculations, we find

$$\mathcal{M}_{\mathrm{d}_{ggg}^{\bar{n}}} = -\frac{\mathrm{i} f^{abc} g^{3}}{16\pi^{2}} \frac{\Gamma(\epsilon)}{\eta} \frac{m^{1-2\epsilon} e^{\epsilon\gamma_{E}} \mu^{2\epsilon}}{\omega_{n} z k_{\perp}^{2}} \left| \frac{\nu}{\omega_{n}} \right|^{\eta} \left[2g_{\perp}^{\mu\nu} k_{\perp}^{\rho} \omega_{n} z (z-1) + g_{\perp}^{\mu\nu} \bar{n}^{\rho} k_{\perp}^{2} z^{2} \right. \\ \left. + g_{\perp}^{\mu\nu} n^{\rho} \omega_{n}^{2} (1-z^{2}) + 4g_{\perp}^{\nu\rho} k_{\perp}^{\mu} \omega_{n} z (1-z) + 4g_{\perp}^{\mu\rho} k_{\perp}^{\nu} \omega_{n} (z-1) + 4k_{\perp}^{\mu} k_{\perp}^{\nu} \bar{n}^{\rho} z (z-1) \right],$$

$$(5.43)$$

$$\mathcal{M}_{\mathrm{d}_{ggg}^{s}} = -\frac{\mathrm{i} f^{abc} g^{3}}{16\pi^{2}} \frac{z}{\omega_{n}^{2} k_{\perp}^{2}} m^{1-2\epsilon-\eta} e^{\epsilon\gamma_{E}} \mu^{2\epsilon} \frac{|\nu|^{\eta}}{\eta} {}_{2} F_{1} \left(\frac{\eta}{2}, \eta; \frac{\eta+2}{2}; -1 \right) \frac{\Gamma(\epsilon + \frac{\eta}{2})}{\Gamma(\frac{\eta}{2} + 1)}$$

$$\times \left[g_{\perp}^{\mu\nu} n^{\rho} \omega_{n}^{3} \frac{1-z^{2}}{z} + 2g_{\perp}^{\mu\nu} k_{\perp}^{\rho} \omega_{n}^{2} (z-1) + g_{\perp}^{\mu\nu} \bar{n}^{\rho} k_{\perp}^{2} z \omega_{n} + 4g_{\perp}^{\mu\rho} k_{\perp}^{\nu} \frac{\omega_{n}^{2} (z-1)}{z} \right.$$

$$\left. + 4g^{\nu\rho} k_{\perp}^{\mu} \omega_{n}^{2} (1-z) + 4k_{\perp}^{\mu} k_{\perp}^{\nu} \bar{n}^{\rho} \omega_{n} (1-z) \right].$$

$$(5.44)$$

We can now combine all three contributions

$$\mathcal{M}_{d_{ggg}} = \mathcal{M}_{d_{ggg}^n} + \mathcal{M}_{d_{ggg}^{\bar{n}}} + \mathcal{M}_{d_{ggg}^s} = \mathcal{O}(\eta^0). \tag{5.45}$$

and find that this subset is indeed free of endpoint divergences.

5.4.2 Vertex emission diagrams

In this section, we sketch the calculation of contributions where the gluon is emitted from an effective vertex. These diagrams are shown in figure 5.12. In this class of diagrams, the emission can either come from the hard interaction vertex as in figures 5.12a- 5.12c or the SCET vertex double quark-gluon vertex in figure 5.12d.

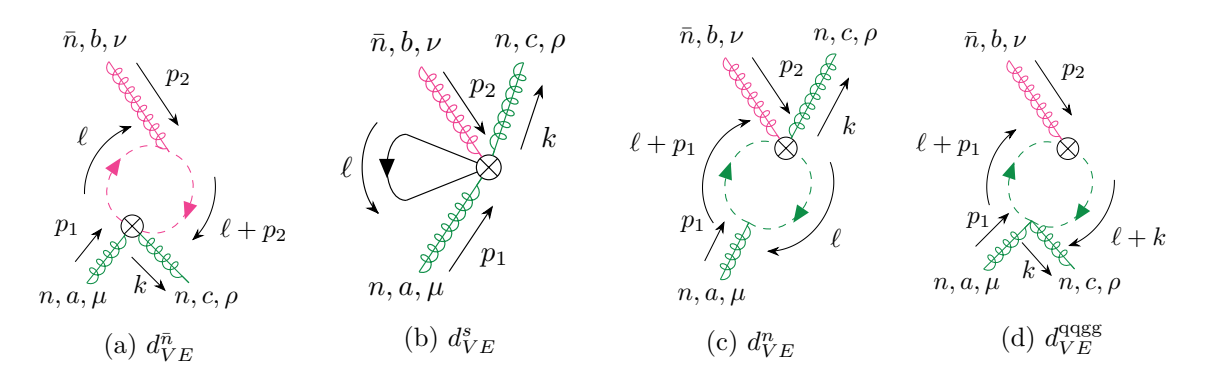


Figure 5.12: d_{VE} diagram class: all diagrams where the emission is attached to an effective vertex.

Contribution from \bar{n} -collinear and soft loops

The \bar{n} -collinear and soft in the class of diagrams are analogous to the leading-order calculation. The contribution from the $d_{VE}^{\bar{n}}$ and the d_{VE}^{s} can be obtained by contracting the leading-order Feynman rule with the gluon field strength at $\mathcal{O}(g)$ which is given in appendix of ref. [279]. This amounts to shifting

$$T^a \to i f^{acd} T^d \frac{g \bar{n}^{\rho}}{\bar{n} \cdot k},$$
 (5.46)

in the leading-order Feynman rule. Note that in our case the gluon is outgoing which leads to an overall minus sign w.r.t ref. [279]. For completeness, we give the resulting Feynman rules in eqs. (E.4) and (E.6). From the simplicity of this modification, it is apparent that we can do the same replacement at the level of the leading-order results. This leads to the following results

$$\mathcal{M}_{d_{VE}^{\bar{n}}} = -\frac{\mathrm{i}f^{abc}g^3}{8\pi^2} \frac{\Gamma(\epsilon)}{\eta} \frac{z}{\omega_n (1-z)} m^{1-2\epsilon} e^{\epsilon\gamma_E} \mu^{2\epsilon} \left| \frac{\nu}{\omega_n} \right|^{\eta} g_{\perp}^{\mu\nu} \bar{n}^{\rho}$$
(5.47)

$$\mathcal{M}_{\mathrm{d}_{VE}^{s}} = \frac{\mathrm{i} f^{abc} g^{3}}{8\pi^{2}} \frac{z}{\omega_{n}(1-z)} \bar{n}^{\rho} g_{\perp}^{\mu\nu} e^{\epsilon\gamma_{E}} \mu^{2\epsilon} m^{1-2\epsilon-\eta} \frac{\mathrm{i}^{\eta}}{\eta} \left| \frac{\nu}{\omega_{n}} \right|^{\eta} {}_{2} F_{1} \left(\frac{\eta}{2}, \eta; \frac{\eta+2}{2}; -1 \right) \frac{\Gamma(\epsilon + \frac{\eta}{2})}{\Gamma(\frac{\eta}{2}+1)}. \tag{5.48}$$

d_{VE}^{qqgg} contribution

For this diagram (shown in figure 5.12d), the additional emission comes from the SCET vertex given in figure 2.6. The evaluation of the ℓ^- , ℓ^+ and ℓ_\perp integrals is completely analogous to the diagram for the leading-order calculation and we find

$$\mathcal{M}_{d_{VE}^{qqgg}} = -\frac{ig^{3}m}{32\pi^{2}} \frac{z}{\omega_{n}} e^{\epsilon\gamma_{E}} \mu^{2\epsilon} \Gamma(\epsilon) \int_{0}^{1} d\xi \left(\frac{1}{\xi} \left| \frac{\xi\omega_{n}}{\nu} \right|^{-\eta} + \frac{1}{1-\xi} \left| \frac{(1-\xi)\omega_{n}}{\nu} \right|^{-\eta} \right)$$

$$\times \left(m^{2} + \frac{k_{\perp}^{2} \xi(\xi-1)}{1-z} \right)^{\epsilon} \frac{f^{abc}(2\xi^{2}z - 2\xi z + 1) + id^{abc}(2\xi-1)}{(\xi z - 1)[(\xi-1)z + 1]}.$$
(5.49)

For the first time in this calculation, we now have an integrand that has a ξ dependence in addition to the Wilson coefficient. This adds extra complication to the integral as it cannot be evaluated directly. Note that the endpoint divergences are isolated and the rest of the integral is

finite in the limits $\xi \to 1$ and $\xi \to 0$. Therefore we can use the following trick

$$\mathcal{I}(\xi) = \int_{0}^{1} d\xi \left(\frac{1}{\xi} + \frac{1}{1 - \xi} \right) f(\xi)
= \int_{0}^{1} d\xi \left\{ \frac{1}{\xi} \left[\left| \frac{\xi \omega_{n}}{\nu} \right|^{-\eta} f(0) \underbrace{-f(0) + f(\xi)}_{\text{regular for } \xi \to 0} \right] + \frac{1}{1 - \xi} \left[\left| \frac{(1 - \xi)\omega_{n}}{\nu} \right|^{-\eta} f(1) \underbrace{-f(1) + f(\xi)}_{\text{regular for } \xi \to 1} \right] \right\},$$
(5.50)

where the subtractions $f(\xi) - f(0)$ and $f(\xi) - f(1)$ cancel in the respective divergent limit and contribute a finite result. In fact, they cancel completely in our calculation once the integral is evaluated. Our final result for this contribution is then given by

$$\mathcal{M}_{d_{VE}^{qqgg}} = -\frac{\mathrm{i}f^{abc}g^3}{16^2} \frac{\Gamma(\epsilon)}{\eta} \frac{z}{\omega_n(1-z)} m^{1-2\epsilon} e^{\epsilon\gamma_E} \mu^{2\epsilon} \left| \frac{\nu}{\omega_n} \right|^{\eta} g_{\perp}^{\mu\nu} \bar{n}^{\rho}. \tag{5.51}$$

d_{VE}^n contribution

Similar to the soft and \bar{n} -collinear contributions, the d_{VE}^n diagram corresponds to the leading-order diagram with a modified effective vertex. However, in this case it is not sufficient to simply modify the prefactor of our leading-order result: In the full theory, the gluon can be emitted from either one of the quarks or the gluon. This leads to the modified Feynman rule eq. (E.2). This Feynman rule has two different sets of δ -function and a different color structure. This leads to a different denominator after resolving the δ -functions:

$$\mathcal{M}_{d_{VE}^{n}} = \int d\xi \int \frac{d\ell^{+} d^{d-2}\ell_{\perp}}{(2\pi)^{d-1}} \frac{g^{3}m}{8\pi} \frac{z}{z-1} C_{bbg}(\xi) \bar{n}^{\rho} g_{\perp}^{\mu,\nu}$$

$$\left[\frac{f^{abc} - id^{abc}}{\left[\omega_{n}(\xi - 1)\ell^{+} + \ell_{\perp}^{2} - m^{2} + i0 \right] \left[\omega_{n}((\xi - 1)z + 1)\ell^{+} + z(\ell_{\perp}^{2} - m^{2} + i0) \right]} + \frac{f^{abc} + id^{abc}}{\left[\omega_{n}\xi\ell^{+} + \ell_{\perp}^{2} - m^{2} + i0 \right] \left[\omega_{n}(\xi z - 1)\ell^{+} + z(\ell_{\perp}^{2} - m^{2} + i0) \right]} \right]. \tag{5.52}$$

We will call the different terms the $\mathcal{M}^+_{d^n_{VE}}$ and $\mathcal{M}^-_{d^n_{VE}}$ contributions corresponding to the relative sign between f^{abc} and $\mathrm{i} d^{abc}$. In the next step, we do the ℓ^+ integral by contours where we have to consider both contributions separately. In figure 5.13, the coefficients of the i0 are shown as a function of ξ . The sign of these coefficients determines whether the corresponding pole in ℓ^+ is in the upper or lower half-plane when doing the ℓ^+ integral. The contour integral only has support for specific values of ξ which imposes a constraint on the ξ integral. We find $1-1/z<\xi<1$ for $\mathcal{M}^-_{d^n_{VE}}$ and $0<\xi<1/z$ for $\mathcal{M}^+_{d^n_{VE}}$ which we will keep in mind for the ξ integral.

After doing the ℓ^+ integral it is straightforward to evaluate the ℓ_{\perp} integral and only the endpoint-divergent ξ integral remains. As in the leading-order calculation, only the Wilson coefficient

$$C_{bbg} = \frac{1}{\xi} + \frac{1}{1 - \xi},\tag{5.53}$$

depends on ξ . Recalling that our two contributions have support for different values of ξ , it is convenient to define three different regions of ξ ,

$$\mathcal{R}^{-} = \left[1 - \frac{1}{z}, 0\right], \qquad \mathcal{R}^{0} = [0, 1], \qquad \mathcal{R}^{+} = \left[1, \frac{1}{z}\right],$$
 (5.54)

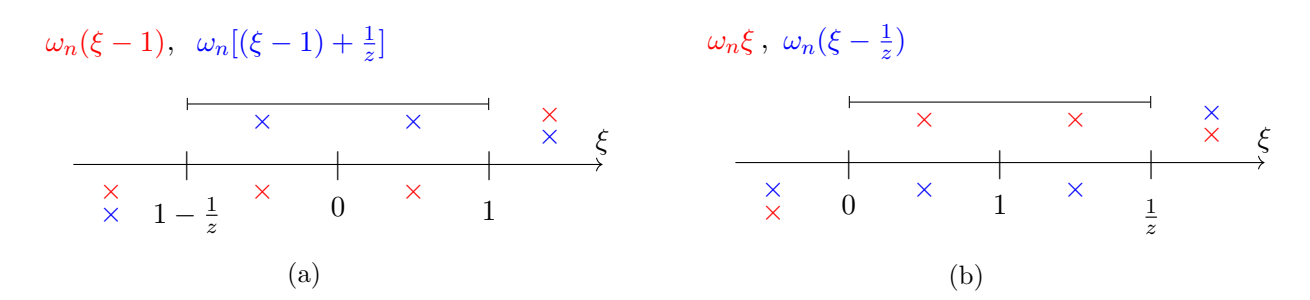


Figure 5.13: Pole analysis for the collinear d_{VE}^n contribution. (a) shows the poles of $\mathcal{M}_{d_{VE}^n}^-$ and (b) shows the poles of the $\mathcal{M}_{d_{VE}^n}^+$ contribution. The black interval marks the region where the contour integral is non-zero.

and divide the ξ integral accordingly. Both contributions, $\mathcal{M}_{d_{VE}}^+$ and $\mathcal{M}_{d_{VE}}^-$, have support in the central region \mathcal{R}^0 where the endpoint divergences appear in both integral limits. Additionally, each term also gets a contribution from one of the outer regions: $\mathcal{M}_{d_{VE}}^+$ from \mathcal{R}^+ and $\mathcal{M}_{d_{VE}}^-$ from \mathcal{R}^- which only diverge in one of the integral limits. As before, we regulate the endpoint divergences with the absolute value regulator and find

$$\mathcal{I}_{\xi,+} = \int_{1}^{\frac{1}{z}} d\xi \left(\frac{1}{\xi} \left| \frac{\xi \omega_{n}}{\nu} \right|^{-\eta} + \frac{1}{1 - \xi} \right) = \left(\frac{1}{z} - 1 \right)^{-\eta} \left| \frac{\nu}{\omega_{n}} \right|^{\eta} \frac{1}{\eta} - \log z,
\mathcal{I}_{\xi,-} = \int_{1 - \frac{1}{z}}^{0} d\xi \left(\frac{1}{\xi} + \frac{1}{1 - \xi} \left| \frac{(1 - \xi)\omega_{n}}{\nu} \right|^{-\eta} \right) = \left(\frac{1}{z} - 1 \right)^{-\eta} \left| \frac{\nu}{\omega_{n}} \right|^{\eta} \frac{1}{\eta} - \log z,
\mathcal{I}_{\xi,0} = \int_{0}^{1} d\xi \left(\frac{1}{\xi} \left| \frac{\xi \omega_{n}}{\nu} \right|^{-\eta} + \frac{1}{1 - \xi} \left| \frac{(1 - \xi)\omega_{n}}{\nu} \right|^{-\eta} \right) = -2 \left| \frac{\nu}{\omega_{n}} \right|^{\eta} \frac{1}{\eta}.$$
(5.55)

After integrating, we can recombine the different contributions and arrive at our result for this diagram

$$\mathcal{M}_{d_{VE}^n} = -\frac{\mathrm{i} f^{abc} g^3}{16\pi^2} \frac{\Gamma(\epsilon)}{\eta} \frac{z}{\omega_n (1-z)} m^{1-2\epsilon} e^{\epsilon \gamma_E} \mu^{2\epsilon} g_{\perp}^{\mu\nu} \bar{n}^{\rho} \left[2 \left| \frac{\nu}{\omega_n} \right|^{\eta} - \left(\frac{1}{z} - 1 \right)^{-\eta} \left| \frac{\nu}{\omega_n} \right|^{\eta} + \eta \log z \right]$$

$$(5.56)$$

Combing all d_{VE} diagrams

We have now calculated all diagrams in figure 5.12 and can finally combine them:

$$\mathcal{M}_{d_{VE}} = \mathcal{M}_{d_{VE}^{\bar{n}}} + \mathcal{M}_{d_{VE}^s} + \mathcal{M}_{d_{VE}^{qqgg}} + \mathcal{M}_{d_{VE}^n} = \mathcal{O}(\eta^0).$$

In the sum all endpoint divergences of this diagram class cancel.

5.4.3 Loop emission diagrams

This sub-class of diagrams is the most complex one as we have a third propagator in the loop which modifies the δ -functions fixing the ℓ^- and ξ integrals. Using the choice of momenta in figure 5.14, both diagrams have the same denominators which simplifies the calculation. As before, we start by doing the ℓ^- integral by resolving the δ -functions.

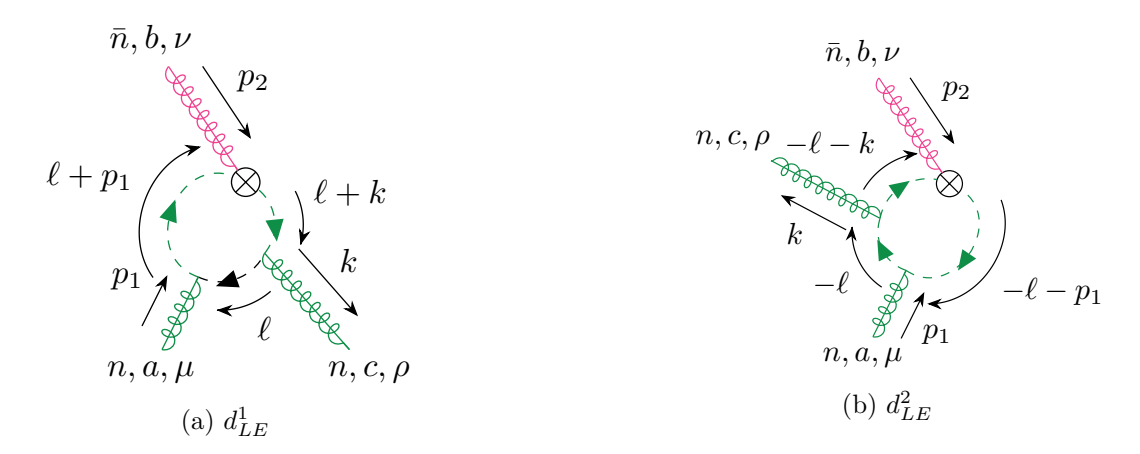


Figure 5.14: d_{LE} -type diagrams: the gluon is emitted from the loop.

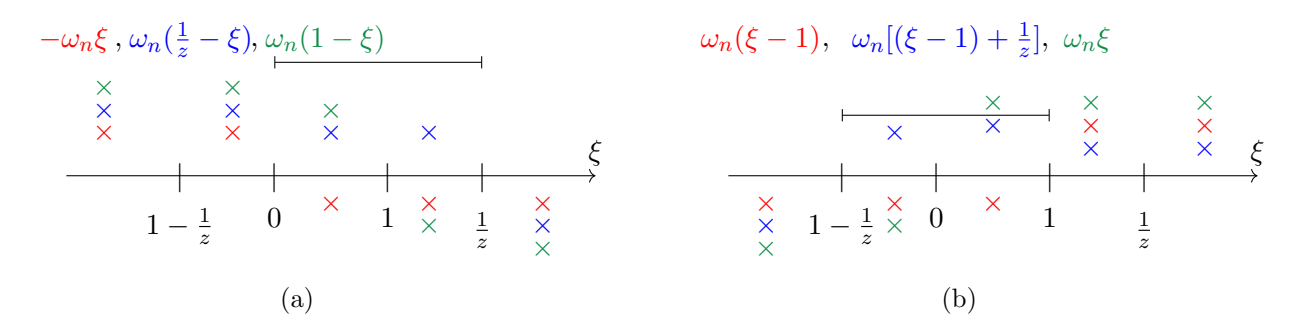


Figure 5.15: Pole analysis for the d_{LE} contributions. (a) shows the poles in the complex ℓ^+ -plane of $\mathcal{M}_{d_{LE}^1}$ and (b) shows the poles of $\mathcal{M}_{d_{LE}^2}$. The black interval marks the region where the contour integral is non-zero.

Next, we do the ℓ^+ integral by contours. Note that as we have three propagators in the loop, there will also be three poles in the complex plane. The coefficients of the i0 in the denominators determine whether the pole will be in the upper or lower-half plane. These coefficients are shown in figure 5.15 as a function of ξ . We find that we get non-zero contributions in the same regions as in the previous section. However, the third pole switches sign when going from the central region \mathcal{R}^0 to one of the outer regions \mathcal{R}^\pm . Therefore all contributions must be considered separately and can only be combined after integrating over ξ . In the next step, we evaluated the ℓ_\perp integral where we need Feynman parameters to combine the denominators. Calculational details on the ℓ_\perp and Feynman parameter integrals are given in appendix F.3.

Now, the only remaining integral is the divergent ξ integral. Once again, we utilize the formula in eq. (5.50) to isolate the endpoint divergences. This approach remains valid even when the integral diverges only in one of the limits, as is the case for the \mathcal{R}^{\pm} regions.

For this class of diagrams, the function $f(\xi)$ is rather complex, preventing a straightforward integration of its finite part over ξ . However, since we only require the full ϵ -dependence of the endpoint-divergent contribution, we can expand the η -finite piece in ϵ before integrating. This allows us to extract the $1/\epsilon$ term, which is free of endpoint divergences.

For the ϵ -finite contribution, we were unable to find a closed-form expression. Nevertheless, our primary focus for now is the structure of the endpoint divergences, leaving the analytic evaluation of the finite contribution for future work. When comparing to the full QCD result in ref. [280] or obtaining phenomenological predictions, the integral can always be evaluated

numerically. For the central region \mathcal{R}^0 , we find

$$\mathcal{M}_{d_{LE}}^{0} = \frac{ig^{3}m(f^{abc} + id^{abc})}{32\pi^{2}} \left| \frac{\nu}{\omega_{n}} \right|^{\eta} e^{\epsilon\gamma_{E}} \mu^{2\epsilon} \frac{\Gamma(\epsilon)}{\eta} \left\{ \epsilon(-1)^{\epsilon} 4^{1+\epsilon} \left[k_{\perp}^{\mu} g_{\perp}^{\nu\rho} - \frac{k_{\perp}^{\nu} g_{\perp}^{\mu\rho}}{z} + \frac{k_{\perp}^{\mu} k_{\perp}^{\nu} \bar{n}^{\rho}}{\omega_{n}} \right] \right. \\
\left. \times (4m^{2} - k_{\perp}^{2})^{-1-\epsilon} {}_{2}F_{1} \left(\frac{1}{2}, \epsilon + 1, \frac{3}{2}, \frac{k_{\perp}^{2}}{k_{\perp}^{2} - 4m^{2}} \right) + \frac{zm^{-2\epsilon}}{\omega_{n}(1-z)} g_{\perp}^{\mu\nu} \bar{n}^{\rho} \right\} + \text{finite}, \quad (5.57)$$

$$\mathcal{M}_{d_{LE}^{2}}^{0} = \frac{ig^{3}m(f^{abc} - id^{abc})}{32\pi^{2}} \left| \frac{\nu}{\omega_{n}} \right|^{\eta} e^{\epsilon\gamma_{E}} \mu^{2\epsilon} \frac{\Gamma(\epsilon)}{\eta} \left\{ \epsilon(-1)^{\epsilon} 4^{1+\epsilon} \left[k_{\perp}^{\mu} g_{\perp}^{\nu\rho} - \frac{k_{\perp}^{\nu} g_{\perp}^{\mu\rho}}{z} + \frac{k_{\perp}^{\mu} k_{\perp}^{\nu} \bar{n}^{\rho}}{\omega_{n}} \right] \right. \\
\left. \times (4m^{2} - k_{\perp}^{2})^{-1-\epsilon} {}_{2}F_{1} \left(\frac{1}{2}, \epsilon + 1, \frac{3}{2}, \frac{k_{\perp}^{2}}{k_{\perp}^{2} - 4m^{2}} \right) + \frac{zm^{-2\epsilon}}{\omega_{n}(1-z)} g_{\perp}^{\mu\nu} \bar{n}^{\rho} \right\} + \text{finite}, \quad (5.58)$$

where we added a "+finite" to indicate the presence of the above mentioned ϵ and η -finite piece. Also note, that both diagrams contribute the exact same result upon the relative sign between f^{abc} and d^{abc} . In the sum the d^{abc} terms will cancel, leaving a pure f^{abc} part as final result which we expect as a d^{abc} contribution would break charge symmetry. For the outer regions, \mathcal{R}^+ and \mathcal{R}^- , we find

$$\mathcal{M}_{d_{LE}^{+}}^{+} = -\frac{ig^{3}(f^{abc} + id^{abc})}{32\pi^{2}}m^{1-2\epsilon}e^{\epsilon\gamma_{E}}\mu^{2\epsilon}\frac{\Gamma(\epsilon)}{\eta}$$

$$\times \left\{ \frac{z}{\omega_{n}(1-z)} \left[\log z - \frac{1}{\eta} \left| \frac{\nu}{\omega_{n}} \right|^{\eta} \left(\frac{1}{z} - 1 \right)^{-\eta} \right] g_{\perp}^{\mu\nu}\bar{n}^{\rho}$$

$$+ \frac{2}{\eta} \left| \frac{\nu}{\omega_{n}} \right|^{\eta} \left(\frac{1}{z} - 1 \right)^{-\eta} \frac{z}{k_{\perp}^{2} - 4m^{2}} \left[k_{\perp}^{\mu} g_{\perp}^{\nu\rho} - \frac{k_{\perp}^{\nu} g_{\perp}^{\mu\rho}}{z} + \frac{k_{\perp}^{\mu} k_{\perp}^{\nu} \bar{n}^{\rho}}{\omega_{n}} \right]$$

$$\times \left[1 + e^{i\pi\epsilon} \frac{4^{\epsilon}(2-\epsilon)m^{2\epsilon}}{(k_{\perp}^{2} - 4m^{2})^{\epsilon}} {}_{2}F_{1} \left(\frac{1}{2}, \epsilon + 1, \frac{3}{2}, \frac{k_{\perp}^{2}}{k_{\perp}^{2} - 4m^{2}} \right) \right] \right\} + \text{finite}, \quad (5.59)$$

$$\mathcal{M}_{d_{LE}^{2}}^{-} = -\frac{ig^{3}(f^{abc} - id^{abc})}{32\pi^{2}} m^{1-2\epsilon} e^{\epsilon\gamma_{E}} \mu^{2\epsilon} \frac{\Gamma(\epsilon)}{\eta}$$

$$\times \left\{ \frac{z}{\omega_{n}(1-z)} \left[\log z - \frac{1}{\eta} \left| \frac{\nu}{\omega_{n}} \right|^{\eta} \left(\frac{1}{z} - 1 \right)^{-\eta} \right] g_{\perp}^{\mu\nu} \bar{n}^{\rho}$$

$$+ \frac{2}{\eta} \left| \frac{\nu}{\omega_{n}} \right|^{\eta} \left(\frac{1}{z} - 1 \right)^{-\eta} \frac{z}{k_{\perp}^{2} - 4m^{2}} \left[k_{\perp}^{\mu} g_{\perp}^{\nu\rho} - \frac{k_{\perp}^{\nu} g_{\perp}^{\mu\rho}}{z} + \frac{k_{\perp}^{\mu} k_{\perp}^{\nu} \bar{n}^{\rho}}{\omega_{n}} \right]$$

$$\times \left[1 + e^{i\pi\epsilon} \frac{4^{\epsilon}(2-\epsilon)m^{2\epsilon}}{(k_{\perp}^{2} - 4m^{2})^{\epsilon}} {}_{2}F_{1} \left(\frac{1}{2}, \epsilon + 1, \frac{3}{2}, \frac{k_{\perp}^{2}}{k_{\perp}^{2} - 4m^{2}} \right) \right] \right\} + \text{finite}. \quad (5.60)$$

Again, the only difference of these two contributions is the relative sign between f^{abc} and d^{abc} . We can now combine all contributions and find that this class of diagram is free of endpoint divergences

$$\mathcal{M}_{d_{LE}} = \mathcal{M}_{d_{LE}^{1}}^{0} + \mathcal{M}_{d_{LE}^{2}}^{0} + \mathcal{M}_{d_{LE}^{1}}^{+} + \mathcal{M}_{d_{LE}^{2}}^{-} = \mathcal{O}(\eta^{0}).$$
 (5.61)

5.5 Cancellation of endpoint divergences

After the rather technical calculation of the collinear emission diagrams in the previous section, we now take a step back to reflect on the conclusions we can draw from the cancellation of the

endpoint divergences. For the form factor, this cancellation is relatively straightforward since the problem involves only two scales, m_b and Q. However, when considering the q_T spectrum, an additional scale is introduced, which affects the coefficient functions of the endpoint divergences. In general, these coefficients can be non-trivial functions of m/k_{\perp} . In this section, we investigate how the additional q_T dependence influences the structure of the endpoint divergences. To do so, we express our diagrams in the factorized form already introduced in our discussion of factorization theorems in section 5.3.

5.5.1 Collinear emission

Let us begin with the collinear emission diagram studied in detail in the previous section. The diagrams from figure 5.10 can be categorized into two distinct classes. In the first class, the gluon is emitted from a subleading-power beam function:

As before, we omit the right-hand side of the cut for better readability. For this class of diagrams alone, the endpoint divergences remain uncanceled. In the second class of collinear emission diagrams, the gluon is emitted from a leading-power collinear vertex or Wilson line. Like the previous class, these diagrams also exhibit endpoint divergences:

Only the sum of both classes is free of such divergences. Remarkably, the endpoint divergences from the non-trivial subleading-power diagrams cancel against those from leading-power emissions multiplying a virtual next-to-leading-power diagram. This is a highly nontrivial result, indicating that the mass and k_T dependence remain factorized at subleading power. Consequently, the coefficient functions do not exhibit a complex dependence on m/k_{\perp} .

5.5.2 Soft emission

When discussing the factorization theorem in section 5.3, we saw that the emitted gluon can have soft or collinear scaling. At this point, we have discussed the collinear emission diagrams in great detail and now want to focus on the diagrams where the emitted gluon is soft. As the sum of all collinear emission diagrams is free of endpoint divergences and the endpoint divergences have to cancel point by point in k, we are free to choose a different regulator for the soft emission diagrams. We choose the pure rapidity regulator [129], as the soft leading-order diagram vanishes using this regulator. Thus, we only have two contributions with a soft leading-power emission –

namely a soft Wilson line multiplying a sub-leading power beam function:

which is already rapidity finite on its own. Further, we have two diagrams where the gluon is emitted from a subleading-power soft function. Since the sum of diagrams in eq. (5.64) is free of endpoint divergences, the same has to happen in the sum of the NLP emission diagrams. Indeed, we find

$$\left(\begin{array}{c} \begin{array}{c} \begin{array}{c} \\ \\ \end{array} \\ \end{array} \right) \times \begin{array}{c} \begin{array}{c} \\ \\ \end{array} \\ \end{array} \right) \otimes \begin{array}{c} \\ \end{array} = \mathcal{O}\left(\eta^{0}\right). \tag{5.65}$$

Just as for the collinear emission, we find that the mass and the transverse momentum dependence factorize and conclude that the coefficient functions of the endpoint divergences do not feature a complex dependence on m/k_{\perp} .

5.6 Summary

In this section, we studied bottom-quark mass effects in the Higgs q_T spectrum. This contribution makes up for about $\mathcal{O}(5-10\%)$ of the gluon fusion process as it is enhanced by the interference with the top-quark loop and thus an important contribution to the Higgs q_T spectrum. The full prediction can be used to measure the quark Yukawa couplings from the initial state.

To set up the notation, we started with the leading-order calculation involving bottom-mass effects. Here, we saw that our individual contributions agree with the results in ref. [269] and the sum of the hard, collinear and soft contributions reproduces the full QCD result. In the LO calculation, we only have two scales, the quark mass and the hard scale (Higgs mass). When calculating the q_T spectrum, we add a third scale to the problem and need to take the different possible scales of q_T into account. In fact, we need a factorization theorem for each kinematic regime, where we focused on $q_T \ll m_b \ll Q$ and $q_T \sim m_b \ll Q$. Further we calculated all collinear real-virtual emission diagrams and saw that the endpoint divergences cancel within different subsets of these diagrams. In fact, the endpoint diverges from subleading-power diagrams cancel and against leading-power emissions. This tell us that the mass and transverse momentum dependence factorize even at sub-leading power, which is one of the main results of this chapter. For the soft emission diagrams, we saw that the subleading-power contributions are η finite on their own when using the pure rapidity regulator. Thus, the sum of contributions featuring a leading-power soft emission has to be finite as well.

The next steps towards understanding the bottom-mass effects in the Higgs q_T spectrum would be to compare the η -finite parts of all diagrams to the full QCD result in the respective limit of k being collinear or soft and to perform the phase space integral over k. In the future, it would also be interesting to renormalize the subleading-power hard, beam and soft functions and obtain a resummed result for this interference term in the Higgs q_T spectrum which we will leave to future work.

Chapter 6

Transverse Momentum Distributions of Heavy Quarks and Heavy Hadrons

In this chapter, we initiate the study of transverse momentum-dependent (TMD) fragmentation functions for heavy quarks, demonstrate their factorization in terms of novel nonperturbative matrix elements in heavy-quark effective theory (HQET), and prove new TMD sum rules that arise from heavy-quark spin symmetry. We discuss the phenomenology of heavy-quark TMD FFs at B factories. We further calculate all TMD parton distribution functions for the production of heavy quarks from polarized gluons within the nucleon and use our results to demonstrate the potential of the future EIC to resolve TMD heavy-quark fragmentation in semi-inclusive DIS, complementing the planned EIC program to use heavy quarks as probes of gluon distributions

This chapter closely follows ref. [3] reflecting the author's contribution. In comparison to ref. [3], section 6.2 was shortened and some calculational details were added in section 6.3.

6.1 Motivation

Hadronization describes the nonperturbative mechanism that confines quarks and gluons produced in high-energy collisions into the experimentally observable color-singlet hadrons. This is a key aspect of every process involving QCD particles, but its fundamental description from first principles remains unknown [53]. We thus rely on phenomenological models to described the hadronization process. The fragmentation of bottom and charm quarks to heavy mesons can play a vital role on the way of gaining a better understanding of the fundamental underlying processes: The mass of the heavy quark imprints as a perturbative scale on the otherwise nonperturbative dynamics of hadronization. The unique properties of heavy quarks as color-charged, but perturbatively accessible objects make them ideally suited as probes of the hadronization cascade, effectively serving as a static color source coupling to the light degrees of freedom. In this chapter, we present the first study of the transverse momentum dependent (TMD) fragmentation functions (FFs) of heavy quarks to heavy hadrons. Our theoretical tool to analyze the fragmentation of heavy quarks is (boosted) Heavy-Quark Effective Theory (bHQET) [97–100, 146,281–284, which has previously been applied to the well-understood collinear (or longitudinal) heavy-quark FFs [285–288]. We demonstrate that applying bHQET to TMD FFs gives rise to novel, universal matrix elements describing the nonperturbative transverse dynamics of light QCD degrees of freedom in the presence of a heavy quark (i.e., a static color source). While

a large part of this work is devoted to developing this new theoretical formalism. Further, we also consider the phenomenology of heavy-quark TMD FFs in e^+e^- collisions and semi-inclusive deep inelastic scattering (SIDIS) which are relevant for existing *B*-factories such as Belle-II and the future EIC, respectively.

These TMD processes are directly sensitive to the nonperturbative transverse dynamics of heavy-quark fragmentation. We note that the TMD fragmentation of light quarks to quarkonia has been studied in ref. [289], in that case by matching onto nonrelativistic QCD, and similarly for light-quark TMD dynamics in hard quarkonium production and decay in ref. [290, 291].

This chapter is structured as follows: In Section 6.2, we analyze heavy-quark TMD FFs and identify the new bHQET matrix elements and perturbative matching coefficients that characterize the fragmentation dynamics. In Section 6.3, we discuss the all-order structure of matching polarized heavy quark TMD PDFs onto collinear PDFs and explicitly compute the $\mathcal{O}(\alpha_s)$ matching onto gluon PDFs. In Section 6.4, we use our results from the previous two sections to outline the prospects for heavy-quark TMD phenomenology at e^+e^- colliders and the future EIC.

6.2 TMDs for heavy quark fragmentation into a heavy hadron

6.2.1 Calculational setup and parametric regimes

We consider the fragmentation of a (possibly polarized) heavy quark Q into a hadron H that contains the heavy quark and carries momentum P_H^{μ} . For this paper, we assume that the heavy hadron polarization is not experimentally reconstructed. We work in QCD with $n_f = n_\ell + 1$ flavors, where the n_ℓ massless quark flavors are denoted by q and the heavy quark Q has a pole mass $m \equiv m_c, m_b \gg \Lambda_{\rm QCD}$. We decompose P_H^{μ} in terms of lightcone momenta as

$$P_H^{\mu} = P_H^{-} \frac{n^{\mu}}{2} + \frac{M_H^2}{P_H^{-}} \frac{\bar{n}^{\mu}}{2} \,, \tag{6.1}$$

where $P_H^- \gg P_H^+ = M_H^2/P_H^-$ is boosted in the frame of the hard scattering and by definition $P_{H,\perp} = 0$, coinciding with the "hadron frame" for fragmentation [147].

We are interested in the dependence of the fragmentation process on the total transverse momentum of additional hadronic radiation X into the final state, which is equal to the initial quark transverse momentum k_{\perp} by momentum conservation, and Fourier conjugate to the transverse spacetime separation b_{\perp} between quark fields.

Since $\Lambda_{\rm QCD} \ll m$, the nonperturbative dynamics in the fragmentation process are constrained by heavy-quark symmetry in all cases, but differences arise depending on the hierarchy between these two parametric scales and the magnitude k_T of the transverse momentum or, equivalently, the inverse of the transverse distance $1/b_T \sim k_T$. Broadly speaking, we will consider the two cases illustrated in figure 6.1. In case (a), which we analyze in section 6.2.3, $k_T \sim \Lambda_{\rm QCD}$ is generated during the nonperturbative fragmentation process itself, while perturbative emissions at the scale $m \gg k_T$ are suppressed. In this case, the heavy hadron carries almost all the longitudinal momentum provided by the initial heavy quark, while the k_T dependence is carried by universal nonperturbative functions describing how the "brown muck" separates from other light hadronic final states. In this regime, "disfavored" fragmentation functions where the valence content of the identified heavy hadron does not match the initial heavy quark, e.g. $Q \to \bar{H}$, $Q \to h$, or $q, g \to H$, are forbidden by heavy-quark symmetry. To simplify the analysis, we will

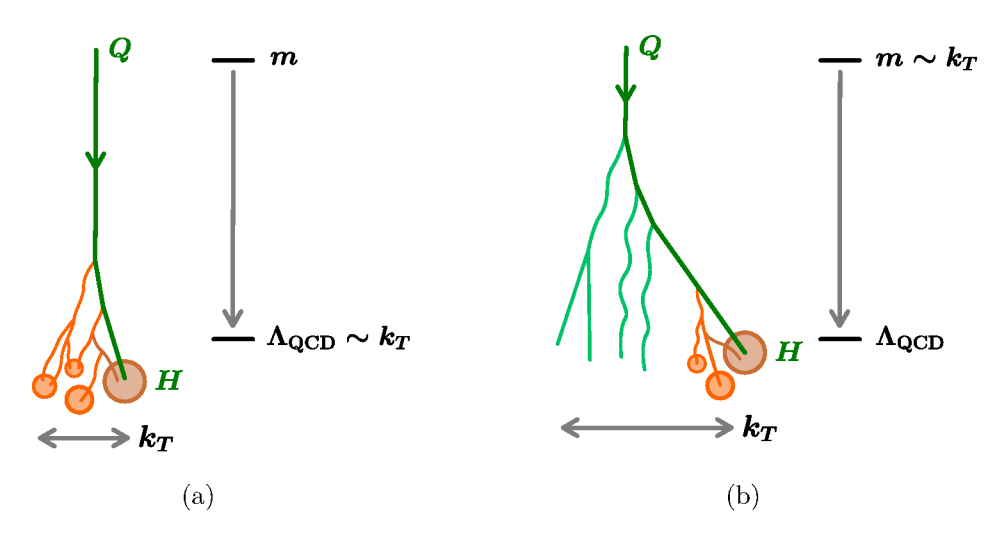


Figure 6.1: Parametric regimes for the fragmentation of a heavy quark Q (green) into a single heavy hadron H with a measurement on transverse momentum. In case (a), the hadron picks up transverse momentum relative to its parent quark as the "brown muck" (brown) coalesces around the quark and splits from other soft hadronic radiation into the final state (orange). In case (b), the transverse and longitudinal momentum distributions are dominated by perturbative emissions at the scale of the heavy quark mass (teal). In this regime, the nonperturbative hadronization process is encoded in a normalization factor, while its effect on the shape of the momentum distribution is subleading.

count

$$1 - z_H \sim 1, \tag{6.2}$$

where z_H is the fraction of the quark's lightcone momentum retained by the hadron H. To be precise, we will assume that the z_H measurement does not probe the precise longitudinal momentum distribution near the endpoint.

In case (b), which we consider in section 6.2.4, the distributions in transverse and longitudinal momentum are determined by perturbative dynamics at the scale $k_T \sim m \gg \Lambda_{\rm QCD}$, while the dynamics of the nonperturbative bound state only contribute a normalization factor. In the case of the unpolarized TMD FF, this normalization factor admits an interpretation as the total probability for Q to fragment into H, as is well known for inclusive heavy hadron production cross sections [285, 286, 292]. In this case, the disfavored fragmentation functions for $Q \to \bar{H}$ or $q \to H$, and $Q \to h$ or $g \to H$, are perturbatively suppressed by $\mathcal{O}(\alpha_s^2)$ and $\mathcal{O}(\alpha_s)$ at the scale $\mu \sim m$, respectively. We stress that we continue to assume eq. (6.2) also in this regime, so longitudinal momentum distributions remain perturbative.

6.2.2 boosted Heavy-Quark Effective Theory

Boosted Heavy-Quark Effective Theory (bHQET) [146,284] describes the application of HQET, to heavy quarks produced in an energetic collision. For a short review on HQET we refer to section 2.3. Recall that the heavy field can be written as

$$\psi_Q(x) = e^{-\mathrm{i}mv \cdot x} h_v(x) \left[1 + \mathcal{O}\left(\frac{1}{m}\right) \right]. \tag{6.3}$$

The dynamic degrees of freedom are heavy-quark fields $h_v(x)$ that are labeled by the timelike direction v^{μ} , which we choose to be the velocity of the heavy hadron,

$$v^{\mu} = \frac{P_H^{\mu}}{M_H}, \qquad v^2 = 1,$$
 (6.4)

For external states, the matching reads $|H, h_H; X\rangle = \sqrt{m} |H_v, h_H; X\rangle$, and we use a nonrelativistic normalization convention for the bHQET states. In addition, the effective theory contains light-quark and gluon degrees of freedom that have isotropic momentum $p^{\mu} \sim \Lambda_{\rm QCD}$ in the rest frame of the heavy hadron. The tree-level matching for these is trivial; in particular, the Wilson line W(x) takes the same form in the effective theory, but consists of gluon fields that only have support on a restricted set of modes.

After performing a field redefinition, a static Wilson line, $Y_v(x)$, takes the place of $h_v(x)$ in all external operators, acting as a static source of soft gluons. The field redefinition as well as $Y_v(x)$ were defined in section 2.3. Specifically, the action of $h_v(x)$ on a product state in the decoupled theory is given by

$$h_v(x) |s_Q, h_Q; s_\ell, h_\ell, f_\ell; X\rangle = u(v, h_Q) Y_v(x) |s_\ell, h_\ell, f_\ell; X\rangle,$$
 (6.5)

where $s_Q = \frac{1}{2}$ and $h_Q = \pm \frac{1}{2}$ are the spin and helicity of the heavy quark, $u(v, h_Q) = u(mv, h_Q)/\sqrt{m}$ is an HQET spinor, and s_ℓ , h_ℓ , and f_ℓ are the total angular momentum, helicity, and flavor content of the light degrees of freedom inside the hadron. (We will specify a helicity axis in the following section.) Physical hadron states of definite angular momentum s_H and helicity h_H also have definite s_ℓ , which is a good quantum number in the heavy-quark limit. In general, they involve a coherent sum over the helicity eigenstates in eq. (6.5),

$$|H_v, h_H\rangle \equiv |s_H, h_H, s_Q, s_\ell\rangle = \sum_{h_Q} \sum_{h_\ell} |s_Q, h_Q; s_\ell, h_\ell\rangle \langle s_Q, h_Q; s_\ell, h_\ell | s_H, h_H\rangle, \qquad (6.6)$$

where we suppressed the common f_{ℓ} and X, and $\langle s_Q, h_Q; s_{\ell}, h_{\ell} | s_H, h_H \rangle$ is a Clebsch-Gordan coefficient. (We take the coefficient to vanish for $h_Q + h_\ell \neq h_H$, i.e., one sum is always eliminated in practice by helicity conservation.) For the case of inclusive fragmentation, it has been known for a long time [107,286] that the factorized form of eq. (6.5) together with parity and eq. (6.6) implies relations between the fragmentation probabilities to different hadron states within the same heavy-quark spin symmetry multiplet, i.e., with the same $s_{\ell} = \frac{1}{2}, 1, \frac{3}{2}, \ldots$ As an example, at the strict leading order in 1/m, an unpolarized charm quark is exactly three times as likely to fragment into an excited spin-1 vector meson (D^*) than into the corresponding pseudoscalar state (D). The physical reason for this is that the light dynamics do not see the heavy-quark spin at leading power, and thus the same nonperturbative matrix elements with given s_{ℓ}, h_{ℓ} appear in several cases. This analysis is simplified by the fact that for unpolarized or linearly polarized heavy quarks, light amplitudes for different helicities cannot interfere. One key goal of the next section will be to work out the consequences of heavy-quark spin symmetry for transverse momentum-dependent fragmentation functions, where transverse quark polarization will let us access this interference for the first time.

6.2.3 Calculating TMD FFs from bHQET for $\Lambda_{\rm QCD} \lesssim k_T \ll m$

Tree-level matching and discrete symmetries

In this section we calculate the TMD FFs for $\Lambda_{\rm QCD} \lesssim k_T \ll m$ using bHQET. We will use methods from HQET that were introduced in section 2.3 and refer the reader to this section for

details. Additionally, we will use the definition of the TMD quark-quark correlator as well as the definitions of the unpolarized and the Collins TMD FFs from section 2.6.3.

Using the tree-level matching onto bHQET in eq. (6.3) at the leading order in $\Lambda_{\rm QCD}/m \sim k_T/m$, the correlator evaluates to

$$\Delta_{H/Q}(z_H, b_\perp) = \frac{m}{z_H} \int \frac{\mathrm{d}b^+}{4\pi} \, e^{\mathrm{i}b^+ (P_H^-/z_H - mv^-)/2} \Big\{ F_H(b_\perp) + \mathcal{O}(\alpha_s) + \mathcal{O}\left(\frac{1}{m}\right) \Big\} \,, \tag{6.7}$$

where F_H is a bHQET bispinor defined by

$$F_H(b_\perp) \equiv \frac{1}{2N_c} \operatorname{Tr} \sum_{X} \left\langle 0 \middle| W^\dagger(b_\perp) h_v(b_\perp) \middle| H_v X \right\rangle \left\langle H_v X \middle| \bar{h}_v(0) W(0) \middle| 0 \right\rangle. \tag{6.8}$$

Note that we have evaluated the matrix element at $b^+ = 0$, which is justified at leading order in 1/m. Using $P_H^- = v^-[m + \mathcal{O}(\Lambda_{\rm QCD})]$, we can perform the b^+ integral,

$$\Delta_{H/Q}(z_H, b_\perp) = \frac{\delta(1 - z_H)}{\bar{n} \cdot v} F_H(b_\perp) + \mathcal{O}\left(\frac{1}{m}\right). \tag{6.9}$$

To analyze the spin structure of $F_H(b_\perp)$, it is convenient to define the auxiliary vector

$$z^{\mu} = v^{\mu} - \frac{\bar{n}^{\mu}}{\bar{n} \cdot v}$$
 with $z^2 = -1$, (6.10)

which defines a unit z axis oriented along the spatial component of \bar{n} in the rest frame. Written out explicitly, $F_H(v,z,b_\perp)$ depends on the three four vectors v^μ , i.e., the label direction in bHQET, corresponding to P_H^μ in the full theory, the spacelike vector z^μ parameterizing the Wilson line direction \bar{n}^μ relative to v^μ , and the spatial separation b_\perp^μ of the fields (with direction $x^\mu \equiv b_\perp^\mu/b_T$, $x^2 = -1$). As these three are orthogonal, they define a unique fourth unit direction $y^\rho = \epsilon^{\mu\nu\rho\sigma}v_\mu x_\nu z_\sigma$ with $y^2 = -1$.

There are three applicable symmetries constraining the form of F_H : first, the correlator only propagates the particle components of the bispinor. Second, from its transformation under hermitian conjugation and, third, from parity conservation. Note that time reversal is broken by the presence of the out states, and thus is not a good symmetry of fragmentation functions [178]. Finally, charge conjugation relates the form of F_H for $Q \to H$ to that of $\bar{Q} \to \bar{H}$, but does not constrain the form of F_H for a given final state. Then, the most general form of $F_H(v, z, b_\perp)$ allowed by Lorentz covariance is given by,

$$F_H(v, z, b_\perp) = \chi_{1,H}(b_T) \frac{1 + \psi}{2} + \chi_{1,H}^\perp(b_T) \not z \frac{\not b_\perp}{b_T} \frac{1 + \psi}{2}$$
(6.11)

with two real-valued scalar coefficient functions $\chi_{1,H}(b_T)$ and $\chi_{1,H}^{\perp}(b_T)$ that can only depend on $v^2 = -z^2 = 1$ and $b_{\perp}^2 = b_T^2$. Recalling the definitions of the unpolarized and the Collins TMD FFs from section 2.6.3

$$D_{1H/q}(z_H, b_T) = \text{tr}\left[\frac{\rlap{/}{n}}{2} \Delta_{H/q}(z_H, b_\perp)\right],$$

$$H_{1H/q}^{\perp(1)}(z_H, b_T) = \text{tr}\left[\frac{\rlap{/}{n}}{2} \frac{\rlap{/}{b}_\perp}{M_H b_T^2} \Delta_{H/q}(z_H, b_\perp)\right],$$
(6.12)

we perform the traces and identify the two functions, $\chi_{1,H}(b_T)$ and $\chi_{1,H}^{\perp}(b_T)$, with the unpolarized and Collins TMD FF, respectively,

$$D_{1H/Q}(z_H, b_T, \mu, \zeta) = \delta(1 - z_H) C_m(m, \mu, \zeta) \chi_{1,H} \left(b_T, \mu, \frac{\sqrt{\zeta}}{m} \right) + \mathcal{O}\left(\frac{1}{m}\right),$$

$$b_T M_H H_{1H/Q}^{\perp(1)}(z_H, b_T, \mu, \zeta) = \delta(1 - z_H) C_m(m, \mu, \zeta) \chi_{1,H}^{\perp} \left(b_T, \mu, \frac{\sqrt{\zeta}}{m} \right) + \mathcal{O}\left(\frac{1}{m}\right). \tag{6.13}$$

We used the known results [293, 294] for the perturbative matching of SCET onto bHQET to generalize our results to all orders in perturbation theory. Here the matching coefficient $C_m = 1 + \mathcal{O}(\alpha_s)$ arises from separately matching the collinear ("unsubtracted") and soft contributions to the TMD FFs onto bHQET and QCD with n_ℓ light flavors, respectively. Starting at two loops, the matching coefficient features rapidity logarithms of the Collins-Soper scale ζ over the mass as a consequence of the large boost separating the heavy hadron rest frame and the frame where the soft radiation is isotropic. The renormalization properties of $\chi_{1,H}$ and $\chi_{1,H}^{\perp}$ follow from eq. (6.13) by consistency with the bHQET matching.

For reference, we can also take suitable traces of eq. (6.11) to obtain explicit definitions of $\chi_{1,H}$ and $\chi_{1,H}^{\perp}$ in terms of bHQET matrix elements,

$$\chi_{1,H}(b_T) = \frac{1}{2} \operatorname{tr} F_H(b_\perp), \qquad \chi_{1,H}^{\perp}(b_T) = \frac{1}{2} \operatorname{tr} \left[\frac{b_\perp}{b_T} \not z F_H(b_\perp) \right].$$
(6.14)

which we dub heavy-quark TMD fragmentation factors.

Heavy-quark spin symmetry

We now return to the full correlator $F_H(b_{\perp})$ defined in eq. (6.8) and analyze its heavy-quark spin symmetry properties, which are particularly transparent when working with sterile fields. To do so, we first decompose the out states as in eq. (6.6). Acting on these out states with sterile heavy-quark fields as in eq. (6.5) yields

$$F_{H}(b_{\perp}) = \frac{1}{2} \sum_{h_{H}} \sum_{h_{Q}, h'_{Q}} \sum_{h_{\ell}, h'_{\ell}} u(v, h_{Q}) \, \bar{u}(v, h'_{Q}) \, \langle s_{Q}, h_{Q}; s_{\ell}, h_{\ell} | s_{H}, h_{H} \rangle \langle s_{H}, h_{H} | s_{Q}, h'_{Q}; s_{\ell}, h'_{\ell} \rangle$$

$$\times \frac{1}{N_{c}} \operatorname{Tr} \sum_{X} \left\langle 0 | W^{\dagger}(b_{\perp}) Y_{v}(b_{\perp}) | s_{\ell}, h_{\ell}, f_{\ell}; X \right\rangle \langle s_{\ell}, h'_{\ell}, f_{\ell}; X | Y_{v}^{\dagger}(0) W(0) | 0 \rangle$$

$$\equiv \frac{1}{2} \sum_{h_{H}} \sum_{h_{Q}, h'_{Q}} \sum_{h_{\ell}, h'_{\ell}} u(v, h_{Q}) \, \bar{u}(v, h'_{Q}) \, \langle s_{Q}, h_{Q}; s_{\ell}, h_{\ell} | s_{H}, h_{H} \rangle \langle s_{H}, h_{H} | s_{Q}, h'_{Q}; s_{\ell}, h'_{\ell} \rangle \, \rho_{\ell, h_{\ell} h'_{\ell}}(b_{\perp}) \, . \tag{6.15}$$

On the last line we defined the spin-density matrix ρ_{ℓ} of the light degrees of freedom $\ell \equiv \{s_{\ell}, f_{\ell}\}$ which encodes all non-perturbative dynamics.

The fact that the same light spin density matrix ρ_{ℓ} appears for all hadrons within the same spin symmetry multiplet (same s_{ℓ} and f_{ℓ} , but different s_H) leads to relations between their TMD FFs in the heavy-quark limit. We now push on towards the combinations that are relevant for an unpolarized hadron and that contribute to the two fragmentation factors at hand.

Unpolarized TMD FF: We begin with the unpolarized quark case and perform the trace in eq. (6.14), which sets $h_Q = h'_Q$ and thus $h_\ell = h'_\ell$,

$$\chi_{1,H}(b_T) = \frac{1}{2} \sum_{h_H} \sum_{h_Q} \sum_{h_\ell} |\langle s_Q, h_Q; s_\ell, h_\ell | s_H, h_H \rangle|^2 \rho_{\ell,h_\ell h_\ell}(b_\perp).$$
 (6.16)

To illustrate this, consider the pseudoscalar case, where

$$s_{\ell} = 1/2, \ s_{H} = 0: \quad \chi_{1,H}(b_{T}) = \frac{1}{4} \left[\rho_{\ell,++}(b_{\perp}) + \rho_{\ell,--}(b_{\perp}) \right],$$
 (6.17)

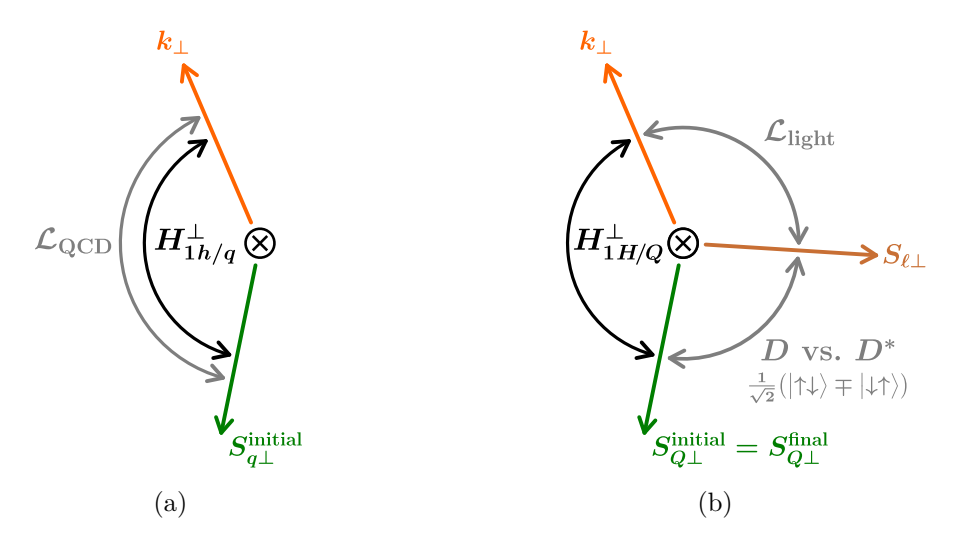


Figure 6.2: Origin of the Collins TMD FF H_1^{\perp} for (a) light and (b) heavy quarks. Here k_{\perp} is the transverse momentum of additional hadronic radiation into the final state, $S_{q\perp}$ (or $S_{Q\perp}$) is the quark transverse polarization vector, and $S_{\ell\perp}$ is the transverse polarization vector of the light hadron constituents.

and we have written helicities as $\pm \equiv \pm \frac{1}{2}$ for short. We see that the unpolarized TMD FF encodes information about the magnitude of the amplitude for producing a given light helicity state. Summing over all hadrons H within the same spin symmetry multiplet M_{ℓ} (i.e., all hadrons with identical light spin and flavor state ℓ), we further define

$$\chi_{1,\ell}(b_T) \equiv \sum_{H \in M_{\ell}} \chi_{1,H}(b_T) = \sum_{h_{\ell}} \rho_{\ell,h_{\ell}h_{\ell}}(b_{\perp}),$$
(6.18)

where we used the completeness relation of the Clebsch-Gordan coefficients

$$\frac{1}{2} \sum_{H} \sum_{h_H} \sum_{h_Q} \sum_{h_\ell} |\langle s_Q, h_Q; s_\ell, h_\ell | s_H, h_H \rangle|^2 = 1.$$
 (6.19)

By evaluating the partial sums in eq. (6.16), it is easy to see that in terms of this baseline, the individual unpolarized TMD fragmentation factors are given by

$$s_{\ell} = \frac{1}{2} : \qquad \chi_{1,H}(b_T) = \frac{1}{4} \chi_{1,\ell}(b_T), \qquad \chi_{1,H^*}(b_T) = \frac{3}{4} \chi_{1,\ell}(b_T),$$
 (6.20)

where for the purpose of this equation we used H as a shorthand for D (\bar{B}) when Q = c (b). These relations are textbook knowledge in the inclusive fragmentation case ($b_T = 0$) [107]. Our analysis shows, for the first time, that they hold without modification and point by point in the distribution when resolving the hadron transverse momentum.

Collins TMD FF: A naive expectation from heavy-quark spin symmetry might be that the Collins FF should be suppressed by 1/m because it encodes a correlation between the initial quark transverse polarization vector and the transverse momentum of hadronic final-state radiation. In the case of light quarks, this correlation arises directly from the nonperturbative dynamics of the QCD Lagrangian, as illustrated in figure 6.2 (a), but in the heavy-quark case it naively seems to require a suppressed magnetic interaction with the heavy-quark spin. We will now see that this

is not the case. As illustrated in figure 6.2 (b), the angle between the final-state heavy-quark and light transverse polarization vectors (i.e, the relative phase between their helicity states) determines which hadron in the spin symmetry multiplet is produced, even without a dynamical heavy-quark spin interaction taking place. Reconstructing this information experimentally thus induces a correlation between the heavy-quark and the light spin state. Crucially, spin symmetry ensures that the final-state heavy-quark spin state is identical to the one it was prepared in. The light spin state in turn is in general correlated with the transverse momentum k_{\perp} of hadronic final-state radiation, since they both arise from the same nonperturbative dynamics of the light degrees of freedom, leading to a Collins effect at the leading order in 1/m. To illustrate this, it is again instructive to consider the case of the pseudoscalar meson,

$$s_{\ell} = 1/2, \ s_{H} = 0: \quad \chi_{1,H}^{\perp}(b_{T}) = \frac{1}{4} \left[\rho_{\ell,-+}(b_{\perp}) - \rho_{\ell,+-}(b_{\perp}) \right]$$
 (6.21)

As expected, the Collins FF in the heavy-quark limit contains information about the strength of the interference, and hence the relative nonperturbative phases, of amplitudes for different light helicities.

As a corollary, we conclude that the Collins FF must vanish at leading order in 1/m when summing over all the hadrons in the spin symmetry multiplet,

$$\sum_{H \in M_{\ell}} \chi_{1,H}^{\perp}(b_T) = 0. \tag{6.22}$$

Concretely, this means that the Collins FF vanishes altogether for $s_{\ell} = 0$ baryons, $\chi_{1,\Lambda_Q} = 0$. For $s_{\ell} = 1/2$ using the same notation as in eq. (6.20), the explicit relation is

$$s_{\ell} = \frac{1}{2} : \qquad \chi_{1,H}^{\perp}(b_T) + \chi_{1,H^*}^{\perp}(b_T) = 0.$$
 (6.23)

Discussion: The spin symmetry relations in eqs. (6.20) and (6.23) are the main results of this section. They hold for all values of b_T , which means that they also hold point by point in k_T upon Fourier transform. Furthermore, they are unaffected by renormalization, as we discuss in the next section. This makes them substantially stronger than the known sum rules for relativistic TMD fragmentation functions. For the light-quark Collins function in particular, the Schäfer-Teryaev sum rule [295] has only been rigorously proven [296] in the bare case.

Relation to bHQET fragmentation probabilities for $\Lambda_{\rm QCD} \ll k_T$

An important property of the TMD fragmentation factors we defined above is their limiting behavior as $k_T \gg \Lambda_{\rm QCD}$ or, equivalently, $b_T \to 0$. In this limit, the unpolarized TMD fragmentation factor $\chi_{1,H}$ is related to the total probability χ_H for the quark to fragment into H, which has previously been analyzed in HQET [285–287],

$$\chi_{1,H}(b_T, \mu, \rho) = C_1(b_T, \mu, \rho) \chi_H + \mathcal{O}(\Lambda_{QCD}^2 b_T^2).$$
(6.24)

where the matrix-element definition of χ_H [288] is equal to $\chi_{1,H}(b_T=0)$ at the bare level,

$$\chi_H \equiv \frac{1}{4N_c} \operatorname{Tr} \operatorname{tr} \oint_{\mathcal{X}} \left\langle 0 \middle| W^{\dagger}(0) h_v(0) \middle| H_v X \right\rangle \left\langle H_v X \middle| \bar{h}_v W \middle| 0 \right\rangle. \tag{6.25}$$

Because χ_H is not renormalized [292], we generally expect a perturbative Wilson coefficient $C_1(b_T, \mu, \zeta) = 1 + \mathcal{O}(\alpha_s)$ to appear in eq. (6.24) at the renormalized level from integrating out

partonic physics at the scale $\mu \sim k_T$. Eq. (6.24) can be considered the leading term of a twist-like expansion of $\chi_{1,H}(b_T)$ in $\Lambda_{\rm QCD}b_T$ at leading order in the strong coupling.¹ In eq. (6.24) we also assumed without detailed proof that corrections to this relation are quadratic in b_T based on the azimuthal symmetry of $\chi_{1,H}(b_T)$.

In contrast to eq. (6.24), the Collins TMD fragmentation factor $\chi_{1,H}^{\perp}$ must vanish at least linearly as $b_T \to 0$ because there is no leading bHQET matrix element it could match onto in this limit.

6.2.4 Matching TMD FFs onto bHQET for $\Lambda_{\rm QCD} \ll m \lesssim k_T$

We next consider case (b) in figure 6.1. In this regime, the transverse and longitudinal momentum distributions are determined by dynamics at the scale $\mu \sim m \sim k_T$ and are fully perturbative. The nonperturbative dynamics in this case are encoded in bHQET matrix elements that involve additional gluon fields or derivatives and that can be nonlocal along the lightcone, but in contrast to the previous section are local in the transverse direction. Similar to a standard twist expansion, these bHQET matrix elements are categorized by their mass dimension, which determines their scaling as $\Lambda_{\rm QCD} \ll m, k_T$, i.e., their mass dimension $\sim \Lambda_{\rm QCD}^n$ is compensated by powers of b_T or 1/m in the Wilson coefficient. This story plays out differently for the unpolarized vs. the Collins TMD FF, which scale as $\mathcal{O}(1)$ and $\mathcal{O}(\Lambda_{\rm QCD} b_T)$, respectively, so we will go through the two cases separately in the following. We note that the expansion of TMD FFs in terms of bHQET operators differs from a standard twist expansion insofar as the HQET field h_v encoding the interactions with the heavy valence quark remains present in all low-energy matrix elements.

Unpolarized TMD FF

For the unpolarized TMD FF, the unique bHQET matrix element that can arise in the infrared at the leading order in 1/m is the total fragmentation probability χ_H as defined in eq. (6.25):

$$D_{1H/Q}(z_H, b_T, \mu, \zeta) = d_{1Q/Q}(z_H, b_T, \mu, \zeta) \chi_H + \mathcal{O}\left(\frac{\Lambda_{\text{QCD}}}{m}\right) + \mathcal{O}(\Lambda_{\text{QCD}}b_T). \tag{6.26}$$

Importantly, we have again made use of the assumption in eq. (6.2) that we are sufficiently far away from (or have fully integrated over) the endpoint regime $z_H \to 1$, as otherwise there would be a nontrivial bHQET shape function on the right-hand side [287, 288]. The unique matching coefficient of χ_H , which we dub the partonic heavy-quark TMD FF $d_{1Q/Q}(z, b_T, \mu, \zeta)$, is a new object that, to our knowledge, appears in our analysis for the first time.² It is independent of the precise hadronic final state, carries the exact dependence on $b_T m \sim 1$, and can be calculated perturbatively by evaluating eqs. (2.182) and (2.185) for partonic final states including at least one heavy quark, i.e.,

$$d_{1Q/Q}(z_H, b_T) = \operatorname{tr}\left[\frac{\rlap{/}{n}}{2} \Delta_{Q/Q}(z_H, b_\perp)\right] = \delta(1 - z_H) + \mathcal{O}(\alpha_s). \tag{6.27}$$

¹It is well known that the formal OPE of relativistic fragmentation functions is ambiguous due to an unconstrained choice of boundary condition at lightcone infinity [297, 298]. While this fundamental issue remains present here, it is interesting to ask whether the case of bHQET TMD fragmentation factors, which are Wilson loops, can provide additional insight into this issue.

²Curiously, the perturbative transverse dynamics of heavy-quark fragmentation $\bar{b} \to B_c$ have previously been evaluated in refs. [299,300]. The complete tree-level result given in the first reference, which starts at $\mathcal{O}(\alpha_s^2)$, can be considered a very specific subset of the NNLO corrections to the TMD FF we define here if we sum over final states. If we tag on the charm instead, their result corresponds to a different perturbative TMD FF $d_{1\,b\bar{c}/b} \sim \alpha_s^2$ whose renormalization, by our analysis, is governed by standard (massive) TMD evolution.

Its rapidity renormalization is governed by the Collins-Soper kernel of a theory with n_{ℓ} massless and one massive quark degree of freedom [205]. We perform a dedicated NLO calculation of $d_{1Q/Q}(z, b_T, \mu, \zeta)$ in chapter 7. Since the dependence on the hadronic final state is purely encoded in χ_H , which satisfies the same spin symmetry relations as in eq. (6.20), we conclude that the unpolarized heavy-quark TMD FF satisfies

$$D_{1H/Q} = \frac{1}{3} D_{1H^*/Q} \,, \tag{6.28}$$

for all values of b_T (or k_T), including $1/b_T \gtrsim m$, up to corrections of $\mathcal{O}(\Lambda_{\rm QCD}/m)$.

Eq. (6.26) continues to be valid for $k_T \gg m$, but features large perturbative logarithms of $b_T m \ll 1$ in this limit. Their resummation is enabled by further factorizing the physics at those two scales. To do so, we can first match the heavy-quark TMD FF onto twist-2 heavy-quark collinear FFs at the scale $\mu \sim m$ [301],

$$D_{1H/Q}(z_H, b_T, \mu, \zeta) = \frac{1}{z_H^2} \sum_i \int \frac{\mathrm{d}z}{z} \, \mathcal{J}_{i/q}(z, b_T, \mu, \zeta) \, D_{H/i}(\frac{z_H}{z}, \mu) + \mathcal{O}(m^2 b_T^2) \,, \tag{6.29}$$

where the sum runs over $i=q,\bar{q},g$. This matching takes the same form as the standard matching of light-quark TMD FFs onto twist-2 FFs at $\mu \sim \Lambda_{\rm QCD}$, except that the highest IR scale here is given by m. The Wilson coefficients $\mathcal{J}_{i/q}(z,b_T,\mu,\zeta)$ encode the perturbative process $q\to i$ in a theory with $n_\ell+1$ massless flavors at the scale $\mu\sim k_T$, with the quark retaining a fraction z of the parent's lightcone momentum, and are known to N³LO [302,303]. In a second step, we perform the well-known [285–288] matching of the collinear FF of a massive quark onto bHQET to separate $\Lambda_{\rm QCD}\ll m$,

$$D_{H/i}(z_H, \mu) = d_{Q/i}(z_H, \mu) \chi_H + \mathcal{O}\left(\frac{\Lambda_{\text{QCD}}}{m}\right), \qquad (6.30)$$

where $d_{Q/i}(z_H, \mu)$ is the perturbative collinear heavy-quark FF for $i \to Q$ [292], which is known to NNLO [304, 305]. Combining eqs. (6.29) and (6.30) and comparing to eq. (6.26), we conclude that the perturbative ingredients are related by

$$d_{1Q/Q}(z_H, b_T, \mu, \zeta) = \frac{1}{z_H^2} \sum_i \int \frac{\mathrm{d}z}{z} \, \mathcal{J}_{i/Q}(z, b_T, \mu, \zeta) \, d_{Q/i}\left(\frac{z_H}{z}, \mu\right) + \mathcal{O}(m^2 b_T^2) \,. \tag{6.31}$$

This refactorization condition for $d_{1Q/Q}$ can serve as a cross check on future perturbative calculations, and in addition enables resumming logarithms of $k_T/m \gg 1$.

Collins TMD FF

To identify the low-energy bHQET matrix element that the Collins TMD FF matches onto in the limit $\Lambda_{\rm QCD} \ll m \sim k_T$, we use a two-step matching procedure formally valid for the hierarchy $\Lambda_{\rm QCD} \ll m \ll k_T$. (We will later show that the result is correct for either hierarchy.) As for the unpolarized TMD FF above, this lets us make use of well-known results for the matching of light-quark TMD FFs onto collinear FFs, which we can then further match onto bHQET.

We start from the diagrammatic small- b_T expansion of the bare Collins TMD FF for light quarks, which is valid for $\Lambda_{\rm QCD} \ll k_T$ and given by $[177, 178, 306]^3$

$$b_T M_h H_{1h/q}^{\perp(1)}(z_h, b_T) = b_T \hat{H}_{h/q}(z_h) + \mathcal{O}(\alpha_s) + \mathcal{O}(\Lambda_{\text{QCD}}^2 b_T^2),$$
 (6.32)

³In the literature, this relation is more commonly given as a tree-level equality between $\hat{H}_{h/q}$ and a weighted k_T integral over the bare momentum-space Collins FF. Using eq. (6.44) and integrating by parts, it is easy to

where $\hat{H}_{h/q}$ is a twist-3 collinear fragmentation matrix element at the scale $\mu \sim \Lambda_{\rm QCD}$.

We now consider the heavy-quark Collins FF and at first assume the hierarchy $\Lambda_{\rm QCD} \ll m \ll k_T$. For the matching at the scale $\mu \sim k_T$, the mass is an infrared scale, and thus the twist expansion in eq. (6.32) immediately carries over. The collinear matrix element $\hat{H}_{H/Q}$ takes the same form as before, but is now defined at the scale $\mu \sim m$. To implement the separation of scales $\Lambda_{\rm QCD} \ll m$, we match $\hat{H}_{H/Q}$ onto bHQET. At tree level, this amounts to a replacement of the quark fields as in eq. (6.3), and after expanding the momentum-conserving phase results in

$$\hat{H}_{H/Q}(z_H) = \delta(1 - z_H) \chi_{H,G} + \mathcal{O}(\alpha_s) + \mathcal{O}\left(\frac{1}{m}\right), \tag{6.33}$$

where $\chi_{H,G} \sim \Lambda_{\rm QCD}$ is a novel subleading bHQET matrix element. Similar to the total fragmentation probability χ_H defined in eq. (6.25), $\chi_{H,G}$ no longer depends on b_{\perp} , but is simply a constant that depends on the identified hadron H.

In the last step, we combine eqs. (6.32) and (6.33) to arrive at our final result for the tree-level matching of the heavy-quark Collins TMD FF onto bHQET:

$$b_T M_H H_{1 H/Q}^{\perp (1)}(z_H, b_T) = \delta(1 - z_H) b_T \chi_{H,G} + \mathcal{O}(\alpha_s) + \mathcal{O}(\Lambda_{\text{QCD}}^2).$$
 (6.34)

Because this derivation assumed $\Lambda_{\rm QCD} \ll m \ll k_T$, eq. (6.34) a priori is only valid up to power corrections in mb_T . However, since we found a nonzero result at our tree-level working order and power corrections in mb_T can only arise from real radiation in the calculation of the Wilson coefficient, eq. (6.34) as written also holds when integrating out both scales simultaneously. We note that additional low-energy matrix elements will in general be generated when performing the matching at higher orders in α_s , but leave a dedicated construction of the basis of bHQET operators at this order in $\Lambda_{\rm QCD}$ to future work.

Conversely, $\chi_{H,G}$ must vanish when summing over all hadrons in the spin symmetry multiplet M_{ℓ} ,

$$\sum_{H \in M_{\ell}} \chi_{H,G} = 0. \tag{6.35}$$

Combining these results at large $k_T \sim m$ with those in eq. (6.23) we conclude that the Collins TMD FF satisfies the following relations for all values of b_T (or k_T),

$$H_{1H/Q}^{\perp} = -H_{1H^*/Q}^{\perp} \,, \tag{6.36}$$

which we have proven here up to corrections of $\mathcal{O}(\Lambda_{\rm QCD}/m)$ and up to radiative corrections at the scale $\mu \sim k_T \sim m$ for large k_T .

6.2.5 Consistency between regimes for $\Lambda_{\rm QCD} \ll k_T \ll m$

Our results in the previous two sections share a common domain of validity when the transverse dynamics are already perturbative, $\Lambda_{\rm QCD} \ll k_T$, but still subject to heavy-quark symmetry, $k_T \ll m$. In this section we analyze the consistency relations that arise from this overlap and relate the perturbative bHQET fragmentation factors to the partonic heavy-quark TMD FFs.

see that this reduces to the derivative of the b_T -space Collins FF at $b_T = 0$. The $\mathcal{O}(\alpha_s)$ corrections to eq. (6.32) were evaluated at finite $k_T > 0$ in ref. [306] and involve twist-3 matrix elements that depend on two independent momentum fractions and reduce to $\hat{H}_{h/q}$ in certain limits by use of the equation of motion. We anticipate that matching these more general matrix elements onto bHQET will reduce the number of independent (residual) momenta to one because the heavy-quark momentum is fixed.

We start with the unpolarized case. Comparing eqs. (6.13) and (6.24), which are valid for $\Lambda_{\rm QCD} \lesssim k_T$, to eq. (6.26), valid for $k_T \lesssim m$, we find the following all-order refactorization relation for the partonic heavy-quark TMD FF in the limit $k_T \ll m$,

$$d_{1Q/Q}(z, b_T, \mu, \zeta) = \delta(1 - z) C_m(m, \mu, \zeta) C_1\left(b_T, \mu, \frac{\sqrt{\zeta}}{m}\right) + \mathcal{O}\left(\frac{1}{b_T m}\right). \tag{6.37}$$

Here we have canceled off the common nonperturbative factors of χ_H . To interpret the z dependence, eq. (6.37) says that counting $1-z\sim 1$, $d_{1Q/Q}$ must approach $\delta(1-z)$ up to an overall factor at the distributional level for $b_Tm\to\infty$, i.e., all Mellin moments of $d_{1Q/Q}$ must become equal in this limit. Eq. (6.37) provides a powerful consistency check of perturbative calculations of $d_{1Q/Q}$ in chapter 7. It also enables the resummation of large perturbative logarithms of $k_T/m\ll 1$, complementing the factorized result in eq. (6.31) for the opposite limit. For the Collins TMD FF we compare eq. (6.13) to eq. (6.34) and use $C_m=1+\mathcal{O}(\alpha_s)$. Canceling off the z dependence, which is trivial at tree level, this yields

$$\chi_{1,H}^{\perp}(b_T,\mu,\rho) = \chi_{H,G} b_T + \mathcal{O}(\alpha_s) + \mathcal{O}(\Lambda_{QCD}^2 b_T^2), \qquad (6.38)$$

which can be interpreted as the leading linear term in a small- b_T expansion of $\chi_{1,H}^{\perp}$, as anticipated in section 6.2.3. As for the Collins function at $k_T \sim m$, we leave a dedicated higher-order matching calculation to future work, which will involve nontrivial Wilson coefficients integrated against at least one additional $\mathcal{O}(\Lambda_{\rm QCD})$ bHQET matrix element.

6.2.6 Model functions and numerical results

For our numerical results we will assume a simple Gaussian model for the unpolarized TMD fragmentation factor,

$$\chi_{1,H}(b_T, \mu_0, \rho_0) = \chi_H \exp\left(-\kappa_H^2 b_T^2\right),$$
(6.39)

where $\kappa_H \sim \Lambda_{\rm QCD}$ has units of GeV. Eq. (6.39) is valid at initial scales $\mu_0 \sim m \, \rho_0 \sim 1/b_T$ of the TMD evolution. We apply a μ^* prescription [49,220] (also known as a "local" b^* prescription) starting at $\mathcal{O}(b_T^4)$ to ensure that μ_0 stays perturbative without polluting nonperturbative corrections at $\mathcal{O}(\Lambda_{\rm QCD}^2 b_T^2)$ [307],

$$\mu_0 = \left(\frac{b_0^4}{b_T^4} + \mu_{\min}^4\right)^{1/4} = \frac{b_0}{b_T} \left[1 + \mathcal{O}(\mu_{\min}^4 b_T^4) \right], \tag{6.40}$$

where $b_0 = 2e^{-\gamma_E} \approx 1.12292$ and we take $\mu_{\min} = 1 \,\mathrm{GeV}$. We take $\zeta_0 \equiv m\rho_0$ to always be equal to its canonical value, $\zeta_0 = (b_0/b_T)^2$. We then use leading-logarithmic (LL) perturbative TMD evolution $U_q(\mu_0, \zeta_0, \mu, \zeta)$ to evolve eq. (6.39) to the overall scales $\mu \sim \sqrt{\zeta} \sim Q$, with Q the hard scattering energy.⁴ This order is sufficient for the exploratory phenomenology we have in mind, and in particular lets us use TMD evolution and β functions in QCD with $n_f = 5$ massless flavors at all scales since the quark decoupling only induces next-to-leading logarithms of $b_T m$. Specifically, we ignore the decoupling relations and NNLL power-like secondary quark mass corrections to the Collins-Soper kernel $\gamma_{\zeta}^q(b_T, \mu)$ that were determined in ref. [205]. We also ignore nonperturbative contributions to the Collins-Soper kernel, since they are orthogonal to

⁴We refer to ref. [307] for the details of our evolution setup.

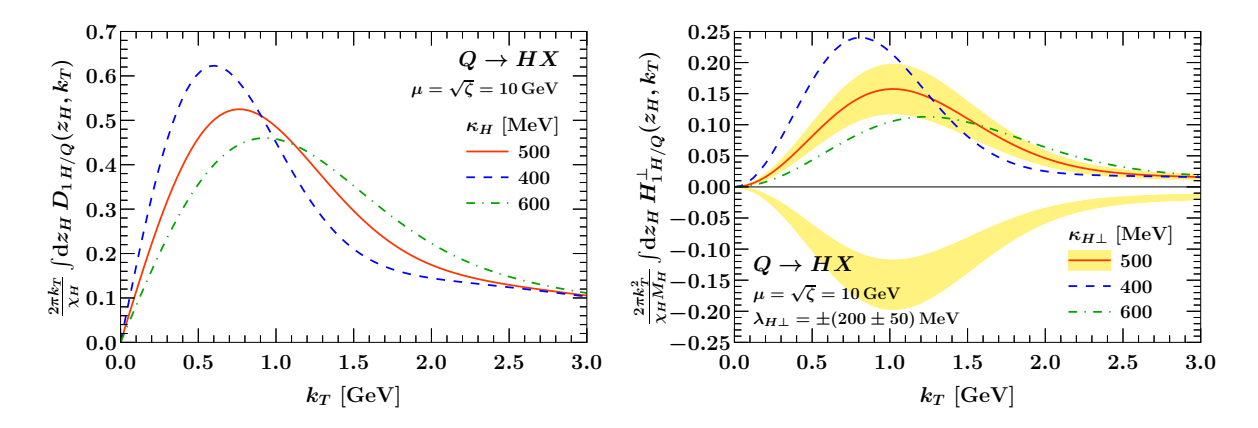


Figure 6.3: Unpolarized heavy-quark (left) and Collins TMD fragmentation functions (right) as a function of k_T and integrated over z_H . All results are normalized to the total fragmentation probability χ_H . The yellow band in the case of the Collins function corresponds to the indicated variations of the sign and magnitude of $\lambda_{H\perp}$. These results are universal for charm and bottom quarks; see the text for details.

the effects we are interested in here. Overall, this results in the following expression for the evolved unpolarized heavy-quark TMD FF,

$$\int_{z_{\text{cut}}} dz_H \, D_{1H/Q}(z_H, b_T, \mu, \zeta) = \chi_H \exp\left(-\kappa_H^2 b_T^2\right) U_q(\mu_0, \zeta_0, \mu, \zeta) \,, \tag{6.41}$$

$$U_q(\mu_0, \zeta_0, \mu, \zeta) = \exp\left[\frac{1}{2}\gamma_{\zeta}^q(b_T, \mu_0) \ln \frac{\zeta}{\zeta_0}\right] \exp\left[\int_{\mu_0}^{\mu} \frac{\mathrm{d}\mu'}{\mu'} \gamma_{\mu}^q(\mu', \zeta)\right] ,$$

where for definiteness we considered the integral over $z_{\rm cut} \leq z_H \leq 1$. To our working order, the right-hand side of eq. (6.41) is independent of $z_{\rm cut}$ as long as $1 - z_{\rm cut} \sim 1$ in order to satisfy eq. (6.2), and also holds for any truncated z_H moment of the TMD FF. Note that the single-parameter model in eq. (6.41) is also accurate at large $k_T \gtrsim m$, cf. eq. (6.26), where it reduces to χ_H and thus is correct up to radiative corrections.

We assume a similar model for the Collins TMD fragmentation factor, but have to account for the suppression at small b_T by modifying the Gaussian,

$$\chi_{1,H}^{\perp}(b_T, \mu_0, \rho_0) = \chi_H \,\lambda_{H\perp} b_T \, \exp\left(-\kappa_{H\perp}^2 b_T^2\right),$$
 (6.42)

where we find it convenient to express the overall effect strength in terms of $\lambda_{H\perp} = \chi_{H,G}/\chi_H \sim \Lambda_{\rm QCD}$, i.e., relative to the total fragmentation probability χ_H . The parameter $\kappa_{H\perp} \sim \Lambda_{\rm QCD}$ controls the relative impact of higher power corrections and is in general distinct from κ_H in eq. (6.39). Combining this with NLL $n_f = 5$ TMD evolution as above, we find, for the evolved heavy-quark Collins function in position space,

$$b_T M_H \int_{z_{\text{cut}}} dz_H H_{1H/Q}^{\perp(1)}(z_H, b_T, \mu, \zeta) = \chi_H \lambda_{H\perp} b_T \exp\left(-\kappa_{H\perp}^2 b_T^2\right) U_q(\mu_0, \zeta_0, \mu, \zeta).$$
 (6.43)

Taking appropriate Bessel integrals [181], we finally transition to momentum space,

$$D_{1H/Q}(z_H, k_T, \mu, \zeta) = \frac{1}{2\pi} \int_0^\infty db_T \, b_T \, J_0(b_T k_T) \, D_{1H/Q}(z_H, b_T, \mu, \zeta) \,,$$

$$\frac{k_T}{M_H} H_{1H/Q}^{\perp}(z_H, k_T, \mu, \zeta) = \frac{M_H}{2\pi} \int_0^\infty db_T \, b_T^2 J_1(b_T k_T) \, H_{1H/Q}^{\perp(1)}(z_H, b_T, \mu, \zeta) \,. \tag{6.44}$$

To evaluate the TMD evolution and the Bessel integrals, we use the numerical implementation of TMD anomalous dimensions, QCD renormalization-group solutions, and double-exponential oscillatory integration in SCETlib [224].

Our results for the z_H -integrated heavy-quark TMD FFs are shown as a function of k_T for different values of the model parameters in figure 6.3. We use $\alpha_s(m_Z) = 0.118\,\text{GeV}$ as the input value for the strong coupling. We note that due to heavy quark flavor symmetry, the charm and bottom-quark TMD FFs are exactly equal at small $k_T \ll m$. In other words, they only depend on the universal Gaussian parameters κ_H (for the unpolarized TMD FF), $\kappa_{H\perp}$ (for the Collins TMD FF), and the Collins effect strength $\lambda_{H\perp}$. At large $k_T \sim m$, the TMD FFs remain independent of the heavy quark mass up to radiative corrections of $\mathcal{O}(\alpha_s)$, which we ignore at our LL working order. These plots are thus identical for both flavors we consider. We point out that the Collins function can in general take any sign, as indicated by the yellow band scanning various values of the effect strength $\lambda_{H\perp}$. The effect of varying the size of higher-power corrections $(\kappa_H, \kappa_{H\perp})$ decreases as k_T increases for both TMD FFs, as expected.

6.3 Polarized heavy-quark TMD PDFs

6.3.1 Calculational setup

In this section we consider the production of a heavy quark Q with pole mass $m = m_c, m_b \gg \Lambda_{\rm QCD}$ from light partons within a polarized nucleon N. The nucleon has momentum

$$P_N^{\mu} = P_N^{-} \frac{n^{\mu}}{2} + \frac{M_N^2}{P_N^{-}} \frac{\bar{n}^{\mu}}{2} \,, \tag{6.45}$$

with $P_N^- \gg P_N^+ = M_N^2/P_N^-$ in the rest frame of the hard scattering that the heavy quark participates in. This time, we are interested in the transverse momentum k_{\perp} of the heavy quark with respect to the nucleon beam axis, which is again Fourier conjugate to the transverse spacetime separation b_{\perp} between quark fields. We recall the spin decomposition of the TMD quark-quark correlator from section 2.6.2 in terms of scalar TMD PDFs

$$\Phi_{Q/N}(x > 0, k_{\perp}) = \left\{ f_{1\,Q/N}(x, k_T) + g_{1L\,Q/N}(x, k_T) \, S_L \gamma_5 + h_{1L\,Q/N}^{\perp}(x, k_T) \, S_L \gamma_5 \frac{\not k_{\perp}}{M_N} + i h_{1\,Q/N}^{\perp}(x, k_T) \, \frac{\not k_{\perp}}{M_N} + \left(\text{terms} \propto S_{\perp} \right) \right\} \frac{\not h}{4} \,. \tag{6.46}$$

As we will see in the next section, the terms proportional to the transverse nucleon polarization S_{\perp} vanish for heavy quarks to all orders in the strong coupling when matched onto the leading (twist-2) collinear PDFs. We will also find that the twist-2 matching for the Boer-Mulders function h_1^{\perp} vanishes at $\mathcal{O}(\alpha_s)$. The remaining TMD PDFs on the first line, for which we will find nonzero results at $\mathcal{O}(\alpha_s)$, are the unpolarized TMD PDF f_1 , the helicity TMD PDF g_{1L} , and the so-called worm-gear L function h_{1L}^{\perp} ; the latter will be of particular significance, and encodes the production of a transversely polarized quark from a linearly polarized nucleon. For

reference, the explicit Hankel transforms relating scalar TMDs in b_T and k_T space read⁵

$$f_{1}(x, k_{T}) = \int \frac{\mathrm{d}b_{T}}{2\pi} b_{T} J_{0}(k_{T}b_{T}) f_{1}(x, b_{T}) ,$$

$$\frac{k_{T}}{M_{N}} h_{1}^{\perp}(x, k_{T}) = M_{N} \int \frac{\mathrm{d}b_{T}}{2\pi} b_{T}^{2} J_{1}(b_{T}k_{T}) h_{1}^{\perp(1)}(x, b_{T}) ,$$

$$g_{1L}(x, k_{T}) = \int \frac{\mathrm{d}b_{T}}{2\pi} b_{T} J_{0}(k_{T}b_{T}) g_{1L}(x, b_{T}) ,$$

$$\frac{k_{T}}{M_{N}} h_{1L}^{\perp}(x, k_{T}) = M_{N} \int \frac{\mathrm{d}b_{T}}{2\pi} b_{T}^{2} J_{1}(b_{T}k_{T}) h_{1L}^{\perp(1)}(x, b_{T}) .$$

$$(6.47)$$

6.3.2 Matching onto twist-2 collinear PDFs

Heavy-quark TMD PDFs are different from their TMD FF counterparts because the heavy quark cannot be part of the initial-state nucleon wave function at the scale $\mu \sim \Lambda_{\rm QCD}$ at leading power in $\Lambda_{\rm QCD}/m$, whereas in the fragmentation case the heavy quark is always part of the final-state heavy hadron until its eventual weak decay. This means that heavy quarks must be pair-produced in initial-state gluon splittings at the scale $\mu \sim m$ instead. In particular, this means there is at least one perturbative emission with transverse momentum $\gtrsim m$ setting the scale of $k_T \gtrsim m$, while the region of $k_T \ll m$ can only be populated by several emissions with small net recoil, which is a power-suppressed configuration. In field theory terms, this means that heavy-quark TMD PDFs can be computed by perturbatively matching them onto collinear twist-2 nucleon PDFs in a theory with n_{ℓ} light flavors, which are the only nonperturbative piece of information in this case. The matching onto twist-2 collinear PDFs is well developed for light quark and gluon TMDs, with notable results including all unpolarized quark matching coefficients through $\mathcal{O}(\alpha_s^3)$ [211,212] and results for polarized TMDs through $\mathcal{O}(\alpha_s^2)$ [311,312], and many of the following steps are standard, see e.g. [147]. Likewise, the $\mathcal{O}(\alpha_s)$ matching of the unpolarized heavy-quark TMD PDF onto gluon collinear PDFs has been given in refs. [205, 301]. We nevertheless aim for a self-contained description, giving us the opportunity to point out the ways in which (polarized) heavy-quark TMD PDFs behave differently.

The bare light-quark and gluon twist-2 collinear correlators are defined as

$$\Phi_{q/N}^{\alpha\alpha'}(x) = \int \frac{\mathrm{d}b^{+}}{4\pi} e^{-\mathrm{i}b^{+}(xP_{N}^{-})/2} \langle N | \bar{\psi}_{q}^{\alpha'}(b) W(b,0) \psi_{q}^{\alpha}(0) | N \rangle,
\Phi_{g/N}^{\mu\nu}(x) = \int \frac{\mathrm{d}b^{+}}{4\pi} e^{-\mathrm{i}b^{+}(xP_{N}^{-})/2} \langle N | F^{-\mu}(b) W(b,0) F^{-\nu}(0) | N \rangle,$$
(6.48)

where $b \equiv (0, b^+, 0)$ in this case and W(b, 0) denotes a straight Wilson line segment. The collinear

⁵We continue to distinguish momentum and position-space functions by their argument. As before, the superscript (1) on the b_T -space functions indicates a b_T derivative and that is specifically required due to the conventional normalization to the hadron mass [181].

⁶Power corrections of this kind, which are known as "intrinsic charm" and have received substantial recent interest on the collinear PDF side [308,309], would be an interesting subject to explore in the TMD case in the future. Very recently, the TMD PDFs for charm quarks within Λ_c baryons, which are leading valence contributions and do not have to be produced from gluons, have been evaluated in a lightfront Hamiltonian model in ref. [310]; while these are phenomenologically inaccessible, it would be interesting to analyze these valence dynamics in the heavy-quark limit as we did for TMD FFs in section 6.2.

correlators are conventionally decomposed as [147]

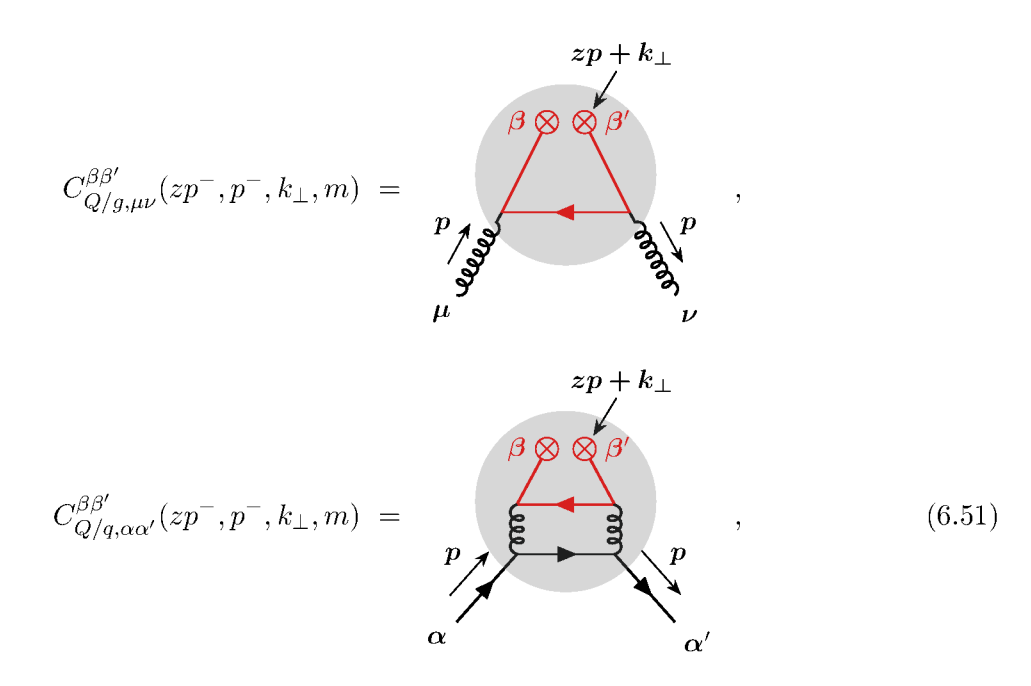
$$\Phi_{q/N}(x > 0) = \left\{ f_{q/N}(x) + g_{q/N}(x) S_L \gamma_5 + h_{q/N}(x) \gamma_5 \mathcal{S}_\perp \right\} \frac{n}{4},
\Phi_{g/N}^{\mu\nu}(x > 0) = -\frac{g_\perp^{\mu\nu}}{2} f_{g/N}(x) + \frac{i\epsilon_\perp^{\mu\nu}}{2} g_{g/N}(x) S_L.$$
(6.49)

in terms of the unpolarized (helicity) quark and gluon PDFs $f_{i/N}$ ($g_{i/N}$) and the transversity quark PDF $h_{q/N}$. The contribution $\propto S_{\perp}$ to the gluon correlator (i.e., the transversity gluon PDF) vanishes identically for spin-0 and spin-1/2 hadrons in the initial state due to helicity conservation [313].

The matching relation between heavy-quark TMD PDFs and twist-2 collinear PDFs holds at the operator level, and constitutes the leading term in the OPE of the former. Taking nucleon matrix elements of the bare operators, the relation for general spin indices reads

$$\Phi_{Q/N}^{\beta\beta'}(x,k_{\perp}) = \int \frac{\mathrm{d}p^{-}}{p^{-}} C_{Q/g,\mu\nu}^{\beta\beta'}(xP_{N}^{-},p^{-},k_{\perp},m) \Phi_{g/N}^{\mu\nu} \left(\frac{p^{-}}{P_{N}^{-}}\right)
+ \sum_{q} \int \frac{\mathrm{d}p^{-}}{p^{-}} C_{Q/q,\alpha\alpha'}^{\beta\beta'}(xP_{N}^{-},p^{-},k_{\perp},m) \Phi_{q/N}^{\alpha\alpha'} \left(\frac{p^{-}}{P_{N}^{-}}\right),$$
(6.50)

where p^- is the lightcone momentum carried by the light parton extracted from the collinear PDF and the sum runs over the n_ℓ light quark flavors. In pure dimensional regularization, the bare matching coefficients are given by the partonic diagrams



where $z = xP_N^-/p^-$ is the fraction of p^- injected into the hard scattering process and we have indicated the heavy quark lines in red. The gray-shaded circles denote the sum of all possible QCD diagrams with these external legs, including gluon attachments to the Wilson lines that are part of the operators indicated by \otimes . We have included the respective lowest-order diagram for illustration. As is standard, matching relations between individual scalar TMD and collinear PDFs follow by inserting eq. (6.49) into eq. (6.50) and tracing the resulting Dirac bispinors $(\dots)^{\beta\beta'}$ against the relevant Dirac structures.

Flavor conservation in QCD implies that a single fermion line has to connect the external light-quark states in eq. (6.51). It follows that contractions with the quark transversity PDF involve an odd number of Dirac matrices on the light-quark line and vanish to all orders, i.e., flavor conservation and chirality for light quark flavors imply that all terms $\propto S_{\perp}$ vanish at twist-2 level in eq. (6.46). This is distinct from e.g. the light-quark transversity TMD PDF, which receives a tree-level contribution from the transversity collinear PDF of the same flavor. As in the case of light-quark TMD PDFs, Lorentz covariance further implies that only unpolarized (helicity) collinear PDFs can contribute to the unpolarized and Boer-Mulders (helicity and worm-gear L) TMD PDFs, matching the dependence on S_L in the spin decomposition. These conclusions are not modified by the inclusion of the soft factor, the rapidity renormalization, and the UV renormalization of the TMD PDFs, all of which are orthogonal to the spin structure. They are likewise unaffected by the renormalization of the collinear PDFs, which acts autonomously on the unpolarized and longitudinally polarized sectors. Passing to renormalized objects, this altogether leaves us with the following four nontrivial matching relations for heavy-quark TMD PDFs onto collinear PDFs,

$$f_{1Q/N}(x, k_T, \mu, \zeta) = \sum_{j} \int \frac{\mathrm{d}z}{z} C_{Q/j}(z, k_T, m, \mu, \zeta) f_{j/N}(\frac{x}{z}, \mu),$$

$$\frac{k_T}{M_N} h_{1Q/N}^{\perp}(x, k_T, \mu, \zeta) = \sum_{j} \int \frac{\mathrm{d}z}{z} C_{Q_{\perp}/j}(z, k_T, m, \mu, \zeta) f_{j/N}(\frac{x}{z}, \mu),$$

$$g_{1LQ/N}(x, k_T, \mu, \zeta) = \sum_{j} \int \frac{\mathrm{d}z}{z} C_{Q_{\parallel}/j_{\parallel}}(z, k_T, m, \mu, \zeta) g_{j/N}(\frac{x}{z}, \mu),$$

$$\frac{k_T}{M_N} h_{1LQ/N}^{\perp}(x, k_T, \mu, \zeta) = \sum_{j} \int \frac{\mathrm{d}z}{z} C_{Q_{\perp}/j_{\parallel}}(z, k_T, m, \mu, \zeta) g_{j/N}(\frac{x}{z}, \mu). \tag{6.52}$$

These relations are the key result of this section, and hold up to power corrections in $\mathcal{O}(\Lambda_{\rm QCD}/k_T)$ and $\mathcal{O}(\Lambda_{\rm QCD}/m)$. Here the subscripts $\lambda, \lambda' = \varnothing, \parallel, \perp$ on $C_{Q_{\lambda}/j_{\lambda'}}(z, k_T, \mu, \zeta)$ label the polarization of the heavy quark and the light parton j, the sum runs over gluons and the n_{ℓ} flavors of light quarks and antiquarks, and we have included a factor of k_T/M_N on the left-hand side as needed to ensure that the matching coefficient is independent of the hadronic state. We have also changed integration variables from p^- in eq. (6.52) to z, exploiting the fact that projections of the matching coefficients onto good components can only depend on z by reparameterization invariance.

Note that in a crucial difference to the light-quark case, the heavy-quark worm-gear L TMD PDF, which involves an odd number of Dirac matrices on the heavy-quark line in eq. (6.51) is allowed at twist-2 level because the quark mass breaks chirality. The same is true for the Boer-Mulders function. In both cases, the original argument of ref. [314] why the twist-2 matching for these functions vanishes to all orders in the light-quark case critically relied on chirality. Conversely, the respective matching coefficients must vanish linearly as $m \to 0$ to afford the helicity flip,

$$\lambda = \varnothing, \parallel : \quad C_{Q_{\perp}/j_{\lambda}}(z, k_T, m, \mu, \zeta) \propto \frac{m}{k_T^3} + \mathcal{O}(m^2).$$
 (6.53)

Lastly, note that to all orders it is only the gluon PDF $f_g(x)$ and the quark singlet PDF $\sum_{i=q,\bar{q}} f_i(x)$ that contribute to the sum $f_{1Q/N} + f_{1\bar{Q}/N}$ due to the invariance of eq. (6.51) under the n_ℓ light flavor symmetry, and similarly for the two polarized cases. The difference $f_{1Q/N} - f_{1\bar{Q}/N}$ of heavy quark and antiquark TMD PDFs receives a nonzero contribution

proportional to $\sum_{i=q} f_i(x) - \sum_{i=\bar{q}} f_i(x)$ starting at $\mathcal{O}(\alpha_s^3)$ due to the relative orientation of the color flow along the fermion lines in eq. (6.51), as in the light-quark case [211, 302, 303]. Inverting the Hankel transforms in eq. (6.47), we find the b_T -space matching relations

$$f_{1Q/N}(x, b_{T}, \mu, \zeta) = \sum_{j} \int \frac{\mathrm{d}z}{z} C_{Q/j}(z, b_{T}, m, \mu, \zeta) f_{j/N}(\frac{x}{z}, \mu),$$

$$b_{T}M_{N} h_{1Q/N}^{\perp(1)}(x, b_{T}, \mu, \zeta) = \sum_{j} \int \frac{\mathrm{d}z}{z} C_{Q_{\perp}/j}(z, b_{T}, m, \mu, \zeta) f_{j/N}(\frac{x}{z}, \mu),$$

$$g_{1LQ/N}(x, b_{T}, \mu, \zeta) = \sum_{j} \int \frac{\mathrm{d}z}{z} C_{Q_{\parallel}/j_{\parallel}}(z, b_{T}, m, \mu, \zeta) g_{j/N}(\frac{x}{z}, \mu),$$

$$b_{T}M_{N} h_{1LQ/N}^{\perp(1)}(x, b_{T}, \mu, \zeta) = \sum_{j} \int \frac{\mathrm{d}z}{z} C_{Q_{\perp}/j_{\parallel}}(z, b_{T}, m, \mu, \zeta) g_{j/N}(\frac{x}{z}, \mu),$$

$$(6.54)$$

where the matching coefficients are given by $(n = 1 \text{ for } \lambda = \perp \text{ and } n = 0 \text{ otherwise})$

$$C_{Q_{\lambda}/j_{\lambda'}}(z, b_T, m, \mu, \zeta) = 2\pi \int dk_T \, k_T J_n(k_T b_T) \, C_{Q_{\lambda}/j_{\lambda'}}(z, k_T, m, \mu, \zeta) \,.$$
 (6.55)

For the dimensionless b_T -space matching coefficients, eq. (6.53) simply reads

$$\lambda = \varnothing, \|: \quad C_{O_{\perp}/j_{\lambda}}(z, b_T, m, \mu, \zeta) \propto mb_T + \mathcal{O}(m^2). \tag{6.56}$$

6.3.3 One-loop evaluation of matching coefficients

At $\mathcal{O}(\alpha_s)$, only the gluon diagram in eq. (6.51) is nonzero. We use standard QCD Feynman rules as well as

$$zp + k_{\perp}$$

$$\chi_{n,\omega} \otimes \chi_{n,k_{\perp}} = \delta(\omega - \ell^{-}) \delta^{(2)}(k_{\perp} - \ell_{\perp}) \Gamma, \qquad (6.57)$$

where $\omega = z p$ and Γ are the Dirac structures that project out the desired TMD PDF. In particular

$$\Gamma = \left\{ \frac{\vec{n}}{2}, \frac{1}{S_L} \frac{\vec{n}}{2} \gamma_5, \frac{M_N}{S_L} \frac{\vec{n}}{2} \frac{\vec{k}_{\perp}}{k_{\perp}^2} \gamma_5, M_N \epsilon^{\alpha \rho} \frac{\vec{n}}{2} \gamma_{\rho} \gamma_5 \frac{k_{\perp, \alpha}}{-k_{\perp}^2} \right\}, \tag{6.58}$$

for the unpolarized, the helicity, the Bœr-Mulders and the worm-gear-L functions. We find the leading-order result

$$C_{Q/g\,\mu\nu}^{\beta\beta'}(zp^{-},p^{-},k_{\perp},m) = \begin{array}{c} zp+k_{\perp} \\ \beta\otimes \beta' \\ p \\ \mu \end{array}$$

$$(6.59)$$

$$= -\frac{\mathrm{i}g^2}{2} \int \frac{\mathrm{d}^4 \ell}{(2\pi)^4} \, \delta(zp^- - p^- - \ell^-) \, \delta^{(2)}(k_\perp - p_\perp - \ell_\perp) \frac{[(\not p + \ell + m)\gamma_\mu(\ell + m)\gamma_\nu(\not p + \ell + m)]^{\beta\beta'}}{[(p + \ell)^2 - m^2 + \mathrm{i}0]^2 (\ell^2 - m^2 + \mathrm{i}0)} \,,$$

where $p = (p^-, 0, 0)$ is the momentum of the external gluon and ℓ is defined as indicated (in the direction of fermion flow).

Dotting eq. (6.59) into the gluon collinear PDF correlator in eq. (6.49) and projecting onto quark spin structures, we find individual momentum-space matching coefficients

$$C_{Q_{\lambda}/g_{\lambda'}}(z, k_T, m, \mu, \zeta) = \frac{\alpha_s(\mu)}{4\pi} C_{Q_{\lambda}/g_{\lambda'}}^{(1)}(z, k_T, m) + \mathcal{O}(\alpha_s^2).$$
 (6.60)

As an example, we calculate $C_{Q/g}(z, k_T, m)$ at $\mathcal{O}(\alpha_s)$ explicitly. The unpolarized TMD PDF matches onto the unpolarized collinear PDF and therefore therefore picks a $g_{\perp}^{\mu\nu}$ from the gluon polarization

$$C_{Q/g}(z, k_T, m) = -\frac{ig^2}{2} \left(-\frac{1}{2} g_{\perp}^{\mu\nu} \right) \int \frac{d^4\ell}{(2\pi)^4} \, \delta(zp^- - p^- - \ell^-) \, \delta^{(2)}(k_{\perp} - p_{\perp} - \ell_{\perp})$$

$$\times \frac{\text{Tr}\left[\frac{\rlap{/}m}{2} (\rlap{/}p + \rlap{/}\ell + m) \gamma_{\mu} (\rlap{/}\ell + m) \gamma_{\nu} (\rlap{/}p + \rlap{/}\ell + m)\right]}{[(p+\ell)^2 - m^2 + i0]^2 (\ell^2 - m^2 + i0)} \, .$$

As the ℓ^- and ℓ_\perp integrals are fixed by δ -functions, we can immediately solve them after taking the trace. The only non-trivial integral is the ℓ^+ integral which can be straightforwardly done by contours

$$C_{Q/g}(z, k_T, m) = -\frac{ig^2}{(2\pi)^4} \int d\ell^+ \frac{(z p^-)^2 \ell^+ + z p^- k_T^2 - m^2 p^- (1+z) - p^- k_T^2}{[z p^- \ell^+ - k_T^2 - m^2 + i0]^2 [\ell^+ p^- (z-1) - k_T^2 - m^2 + i0]}$$

$$= \frac{\alpha_s}{4\pi^2} \frac{k_T^2 (1 - 2z + 2z^2) + m^2}{(k_T^2 + m^2)^2}.$$
(6.61)

Then, the leading-order coefficient functions for all relevant TMD PDFs are given by

$$C_{Q/g}^{(1)}(z, k_T, m) = T_F \Theta(z)\Theta(1-z) \frac{2}{\pi} \frac{k_T^2 (1-2z+2z^2) + m^2}{(k_T^2 + m^2)^2},$$

$$C_{Q_{\perp}/g}^{(1)}(z, k_T, m) = 0,$$

$$C_{Q_{\parallel}/g_{\parallel}}^{(1)}(z, k_T, m) = T_F \Theta(z)\Theta(1-z) \frac{2}{\pi} \frac{k_T^2 (2z-1) + m^2}{(k_T^2 + m^2)^2},$$

$$C_{Q_{\perp}/g_{\parallel}}^{(1)}(z, k_T, m) = T_F \Theta(z)\Theta(1-z) \frac{4}{\pi} \frac{mk_T (z-1)}{(k_T^2 + m^2)^2}.$$
(6.62)

As a nontrivial check, we have confirmed that using massive SCET Feynman rules [315] results in the same expressions after performing the spin traces and integrating over the loop momentum. Note that the projection of the $\mathcal{O}(\alpha_s)$ twist-2 matching diagram onto the Boer-Mulders function remains zero even for finite quark masses. This is expected because the Boer-Mulders function is odd under time reversal [316], i.e., it changes sign depending on whether the Wilson lines in the operator point to the future (SIDIS) or the past (Drell-Yan). The diagram in eq. (6.59) does not yet feature gluon attachments to the Wilson lines that could resolve their direction, and thus its projection onto the Boer-Mulders function has to vanish. Starting at $\mathcal{O}(\alpha_s^2)$, the matching coefficient can in general receive nonzero contributions from the absorptive part of real-virtual diagrams because chirality is broken by the quark mass, and it would be interesting to investigate these contributions further.

Evaluating the inverse Hankel transforms in eq. (6.55), we find the position space matching coefficients

$$C_{Q_{\lambda}/g_{\lambda'}}(z, b_T, m, \mu, \zeta) = \frac{\alpha_s(\mu)}{4\pi} C_{Q_{\lambda}/g_{\lambda'}}^{(1)}(z, b_T m) + \mathcal{O}(\alpha_s^2),$$
 (6.63)

which at this order only depend on the dimensionless combination $b_T m$ and are given by

$$C_{Q/g}^{(1)}(z, b_T m) = T_F \Theta(z)\Theta(1-z) 4 \Big[(1-2z+2z^2) K_0(b_T m) + z(1-z) b_T m K_1(b_T m) \Big],$$

$$C_{Q_{\perp}/g}^{(1)}(z, b_T m) = 0,$$

$$C_{Q_{\parallel}/g_{\parallel}}^{(1)}(z, b_T m) = T_F \Theta(z)\Theta(1-z) 4 \Big[(2z-1) K_0(b_T m) + (1-z) b_T m K_1(b_T m) \Big],$$

$$C_{Q_{\perp}/g_{\parallel}}^{(1)}(z, b_T m) = T_F \Theta(z)\Theta(1-z) 4(z-1) b_T m K_0(b_T m),$$

$$(6.64)$$

where K_0 and K_1 are modified Bessel functions of the second kind. These are the main analytic results of this section. The unpolarized matching coefficient $C_{Q/g}^{(1)}$ has been computed long ago [301], and we agree with the b_T -space expression given in that reference as well as with the k_T -space result in ref. [205]. The results for the polarization-dependent matching coefficients are new.

6.3.4 Consistency with the light-quark limit

For $\Lambda_{\rm QCD} \ll m \ll k_T$, heavy-quark TMD PDFs can be determined using a two-step matching [205]. First, the TMD operators at the scale $\mu \sim k_T$ are matched onto collinear PDFs in a theory with $n_\ell + 1$ massless quark flavors, which results in the standard massless TMD matching coefficients. In a second step, the $n_\ell + 1$ -flavor PDFs are matched onto those in a theory with n_ℓ flavors at the scale $\mu \sim m$. At fixed order, this implies the following consistency relation for the unpolarized and linearly polarized massive TMD matching coefficients,

$$C_{Q/k}(z, b_T, m, \mu, \zeta) = \sum_{j} \int \frac{\mathrm{d}z'}{z'} C_{Q/j}(z', b_T, \mu, \zeta) \, \mathcal{M}_{j/k} \left(\frac{z}{z'}, m, \mu\right) + \mathcal{O}(m^2 b_T^2) \,, \tag{6.65}$$

$$C_{Q_{\parallel}/k_{\parallel}}(z, b_T, m, \mu, \zeta) = \sum_{j} \int \frac{\mathrm{d}z'}{z'} \, C_{Q_{\parallel}/j_{\parallel}}(z', b_T, \mu, \zeta) \, \mathcal{M}_{j_{\parallel}/k_{\parallel}} \left(\frac{z}{z'}, m, \mu\right) + \mathcal{O}(m^2 b_T^2) \,,$$

where $\mathcal{M}_{j_{\lambda}/k_{\lambda}}$ denotes the PDF matching function, the sum runs over all light degrees of freedom, and the subscript $\lambda = \emptyset$, \parallel again labels the polarization of the heavy quark and the light partons j and k. Perturbatively expanding the matching functions as

$$C_{i_{\lambda}/j_{\lambda}}(z',b_{T},\mu,\zeta) = \delta_{ij}\,\delta(1-z) + \sum_{n=1}^{\infty} \left(\frac{\alpha_{s}(\mu)}{4\pi}\right)^{n} C_{i_{\lambda}/j_{\lambda}}^{(n)}(z,b_{T},\mu,\zeta),$$

$$\mathcal{M}_{j_{\lambda}/k_{\lambda}}(z,m,\mu) = \delta_{jk}\,\delta(1-z) + \sum_{n=1}^{\infty} \left(\frac{\alpha_{s}(\mu)}{4\pi}\right)^{n} \mathcal{M}_{j_{\lambda}/k_{\lambda}}^{(n)}(z,m,\mu),$$
(6.66)

these relations simplify for our dimensionless $\mathcal{O}(\alpha_s)$ coefficient functions in b_T space,

$$C_{Q_{\lambda}/q_{\lambda}}^{(1)}(z,b_{T}m) = C_{q_{\lambda}/q_{\lambda}}^{(1)}(z,b_{T},\mu) + \mathcal{M}_{q_{\lambda}/q_{\lambda}}^{(1)}(z,m,\mu), \qquad (6.67)$$

where the μ dependence has to cancel within the matching coefficient. For the unpolarized case, this relation has previously been verified in refs. [205, 301]. At NLO, the polarized PDF matching function relevant for our case is given by [317]

$$\mathcal{M}_{Q_{\parallel}/g_{\parallel}}^{(1)}(z,m,\mu) = T_F(2z-1)\ln\frac{\mu^2}{m^2}$$
 (6.68)

The massless matching coefficient for the quark helicity TMD PDF onto the collinear gluon helicity PDF was calculated in ref. [311],

$$C_{q_{\parallel}/g_{\parallel}}^{(1)}(z, b_T, \mu, \zeta) = 4T_F \left[(2z - 1) \ln \frac{2e^{-\gamma_E}}{\mu b_T} + (1 - z) \right]. \tag{6.69}$$

Using $K_0(x) = -\ln \frac{2e^{-\gamma_E}}{x} + \mathcal{O}(x)$, it is straightforward to see that our result in eq. (6.64) indeed satisfies eq. (6.67).

By contrast, the worm-gear L matching coefficient is suppressed by one power of the mass, see eq. (6.56), and therefore cannot be reproduced by a leading-power PDF matching at the scale $\mu \sim m$. Interestingly, it contains a logarithm of mb_T at subleading power,

$$C_{Q_{\perp}/g_{\parallel}}^{(1)}(z, b_T m) = 4T_F b_T m(z - 1) \ln \frac{2e^{-\gamma_E}}{mb_T} + \mathcal{O}(m^3 b_T^3).$$
 (6.70)

Unlike the leading-power logarithms in $C_{Q/g}^{(1)}$ and $C_{Q_{\parallel}/g_{\parallel}}^{(1)}$, this logarithm cannot be resummed by the evolution of n_{ℓ} + 1-flavor PDFs between $\mu \sim m$ and $\mu \sim 1/b_T$. Subleading-power mass logarithms in amplitudes that require a helicity flip have received much attention in the context of Higgs boson production through a bottom-quark loop, see e.g. refs. [269–271, 318, 319], and it would be interesting to understand whether the logarithm in eq. (6.70) might be amenable to similar techniques.

6.3.5 Numerical results for TMD PDFs

For numerics, we evaluate eq. (6.54) at the boundary scales $\mu_0 \sim \sqrt{\zeta_0} \sim 1/b_T$ given in and below eq. (6.40), perform the TMD evolution back to $\mu = \sqrt{\zeta} = Q$ as described around eq. (6.41), and finally take a numerical Fourier transform as in eq. (6.47). E.g., we have

$$f_1(x, b_T, \mu, \zeta) = U_q(\mu_0, \zeta_0, \mu, \zeta) \frac{\alpha_s(\mu_0)}{4\pi} \int \frac{\mathrm{d}z}{z} C_{Q/g}^{(1)}(z, b_T m) f_g\left(\frac{x}{z}, \mu_0\right)$$
(6.71)

for the evolved unpolarized heavy-quark TMD PDF, and similarly for the other cases. For the input collinear gluon PDFs we use the NNPDF31_nnlo_as_0118 unpolarized proton PDF set [320] together with the NNPDFpol11_100 set for the polarized case [321]. Our input values for the strong coupling and the quark pole masses were given in section 6.2.6.

In figure 6.4, we show our numerical results for the heavy quark TMD PDFs for producing a charm or bottom quark from a longitudinally polarized proton as a function of k_T and x, respectively. The bottom quark TMD PDFs have a wider peak in k_T compared to the charm because of its larger mass, as can be understood from the fact that the expressions in eq. (6.64) only depend on mb_T up to RG effects. Note also that the worm-gear L function (after including a Jacobian $2\pi k_T$) is quadratic in the small k_T region with a coefficient proportional to $1/m^3$, whereas the unpolarized and helicity TMD PDFs are linear in k_T . As this approximation is valid to higher k_T in the case of the bottom quark than that of the charm, the bottom-quark

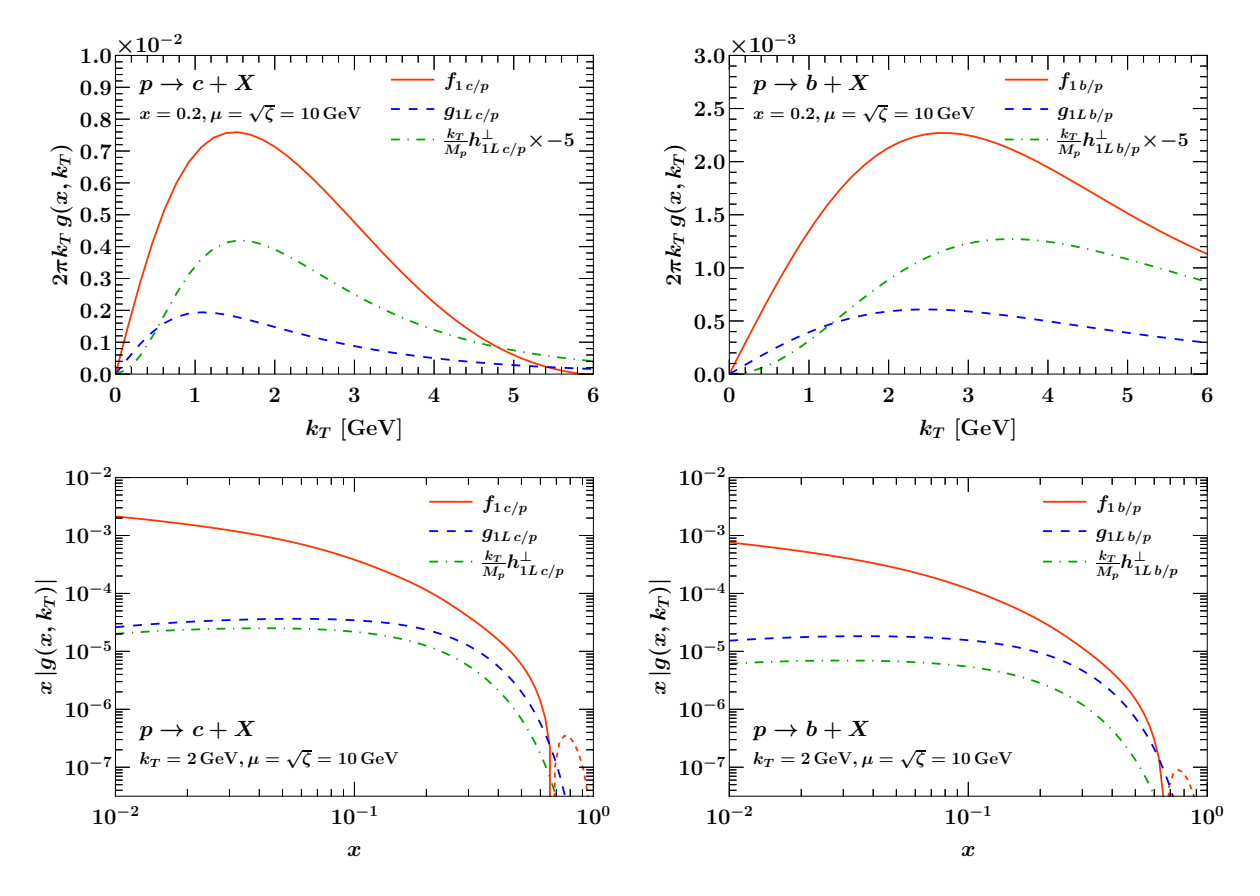


Figure 6.4: TMD PDFs for producing a charm (left) or bottom quark (right) from gluons within a longitudinally polarized proton as a function of k_T at fixed x (top) or vice versa (bottom). Dashed red lines in the bottom two panels indicate negative sign.

TMD PDF has a numerically smaller value over a wide range. As x decreases, the unpolarized heavy-quark TMD PDF rises much more rapidly than the polarized ones, as expected from the smaller gluon polarization fraction at smaller x. We point out that the unpolarized TMD PDF changes sign at very high $x \geq 0.6$, indicating a need for resumming subleading-power threshold logarithms of 1-x using e.g. the tools of refs. [322].

6.4 Towards phenomenology with heavy-quark TMDs

In this section, we present our phenomenological studies for heavy quark TMDs. A brief overview including a sketch of the relevant processes was already given in section 2.6.4.

6.4.1 Accessing heavy-quark TMDs in e^+e^- collisions

In e^+e^- collisions, TMD fragmentation functions may be accessed from double-inclusive measurements with two identified hadrons, $e^+e^- \to H_aH_bX$. For instance, the six-fold differential cross section for this process in the TMD limit $P_{a,T}$, $M_{a,b} \ll Q$ is given by [323, 324]

$$\frac{\mathrm{d}\sigma_{e^+e^-\to H_a H_b X}}{\mathrm{d}\cos\theta\,\mathrm{d}\phi\,\mathrm{d}z_a\,\mathrm{d}z_b\,\mathrm{d}^2\vec{P}_{a,T}} = \frac{3\alpha_{\mathrm{em}}^2}{Q^2} \left[\left(\frac{1}{2} - y + y^2 \right) W_{\mathrm{incl}}(Q^2, z_a, z_b, P_{a,T}/z_a) + y(1-y)\cos(2\phi_0) W_{\cos(2\phi_0)}(Q^2, z_a, z_b, P_{a,T}/z_a) \right] + (\text{odd under } y \leftrightarrow 1-y),$$
(6.72)

where $\cos\theta$ and ϕ are the spherical coordinates of hadron H_b with respect to the incoming beams in the center-of-mass frame, z_a and z_b are the lightcone momentum fractions of the two hadrons, and $\vec{P}_{a,T}$ is the transverse momentum of hadron H_a . On the right-hand side, $\alpha_{\rm em}$ is the fine-structure constant, Q is the center-of-mass energy of the collision, $y=(1+\cos\theta)/2$, and ϕ_0 is the azimuthal angle of $\vec{P}_{a,T}$ measured relative to the plane spanned by H_b and the beams. The hadronic structure functions factorize into TMD FFs,

$$W_{\text{incl}}(Q^{2}, z_{a}, z_{b}, q_{T}) = \mathcal{F}_{ee} \left[\mathcal{H} D_{1} D_{1} \right],$$

$$W_{\cos(2\phi_{0})}(Q^{2}, z_{a}, z_{b}, q_{T}) = \mathcal{F}_{ee} \left[\mathcal{H} H_{1}^{\perp(1)} H_{1}^{\perp(1)} \right],$$
(6.73)

where \mathcal{F}_{ee} denotes a weighted sum over flavors and a convolution of two TMD FFs (i.e., a product in b_T space) at total partonic transverse momentum $q_T = P_{a,T}/z_a$,

$$\mathcal{F}_{ee} \Big[\mathcal{H} D^{(n)} D^{(m)} \Big] = z_a^2 z_b^2 \int_0^\infty \frac{\mathrm{d}b_T b_T}{2\pi} (M_a b_T)^n (M_b b_T)^m J_{n+m}(b_T q_T) \\ \times \sum_{i,j} \mathcal{H}_{ee \to ij}(Q^2, \mu) D_{H_a/i}(z_a, b_T, \mu, Q^2) D_{H_b/j}(z_b, b_T, \mu, Q^2) , \qquad (6.74)$$

and the hard function describing the pair production of quarks is given by

$$\mathcal{H}_{ee \to ij}(Q^2, \mu) = \delta_{i\bar{j}} \left\{ e_i^2 - 2v_e v_i e_i \operatorname{Re} \left[P_Z(Q^2) \right] + (v_e^2 + a_e^2)(v_i^2 + a_i^2) \left| P_Z(Q^2) \right|^2 \right\}.$$
 (6.75)

Here we have kept the contribution from Z boson exchange and Z-photon interference, as relevant for measurements on the Z pole, where $P_Z(Q^2) = Q^2/(Q^2 - m_Z^2 + i\Gamma_Z m_Z)$ is the reduced Z propagator and e_f (v_f , a_f) are the electromagnetic charge (vector, axial coupling to the Z) of a fermion f. We may assume that the experimental measurement involves an integral over symmetric ranges in $\cos \theta$ such that the forward-backward asymmetry and an associated odd Collins effect in eq. (6.72) drop out.

Crucially, the TMD factorization theorems in eqs. (6.72) and (6.73) only assume that the hard scale $Q \sim z_a Q \sim z_b Q$ is large compared to all other scales, i.e., all masses and transverse momenta, and therefore hold for *both* light-quark and heavy-quark fragmentation at $z_{a,b} \sim 1$ without modification. In particular, the heavy quarks are approximately massless at the scale

 $\mu \sim Q$ at which they are produced, and their polarization states are thus fully entangled. The hard function in eq. (6.75) could be modified to account for the effect of perturbative spin flips, but this amounts to retaining power corrections in m/Q further suppressed by powers of α_s . Importantly, this means that a characteristic $\cos(2\phi_0)$ modulation (the Collins effect) is present both for light and for heavy quarks at leading power and at tree level. As is commonly done for light quarks, the Collins effect strength

$$R_{\cos(2\phi_0)}(Q^2, q_T) \equiv \frac{\int dz_a \int dz_b W_{\cos(2\phi_0)}(Q^2, z_a, z_b, q_T)}{\int dz_a \int dz_b W_{\text{incl}}(Q^2, z_a, z_b, q_T)}$$
(6.76)

can be accessed by taking suitable ratios of weighted cross sections, which we here take to be integrated over z_a and z_b as likely relevant for an initial study of the heavy-quark Collins effect.

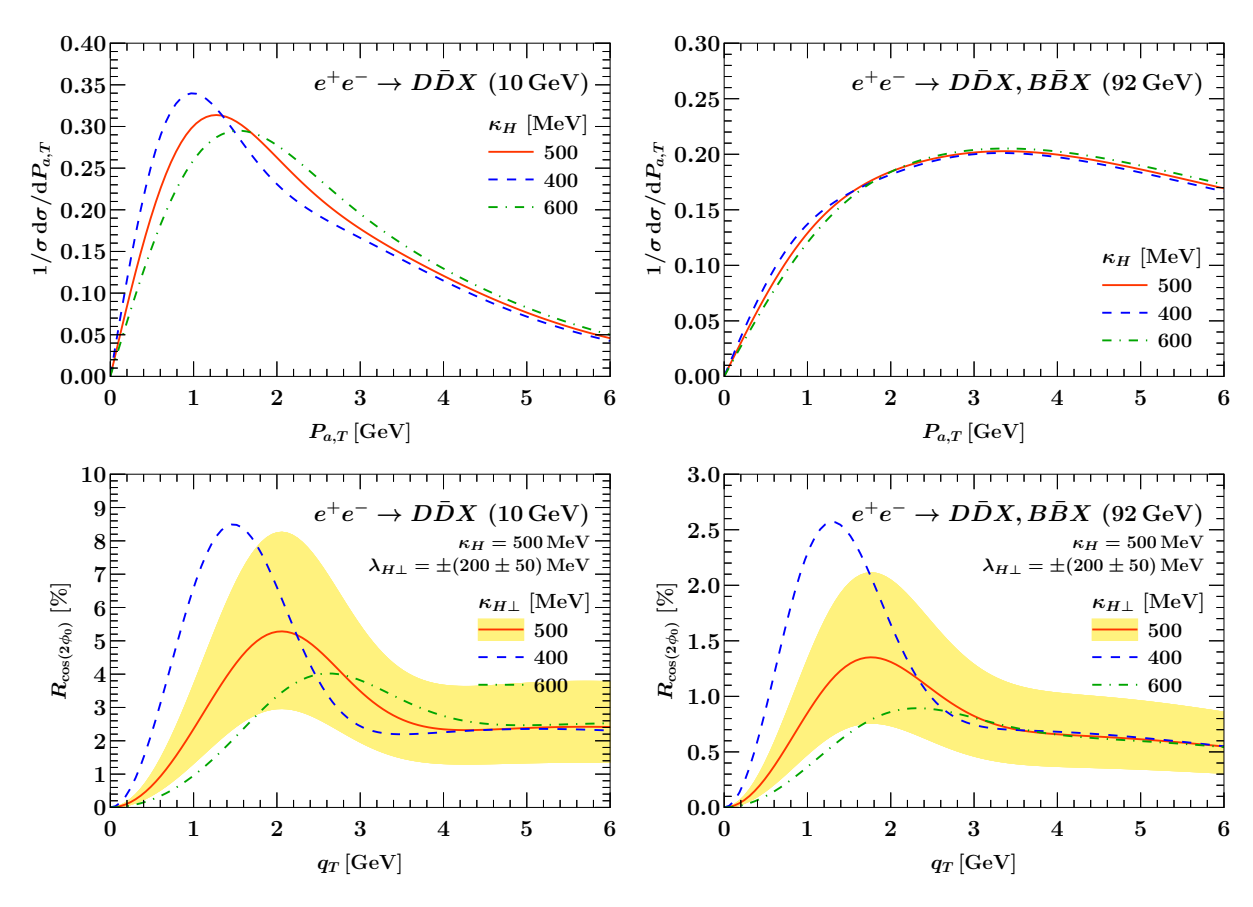


Figure 6.5: Normalized TMD cross sections (top) and Collins effect strengths (bottom) for charm quarks at $Q = 10 \,\text{GeV}$ (left) and charm and bottom quarks at $Q = m_Z$ (right) as a function of P_{aT} and integrated over z_H . The yellow bands in the case of the Collins effect correspond to the indicated variations of the sign and magnitude of $\lambda_{H\perp}$.

In figure 6.5 we show the predicted $e^+e^- \to D\bar{D}X$ or $B\bar{B}X$ cross sections as a function of hadron transverse momentum $P_{a,T}$, and the Collins effect strength $R_{\cos(2\phi_0)}$ as a function of q_T . The universality for charm and bottom quarks follows along the same lines as for figure 6.3, and holds as long as the center-of-mass energy is sufficient to produce the quark-antiquark pair in a boosted state. This is the case for charm mesons at typical continuum center-of-mass energies at existing B factories, such as Belle II [325], and for both charm and bottom mesons at higher values of Q such as at the Z pole. The Collins effect is smaller at higher center-of-mass

Chapter 6 – Transverse Momentum Distributions of Heavy Quarks and Heavy Hadrons

energies because $\chi_{1,H}^{\perp}$ is linearly suppressed in b_T compared to the unpolarized, which means it predominantly contributes at larger values of b_T where the Sudakov suppression at higher energies tends to be stronger.

We show the results of varying κ_H (κ_H^{\perp}) for the unpolarized (Collins) TMD FF, and illustrate the variation of $\lambda_{H\perp}$ by the yellow band, exactly as in figure 6.3. Note that the information about the absolute sign of the Collins function is lost in e^+e^- collisions, i.e., for two charge-conjugate hadrons we end up with a positive effect strength for any value of $\lambda_{H\perp} = \lambda_{\bar{H}\perp}$ since the effect is proportional to the square of the Collins function. One may nevertheless extract the relative factor between e.g. the D and D^* Collins function, which heavy-quark spin symmetry predicts to be exactly minus one, see eq. (6.36), by measuring the Collins effect separately for $e^+e^- \to D\bar{D}X$ and $e^+e^- \to D^*\bar{D}X$. Explicitly, our prediction from heavy-quark spin symmetry reads

$$R_{\cos(2\phi_0)}^{D\bar{D}} = -\frac{1}{3}R_{\cos(2\phi_0)}^{D^*\bar{D}} = -\frac{1}{3}R_{\cos(2\phi_0)}^{D\bar{D}^*} = +\frac{1}{9}R_{\cos(2\phi_0)}^{D^*\bar{D}^*}$$
(6.77)

We point out that for generic $\mathcal{O}(\Lambda_{\rm QCD})$ model parameters, the Collins effect strength reaches the several-percent level for continuum open charm production at existing B factories, in line with our expectation of an effect strength that is comparable to the light quark case, making a future dedicated measurement (or search) appear very feasible.

Comment on claims regarding a mass suppression of the Collins effect

In e^+e^- collisions, the "intrinsic" heavy-quark Collins effect we analyzed above has been disregarded so far. Note that this effect is in general distinct from the large background contribution of $D\bar{D}$ weak decays to e.g. a measurement of the Collins effect on a $K\bar{K}$ sample. This contribution is indeed considered in experimental analyses [326–329] and subtracted as a background using Monte-Carlo simulations and heavy-quark enriched samples, but cannot be immediately interpreted as a sign of a (nonperturbative) Collins effect since the progenitor $D\bar{D}$ pair in this case is not constrained to be near the back-to-back limit by the measurement, meaning that e.g. perturbative gluon emissions can also induce azimuthal correlations on the $D\bar{D}$ pair and thus their weak decay products.

Ref. [326] mentions that it would be possible to look for the intrinsic heavy-quark Collins effect with some further improvements to their analysis, but also incorrectly expects that the Collins effect should be parametrically suppressed by the mass of heavy quarks. The argument sketched in that reference (see beginning of their section IV) is that helicity flips should wash out the spin correlation between the heavy quark and the antiquark. This is not the case, as we have argued above: The quarks are approximately massless at the scale $\mu \sim Q$ at which they are produced, and thus are produced with fully entangled spin states, such that there is no suppression by the mass from physics at this scale. Similarly, in our detailed analysis of the Collins FF at the scale $\mu \leq k_T \leq m$, we find no suppression of the effect by the mass, and the Collins effect in particular is fully allowed by heavy-quark symmetry when accounting for the presence of lightlike Wilson lines. Note that this is not contradictory to the fact that we do find a suppression of the Collins effect by $\Lambda_{\rm QCD}/k_T$ at large k_T , since this suppression is exactly commensurate with the twist suppression of the two Collins functions in the light-quark case, which has been mapped out extensively [326–330]. We conclude that the prospects for a measurement of the intrinsic, nonperturbative heavy-quark Collins effect at B factories are even better than anticipated in ref. [326].

6.4.2 Accessing heavy-quark TMDs at the future EIC

TMD fragmentation functions may also be accessed from single-inclusive measurements with one identified hadron in electron-nucleon collisions, $e^-(\ell) + N(P) \rightarrow e^-(\ell') + H(P_H) + X$, where the scattering is mediated by an off-shell photon with momentum $q = \ell - \ell'$ (and $Q^2 \equiv -q^2 > 0$). The fully differential cross section for this process in the TMD regime reads [112,147,171,172,331]

$$\frac{\mathrm{d}\sigma_{eN\to eHX}}{\mathrm{d}x\,\mathrm{d}y\,\mathrm{d}z_{H}\,\mathrm{d}^{2}\vec{P}_{H,T}} = \sigma_{0} \Big\{ W_{UU,T}(Q^{2}, x, z_{H}, \vec{P}_{H,T}/z_{H})
+ \lambda_{e}S_{L}\sqrt{1 - \epsilon^{2}}W_{LL}(Q^{2}, x, z_{H}, \vec{P}_{H,T}/z_{H})
+ S_{L}\,\epsilon\,\sin(2\phi_{H})\,W_{UL}^{\sin(2\phi_{H})}(Q^{2}, x, z_{H}, \vec{P}_{H,T}/z_{H}) \Big\}.$$
(6.78)

On the left-hand side, $x = Q^2/(2P \cdot q)$, $y = (P \cdot q)/(P \cdot \ell)$, $z_H = (P \cdot P_H)/(P \cdot q)$, and $\vec{P}_{H,T}$ is the outgoing hadron's transverse momentum relative to \vec{q} in the Breit frame. On the right-hand side,

$$\sigma_0 = \frac{\alpha_{\rm em}^2 \pi y}{z_H Q^2 (1 - \epsilon)}, \qquad \epsilon = \frac{1 - y}{1 - y + y^2 / 2},$$
(6.79)

up to power corrections in xM_N/Q , $xM_HM_N/(z_HQ^2)$, or $xP_{H,T}M_N/(z_HQ^2)$, all of which are small in the TMD regime of interest, and ϕ_H is the azimuthal angle of the hadron transverse momentum in the Trento (photon) frame [171]. The beam polarization information is encoded in the lepton beam helicity λ_e and the covariant nucleon spin vector $S^{\mu} = (0, S_T \cos \phi_S, S_T \sin \phi_S, -S_L)$ as decomposed in the Trento frame. We have dropped terms proportional to S_T , which cannot be populated by leading-power heavy-quark TMD PDFs, see section 6.3. We have also dropped terms proportional to the Boer-Mulders function, whose twist-2 matching in the heavy-quark case is suppressed by at least one additional power of α_s . The hadronic structure functions factorize in terms of one TMD PDF and one TMD FF each,

$$W_{UU,T}(Q^{2}, x, z_{H}, \vec{q}_{T}) = \mathcal{F}_{eN} \left[\mathcal{H} f_{1} D_{1} \right],$$

$$W_{LL}(Q^{2}, x, z_{H}, \vec{q}_{T}) = \mathcal{F}_{eN} \left[\mathcal{H} g_{1L} D_{1} \right],$$

$$W_{UL}^{\sin(2\phi_{H})}(Q^{2}, x, z_{H}, \vec{q}_{T}) = -\mathcal{F}_{eN} \left[\mathcal{H} h_{1L}^{\perp(1)} H_{1}^{\perp(1)} \right],$$
(6.80)

where the convolution in transverse momentum may be written in position space as [181]

$$\mathcal{F}_{eN}\Big[\mathcal{H}\,g^{(n)}\,D^{(m)}\Big] = 2z_H \int_0^\infty \frac{\mathrm{d}b_T\,b_T}{2\pi} (M_N b_T)^n (-M_H b_T)^m J_{n+m}(b_T q_T) \\ \times \sum_i \mathcal{H}_{ei \to ei}(Q^2, \mu) \,g_{i/N}(x, b_T, \mu, Q^2) \,D_{H/i}(z_H, b_T, \mu, Q^2) \,, \tag{6.81}$$

and the hard function for scattering a quark off a virtual photon is

$$\mathcal{H}_{ei \to ei}(Q^2, \mu) = |e_i|^2 + \mathcal{O}(\alpha_s). \tag{6.82}$$

As for e^+e^- collisions, the TMD factorization theorems in eq. (6.80) only assume that the hard scale $Q \sim zQ$ is large compared to all low scales, and thus hold for both light and heavy hadron production without modification. Again, the heavy quark is approximately massless at the hard scale such that helicity is conserved during the hard scattering. This means that while

Chapter 6 – Transverse Momentum Distributions of Heavy Quarks and Heavy Hadrons

$\sigma(eN \to eHX)$ [pb]	c, x > 0.01	c, x > 0.1	b, x > 0.01	b, x > 0.1
$q_T < 2 \mathrm{GeV}, Q > 4 \mathrm{GeV}$	84	3.47	18	0.65
$q_T < 4 \mathrm{GeV}, Q > 10 \mathrm{GeV}$	16	1.45	4.9	0.42

Table 6.1: Total cross sections in picobarn for producing charm (left two columns) or bottomquark hadrons (right two columns) in the TMD region at the future $18 \times 275 \,\text{GeV}^2$ EIC for different cuts on $x > x_{\min}$, $Q > Q_{\text{cut}}$, $q_T = P_{H,T}/z < q_T^{\text{cut}}$. See the text for further details on the acceptance cuts we consider.

the production mechanisms for longitudinally or transversely polarized heavy quarks from an incoming nucleon are different from light quarks (and are fully perturbative), the way they imprint on the distribution of final-state hadrons is the same, leaving nonzero spin asymmetries

$$A_{LL}(Q^{2}, x, q_{T}) = \frac{\int dz_{H} W_{LL}(Q^{2}, x, z_{H}, \vec{q}_{T})}{\int dz_{H} W_{UU,T}(Q^{2}, x, z_{H}, \vec{q}_{T})},$$

$$A_{UL}^{\sin(2\phi_{H})}(Q^{2}, x, q_{T}) = \frac{\int dz_{H} W_{UL}^{\sin(2\phi_{H})}(Q^{2}, x, z_{H}, \vec{q}_{T})}{\int dz_{H} W_{UU,T}(Q^{2}, x, z_{H}, \vec{q}_{T})}.$$
(6.83)

In particular, the $\sin(2\phi_H)$ modulation induced by a nucleon beam polarization flip gives direct access to the heavy-quark Collins function including its sign, which is not accessible in e^+e^- collisions.

To assess the statistical power of the future EIC to constrain charm and bottom quark TMD dynamics, we first estimate the expected sample size of heavy hadrons in electron-proton collisions. To do so, we consider the total cross section for producing a heavy quark in the TMD region summed over beam polarizations,

$$\sigma_{eN\to eHX}(Q_{\text{cut}}, q_T^{\text{cut}}) = \int dx \, dy \, dz_H \, d^2 \vec{P}_{H,T} \, \frac{d\sigma_{eN\to eHX}}{dx \, dy \, dz_H \, d^2 \vec{P}_{H,T}}$$

$$\times \Theta(q_T^{\text{cut}} - P_{H,T}/z_H) \, \Theta(Q - Q_{\text{cut}}) \, \Theta_{\text{DIS}}(x, y)$$

$$= \sigma_0 \int dx \, dy \, dz_H \, \Theta(Q - Q_{\text{cut}}) \, \Theta_{\text{DIS}}(x, y) \, 2z_H^3 \int_0^\infty db_T \, q_T^{\text{cut}} \, J_1(b_T q_T^{\text{cut}})$$

$$\times \sum_i \mathcal{H}_{ei\to ei}(Q^2, \mu) \, f_{1i/N}(x, b_T, \mu, Q^2) \, D_{1H/i}(z_H, b_T, \mu, Q^2) \, ,$$

$$(6.84)$$

where $\Theta_{\text{DIS}}(x,y)$ denotes DIS acceptance cuts given by

$$x > x_{\min},$$
 $0.01 < y < 0.95,$ $W^2 = \left(\frac{1}{x} - 1\right)Q^2 > 100 \,\text{GeV}^2.$ (6.85)

We consider the EIC at beam energies $E_e=18\,\mathrm{GeV}$ and $E_N=275\,\mathrm{GeV}$. Any experimental cuts on $z_H>z_\mathrm{cut}$ and the additional prefactor of z_H^3 in eq. (6.84) are irrelevant at our working order because the heavy quark carries all the energy in all regimes, i.e., $z_H=1$ either at leading power in the heavy-quark expansion or at the leading perturbative order, see the comments below eq. (6.41). For this estimate we set $\kappa_H=0$ in the unpolarized heavy-quark TMD FF, since the total integral of the cross section up to $q_T^\mathrm{cut}\gg\Lambda_\mathrm{QCD}$ is independent of it up to corrections of $\mathcal{O}(\Lambda_\mathrm{QCD}^2/q_T^\mathrm{cut})$ [307], and sum over all heavy hadrons containing the heavy quark, exploiting $\sum_H \chi_H = 1$. This means that the total rate at which heavy quarks are produced is predicted fully perturbatively, as expected.

Our results for the expected total charm and bottom-quark TMD cross sections are given in table 6.1 for $Q_{\rm cut}=4\,{\rm GeV}$ and $Q_{\rm cut}=10\,{\rm GeV}$, where higher $Q_{\rm cut}$ allows for mapping out the TMD region to higher q_T before encountering power corrections, but at the cost of much lower rates. (We have also adjusted $q_T^{\rm cut}$ accordingly in each case.) Scaled to an integrated luminosity of $10\,{\rm fb^{-1}}$, we expect a total charm quark sample of 35×10^3 in the TMD region for the loose cut on Q and in the region x>0.1 where polarization effects are expected to be most pronounced, see figure 6.4, and where a measurement of the $\sin(2\phi_H)$ asymmetry is the most promising. This suggests that even with this limited integrated luminosity, percent-level asymmetries should be statistically resolvable.

In figure 6.6 we show the results for the unpolarized SIDIS cross section with a D(B) meson in the final state, and for the two spin asymmetries defined in eq. (6.83). Note that the effect of different κ_H in the unpolarized TMD fragmentation function is negligible in the cross section and the A_{LL} asymmetry, which as expected are dominated by perturbative physics. The A_{LL} asymmetry is very sizable at $\sim 30\%$ at the chosen value of x=0.2. On the other hand, the A_{UL} asymmetry is substantially smaller (1-2%) for the generic $\mathcal{O}(\Lambda_{\rm QCD})$ parameters we picked here due to the smaller value of both h_{1L}^{\perp} compared to g_{1L} and H_1^{\perp} compared to D_1 in most of the contributing TMD region, see figures 6.3 and 6.4 and the surrounding discussion. The numerically smaller value of h_{1L}^{\perp} for bottom quarks discussed around figure 6.4 is likewise reflected in the size of the asymmetry for bottom compared to charm quarks. We emphasize that a measurement of A_{UL} , compared to the Collins effect in e^+e^- collisions, has the unique benefit of accessing the absolute sign of the heavy-quark Collins function. Resolving this sign should well be possible within the expected statistics at the future EIC. While we leave the study of systematic effects (such as luminosity uncertainties) to future work, we note that the requirements that the established heavy-flavor/gluon distribution program of the EIC places on instrumentation have already been analyzed in depth in ref. [179]. Among these requirements are secondary vertex reconstruction capabilities and the momentum resolution on soft pions from D decays, all of which will also benefit the kind of differential measurements of semi-inclusive heavy-quark fragmentation that we propose here.

6.5 Summary

In this chapter, we discussed the transverse momentum-dependent (TMD) dynamics of bottom or charm quarks with mass $m \equiv m_c, m_b \gg \Lambda_{\rm QCD}$ fragmenting into heavy hadrons which were studied in [3] for the first time. We considered two parametric regimes for the transverse momentum k_T , (a) $\Lambda_{\rm QCD} \lesssim k_T \ll m$, where the hadron transverse momentum k_T is determined by nonperturbative soft radiation into the final state, and (b) $\Lambda_{\rm QCD} \ll m \lesssim k_T$, where k_T is set by perturbative emissions. We assumed throughout that the heavy quark is produced at a hard scale $Q \gg m, k_T$, i.e., it is boosted in the frame of the hard scattering, such that standard TMD factorization applies at the scale Q and only the low-energy TMD matrix elements are modified by the heavy quark dynamics. In both regimes, the dynamics at scales below the heavy quark mass are constrained by heavy-quark symmetry and encoded in novel low-energy matrix elements in boosted Heavy-Quark Effective Theory (bHQET)

We showed that in regime (a), the unpolarized and Collins TMD fragmentation functions (FF) match onto new, universal nonperturbative bHQET matrix elements $\chi_{1,H}(k_T)$ and $\chi_{1,H}^{\perp}(k_T)$, which we dubbed TMD fragmentation factors. In regime (b), we found new inclusive bHQET matrix elements, $\chi_{1,H}$ and $\chi_{1,H}^{\perp}$. An important new ingredient in this analysis is the unpolarized

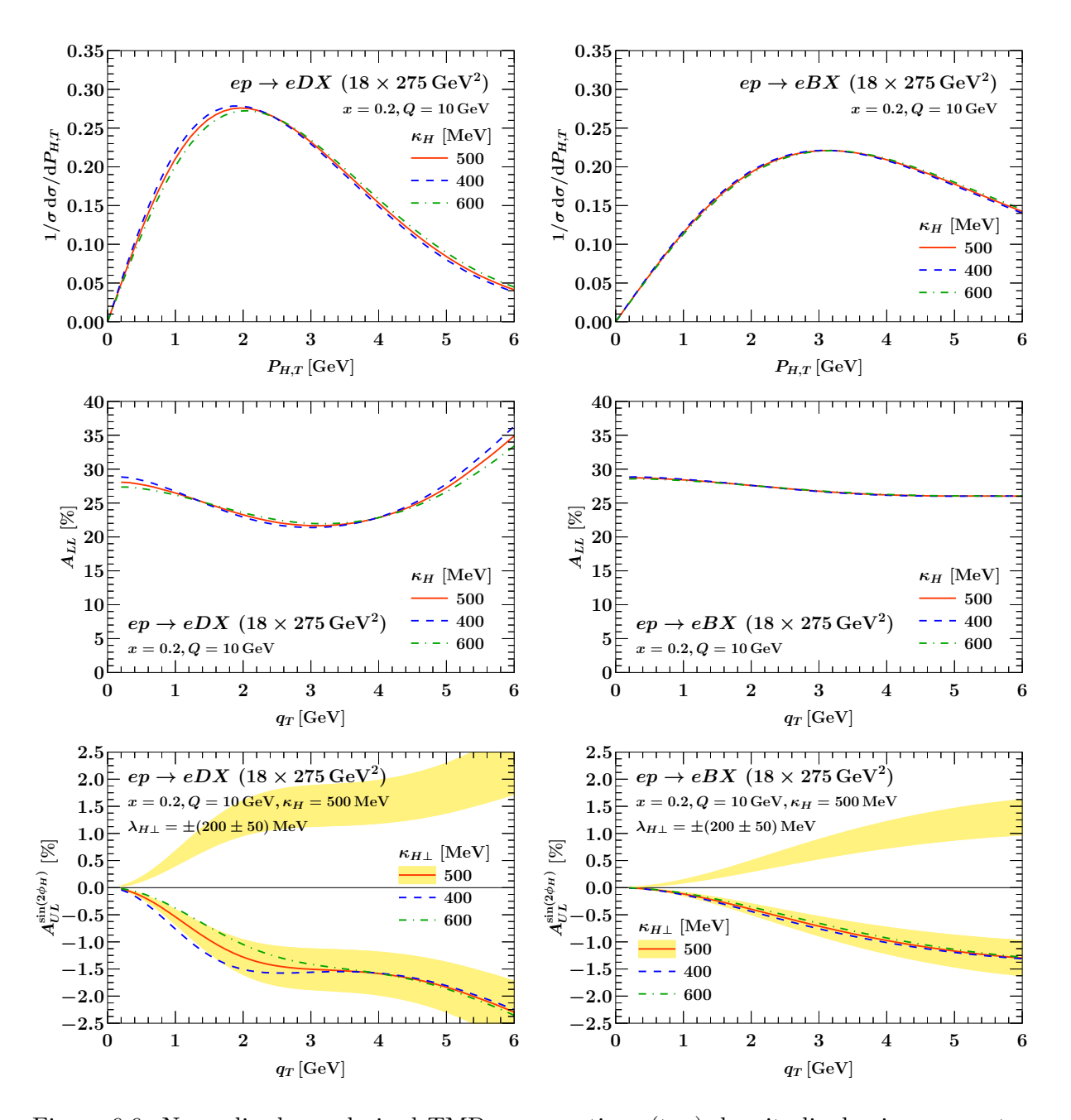


Figure 6.6: Normalized unpolarized TMD cross sections (top), longitudinal spin asymmetry (center), and $\sin(2\phi_H)$ spin asymmetry (right) for charm quarks (left) and bottom quarks (right) at the future EIC. The yellow bands correspond to the indicated variations of the sign and magnitude of $\lambda_{H\perp}$, i.e., the heavy-quark Collins function.

partonic heavy quark TMD FF $d_{1Q/Q}$, a perturbative Wilson coefficient that appears in our analysis for the first time and that we expect to appear also in other contexts. Further, we proved new TMD sum rules that arise from heavy-quark symmetry. We want to point out that an improved field-theoretic understanding of heavy-quark fragmentation will also benefit the description of heavy flavor in Monte-Carlo generators for the LHC [332], where many key searches and Higgs coupling measurements involve final-state charm or bottom quarks.

To extend our analysis to the possible phenomenology at the future Electron-Ion Collider (EIC), we also considered the production of polarized heavy quarks from a polarized nucleon, which is encoded in all-order matching relations between heavy-quark TMD PDFs and twist-2 collinear light-parton PDFs. We find nontrivial matching coefficients at $\mathcal{O}(\alpha_s)$ for the heavy-quark worm-gear L and helicity TMD PDFs onto the gluon helicity collinear PDF, both of which we computed explicitly for the first time. We anticipate that the heavy-quark Boer-Mulders function will receive a contribution from the twist-2 collinear gluon PDF starting at $\mathcal{O}(\alpha_s^2)$, where it becomes allowed by time-reversal invariance.

Combining the standard TMD factorization theorems for e^+e^- to hadrons and SIDIS with simple numerical models for the new nonperturbative functions we identified, we provided predictions for unpolarized heavy-quark TMD cross sections, the Collins effect strength for heavy quarks at e^+e^- colliders (and in particular for $c\bar{c}$ continuum production at current B factories), as well as for the relevant spin asymmetries at the future EIC. We find that a measurement of the intrinsic heavy-quark Collins effect is well within reach of existing B factories, and is motivated by the rich nonperturbative structure of the heavy-quark Collins function that our analysis revealed. The fact that transversely polarized heavy quarks are produced from linearly polarized nucleons at a significant rate, as encoded in the worm-gear L matching coefficient, in addition provides a clean avenue for probing the heavy-quark Collins functions in heavy-quark SIDIS at the future EIC, including its absolute sign.

The theoretical framework we developed in this chapter paves the way for many promising future applications: While we only considered the case of unpolarized heavy hadrons in this work, an immediate next application of our framework are polarized vector mesons or baryons containing heavy quarks. This gives access to a larger set of transverse-momentum dependent polarized fragmentation functions [323, 333, 334] which in the heavy-quark case resolve the light spin density matrix in even greater detail and obey additional sum rules. Another promising prospect is to consider heavy-quark TMD fragmentation within jets, which makes its rich physics accessible in hadron collisions. This extension is in fact straightforward because our results for the heavy-quark TMD FFs hold independent of the factorization theorem they appear in. This makes it possible to insert them into the hadron-in-jet frameworks of refs. [335, 336] as long as $Q \sim p_T^{\rm jet} R \gg m, k_T$. Yet another possibility, which could mitigate the effect of nonglobal logarithms that can become nonperturbative in our regime of interest, would be to apply grooming to the jet and study the hadron transverse momentum spectrum with respect to the groomed jet axis [337, 338].

Other natural extensions are higher-order calculations of the various new partonic matching coefficients we introduced in this chapter, which will reduce the perturbative uncertainties on the lowest-order theory predictions we provided here. This will also involve analyzing the renormalon structure and optimizing the choice of quark mass scheme. In addition, one could consider the matching onto subleading bHQET fragmentation matrix elements (for TMD FFs) or onto

Chapter 6 – Transverse Momentum Distributions of Heavy Quarks and Heavy Hadrons

twist-3 collinear PDFs (for TMD PDFs, extending the work of ref. [339] to the massive case), which would make it possible to interpret phenomenological extractions in terms of higher-point correlation functions. Higher-order resummed predictions for heavy-quark TMD spectra then immediately follow from our factorization results by solving the attendant renormalization group equations, and will serve as powerful, highly differential benchmarks of the heavy-quark physics encoded in present and future parton showers, including their interface with hadronization models, on which our field-theory analysis of the nonperturbative dynamics places rigorous constraints.

In conclusion, our analysis reveals that a wealth of information on the all-order and nonperturbative structure of QCD resides in the transverse momentum dependence of heavy-quark fragmentation. An experimental exploration of this new subfield of TMD physics is in immediate reach of existing B factories and will be an exciting addition to the planned heavy-flavor physics program of the future EIC.

Chapter 7

TMD heavy-quark fragmentation at NLO

In this chapter we calculate all TMD FFs involving heavy quarks and the associated TMD matrix element in HQET to next-to-leading order in the strong coupling. Our results confirm the renormalization properties, large-mass, and small-mass consistency relations predicted in ref. [3].

This chapter is based on ref. [1] reflecting the author's contribution. Compared to ref. [1], we shortened the calculation of $d_{1Q/Q}$ section 7.3 and omitted sections 4, 6, 7 and 8.

7.1 Motivation

The fragmentation of heavy (bottom or charm) quarks into the experimentally observed heavy meson and baryon states is of particular interest because the mass of the quark imprints as a perturbative scale on the otherwise nonperturbative process of hadronization. In the last chapter, we discussed study of transverse momentum-dependent (TMD) fragmentation functions (FFs) for the formation of heavy hadrons from a parent heavy quark initiated in ref. [3]. Our work generalized the well-studied case where only the collinear momentum fraction of the hadron is resolved [285–288,292] (see refs. [340] for a recent precision study on data), and is part of a larger, ongoing research effort to understand differential jet and fragmentation functions involving heavy quarks, heavy hadrons, and heavy-quark bound states [3, 289, 338, 341–345]. In this context, TMD FFs are unique in the wealth of information they can provide on the hadronization process, essentially offering a full three-dimensional view of the fragmentation cascade.

In this chapter, we present the results for all unpolarized heavy-quark TMD FFs at perturbative transverse momenta to complete next-to-leading order (NLO) in the strong coupling. Our final results in position space agree with those of a recent calculation by another group [344] that used a highly orthogonal organization of singularities in the intermediate momentum-space steps, providing a strong independent cross check.

Importantly, the factorization paradigm ensures that the heavy-quark TMD FFs appear as universal building blocks across predictions for a large number of processes involving final-state heavy quarks. In the previous, we explicitly considered their phenomenology in heavy-hadron pair production in the back-to-back limit in e^+e^- collisions and in (polarized) semi-inclusive DIS at the future Electron-Ion Collider [179], cf. ref. [346] for recent dedicated projections for

polarized collinear parton distribution functions (PDFs) and FFs involving heavy quarks at the EIC. However, the applicability of heavy-quark TMD FFs is much wider: Applications of immediate phenomenological interest range from Z+hadron [347] and dihadron [348] azimuthal decorrelations in pp and pA collisions to hadron-in-jet transverse-momentum distributions [335, 336], transverse momentum-like event shapes (extending the calculation of mass effects in thrust-like event shapes [294, 349–351]), and energy-energy correlators in the back-to-back limit in e^+e^- [352], ep and eA [353, 354], and pp collisions [355, 356]. In all of these cases, factorization formulas involving TMD FFs have been derived, and the NLO results we present in this chapter enable one to fully account for the effect of quark masses and accurately capture their highly nontrivial interplay with transverse momenta in all of these processes.

7.2 Theoretical framework

7.2.1 Heavy-quark TMD FFs

We study the fragmentation of a heavy quark Q with pole mass $m \gg \Lambda_{\rm QCD}$ into an unpolarized heavy hadron H and additional fragmentation products X. We work in QCD with $n_f = n_\ell + 1$ flavors, where n_ℓ is the number of massless quark flavors. Just as in chapter 6, we work in the "hadron frame" for fragmentation [147] where $P_H^{\mu} = (P_H^-, M_H^2/P_H^-, 0)$, with M_H the hadron mass, and $P_{H,\perp} = 0$ by definition.

In section 6.2.4, we showed that up to a factor of the total probability for Q to fragment into H, the distribution differential in $k_T = P_{X,T} \sim M_H$ and the lightcone momentum fraction z_H of the original quark retained by H is governed by a new perturbative matching coefficient, the partonic heavy-quark TMD FF $d_{1Q/Q}(z, k_T, \mu, \zeta)$,

$$D_{1H/Q}(z_H, b_T, \mu, \zeta) = d_{1Q/Q}(z_H, b_T, \mu, \zeta) \chi_H + \mathcal{O}\left(\frac{\Lambda_{\text{QCD}}}{m}\right) + \mathcal{O}(\Lambda_{\text{QCD}}b_T). \tag{7.1}$$

Making all regulators explicit, the formal definition of $d_{1Q/Q}$ at the bare level reads

$$d_{1Q/Q}^{\text{bare}}(z, b_T, \epsilon, \eta, \zeta/\nu^2) = \frac{1}{2z^{1-2\epsilon}N_c} \int \frac{\mathrm{d}b^+}{4\pi} e^{\mathrm{i}b^+(p^-/z)/2}$$

$$\times \text{Tr} \sum_{X} \operatorname{tr} \left[\frac{\vec{n}}{2} \left\langle 0 \middle| W_{\eta}^{\dagger}(b) \psi_Q(b) \middle| QX \right\rangle \left\langle QX \middle| \bar{\psi}_Q(0) W_{\eta}(0) \middle| 0 \right\rangle \right],$$
(7.2)

where we work in $d=4-2\epsilon$ spacetime dimensions, N_c is the number of colors, Tr (tr) indicates a trace over color (spin), and \mathcal{L}_X indicates a sum over all possible partonic final states combined with an integral over their phase space. The fields in the first matrix element are evaluated at a spacetime position $b \equiv (0, b^+, b_\perp)$ with b_\perp Fourier conjugate to k_\perp , and $b_T^2 \equiv -b_\perp^2$ and $k_T^2 = -k_\perp^2$, respectively. The heavy quark in the external state carries momentum $p^\mu = (p^-, m^2/p^-, 0)$, i.e., the above definition is equal to the hadron-level definition of the heavy-quark TMD FF $D_{1H/Q}$, but with H replaced by Q itself in the external state and restricting to partonic final states X [3]. The definition in eq. (7.2) is given in terms of the heavy-quark field renormalized on shell,

$$\psi_Q^{\text{bare}}(x) = Z_{\psi, \text{OS}}^{1/2}(m, \mu, \epsilon) \,\psi_Q(x) \,, \tag{7.3}$$

and in terms of Wilson lines $W_{\eta}(x)$ defined as anti-path ordered exponentials of gauge fields extending to positive infinity along the lightcone direction \bar{n}^{μ} ,

$$W_{\eta}(x) = \bar{P} \left[\exp \left(-ig \int_{0}^{\infty} ds \, \bar{n} \cdot A(x + \bar{n}s) \right) \right]_{\eta}. \tag{7.4}$$

The subscript η indicates the presence of an additional rapidity regulator. In explicit calculations, we will use the so-called η regulator of refs. [113, 118]. The final result for the bare matrix element depends on ζ/ν^2 , with $\zeta \equiv (p^-/z)^2$ the Collins-Soper scale.

In terms of the bare collinear matrix element in eq. (7.2), the renormalized partonic heavy-quark TMD FF is given by

$$d_{1\,Q/Q}(z,b_T,\mu,\zeta) = \lim_{\epsilon \to 0} Z_{\rm UV}(\mu,\zeta,\epsilon) \lim_{\eta \to 0} \left[d_{1\,Q/Q}^{\rm bare}(z,b_T,\epsilon,\eta,\zeta/\nu^2) \sqrt{S}(b_T,m,\epsilon,\eta,\nu) \right], \quad (7.5)$$

where S is the universal bare TMD soft function for the η regulator, which cancels all poles of η and the associated ν dependence, and is independent of the heavy-quark mass up to secondary quark mass effects starting at two loops. By contrast, the $\overline{\rm MS}$ renormalization factor $Z_{\rm UV}$ for quark TMDs is independent of the mass to all orders by RG consistency with the hard matching coefficient at the hard scattering energy $Q \sim p^-/z \gg m \sim k_T \sim 1/b_T$. While soft subtractions (known as zero bins in the SCET literature) generally need to be accounted for in both virtual and real collinear diagrams when computing the bare collinear matrix element itself, we have explicitly verified that they lead to scaleless integrals for our choice of regulator, also in the presence of the quark mass.

7.2.2 Nonvalence contributions

There are two further ways in which heavy quarks can participate in the TMD fragmentation process for $m \sim k_T \sim 1/b_T \gg \Lambda_{\rm QCD}$; these were sketched in ref. [3], but we spell them out here explicitly. In one case, the resolved final state is a heavy hadron H, while the parent parton $i = q, q, \bar{q}$ is light,

$$D_{1H/i}(z_H, b_T, \mu, \zeta) = d_{1Q/i}(z_H, b_T, \mu, \zeta) \chi_H + \mathcal{O}(\Lambda_{QCD}).$$
 (7.6)

Here χ_H is again the universal inclusive fragmentation probability for $Q \to H$, while the bare matching coefficient $d_{1\,Q/i}$ is obtained from eqs. (7.2) and (7.5) after replacing the heavy-quark fields in the bare correlator by suitable unpolarized combinations of gluon or light-quark fields. In the other case, the resolved final-state hadron h is light. In this case the TMD FF $D_{1\,h/i}$ for $i=g,q,\bar{Q},Q,\bar{Q}$ has to be matched onto collinear fragmentation functions $D_{h/j}$ at the scale $\Lambda_{\rm QCD}$ where all degrees of freedom $j=g,q,\bar{q}$ are light,

$$D_{1h/i}(z_H, b_T, \mu, \zeta) = \frac{1}{z_H^2} \sum_{i} \int \frac{dz}{z} \, \mathcal{J}_{j/i}(z, b_T, m, \mu, \zeta) \, D_{h/j}\left(\frac{z_H}{z}, \mu\right) + \mathcal{O}(\Lambda_{QCD}) \,. \tag{7.7}$$

This has the standard form of matching TMD FFs onto collinear FFs, but note that we include the mass as an additional third argument of the matching coefficient to make explicit that even when i is light, the heavy quark may in general contribute to the matching at $\mu \sim m \sim k_T$ through closed loops.

7.2.3 bHQET fragmentation factors and the large-mass limit

In ref. [3], we showed that for transverse momenta $k_T \ll m$, the TMD dynamics are governed by new (and in general nonperturbative) matrix elements defined in boosted HQET [146,284] that we dubbed TMD fragmentation factors. Specifically, for $\Lambda_{\rm QCD} \lesssim k_T \ll m$ and counting

$$1 - z_H \sim 1, \tag{7.8}$$

which amounts to integrating over wide bins in z_H or taking low z_H moments, the TMD FF for producing a heavy hadron H off a heavy quark Q factorizes as [3]

$$D_{1H/Q}(z_H, b_T, \mu, \zeta) = \delta(1 - z_H) C_m(m, \mu, \zeta) \chi_{1,H} \left(b_T, \mu, \frac{\sqrt{\zeta}}{m} \right) + \mathcal{O}\left(\frac{1}{m}\right), \tag{7.9}$$

where $C_m(m, \mu, \zeta)$ is generated by separately matching collinear and soft modes at the scale $\mu \sim m$ onto HQET and QCD with n_ℓ flavors, respectively [293]; explicit expressions for C_m and other perturbative ingredients to the order required for our perturbative checks are given in appendix B.3.

In eq. (7.9), the TMD dynamics are encoded in the unpolarized TMD fragmentation factor $\chi_{1,H}$. For $\Lambda_{\rm QCD} \ll k_T \sim 1/b_T$, we showed in ref. [3] that it is given by a product of the total fragmentation probability χ_H and a perturbative matching coefficient C_1 ,

$$\chi_{1,H}(b_T, \mu, \rho) = C_1(b_T, \mu, \rho) \chi_H + \mathcal{O}(\Lambda_{QCD}^2 b_T^2),$$
(7.10)

where C_1 was calculated in ref. [1]. Here we have also introduced the shorthand $\rho \equiv v^- = \sqrt{\zeta}/m$ for the boost of the hadron.

At the partonic level, eqs. (7.9) and (7.10) together imply the following consistency condition for the partonic heavy-quark TMD FF in the limit $m \gg k_T \sim 1/b_T$ [3],

$$d_{1Q/Q}(z, b_T, \mu, \zeta) = \delta(1 - z) C_m(m, \mu, \zeta) C_1\left(b_T, \mu, \frac{\sqrt{\zeta}}{m}\right) + \mathcal{O}\left(\frac{1}{b_T m}\right), \tag{7.11}$$

and in section 7.4.1 we will use this relation as a check of our one-loop results. By contrast, nonvalence (or disfavored) partonic heavy-quark TMD FFs become power-suppressed in the heavy-quark limit,

$$i \neq Q : d_{1Q/i}(z, b_T, \mu, \zeta) = \mathcal{O}\left(\frac{1}{b_T m}\right).$$
 (7.12)

The indirect effect $(D_{1\,h/i},\,i\neq Q,\bar{Q})$ of the heavy quark on light-hadron production for $m\gg k_T$ is leading in 1/m. It is governed by virtual contributions from collinear and soft so-called mass modes and thus follows exactly the TMD PDF case [205]. Finally, the direct contribution $(D_{1\,h/Q})$ to light-hadron production becomes strongly peaked at $z_h\to 0$ in the limit $m\gg k_T\gtrsim \Lambda_{\rm QCD}$, but for any finite value of z_h (or argument z of $\mathcal{J}_{j/Q}$ at the partonic level) is kinematically suppressed as $m\gg k_T$; we will verify this latter behavior in section 7.4.1, but leave a dedicated analysis of its $z_h\to 0$ behavior – which is known to be subtle in fragmentation [357] – to future work.

7.2.4 Consistency conditions in the light-quark limit

In the case when the heavy-quark is light compared to k_T , the matching at the scale $\mu \sim k_T$ takes exactly the standard form for matching TMD FFs onto twist-2 collinear FFs [3],

$$D_{1\,\mathfrak{h}/Q}(z_{\mathfrak{h}}, b_{T}, \mu, \zeta) = \frac{1}{z_{\mathfrak{h}}^{2}} \sum_{i} \int \frac{\mathrm{d}z}{z} \, \mathcal{J}_{i/q}(z, b_{T}, \mu, \zeta) \, D_{\mathfrak{h}/i}^{(n_{\ell}+1)} \left(\frac{z_{\mathfrak{h}}}{z}, \mu\right) + \mathcal{O}(m^{2}b_{T}^{2}) \,, \tag{7.13}$$

where $\mathfrak{h}=h,H$ may be both a heavy or a light hadron and $D_{\mathfrak{h}/j}^{(n_\ell+1)}$ are collinear FFs in a theory with n_ℓ light and one massive flavor, i.e., the mass is the highest IR scale in the twist-2 matching. Importantly, the TMD FF matching coefficients $\mathcal{J}_{i/q}$ are independent of these details

in the IR and are thus given by the universal TMD FF matching coefficients in a theory with $n_f = n_\ell + 1$ light degrees of freedom, which are known to N³LO [302, 303]. The problem of the mass dependence is thus reduced to the well-understood behavior of the collinear FFs, which differs depending on whether \mathfrak{h} is heavy or light [358, 359],

$$D_{H/i}^{(n_{\ell}+1)}(z_{H},\mu) = d_{Q/i}(z_{H},\mu) \chi_{H} + \mathcal{O}\left(\frac{\Lambda_{\text{QCD}}}{m}\right),$$

$$D_{h/i}^{(n_{\ell}+1)}(z_{h},\mu) = \sum_{j} \int \frac{\mathrm{d}z}{z} \, \mathcal{M}_{j/i,T}(z,m,\mu) \, D_{h/j}^{(n)}\left(\frac{z_{h}}{z},\mu\right). \tag{7.14}$$

Here $d_{Q/i}(z_H, \mu)$ is the partonic *collinear* heavy-quark FF and $\mathcal{M}_{j/i,T}$ is the timelike matching function governing the flavor decoupling in light-hadron collinear FFs.

Comparing eqs. (7.1), (7.6), and (7.7) to eqs. (7.13) and (7.14), we can read off the following leading-power behavior of the relevant perturbative heavy-quark TMD matrix elements in the limit $m \ll k_T \sim 1/b_T$ [3],

$$d_{1Q/i}(z, b_T, \mu, \zeta) = \frac{1}{z^2} \sum_{j} \int \frac{\mathrm{d}z'}{z'} \, \mathcal{J}_{j/i}(z', b_T, \mu, \zeta) \, d_{Q/j}\left(\frac{z}{z'}, \mu\right),$$

$$\mathcal{J}_{k/i}(z, b_T, m, \mu, \zeta) = \frac{1}{z^2} \sum_{j} \int \frac{\mathrm{d}z'}{z'} \, \mathcal{J}_{j/i}(z', b_T, \mu, \zeta) \, \mathcal{M}_{k/j, T}\left(\frac{z}{z'}, m, \mu\right). \tag{7.15}$$

In section 7.4.2, we will use these expressions, together with the various known ingredients on the right-hand side, to perform cross checks of our one-loop results in section 7.3 in all channels.

7.3 Partonic heavy-quark TMD fragmentation at NLO

For ease of calculation, we will perform our calculation of the bare collinear matrix element as well as its renormalization in momentum space, i.e., as a function of z and k_T , and later compute various integral transforms of the renormalized object directly. Passing to momentum space, the one-loop correction to the renormalized heavy-quark TMD FF in eq. (7.5) reads

$$d_{1Q/Q}^{(1)}(z, k_T, \mu, \zeta) = \lim_{\epsilon \to 0} \left\{ \delta(1 - z) \frac{1}{\pi} \delta(k_T^2) Z_{\text{UV}}^{(1)}(\mu, \zeta, \epsilon) + \lim_{\eta \to 0} \left[d_{1Q/Q}^{\text{bare}(1)}(z, k_T, \epsilon, \eta, \zeta/\nu^2) + \delta(1 - z) \frac{1}{2} S^{(1)}(k_T, \epsilon, \eta, \nu) \right] \right\},$$
(7.16)

where we have used that $d_{1\,Q/Q}^{(0)} = \delta(1-z)\,\frac{1}{\pi}\delta(k_T^2)$ at tree level. (Here and in the following we use the same symbol for functions of b_T and their Fourier transforms, as the meaning is always clear from the argument.) Note that in our implementation of dimensional regularization in the transverse plane, we make use of the azimuthal symmetry of the unpolarized TMD FF and take the curly braces in eq. (7.16) to be a density in πk_T^2 for convenience, i.e., they have an integer mass dimension of -2, where the factor of π ensures that final results in d=4 are properly normalized azimuthally symmetric densities in vectorial \vec{k}_T [360,361]. With these preliminaries, the bare collinear matrix element in momentum space is given by

$$d_{1Q/Q}^{\text{bare}}(z, k_T, \epsilon, \eta, \zeta/\nu^2) = \frac{1}{2z^{1-2\epsilon}N_c} \int \frac{d\Omega_{2-2\epsilon}}{2\pi} k_T^{-2\epsilon} \operatorname{Tr} \sum_{X} \operatorname{tr} \left[\frac{\vec{n}}{2} \left\langle 0 \middle| W_{\eta}^{\dagger} \psi_Q \middle| QX \right\rangle \right] \times \left\langle QX \middle| \left[\delta \left(p^{-}/z + i\partial^{-} \right) \delta^{(2-2\epsilon)} \left(k_{\perp}^{\mu} + i\partial_{\perp}^{\mu} \right) \bar{\psi}_Q W_{\eta} \right] \middle| 0 \right\rangle \right].$$
 (7.17)

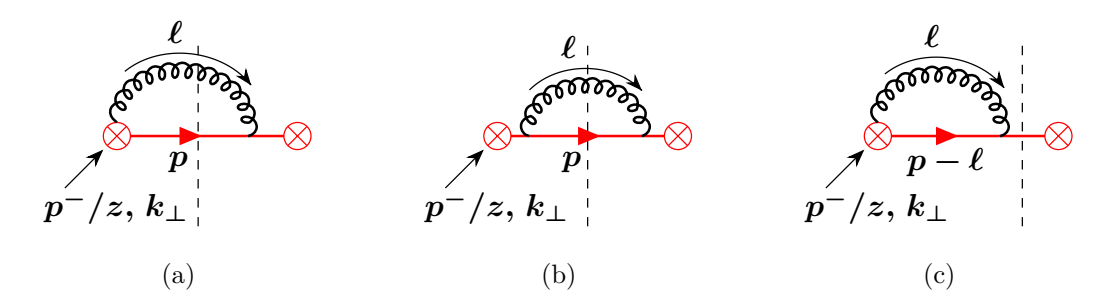


Figure 7.1: Diagrams contributing to the partonic heavy-quark TMD FF in Feynman gauge. Heavy quark propagators and field insertions are indicated in red. In diagrams (a) and (c) the gluon attaches to the Wilson lines that are part of the operators denoted by \otimes . The dashed line indicates on-shell cuts. Mirror diagrams for (a) and (c) are understood and are included in expressions given in the text.

Here $d\Omega_{2-2\epsilon}$ is the solid angle element for k_{\perp}^{μ} in $2-2\epsilon$ dimensions and the δ functions involving derivative operators on the second line act on the fields to their right, i.e., they fix the total minus and perpendicular momentum injected into the compound operator.

Compared to a direct calculation in position space, which involves expanding Bessel-like hypergeometric functions in the dimensional regulator, the main challenge in the momentum-space calculation is the careful distributional treatment of the singularity structure prior to expanding in ϵ , which we address in section 7.3.1. Renormalized results in momentum space are presented in section 7.3.2, which we independently verify and further simplify by moving to cumulant space in section 7.3.3.

7.3.1 Bare real-emission diagrams and distributional expansion

The two contributing real-emission diagrams in Feynman gauge are given in figure 7.1 (a) and (b), where X = g is a single gluon. Including the mirror diagram for (a), their contributions to $d_{1\,Q/Q}^{\rm bare\,(1)}$ evaluate to

$$d_{1\,Q/Q}^{\text{bare}\,(a)} = \frac{\alpha_s C_F}{4\pi} \frac{e^{\epsilon \gamma_E}}{\Gamma(1-\epsilon)} \left(\frac{\mu}{k_T}\right)^{2\epsilon} \left(\frac{\sqrt{\zeta}}{\nu}\right)^{-\eta} \frac{1}{\pi z^{2-2\epsilon}} \frac{z^{\eta}}{\bar{z}^{1+\eta}} \frac{4z^3}{k_T^2 z^2 + m^2 \bar{z}^2},$$
(7.18)
$$d_{1\,Q/Q}^{\text{bare}\,(b)} = \frac{\alpha_s C_F}{4\pi} \frac{e^{\epsilon \gamma_E}}{\Gamma(1-\epsilon)} \left(\frac{\mu}{k_T}\right)^{2\epsilon} \frac{1}{\pi z^{2-2\epsilon}} 2z^2 \bar{z}$$
$$\times \left[\frac{k_T^2 z^2 + m^2 (1 - 4z + z^2) - \epsilon (k_T^2 z^2 + m^2 \bar{z}^2)}{(k_T^2 z^2 + m^2 \bar{z}^2)^2}\right],$$
(7.19)

where we defined the shorthand $\bar{z} \equiv 1 - z$ and $\alpha_s = \alpha_s(\mu)$ is the renormalized $\overline{\text{MS}}$ coupling. Note that to our working order, all results in this paper are independent of whether they are expressed in terms of $\alpha_s^{(n_f)}$ or $\alpha_s^{(n_\ell)}$. We suppress overall factors of $\Theta(z)$, $\Theta(\bar{z})$, or $\Theta(k_T^2)$ from the final-state on-shell conditions in the following, but stress that they are formally present in all the distributional identities we use or derive, and also multiply all finite remainder terms. The two seemingly simple expressions above feature an intricate interplay of singularities as $k_T \to 0$ and/or $z \to 1$ ($\bar{z} \to 0$), which in particular arise as the quark propagator goes on shell for $k_T^2 z^2 + m^2 \bar{z}^2 \to 0$. At this step, the singularities are regulated by powers of $\bar{z}^{-\eta}$, dimensional regularization, or both. However, if we restrict to finite z < 1 and $k_T > 0$, the limits $\eta \to 0$ and $\epsilon \to 0$ can be taken right away and all other contributions in the renormalized one-loop formula

including the virtual diagrams drop out in eq. (7.16), leaving behind a finite result from the sum of (a) and (b),

$$z < 1 \text{ and } k_T > 0 : d_{1Q/Q}^{(1)}(z, k_T, \mu, \zeta) = \frac{\alpha_s C_F}{4\pi} \frac{2}{\pi} \frac{k_T^2 z^2 (1 + z^2) + m^2 \bar{z}^4}{\bar{z} (k_T^2 z^2 + m^2 \bar{z}^2)^2}.$$
 (7.20)

This is, exactly the differential splitting probability for $Q\bar{Q} \to (Qg)\bar{Q}$ in the quasi-collinear limit [362,363], but the field-theoretic definition of $d_{1Q/Q}$ provides us with explicit regulators controlling the singular limits. It is in this sense that the heavy-quark TMD FF, after including the virtual diagram and performing the renormalization, will provide a fully differential extension of the splitting probability into the unresolved limit(s) that is finite in d=4, universal, and embedded in factorization theorems.

We employ a distributional expansion to systematically isolate divergences using plus distributions. The contribution from diagram (a) features a $1/\eta$ pole which cancels when combined with the η -regulated soft function

$$\frac{1}{2}S^{(1)}(k_T, \epsilon, \eta, \nu) = \frac{\alpha_s C_F}{4\pi} \frac{e^{\epsilon \gamma_E}}{\Gamma(1 - \epsilon)} \left(\frac{\mu}{k_T}\right)^{2\epsilon} \frac{1}{\pi k_T^2} \left[+\frac{4}{\eta} + 2\ln\frac{\nu^2}{k_T^2} + \mathcal{O}(\eta) \right]. \tag{7.21}$$

We can now take the $\eta \to 0$ limit and referred to combined result as $d_{1Q/Q}^{\mathrm{bare}(a+s)}$. The second diagram in figure 7.1 does not need a rapdity regularization. In order to expand in the dimensional regulator, expand our results in terms of as generalized plus distributions with two variables cf. ref. [364] and use the HypExp 2.0 package [365] to expand in ϵ . For details of this calculation we refer to ref. [1]. The finite terms involving the one and two-dimensional plus distributions are lengthy and reappear in our renormalized result below, so we only quote the poles for reference:

$$d_{1Q/Q}^{\text{bare}(a+s)} + d_{1Q/Q}^{\text{bare}(b)} = \frac{\alpha_s C_F}{4\pi} \frac{1}{\pi z^2} \left\{ \delta(\bar{z}) \delta(k_T^2) \left(-\frac{2}{\epsilon} \ln \frac{\zeta}{m^2} + \frac{2}{\epsilon} \right) + \mathcal{O}(\epsilon^0) \right\}. \tag{7.22}$$

7.3.2 Virtual contributions and UV renormalization

The virtual diagram (c) from figure 7.1 is common to any collinear matrix element involving massive fermions and can be evaluated in a straightforward way using integration by contours for the ℓ^+ component of the loop momentum ℓ , Feynman parametrization for the ℓ_{\perp} integral, and an analytic ℓ^- integral at the end. Including the mirror diagram, the result reads

$$d_{1Q/Q}^{\text{bare}(c)} = \frac{\alpha_s C_F}{4\pi} \,\delta(1-z) \frac{1}{\pi} \delta(k_T^2) \, \frac{2e^{\epsilon \gamma_E} \Gamma(\epsilon)}{\epsilon (1-2\epsilon)} \frac{\mu^{2\epsilon}}{m^{2\epsilon}} \,, \tag{7.23}$$

and contributes a double $1/\epsilon^2$ pole. So far our calculation was performed in terms of bare quark fields, and we still have to account for eq. (7.3). We use the standard on-shell renormalization factor for a quark field with pole mass m in dimensional regularization,

$$Z_{\psi,\text{OS}} \equiv 1 + Z_{\psi,\text{OS}}^{(1)} + \mathcal{O}(\alpha_s^2), \qquad Z_{\psi,\text{OS}}^{(1)} = -\frac{\alpha_s C_F}{4\pi} \left(\frac{3}{\epsilon} + 3\ln\frac{\mu^2}{m^2} + 4\right).$$
 (7.24)

The $\overline{\text{MS}}$ UV renormalization factor for quark TMD PDFs and FFs is likewise well known and independent of the mass [170],

$$Z_{\text{UV}}^{(1)}(\mu,\zeta,\epsilon) = -\frac{\alpha_s C_F}{4\pi} \left\{ \frac{2}{\epsilon^2} + \frac{3}{\epsilon} - \frac{2}{\epsilon} \ln \frac{\zeta}{\mu^2} \right\}. \tag{7.25}$$

It precisely cancels the left-over poles from the mass renormalization when inserting both into eq. (7.16), as expected. We thus confirm by an explicit one-loop calculation that the TMD FF for heavy quarks obeys standard TMD evolution equations, with secondary mass effects in the Collins-Soper kernel at higher loop orders understood [205].

Taking the $\epsilon \to 0$ limit, we obtain our final result for the $\mathcal{O}(\alpha_s)$ correction to the renormalized partonic heavy-quark TMD FF:

$$d_{1Q/Q}^{(1)}(z, k_T, \mu, \zeta) = \frac{\alpha_s C_F}{4\pi} \frac{1}{\pi z^2} \left\{ \delta(\bar{z}) \left[2 \ln \frac{\zeta}{\mu^2} \mathcal{L}_0(k_T^2, \mu^2) + 2 \ln \frac{\mu^2}{m^2} \mathcal{L}_0(k_T^2, m^2) - \ln^2 \frac{\mu^2}{m^2} \delta(k_T^2) + 3 \ln \frac{\mu^2}{m^2} \delta(k_T^2) \right] + \frac{1}{m^2} \left[\frac{2xz^4(1+z^2) + 2z^2\bar{z}^4}{\bar{z}(xz^2 + \bar{z}^2)^2} \right]_{+,+} + \delta(k_T^2) \left[\frac{2(1+z^2)}{\bar{z}} \ln \left(1 + \frac{z^2}{\bar{z}^2} \right) - \frac{4z^3}{\bar{z}(1-2\bar{z}z)} \right]_{+} + \delta(\bar{z}) \frac{1}{m^2} \left[-\frac{2+3x+4x^2+3x^3+\pi\sqrt{x}(2+7x+x^2)+x(1+7x+2x^2)\ln x}{x(1+x)^3} \right]_{+} + \delta(\bar{z}) \delta(k_T^2) \left(5 - \frac{\pi}{2} - \frac{2\pi^2}{3} \right) \right\},$$

$$(7.26)$$

where we use the dimensionless variable $x \equiv k_T^2/m^2$. Eq. (7.26) is the main result of this section. The one- and two-dimensional plus distributions are defined in appendix C. Up to the terms on the first line of the right-hand side, which are predicted by the RGE and vanish for $\zeta = \mu^2 = m^2$, we have cast the heavy-quark TMD FF precisely in the form of a two-dimensional plus distribution with nontrivial functions of z and k_T living on the respective boundaries and an overall boundary contribution at z = 1 and $k_T = 0$. Of course, the total contribution in the bulk at z < 1 and $k_T > 0$, which can simply be read off from the content of the $[\dots]_{+,+}$ brackets accounting for the prefactor of $1/z^2$, is still equal to the simple result we found in eq. (7.20).

7.3.3 Cumulant space and position space results

Fixed-order subtraction methods, as well as certain q_T resummation formalisms like the RadISH approach [252], require the cumulative distribution in k_T integrated over transverse momenta \vec{k}_T with $|\vec{k}_T| \leq k_T^{\text{cut}}$ as an input,

$$d_{1Q/Q}(z, k_T^{\text{cut}}, \mu, \zeta) \equiv \pi \int^{(k_T^{\text{cut}})^2} d(k_T^2) d_{1Q/Q}(z, k_T, \mu, \zeta)$$
 (7.27)

often simply referred to as the cumulant. As for the Fourier transform we will indicate the cumulative distribution simply through its argument $k_T^{\rm cut}$.

Our final result for the NLO correction to the renormalized heavy-quark TMD FF in cumulant space reads

$$d_{1Q/Q}^{(1)}(z, k_T^{\text{cut}}, \mu, \zeta) = \frac{\alpha_s C_F}{4\pi} \frac{1}{z^2} \left\{ \delta(1-z) \left[-4 \ln \frac{\mu}{k_T^{\text{cut}}} \ln \frac{\zeta}{m^2} + 4 \ln^2 \frac{\mu}{m} + 6 \ln \frac{\mu}{m} - 4 \ln^2 \frac{k_T^{\text{cut}}}{m} + 4 - \frac{\pi^2}{6} \right] - 4 \left(1 - 2 \ln \frac{k_T^{\text{cut}}}{m} \right) \mathcal{L}_0(1-z) - 8 \mathcal{L}_1(1-z) + \mathcal{R} \left[z, \left(\frac{k_T^{\text{cut}}}{m} \right)^2 \right] \right\},$$
 (7.28)

where we defined

$$\mathcal{R}(z, x_{\text{cut}}) \equiv \frac{4 - 4z(1 - x_{\text{cut}}z)}{\bar{z}^2 + x_{\text{cut}}z^2} + 4\ln\frac{\bar{z}^2}{x_{\text{cut}}} + \frac{1}{\bar{z}}\left[2(1 + z^2)\ln\left(1 + \frac{x_{\text{cut}}z^2}{\bar{z}^2}\right) - 4z\ln\frac{x_{\text{cut}}}{\bar{z}^2}\right]. \quad (7.29)$$

We note that $\mathcal{R}(z, x_{\text{cut}}) = \mathcal{O}(\bar{z}^0)$ for $z \to 1$ and also $\mathcal{R}(z, x_{\text{cut}}) = \mathcal{O}(z^0)$ for $z \to 0$, so it is integrable in all limits. For later reference we note its total integral,

$$\int_{0}^{1} dz \, \mathcal{R}(z, x_{\text{cut}}) = -4 \text{Li}_{2} \left(1 + \frac{1}{i\sqrt{x_{\text{cut}}}} \right) - 4 \text{Li}_{2} \left(1 - \frac{1}{i\sqrt{x_{\text{cut}}}} \right) - \frac{3x_{\text{cut}}^{2} + 3x_{\text{cut}} + 2}{(1 + x_{\text{cut}})^{2}} \ln x_{\text{cut}} + \frac{2x_{\text{cut}}(x_{\text{cut}} - \pi\sqrt{x_{\text{cut}}} + 1)}{(1 + x_{\text{cut}})^{2}}.$$
 (7.30)

We now move on to position-space results in terms of the \vec{b}_T variable Fourier-conjugate to \vec{k}_T , which are the key input for producing resummed predictions from solving multiplicative b_T -space RGEs and Fourier-transforming the final result. As is standard, the two-dimensional Fourier transform of the azimuthally symmetric renormalized TMD FF at hand is simply given by a Fourier-Bessel (or Hankel) transform of zeroth order,

$$d_{1Q/Q}(z, b_T, \mu, \zeta) = 2\pi \int_0^\infty dk_T \, k_T \, J_0(b_T k_T) \, d_{1Q/Q}(z, k_T, \mu, \zeta) \,, \tag{7.31}$$

where J_n is the nth-order Bessel function of the first kind. Evaluating the relevant Hankel transforms, our result for the NLO correction to the renormalized heavy-quark TMD FF in position space reads

$$d_{1Q/Q}^{(1)}(z, b_T, \mu, \zeta) = \frac{\alpha_s C_F}{4\pi} \frac{1}{z^2} \left\{ \delta(1-z) \left[-2L_b \ln \frac{\zeta}{m^2} + 4\ln^2 \frac{\mu}{m} + 6\ln \frac{\mu}{m} - L_y^2 + 4 - \frac{\pi^2}{6} \right] - 4(1+L_y) \mathcal{L}_0(1-z) - 8\mathcal{L}_1(1-z) + \tilde{\mathcal{R}}(z, b_T m) \right\},$$
(7.32)

where we have used the shorthands

$$L_b \equiv 2 \ln \frac{b_T \mu}{2e^{-\gamma_E}}, \qquad y \equiv b_T m, \quad L_y \equiv 2 \ln \frac{y}{2e^{-\gamma_E}},$$
 (7.33)

and the regular term $\mathcal{R}(y)$ is again integrable for $z \to 0, 1$ and given by

$$\tilde{\mathcal{R}}(z,y) \equiv y \int_0^\infty dt \, J_1(ty) \, \mathcal{R}(z,t^2)$$

$$= \frac{4}{\bar{z}} \left[1 + L_y + (1+z^2) K_0 \left(\frac{y\bar{z}}{z} \right) - y\bar{z} K_1 \left(\frac{y\bar{z}}{z} \right) + 2 \ln \bar{z} \right]. \tag{7.34}$$

7.3.4 Nonvalence channels at $\mathcal{O}(\alpha_s)$

For completeness we also compute the partonic TMD FFs (or TMD FF matching coefficients onto collinear distributions) for all remaining partonic channels involving heavy quarks. The relevant diagrams at $\mathcal{O}(\alpha_s)$ are given in figure 7.2, where we labeled the identified final-state "hadron" by the momentum p. Note that for diagrams (b) and (c) compared to the otherwise identical diagrams in figure 7.1, this also changes the definition of k_{\perp} , as the coordinate system needs to be adjusted such that the gluon now has vanishing transverse momentum. Results for antiquarks are identical at this order. For the $g \to Q$ contribution, diagram (a) evaluates to

$$d_{1Q/g}^{(1)}(z,k_T) = \frac{\alpha_s}{4\pi} T_F \frac{2}{\pi z^2} \frac{k_T^2 z^4 (2z^2 - 2z + 1) + m^2 z^2}{(k_T^2 z^2 + m^2)^2}.$$
 (7.35)

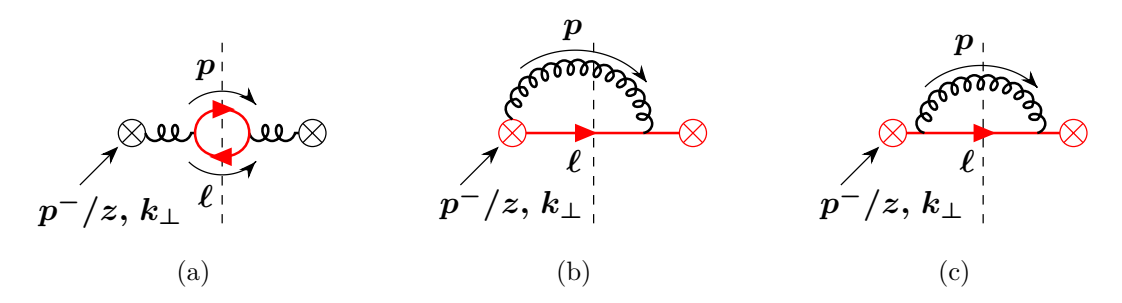


Figure 7.2: Diagrams contributing to the gluon-initiated partonic heavy-quark TMD FF and the mass-dependent TMD FF matching coefficients at $\mathcal{O}(\alpha_s)$. Heavy quark propagators and field insertions are indicated in red. The mirror diagrams for (a) and (b) are understood and are included in expressions given in the text.

For gluon production off the heavy quark, we find after summing over diagrams (b) and (c) and including the mirror diagram for (b),

$$\mathcal{J}_{g/Q}^{(1)}(z, k_T, m) = \frac{\alpha_s}{4\pi} C_F \frac{2}{\pi} \frac{k_T^2 (z^2 - 2z + 2) + m^2 z^2}{z(k_T^2 + m^2)^2}.$$
 (7.36)

It is straightforward to verify from eq. (7.20) that at 0 < z < 1 and $k_T > 0$ the above expression satisfies $1/z^2 \mathcal{J}_{g/Q}^{(1)}(z,k_T,m) = d_{1Q/Q}^{(1)}(1-z,k_T\frac{z}{1-z})$, as expected from $z \leftrightarrow 1-z$ and the simultaneous change of coordinate system; similarly, $d_{1Q/g}^{(1)}(z,k_T) = d_{1Q/g}^{(1)}(1-z,k_T\frac{z}{1-z})$. Note that the bare results in eqs. (7.35) and (7.36) are finite at z > 0 in d = 4 and without a rapidity regulator on their own, as expected because there is no cross term with the soft function or the UV renormalization at this order. This is in particular the case as $k_T \to 0$, where all singularities in k_T are now cut off by the mass for any value of z > 0.

The effect of the heavy quark on the gluon-onto-gluon matching coefficient at one loop can be written as

$$\mathcal{J}_{q/q}^{(1)}(z, k_T, m, \mu, \zeta) \equiv \mathcal{J}_{q/q}^{(1, n_\ell)}(z, k_T, \mu, \zeta) + \Delta \mathcal{J}_{q/q}^{(1, h)}(z, k_T, m), \qquad (7.37)$$

and arises purely from its contribution to the gluon wave function renormalization; here $\mathcal{J}_{g/g}^{(1,n_{\ell})}(z,k_T)$ is the well-known NLO matching coefficient for the gluon TMD onto the collinear gluon FF in the case where both are defined in a purely light theory with n_{ℓ} flavors, see eq. (B.19). After $\overline{\text{MS}}$ -renormalizing the matching coefficient, the net result is

$$\Delta \mathcal{J}_{g/g}^{(1)}(z, k_T, m, \mu) = \frac{\alpha_s T_F}{4\pi} \,\delta(1-z) \frac{1}{\pi} \delta(k_T^2) \,\frac{4}{3} \ln \frac{m^2}{\mu^2} \,. \tag{7.38}$$

This agrees with ref. [366], where the same contribution was recently revisited as part of computing all secondary heavy-quark effects in the two-loop gluon TMD PDF; we refer to that reference for a detailed discussion of how it ensures the proper TMD renormalization properties when connecting the theories with n_{ℓ} and $n_{\ell} + 1$ quark degrees of freedom. Taking cumulant integrals, we find

$$d_{1Q/g}^{(1)}(z, k_T^{\text{cut}}) = \frac{\alpha_s}{4\pi} T_F \frac{2}{z^2} \left\{ (2z^2 - 2z + 1) \ln(x_{\text{cut}}z^2 + 1) + \frac{2x_{\text{cut}}(1 - z)z^3}{x_{\text{cut}}z^2 + 1} \right\},$$

$$\mathcal{J}_{g/Q}^{(1)}(z, k_T^{\text{cut}}, m) = \frac{\alpha_s}{4\pi} C_F \frac{2}{z} \left\{ (z^2 - 2z + 2) \ln(x_{\text{cut}} + 1) + \frac{2x_{\text{cut}}(z - 1)}{1 + x_{\text{cut}}} \right\},$$
(7.39)

where $x_{\text{cut}} \equiv (k_T^{\text{cut}}/m)^2$. Finally, taking a J_1 Hankel transform of the cumulant results, we arrive at the following b_T -space results:

$$d_{1Q/g}^{(1)}(z,b_T) = \frac{\alpha_s}{4\pi} T_F \frac{4}{z^2} \left\{ (2z^2 - 2z + 1) K_0 \left(\frac{b_T m}{z} \right) + b_T m (1-z) K_1 \left(\frac{b_T m}{z} \right) \right\},$$

$$\mathcal{J}_{g/Q}^{(1)}(z,b_T,m) = \frac{\alpha_s}{4\pi} C_F \frac{4}{z} \left\{ (z^2 - 2z + 2) K_0 (b_T m) - b_T m (1-z) K_1 (b_T m) \right\}. \tag{7.40}$$

7.4 Consistency checks in the large and small-mass limits

7.4.1 Large-mass limit

To check the behavior of our final position-space results for $d_{1Q/Q}$ in eq. (7.32), we first note that the result is exponentially suppressed at z < 1 for $y \equiv mb_T \gg 1$ as a consequence of eq. (7.8) and the large-argument behavior of the Bessel K functions, i.e., it is given by $\delta(1-z)$ up to a proportionality factor. To verify the prediction from the heavy-quark limit in eq. (7.11), it is then sufficient to compare the total z integral (or any other z moment) of both sides of eq. (7.11). The total z integral yields

$$\int dz \, d_{1\,Q/Q}^{(1)}(z, b_T, \mu, \zeta) = \frac{\alpha_s C_F}{4\pi} \left\{ -2L_b \ln \frac{\zeta}{m^2} + 4\ln^2 \frac{\mu}{m} + 6\ln \frac{\mu}{m} + 4 - L_y^2 - \frac{\pi^2}{6} - \frac{4\pi}{y} + 4\mathcal{L}_0(y^2, b_0^2) + 12\delta(y^2) + \mathcal{O}\left(\frac{1}{y^3}\right) \right\}.$$
(7.41)

Here we used eq. (7.30) for the total z integral of the cumulant-space remainder term $\mathcal{R}(z, k_T^{\mathrm{cut}}/m)$, which we then power expanded for small k_T^{cut}/m , letting us evaluate the total z integral of eq. (7.34) power by power in 1/m. We point out the interesting observation that the first subleading $\mathcal{O}(1/m)$ correction in eq. (7.41) is free of large logarithms $L_y \equiv 2 \ln \frac{y}{b_0}$, $b_0 \equiv 2e^{-\gamma_E}$, suggesting a simple structure if factorized in terms of subleading $\mathcal{O}(1/m)$ TMD matrix elements in bHQET. On the other hand, the terms at the next order require plus regularization in b_T space due to their $1/y^2$ scaling and do feature a single-logarithmic term $\mathcal{L}_0(y^2, b_0^2)$.

For completeness, we may also expand the nonvalence results in eq. (7.40) for $y \gg 1$ at finite values of 0 < z < 1 in a similar way, which simply yields

$$d_{1Q/g}^{(1)}(z,b_T) = \frac{\alpha_s T_F}{4\pi} \frac{1}{z^2} \left\{ 8z^2 \, \delta(y^2) + \mathcal{O}\left(\frac{1}{y^3}\right) \right\},\,$$

$$\mathcal{J}_{g/Q}^{(1)}(z,b_T,m) = \frac{\alpha_s C_F}{4\pi} \left\{ 8z \, \delta(y^2) + \mathcal{O}\left(\frac{1}{y^3}\right) \right\},\,$$
(7.42)

i.e., both channels are in fact suppressed by $1/m^2$ at finite z.

7.4.2 Small-mass limit

Expanding eqs. (7.32) and (7.40) for small values of the mass, $y \equiv mb_T \ll 1$, we obtain:

$$d_{1Q/Q}^{(1)}(z_{H},b_{T},\mu,\zeta) = \frac{\alpha_{s}C_{F}}{4\pi} \frac{1}{z^{2}} \left\{ \delta(1-z) \left[-2L_{b} \ln \frac{\zeta}{m^{2}} + 4 \ln^{2} \frac{\mu}{m} + 6 \ln \frac{\mu}{m} - L_{y}^{2} + 4 - \frac{\pi^{2}}{6} \right] \right.$$

$$-4(1+L_{y}) \mathcal{L}_{0}(1-z) - 8\mathcal{L}_{1}(1-z)$$

$$+4+2L_{y}(1+z) + \frac{8 \ln \bar{z} - 4(1+z^{2}) \ln \frac{\bar{z}}{z}}{\bar{z}}$$

$$+y^{2} \left(\frac{1}{z^{2}} - z - \frac{L_{y}(1+z)^{2}\bar{z}}{2z^{2}} - \frac{(1+z)^{2}\bar{z} \ln \frac{\bar{z}}{z}}{z^{2}} \right) + \mathcal{O}(y^{4}) \right\},$$

$$d_{1Q/g}^{(1)}(z_{H},b_{T},\mu,\zeta) = \frac{\alpha_{s}T_{F}}{4\pi} \left\{ -2L_{y}[2(z-1)z+1] - 4(z-1)z + 4[2(z-1)z+1] \ln z + y^{2} \left(-\frac{L_{y}(1-2z)^{2}}{2z^{2}} + \frac{3(z-1)z+1}{z^{2}} + \frac{(1-2z)^{2} \ln z}{z^{2}} \right) + \mathcal{O}(y^{4}) \right\},$$

$$\mathcal{J}_{g/Q}^{(1)}(z_{H},b_{T},\mu,\zeta) = \frac{\alpha_{s}C_{F}}{4\pi} \left\{ -\frac{2L_{y}[(z-2)z+2]}{z} + \frac{4(z-1)}{z} + \frac{4(z-1)}{z^{2}} + \frac{4(z-1)}{z^{2}} \right\}$$

$$+y^{2} \left(-\frac{L_{y}(z-2)^{2}}{2z} + z + \frac{3}{z} - 3 \right) + \mathcal{O}(y^{4}) \right\}.$$

$$(7.43)$$

It is straightforward to verify that the leading $\mathcal{O}(y^0)$ terms are in full agreement with the prediction in eq. (7.15) using the one-loop ingredients collected in our notation in Appendix B.3. At leading power, the logarithms $L_y \equiv 2 \ln \frac{y}{2e^{-\gamma_E}}$ in all channels are predicted by the timelike DGLAP evolution between the TMD matching coefficients at $\mu \sim 1/b_T$ and the matching kernels and partonic collinear FFs at $\mu \sim m$. The $\mathcal{O}(y^2)$ terms, which we here give explicitly, likewise feature single logarithms L_y in all partonic channels, and can be used to investigate the $\mathcal{O}(b_T^2)$ twist-4 matching of TMD FFs in a physics setup where the low scale matrix elements at $\mu \sim m$ are perturbatively calculable.

7.5 Summary

In this section, we calculated all heavy-quark transverse-momentum dependent fragmentation functions (TMD FFs) to next-to-leading order (NLO) in the strong coupling. We provided explicit results in transverse momentum (k_T) space – both for the differential and the cumulative distribution – and in the conjugate position (b_T) space, retaining the exact dependence on k_T/m and $b_T m$, respectively, with m the mass of the heavy quark. Our calculations provide the last missing key ingredient for a complete next-to-next-to-leading logarithmic (NNLL) description of the transverse momentum distributions of observed heavy hadrons, capturing all quark mass effects. Our results also enable the extension of fixed-order subtraction methods to quasi-collinear limits involving final-state heavy quarks. As an immediate application of our results is the complete quark mass dependence of the energy-energy correlator (EEC) in the back-to-back limit at $\mathcal{O}(\alpha_s)$ which we discuss in detail in ref. [1].

Chapter 8

Conclusion

In this thesis, we have studied the effects of heavy quarks in QCD where we largely focused on Higgs boson prodution via quark interactions. Quark-mass effects are often neglected in QCD calculations as they only contribute at subleading power. However, in this era of high precision physics subleading effects become more and more important and can no longer be ignored. Recalling the multiple shortcomings of the Standard Model and the fact that as of today no direct evidence for New Physics beyond the Standard Model was found, the most promising approach is to compare high-precision measurements and theoretical predictions to look for deviations for the SM. This is particularly important for Higgs related processes as measuring and constraining the Higgs boson's properties is one of the key goals of the experiments at the LHC. An important tool for the results in this thesis are effective field theories. We used Soft-Collinear effective field theory to resum large logarithms as well as to identify the relevant diagrammatic contributions in the effective field theory. We further used boosted Heavy Quark effective theory to factorize perturbative and nonperturbative physics when discussing heavy-quark transverse-momentum dependent (TMD) fragmentation functions.

Higgs boson production via quark annihilation

We studied the transverse momentum spectrum for Higgs boson production via quark annihilation where we considered b, c and s quarks as initial state quarks. This process is interesting as it provides access to the quark Yukawa couplings in Higgs production. Further, the transverse momentum spectrum is sensitive to the quark flavor. A precise prediction for this process therefore has the potential to constrain the quark Yukawa couplings which presents an orthogonal approach for measurements from the Higgs boson decaying to a quark anti-quark pair. These measurements are rather involved and an alternative is in high demand. We have used Soft-Collinear effective theory to resum large logarithms of q_T/m_H up to N³LL' order and matched these results to fixed-order calculations where we constructed an approximation for the $\mathcal{O}(\alpha_s^3)$ contribution. In this instance, the standard procedure for matching the resummed and fixed-order contributions led to unphysically large uncertainties and we presented a modified matching procedure to resolve this issue. Our result provides the most precise prediction for the transverse momentum spectrum of quark initiated Higgs production to this day. Indeed, we could see that at N³LL'+aN³LO the uncertainties are sufficiently small to distinguish the different quark channels. Thus, these predictions could be use to constrain the Yukawa couplings from fitting to the shape of the spectra. However, we also noted that quark-mass effects become important at this high order and it would be interesting to include them in the future.

Bottom-quark effects in Higgs boson production via gluon fusion

Moreover, we studied bottom-mass effects for the Higgs transverse momentum spectrum in the gluon fusion process for the first time. In the gluon fusion process, the dominant contribution comes from a massive top-quark loop, with contributions from other quarks often neglected. However, to fully exploit high-precision measurements at the LHC, it becomes essential to account for subleading effects. In particular, the contribution from the bottom quark can no longer be ignored. The interference between the top- and bottom-quark contributions plays a significant role and is crucial for measuring the bottom-Yukawa coupling in Higgs production. These mass-effects appear at next-to-leading power and, so far, have only been considered for the form factor with just a Higgs boson in the final state. We saw that the emitted gluon introduces an additional scale, q_T , making it a three-scale problem with $m_b \ll m_H$, where m_b is the bottom mass and m_H is the Higgs mass. As a result, we had to consider different kinematic regimes and consider a factorization formulæ for the different cases. As the bottom-mass effects only appear at subleading power these contributions are plagued by endpoint divergences. For the q_T spectrum the cancellation of these endpoint divergence is particularly subtle as the coefficients of these divergences could in general be nontrivial functions of the emitted gluon momentum, k, and the b-mass. The cancellation of these divergences across different sets of diagrams indicated that the mass and the q_T dependence factorize in the factorization theorem to lowest logarithmic order which is a highly non-trivial result. Once we have a resummed prediction for this contribution, it can be combined with the N³LL'+aN³LO predictions for quark initiated Higgs production and leading-power gluon fusion to fit the Yukawa coupling from the initial state.

NNLO+PS prediction for Higgs production via quark annihilation

High precision prediction are essential to fully exploit high precision measurements at the LHC. However, an analytic expression of a kinematic distribution is often not sufficient for a comparison to experimental data. The final states from the hard interaction hadronize and form jets before they are detected. These additional steps are modeled by event generators where a parton shower describes the formation of jets.

We presented first steps towards an NNLO prediction matched to a parton shower for Higgs production via quark annihilation. To achieve this, we implemented a new combination of resolution variables in the Geneva approach. We choose the transverse momentum q_T and 1-jettiness with a transverse momentum-like measure as resolution variables to distinguish events with zero, one or more jets. The two resolution variables are resummed to NNLL' and NLL' accuracy, respectively. Commonly used parton shower algorithms tend to be ordered in transverse momentum. We, thus, expect that our choice of resolution variables will facilitate the matching to the parton shower.

Heavy quark TMDs

From years of studying particles collisions we know that partons form color-neutral bound states before they are detected. However, the fundamental process behind hadronization is still to be understood. The fragmentation of heavy quarks is particularly well suited to study the fragmentation process as they form a heavy hadron which can be identified in a zoo of light hadrons. For light quark fragmentation, on the other hand, it is impossible to tell which

of the final state hadrons contains the parent quark. In this thesis we studied heavy-quark TMD fragmentation functions (FFs) for the first time. A better understanding of heavy-quark fragmentation also paves the way for improvements in heavy flavor modeling in Monte-Carlo generators. These are used for many key searches and Higgs coupling measurements which involve final-state charm or bottom quarks. Heavy quark TMD FFs offer broad phenomenological applications such as the application of TMD fragmentation functions within jets. We are looking forward to many interesting future applications. Further, we calculated all heavy quark TMD PDFs which enabled us to perform first phenomenological studies for existing B-factories and the future EIC involving heavy quark TMDs.

TMD heavy-quark fragmentation at NLO

Moreover, we calculated all TMD fragmentation functions for heavy quarks to next-to-leading order in the strong coupling. Our calculations confirm the renormalization properties as well as large-mass and small-mass consistency relations predicted in earlier work. These results present the last missing ingredient for a NNLL resummation of transverse momentum distributions of heavy hadrons.

Concluding remarks

With first analysis of LHC run 3 data coming up and the high-luminosity LHC around the corner, the era of precision measurements has only just begun. In this thesis, we covered a broad range of topics in QCD starting from high-precision phenomenological prediction over analytic calculations of subleading-power contributions for gluon fusion to hadronization and heavy quark TMDs. Hopefully some of these topics will help gaining an even better understanding of the underlying theory. We are looking forward to comparing our new predictions against upcoming measurements.

Appendix A

Notation and conventions

A.1 Lightcone coordinates

Lightcone coordinates can be written in terms of two lightlike vectors n^{μ} and \bar{n}^{μ} with $n^2 = \bar{n}^2 = 0$ and $n \cdot \bar{n} = 2$. One possible choice is

$$n^{\mu} = (1, 0, 0, 1), \qquad \bar{n}^{\mu} = (1, 0, 0, 1)$$
 (A.1)

Now any four-vector can be written in the lightcone basis as

$$p^{\mu} = p^{+} \frac{\bar{n}^{\mu}}{2} + p^{-} \frac{n^{\mu}}{2} + p_{\perp}^{\mu} \equiv (p^{+}, p^{-}, p_{\perp}), \qquad (A.2)$$

where

$$p^+ \equiv n \cdot p = p^0 - p^3, \quad p^- \equiv \bar{n} \cdot p = p^0 + p^3, \quad p_\perp \equiv (0, p_1, p_2, 0).$$
 (A.3)

Then the inner product of two vectors is given by

$$p \cdot q = \frac{p^+ q^-}{2} + \frac{p^- q^+}{2} + p_\perp \cdot q_\perp. \tag{A.4}$$

The transverse vectors with subscript \bot are always Minkowskian, $p_{\bot}^2 \equiv p_{\bot} \cdot p_{\bot} \leq 0$, and we denote their magnitude by $p_T = \sqrt{-p_{\bot}^2}$ such that $p_T^2 \geq 0$. For *n*-collinear momenta we take the p^- component to be large such that $p^- \gg p_{\bot} \gg p^+$. The metric tensor in transverse space is given by

$$g_{\perp}^{\mu\nu} = g^{\mu\nu} - \frac{n^{\mu}\bar{n}^{\nu}}{2} - \frac{n^{\nu}\bar{n}^{\mu}}{2},$$
 (A.5)

and the antisymmetric tensor in transverse space is

$$\epsilon_{\perp}^{\mu\nu} = \epsilon^{\mu\nu\rho\sigma} \frac{\bar{n}_{\rho} n_{\sigma}}{2},\tag{A.6}$$

where we use the convention $\epsilon^{0123} = +1$.

A.2 Fourier transforms

Our convention for the Fourier conjugate of a function $f(\vec{k}_T)$ is given by

$$f(\vec{b}_T) = \int d^2 \vec{k}_T f(\vec{k}_T) e^{i\vec{b}_T \cdot \vec{k}_T}.$$
 (A.7)

The inverse Fourier transform is given by

$$f(\vec{k}_T) = \int \frac{d^2 \vec{b}_T}{(2\pi)^2} f(\vec{b}_T) e^{-i\vec{b}_T \cdot \vec{k}_T}.$$
 (A.8)

We use the same notation for the function and its Fourier conjugate. It will always be clear from the context and the argument whether we are referring to the function itself or its Fourier conjugate. If the function $f(\vec{k}_T)$ or $f(\vec{b}_T)$ has no angular dependence and therefor only depends on the magnitude $k_T \equiv |\vec{k}_T|$ or $b_T \equiv |\vec{b}_T|$, respectively, the Fourier conjugate and its inverse simplify to Hankel transforms

$$f(b_T) = 2\pi \int_0^\infty dk_T \, k_T J_0(k_T b_T) f(k_T), \tag{A.9}$$

$$f(k_T) = k_T \int_0^\infty db_T J_0(k_T b_T) f(b_T),$$
 (A.10)

where J_0 is the zeroth Bessel function of the first kind.

Appendix B

Perturbative ingredients

B.1 Anomalous dimensions

In this section, we give the anomalous dimensions needed for the N³LL' resummation. The μ dependence of the strong coupling is governed by the QCD β -function

$$\mu \frac{\mathrm{d}\alpha_s(\mu)}{\mathrm{d}\mu} \equiv \beta[\alpha_s(\mu)], \qquad \beta(\alpha_s(\mu)) = -2\alpha_s(\mu) \sum_{n=0}^{\infty} \beta_n \left(\frac{\alpha_s(\mu)}{4\pi}\right)^{n+1}, \tag{B.1}$$

The coefficients up to four loops in the $\overline{\rm MS}$ scheme are [66–69]

$$\beta_{0} = \frac{11}{3} C_{A} - \frac{4}{3} T_{F} n_{f},$$

$$\beta_{1} = \frac{34}{3} C_{A}^{2} - \left(\frac{20}{3} C_{A} + 4C_{F}\right) T_{F} n_{f},$$

$$\beta_{2} = \frac{2857}{54} C_{A}^{3} + \left(C_{F}^{2} - \frac{205}{18} C_{F} C_{A} - \frac{1415}{54} C_{A}^{2}\right) 2T_{F} n_{f} + \left(\frac{11}{9} C_{F} + \frac{79}{54} C_{A}\right) 4T_{F}^{2} n_{f}^{2},$$

$$\beta_{3} = \frac{149753}{6} + 3564\zeta_{3} - \left(\frac{1078361}{162} + \frac{6508}{27}\zeta_{3}\right) n_{f} + \left(\frac{50065}{162} + \frac{6472}{81}\zeta_{3}\right) n_{f}^{2} + \frac{1093}{729} n_{f}^{3},$$
(B.2)

where for β_3 we inserted the SU(3) color factors in order to keep the notation compact. The renormalized quark mass is given by

$$\mu \frac{\mathrm{d}m(\mu)}{\mathrm{d}\mu} = m(\mu)\gamma_m(\mu), \qquad \gamma_m(\mu) = \sum_{n=0}^{\infty} \gamma_{m,n} \left(\frac{\alpha_s(\mu)}{4\pi}\right)^{n+1}$$
(B.3)

where the coefficients are known up to five loops [77–83]. We only require the coefficients up to three loops:

$$\gamma_{m0} = -6C_F,$$

$$\gamma_{m1} = -2C_F \left(\frac{3}{2} C_F + \frac{97}{6} C_A - \frac{10}{3} T_F n_f \right),$$

$$\gamma_{m2} = -2C_F \left[\frac{11413}{108} C_A^2 - \frac{129}{4} C_F C_A + \frac{129}{2} C_F^2 + C_A T_F n_f \left(-\frac{556}{27} - 48\zeta_3 \right) + C_F T_F n_f \left(-46 + 48\zeta_3 \right) - \frac{140}{27} T_F^2 n_f^2 \right].$$
(B.4)

The cusp anomalous dimension is expanded as

$$\Gamma_{\text{cusp}}^{i}(\alpha_s) = \sum_{n=0}^{\infty} \Gamma_n^{i} \left(\frac{\alpha_s}{4\pi}\right)^{n+1},$$
(B.5)

where i indicates whether the process is quark (i = q) or gluon(i = q) induced. We have

$$\Gamma_n^q = C_F \Gamma_n, \qquad \Gamma_n^g = C_A \Gamma_n,$$
(B.6)

with the quadratic Casimir operators of QCD. The $\overline{\rm MS}$ coefficients are given by [90, 91, 216]

$$\Gamma_0 = 4$$
.

$$\Gamma_{1} = 4 \left[C_{A} \left(\frac{67}{9} - \frac{\pi^{2}}{3} \right) - \frac{20}{9} T_{F} n_{f} \right] = \frac{4}{3} \left[(4 - \pi^{2}) C_{A} + 5\beta_{0} \right],$$

$$\Gamma_{2} = 4 \left[C_{A}^{2} \left(\frac{245}{6} - \frac{134\pi^{2}}{27} + \frac{11\pi^{4}}{45} + \frac{22\zeta_{3}}{3} \right) + C_{A} T_{F} n_{f} \left(-\frac{418}{27} + \frac{40\pi^{2}}{27} - \frac{56\zeta_{3}}{3} \right) + C_{F} T_{F} n_{f} \left(-\frac{55}{3} + 16\zeta_{3} \right) - \frac{16}{27} T_{F}^{2} n_{f}^{2} \right].$$
(B.7)

The expansion of the non-cusp anomalous dimension reads

$$\gamma(\alpha_s) = \sum_{n=0}^{\infty} \gamma_n \left(\frac{\alpha_s}{4\pi}\right)^{n+1}.$$
 (B.8)

As we are only considering the resummation of a quark-induced process, we only give the $\overline{\rm MS}$ coefficients for the quark non-cusp anomalous dimension [213, 367–369]

$$\gamma_{C,0}^{q} = -3C_{F},$$

$$\gamma_{C,1}^{q} = -C_{F} \left[C_{A} \left(\frac{41}{9} - 26\zeta_{3} \right) + C_{F} \left(\frac{3}{2} - 2\pi^{2} + 24\zeta_{3} \right) + \beta_{0} \left(\frac{65}{18} + \frac{\pi^{2}}{2} \right) \right],$$

$$\gamma_{C,2}^{q} = -C_{F} \left[C_{A}^{2} \left(\frac{66167}{324} - \frac{686\pi^{2}}{81} - \frac{302\pi^{4}}{135} - \frac{782\zeta_{3}}{9} + \frac{44\pi^{2}\zeta_{3}}{9} + 136\zeta_{5} \right) + C_{F}C_{A} \left(\frac{151}{4} - \frac{205\pi^{2}}{9} - \frac{247\pi^{4}}{135} + \frac{844\zeta_{3}}{3} + \frac{8\pi^{2}\zeta_{3}}{3} + 120\zeta_{5} \right) + C_{F}^{2} \left(\frac{29}{2} + 3\pi^{2} + \frac{8\pi^{4}}{5} + 68\zeta_{3} - \frac{16\pi^{2}\zeta_{3}}{3} - 240\zeta_{5} \right) + C_{A}\beta_{0} \left(-\frac{10781}{108} + \frac{446\pi^{2}}{81} + \frac{449\pi^{4}}{270} - \frac{1166\zeta_{3}}{9} \right) + \beta_{1} \left(\frac{2953}{108} - \frac{13\pi^{2}}{18} - \frac{7\pi^{4}}{27} + \frac{128\zeta_{3}}{9} \right) + \beta_{0}^{2} \left(-\frac{2417}{324} + \frac{5\pi^{2}}{6} + \frac{2\zeta_{3}}{3} \right) \right].$$
(B.9)

For quark-initiated Higgs production, we need the quark non-cusp and the mass anomalous dimension. Then the non-cusp anomalous dimension is given by [207]

$$\gamma = 2\gamma_C^q - \gamma_m. \tag{B.10}$$

B.2 Hard function and quark scalar-current matching coefficient

For our N³LL'+aN³LO prediction in chapter 3, we also require the hard function up to three loops. The hard function, $H(Q, \mu)$, is given in terms of the hard Wilson coefficient $C(Q, \mu)$

$$H(Q,\mu) = |C(Q,\mu)|^2.$$
 (B.11)

The RGE for hard Wilson coefficients is given by [207]

$$\mu \frac{\mathrm{d}}{\mathrm{d}\mu} C(Q, \mu) = \left\{ \Gamma_{\mathrm{cusp}}[\alpha_s(\mu)] \log \frac{-Q - \mathrm{i}0}{\mu^2} + \gamma [\alpha_s(\mu)] \right\} C(Q, \mu). \tag{B.12}$$

The perturbative expansion of the Wilson coefficient can be written as

$$C(Q,\mu) = \sum_{n=0}^{\infty} C^{(n)}(L) \left[\frac{\alpha_s(\mu)}{4\pi} \right]^n.$$
 (B.13)

with

$$L = \ln \frac{Q - i0}{\mu^2}, \qquad C_n = C^{(n)}(0).$$
 (B.14)

Then the parturbative expansion of eq. (B.12) is given by [207]

$$C^{(0)} = 1,$$

$$C^{(1)}(L) = -\frac{L^2}{4}\Gamma_0 - \frac{L}{2}\gamma_0 + C_1,$$

$$C^{(2)}(L) = \frac{L^4}{32}\Gamma_0^2 + \frac{L^3}{24}\Gamma_0(2\beta_0 + 3\gamma_0) + \frac{L^2}{8}(2\beta_0\gamma_0 + \gamma_0^2 - 2C_1\Gamma_0 - 2\Gamma_1)$$

$$-\frac{L}{2}(2C_1\beta_0 + C_1\gamma_0 + \gamma_1) + C_2,$$

$$C^{(3)}(L) = -\frac{L^6}{384}\Gamma_0^3 - \frac{L^5}{192}\Gamma_0^2(4\beta_0 + 3\gamma_0) + \frac{L^4}{96}\Gamma_0(-4\beta_0^2 - 10\beta_0\gamma_0 - 3\gamma_0^2 + 3C_1\Gamma_0 + 6\Gamma_1)$$

$$+\frac{L^3}{48}\left[-8\beta_0^2\gamma_0 - 6\beta_0\gamma_0^2 - \gamma_0^3 + \Gamma_0(16C_1\beta_0 + 6C_1\gamma_0 + 6\gamma_1 + 4\beta_1) + \Gamma_1(8\beta_0 + 6\gamma_0)\right]$$

$$+\frac{L^2}{8}\left[C_1(8\beta_0^2 + 6\beta_0\gamma_0 + \gamma_0^2 - 2\Gamma_1) + 2\beta_1\gamma_0 + 4\beta_0\gamma_1 + 2\gamma_0\gamma_1 - 2C_2\Gamma_0 - 2\Gamma_2\right]$$

$$-\frac{L}{2}(4C_2\beta_0 + 2C_1\beta_1 + C_2\gamma_0 + C_1\gamma_1 + \gamma_2) + C_3,$$
(B.15)

where the tree-level result is normalized such that $C_0 = 1$. Here Γ_n are the appropriate quark or gluon cusp anomalous dimension coefficients, γ_n are the non-cusp anomalous dimension coefficients, β_n are the coefficients of the QCD β -function and C_n are the non-logarithmic constant terms.

B.2.1 Quark scalar-current matching coefficient

For our N³LL'+aN³LO prediction for quark initiated Higgs production we need the quark scalar-current matching coefficient up to three loops. The corresponding form factor has been

calculated to three loops [199]. The coefficients are given by [207]

$$\begin{split} C_{q\bar{q}\,1} &= C_F(-2+\zeta_2)\,, \\ C_{q\bar{q}\,2} &= C_F \left[C_F \left(6 + 14\zeta_2 - \frac{83}{10}\zeta_2^2 - 30\zeta_3 \right) + C_A \left(-\frac{467}{81} - \frac{103}{18}\zeta_2 + \frac{44}{5}\zeta_2^2 + \frac{151}{9}\zeta_3 \right) \right. \\ &\quad + n_f \left(\frac{200}{81} + \frac{5}{9}\zeta_2 + \frac{2}{9}\zeta_3 \right) \right] \,, \\ C_{q\bar{q}\,3} &= C_F \left[C_A^2 \left(-\frac{6152}{189}\zeta_3^3 + \frac{10093}{135}\zeta_2^2 + \frac{326}{3}\zeta_2\zeta_3 - \frac{264515}{1458}\zeta_2 - \frac{1136}{9}\zeta_3^2 + \frac{107648}{243}\zeta_3 \right. \\ &\quad + \frac{106}{9}\zeta_5 + \frac{5964431}{26244} \right) \\ &\quad + C_F C_A \left(-\frac{12676}{315}\zeta_2^3 - \frac{893}{270}\zeta_2^2 - \frac{3049}{9}\zeta_2\zeta_3 + \frac{31819}{81}\zeta_2 + \frac{296}{3}\zeta_3^2 - \frac{4820}{27}\zeta_3 \right. \\ &\quad - \frac{1676}{9}\zeta_5 - \frac{9335}{81} \right) \\ &\quad + C_F \left(\frac{37729}{630}\zeta_2^3 - 77\zeta_2^2 + 178\zeta_2\zeta_3 - \frac{353}{3}\zeta_2 + 16\zeta_3^2 - 654\zeta_3 + 424\zeta_5 + \frac{575}{3} \right) \\ &\quad + C_A n_f \left(-\frac{476}{135}\zeta_2^2 + \frac{4}{3}\zeta_2\zeta_3 + \frac{33259\zeta_2}{729} - \frac{2860}{27}\zeta_3 - \frac{4}{3}\zeta_5 - \frac{521975}{13122} \right) \\ &\quad + C_F n_f \left(-\frac{61}{27}\zeta_2^2 - \frac{38}{9}\zeta_2\zeta_3 - \frac{6131}{162}\zeta_2 + \frac{11996}{81}\zeta_3 - \frac{416}{9}\zeta_5 + \frac{35875}{972} \right) \\ &\quad + n_f^2 \left(-\frac{188}{135}\zeta_2^2 - \frac{212}{81}\zeta_2 - \frac{200}{243}\zeta_3 + \frac{2072}{6561} \right) \right]. \end{split} \tag{B.16}$$

B.3 Heavy and light matching coefficients

In this appendix we collect various perturbative ingredients from elsewhere in the literature in our notation, as used for cross-checks of our results in chapter 7. The following expressions are all accurate to one-loop order.

This section follows the appendix on perturbative ingredients from ref. [1].

B.3.1 Large-mass limit

The combined collinear and soft mass matching coefficient C_m see also ref. [3] for our notation, is given by [293]

$$C_m(m,\mu,\zeta) = 1 + \frac{\alpha_s C_F}{4\pi} \left(4 \ln^2 \frac{\mu}{m} + 2 \ln \frac{\mu}{m} + 4 + \frac{\pi^2}{6} \right) + \mathcal{O}(\alpha_s^2).$$
 (B.17)

At this order, it is also equal to the matching coefficient $H_{m,n}^{Q \to h_v}(m,\mu,\nu/\sqrt{\zeta})$ (defined in ref. [293], without the superscript) for matching massive collinear quark modes with label momentum $\sqrt{\zeta}$ onto bHQET on their own, whereas the additional contribution $\sqrt{H_{m,s}}(m,\mu,\nu)$ from matching secondary soft heavy quarks onto light soft modes becomes nontrivial at $\mathcal{O}(\alpha_s^2)$. Two-loop expressions for both are given in ref. [293], where they were extracted from the NNLO heavy-quark form factor [370, 371]. At that order, there is also a nonzero ζ dependence that arises from the rapidity renormalization of $H_{m,n}^{Q \to h_v}$ and $H_{m,s}$. The two-loop expression for secondary heavy-quark effects on the light-to-light collinear matching coefficient $H_{m,n}^{q \to q}$ is given in ref. [205] as H_c , where it was extracted from the results of refs. [293, 372]. The renormalized TMD soft

function for both the η regulator of ref. [113,118] and the exponential regulator of ref. [128] reads

$$\sqrt{S}(b_T, m, \mu, \nu) = 1 + \frac{\alpha_s C_F}{4\pi} \left[-L_b^2 + 4L_b \ln \frac{\mu}{\nu} - \frac{\pi^2}{6} \right].$$
 (B.18)

B.3.2 Small-mass limit

The massless TMD FF matching coefficients are given by [147, 303, 373]

$$\mathcal{J}_{q/q}(z, b_T, \mu, \zeta) = \delta(1 - z) + \frac{\alpha_s C_F}{4\pi} \left[\frac{4(1 + z^2) \ln(z)}{1 - z} - 4L_b \mathcal{L}_0(1 - z) \right]
+ \delta(1 - z) \left(-L_b^2 - 2L_b \ln \frac{\zeta}{\mu^2} - \frac{\pi^2}{6} \right) + 2L_b(z + 1) + 2(1 - z) \right],
\mathcal{J}_{g/q}(z, b_T, \mu, \zeta) = \frac{\alpha_s C_F}{4\pi} \left[\frac{4(z^2 - 2z + 2) \ln z}{z} - \frac{2L_b(z^2 - 2z + 2)}{z} + 2z \right],
\mathcal{J}_{g/g}(z, b_T, \mu, \zeta) = \delta(1 - z) + \frac{\alpha_s C_A}{4\pi} \left[\delta(1 - z) \left(-L_b^2 - 2L_b \ln \frac{\zeta}{\mu^2} - \frac{\pi^2}{6} \right) - 4L_b \mathcal{L}_0(1 - z) \right]
+ \frac{8(z^2 - z + 1)^2 \ln z}{(1 - z)z} + \frac{4L_b(z^3 - z^2 + 2z - 1)}{z} \right]
\mathcal{J}_{g/g}(z, b_T, \mu, \zeta) = \frac{\alpha_s T_F}{4\pi} \left[2(4z^2 - 4z + 2) \ln z - 2L_b(2z^2 - 2z + 1) + 4(1 - z)z \right].$$
(B.19)

The collinear heavy-quark FFs $d_{Q/Q}(z,\mu)$ and $d_{Q/g}(z,\mu)$ are given by [358]

$$d_{Q/Q}(z,\mu) = \delta(1-z) + \frac{\alpha_s}{4\pi} C_F \left\{ \ln \frac{\mu^2}{m^2} \left[4\mathcal{L}_0(1-z) + 3\delta(1-z) - 2(z+1) \right] - 4\mathcal{L}_0(1-z) - 8\mathcal{L}_1(1-z) + 4\delta(1-z) + 2(z+1) \left[2\ln(1-z) + 1 \right] \right\},$$

$$d_{Q/g}(z,\mu) = \frac{\alpha_s}{4\pi} T_F \left[2z^2 + 2(1-z)^2 \right] \ln \frac{\mu^2}{m^2},$$
(B.20)

The decoupling kernels relating collinear FFs in theories with $n_f = n_\ell + 1$ and n_ℓ active flavors are given by [359]

$$\mathcal{M}_{g/g}(z,\mu) = \delta(1-z) + \frac{\alpha_s T_F}{4\pi} \,\delta(1-z) \left(-\frac{4}{3}\right) \ln \frac{\mu^2}{m^2}$$

$$\mathcal{M}_{g/Q}(z,\mu) = \frac{\alpha_s}{4\pi} C_F \frac{1 + (1-z)^2}{z} \left(2 \ln \frac{\mu^2}{m^2} - 2 - 4 \ln z\right). \tag{B.21}$$

In both eqs. (B.20) and (B.21) we have rewritten the original results in terms of the minimal distributional basis of $\delta(1-z)$ and $\mathcal{L}_n(1-z)$.

Appendix C

Plus distributions

This appendix follows the appendix on plus distributions from ref. [1].

Plus distributions in a variable x formally arise in perturbative calculations as

$$f(x,\epsilon) = [f(x,\epsilon)]_{+} + \delta(x) F(\epsilon), \qquad F(\epsilon) = \int_{0}^{1} dx' f(x',\epsilon),$$
 (C.1)

where $f(x, \epsilon) \sim x^{-1-\epsilon} + \mathcal{O}(x^0)$ has a dimensionally regulated singular limit $x \to 0$ on the first left-hand side. By contrast, on the right-hand side $f(x, \epsilon)$ can be expanded in ϵ since each term in the expansion is now regulated by dimensional regularization, whereas the explicit poles are isolated in the total integral $F(\epsilon)$. The one-dimensional plus distribution is defined through their action on test functions g(x),

$$\int dx [f(x)]_{+} g(x) \equiv \int dx f(x) [g(x) - g(0) \Theta(1 - x)], \qquad (C.2)$$

where f(x) diverges at most as $x^{-1-\alpha}$ with $\alpha < 1$ for $x \to 1$ and we assume that g(x) is differentiable as $x \to 0$. The integral of $[f(x)]_+$ against the constant test function over the [0,1] vanishes by construction. The generalization of eq. (C.2) to two dimensions is given by

$$f(x,z,\epsilon) = \left[f(x,z,\epsilon) \right]_{+,+} + \delta(x) \left[F_x(z,\epsilon) \right]_{+} + \delta(\bar{z}) \left[F_z(x,\epsilon) \right]_{+} + \delta(x) \delta(\bar{z}) F_{xz}(\epsilon) , \qquad (C.3)$$

where

$$F_x(z,\epsilon) \equiv \int_0^1 dz' f(x,z',\epsilon) , \qquad F_z(x,\epsilon) \equiv \int_0^1 dx' f(x',z,\epsilon) ,$$

$$F_{xz}(\epsilon) \equiv \int_0^1 dx \int_0^1 dz' f(x,z',\epsilon)$$
(C.4)

and the two-dimensional plus bracket $[\dots]_{+,+}$ is defined through its action on test functions g(x,z) as

$$\int_{0}^{1} dx \int_{0}^{1} dz \left[f(x, z, \epsilon) \right]_{+,+} g(x, z)
\equiv \int_{0}^{1} dx \int_{0}^{1} dz f(x, z, \epsilon) \left[g(x, z) - g(0, z) - g(x, 0) + g(0, 0) \right].$$
(C.5)

Appendix C – Plus distributions

For logarithmic plus distributions with homogeneous power counting $\sim 1/x$ and their analogs for dimensionful variables, we further define the shorthands

$$\mathcal{L}_n(x) \equiv \left[\frac{\Theta(x) \ln^n x}{x} \right]_+, \quad \mathcal{L}_n(k,\mu) \equiv \frac{1}{\mu} \mathcal{L}_n\left(\frac{k}{\mu}\right), \quad \mathcal{L}_n(k_T^2,\mu^2) \equiv \frac{1}{\mu^2} \mathcal{L}_n\left(\frac{k_T^2}{\mu^2}\right). \tag{C.6}$$

The definition in eq. (C.2) enables expansions in a regulator $\alpha \sim \epsilon, \eta$ as follows,

$$\frac{\Theta(x)}{x^{1+\alpha}} = -\frac{\delta(x)}{\alpha} + \left[\frac{\Theta(x)}{x^{1+\alpha}}\right]_{+} = -\frac{\delta(x)}{\alpha} + \mathcal{L}_0(x) - \alpha \mathcal{L}_1(x) + \mathcal{O}(\alpha^2), \quad (C.7)$$

$$\frac{\Theta(x) \ln x}{x^{1+\alpha}} = -\frac{\delta(x)}{\alpha^2} + \left[\frac{\Theta(x) \ln x}{x^{1+\alpha}} \right]_+ = -\frac{\delta(x)}{\alpha^2} + \mathcal{L}_1(x) + \mathcal{O}(\alpha). \tag{C.8}$$

To relate plus distributions $\mathcal{L}_n(k,\mu)$ with different boundary conditions $\mu_{1,2}$, it is useful to shift one of the boundary conditions by making use of identities like

$$\mathcal{L}_{0}(k,\mu_{2}) = \mathcal{L}_{0}(k,\mu_{1}) + \delta(k) \ln \frac{\mu_{1}}{\mu_{2}},$$

$$\mathcal{L}_{1}(k,\mu_{2}) = \mathcal{L}_{1}(k,\mu_{1}) + \mathcal{L}_{0}(k,\mu_{1}) \ln \frac{\mu_{1}}{\mu_{2}} + \delta(k) \frac{1}{2} \ln^{2} \frac{\mu_{1}}{\mu_{2}}.$$
(C.9)

Appendix D

Additional figures

The q_T spectrum in Higgs Production via Quark Annihilation

This appendix follows the appendix from ref. [2].

In this section, we study the impact of different PDFs sets on our results for the q_T spectrum for quark initiated Higgs production. In figure D.1, we assess the impact of changing the PDF set from MSHT20nnlo to MSHT20an3lo [374]. The left panel shows the q_T spectrum at different resummation orders for the MSHT20an3lo PDF set. As expected, the perturbative convergence is equally good as for our default choice in chapter 3. The right panel shows the highest order $(N^3LL'+N^3LO)$ for both PDF sets normalized to our default MSHT20nnlo set. Although the difference for the b-quark PDF between the two sets is quite significant, this is not reflected in our final results for the q_T spectrum. The largest difference appears below $q_T \lesssim 20\,\text{GeV}$, where the MSHT20an3lo PDF leads to a 5-10% increase in the spectrum.

In figure D.2, we examine how changing the PDF set from MSHT20nnlo to CT18NNLO [375] and NNPDF31_nnlo_as_0118 [320] affects our result. For this purpose, we compare the highest order for all three PDF sets normalized to our default MSHT20nnlo set. The impact of changing the PDF set is minor for all values of q_T and smaller than the difference between MSHT20nnlo and MSHT20an3lo.

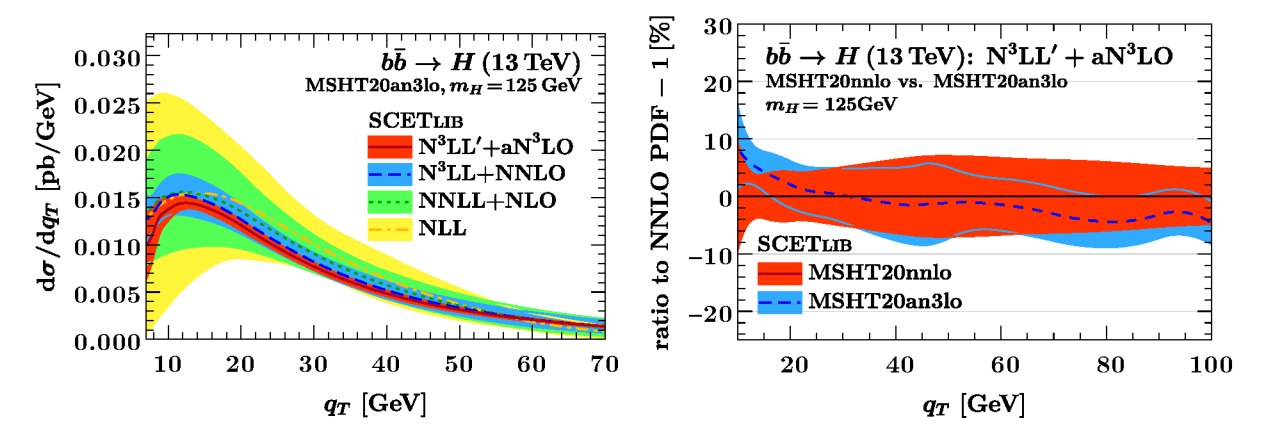


Figure D.1: Comparison of the MSHT20nnlo and the MSHT20an3lo PDF sets for $b\bar{b} \to H$.

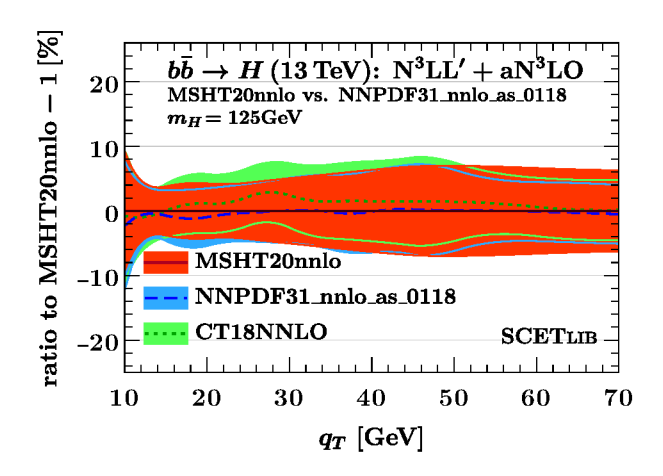


Figure D.2: Comparison of the CT18NNLO and the NNPDF31_nnlo_as_0118 PDF sets with the MSHT2Onnlo PDF set for $b\bar{b}\to H$.

Appendix E

Feynman rules

In this appendix, we give all Feynman rule that were used for our calculations in chapter 5. For the derivation of these Feynman rules, we wrote down the full QCD diagram and expanded the momenta in the appropriate soft or n_i -collinear limit.

Springs with lines denote collinear gluon, regular springs soft gluons, dashed fermion lines collinear quarks and regular fermion lines soft quarks. We again used our color coding from chapter 5 where n-collinear gluons are shown in green and \bar{n} -collinear gluons are shown in magenta. Then the collinear Feynman rules are give by

$$\begin{array}{ll}
 & = gT^{b} \left(\frac{1}{k_{1}^{-}} - \frac{1}{k_{2}^{-}} \right) \frac{\vec{n}}{2} \gamma_{\perp}^{\nu} \delta(\omega_{1} - k_{1}^{-}) \delta(\omega_{2} + k_{2}^{-}) \delta(p^{+} - q^{+}) \\
 & = -gT^{b} C_{bbg}(\xi) \frac{\vec{n}}{2} \gamma_{\perp}^{\nu} \delta(\omega_{n} - k_{2}^{-} + k_{1}^{-}) \delta(\xi \omega - k_{2}^{-}) \delta(p^{+} - q^{+}), \quad \text{(E.1)} \\
 & \bar{n}, b, \nu \\
 & \bar{n}, b, \nu \\
 & = g^{2} C_{bbg}(\xi) \frac{\bar{n}^{\rho}}{\omega_{n}} \frac{\vec{n}}{2} \gamma_{\perp}^{\nu} - \delta(p^{+} - q^{+}) \\
 & \times \left[T^{b} T^{c} \delta(\omega_{n} - k_{2}^{-} + k_{1}^{-} + k^{-}) \delta(\xi \omega - k_{2}^{-} + k^{-}) \\
 & - T^{c} T^{b} \delta(\omega_{n} - k_{2}^{-} + k_{1}^{-} + k^{-}) \delta(\xi \omega - k_{2}^{-}) \right], \quad \text{(E.2)}
\end{array}$$

For eq. (E.2), we also checked that the derivation from the full QCD diagram and using collinear gauge invariance in SCET yield the same result. For the \bar{n} -collinear contribution, the leading-order Feynman rule is obtained from symmetry: interchanging $(n \to \bar{n})$ switches n- and

 \bar{n} -collinear modes.

$$\begin{array}{ccc}
n, b, \nu & & & \\
k_2 & & & & \\
\bar{n} & & & & \\
& & & & \\
& & & & \\
& & & & \\
& & & \\
& & & \\
& & & \\
& & & \\
& & & \\
& & & \\
& & & \\
& & & \\
& & & \\
& & & \\
& & & \\
& & & \\
& & & \\
& & \\
& & & \\
& & & \\
& & & \\
& & \\
& & & \\
& & \\
& & \\
& & \\
& & \\
& & \\
& & \\
& & \\
& & \\
& & \\
& & \\
& & \\
& & \\
& & \\
& & \\
& & \\
& & \\
& & \\
& & \\
& & \\
& & \\
& & \\
& & \\
& & \\
& & \\
& & \\
& & \\
& & \\
& & \\
& & \\
& & \\
& & \\
& & \\
& & \\
& & \\
& & \\
& & \\
& & \\
& & \\
& & \\
& & \\
& & \\
& & \\
& & \\
& & \\
& & \\
& & \\
& & \\
& & \\
& & \\
& & \\
& & \\
& & \\
& & \\
& & \\
& & \\
& & \\
& & \\
& & \\
& & \\
& & \\
& & \\
& & \\
& & \\
& & \\
& & \\
& & \\
& & \\
& & \\
& & \\
& & \\
& & \\
& & \\
& & \\
& & \\
& & \\
& & \\
& & \\
& & \\
& & \\
& & \\
& & \\
& & \\
& & \\
& & \\
& & \\
& & \\
& & \\
& & \\
& & \\
& & \\
& & \\
& & \\
& & \\
& & \\
& & \\
& & \\
& & \\
& & \\
& & \\
& & \\
& & \\
& & \\
& & \\
& & \\
& & \\
& & \\
& & \\
& & \\
& & \\
& & \\
& & \\
& & \\
& & \\
& & \\
& & \\
& & \\
& & \\
& & \\
& & \\
& & \\
& & \\
& & \\
& & \\
& & \\
& & \\
& & \\
& & \\
& & \\
& & \\
& & \\
& & \\
& & \\
& & \\
& & \\
& & \\
& & \\
& & \\
& & \\
& & \\
& & \\
& & \\
& & \\
& & \\
& & \\
& & \\
& & \\
& & \\
& & \\
& & \\
& & \\
& & \\
& & \\
& & \\
& & \\
& & \\
& & \\
& & \\
& & \\
& & \\
& & \\
& & \\
& & \\
& & \\
& & \\
& & \\
& & \\
& & \\
& & \\
& & \\
& & \\
& & \\
& & \\
& & \\
& & \\
& & \\
& & \\
& & \\
& & \\
& & \\
& & \\
& & \\
& & \\
& & \\
& & \\
& & \\
& & \\
& & \\
& & \\
& & \\
& & \\
& & \\
& & \\
& & \\
& & \\
& & \\
& & \\
& & \\
& & \\
& & \\
& & \\
& & \\
& & \\
& & \\
& & \\
& & \\
& & \\
& & \\
& & \\
& & \\
& & \\
& & \\
& & \\
& & \\
& & \\
& & \\
& & \\
& & \\
& & \\
& & \\
& & \\
& & \\
& & \\
& & \\
& & \\
& & \\
& & \\
& & \\
& & \\
& & \\
& & \\
& & \\
& & \\
& & \\
& & \\
& & \\
& & \\
& & \\
& & \\
& & \\
& & \\
& & \\
& & \\
& & \\
& & \\
& & \\
& & \\
& & \\
& & \\
& & \\
& & \\
& & \\
& & \\
& & \\
& & \\
& & \\
& & \\
& & \\
& & \\
& & \\
& & \\
& & \\
& & \\
& & \\
& & \\
& & \\
& & \\
& & \\
& & \\
& & \\
& & \\
& & \\
& & \\
& & \\
& & \\
& & \\
& & \\
& & \\
& & \\
& & \\
& & \\
& & \\
& & \\
& & \\
& & \\
& & \\
& & \\
& & \\
& & \\
& & \\
& & \\
& & \\
& & \\
& & \\
& & \\
& & \\
& & \\
& & \\
& & \\
& & \\
& & \\
& & \\
& & \\
&$$

$$\frac{k_{2}}{\bar{n}} = -igT^{d}f^{dcb}\frac{\bar{n}^{\rho}}{k^{-}}C_{bbg}(\xi)\frac{n}{2}\gamma_{\perp}^{\nu}\delta(p^{-}-q^{-})\delta(\omega_{n}-k_{2}^{+}+k_{1}^{+})\delta(\xi\omega-k_{2}^{+}).$$
(E.4)

The soft Feynman rules are given by

$$\begin{array}{ccc}
\bar{n}, b, \nu & & \\
s & & p_2 \\
k_1 & & p_2 \\
k_1 & & p_1
\end{array} = g^2 \left(\frac{T^a T^b}{k_2^+ k_1^-} + \frac{T^a T^b}{k_2^- k_1^+}\right) \gamma_{\perp}^{\nu} \frac{\eta \bar{\eta}}{4} \gamma_{\perp}^{\mu}, \tag{E.5}$$

$$\begin{array}{ccc}
 & \bar{n}, b, \nu \\
 & & p_2 \\
 & n, c, \rho \\
 & k_1 & k_1 \\
 & k_1 & k_2 \\
 & k_1 & k_2 \\
 & k_1 & k_1 \\
 & k_2 & k_1 \\
 & k_1 & k_2 \\
 & k_1 & k_1 \\
 & k_2 & k_2 \\
 & k_1 & k_1 \\
 & k_2 & k_2 \\
 & k_1 & k_2 \\
 & k_1 & k_2 \\
 & k_2 & k_2 \\
 & k_1 & k_2 \\
 & k_2 & k_2 \\
 & k_1 & k_2 \\
 & k_2 & k_2 \\
 & k_1 & k_2 \\
 & k_2 & k_2 \\
 & k_1 & k_2 \\
 & k_2 & k_2 \\
 & k_1 & k_2 \\
 & k_2 & k_2 \\
 & k_1 & k_2 \\
 & k_2 & k_2 \\
 & k_1 & k_2 \\
 & k_2 & k_2 \\
 & k_1 & k_2 \\
 & k_1 & k_2 \\
 & k_2 & k_2 \\
 & k_1 & k_2 \\
 & k_2 & k_2 \\
 & k_1 & k_2 \\
 & k_2 & k_2 \\
 & k_1 & k_2 \\
 & k_2 & k_2 \\
 & k_1 & k_2 \\
 & k_1 & k_2 \\
 & k_2 & k_2 \\
 & k_1 & k_2 \\
 & k_2 & k_2 \\
 & k_1 & k_2 \\
 & k_1 & k_2 \\
 & k_2 & k_2 \\
 & k_1 & k_2 \\
 & k_1 & k_2 \\
 & k_2 & k_2 \\
 & k_1 & k_2 \\$$

Appendix F

Calculational details

In this appendix, we give some details of the calculations carried out in chapter 5.

F.1 Leading-order soft contribution

We start with calculational details on the leading-order soft calculation carried out in section 5.2.2. In the first step, we want to solve the ℓ_0 integral by contours.

$$\mathcal{M}_{s} = \int \frac{\mathrm{d}\ell_{0} \mathrm{d}\ell_{z} \mathrm{d}^{2-2\epsilon}\ell_{\perp}}{(2\pi)^{d}} \frac{-\mathrm{i}g^{2}\mu^{2\epsilon}\delta^{ab}g_{\perp}^{\mu\nu}}{(\ell_{0} - \ell_{z} + \mathrm{i}0)(\ell_{0} + \ell_{z} - \mathrm{i}0)} \frac{1}{\ell_{\perp}^{2} + \ell_{0}^{2} - \ell_{z}^{2} - m^{2} + \mathrm{i}0}$$

$$= \int \frac{\mathrm{d}\ell_{0} \mathrm{d}\ell_{z} \mathrm{d}^{2-2\epsilon}\ell_{\perp}}{(2\pi)^{d}} \frac{-\mathrm{i}g^{2}\mu^{2\epsilon}\delta^{ab}g_{\perp}^{\mu\nu}}{(\ell_{0} - \ell_{z} + \mathrm{i}0)(\ell_{0} + \ell_{z} - \mathrm{i}0)}$$

$$\times \frac{1}{(\ell_{0} + \sqrt{\ell_{z}^{2} - \ell_{\perp}^{2} + m^{2} - \mathrm{i}0})(\ell_{0} - \sqrt{\ell_{z}^{2} - \ell_{\perp}^{2} + m^{2} - \mathrm{i}0})}, \tag{F.1}$$

where we can read off the poles in the complex ℓ_0 -plane:

$$\ell_0^{1,2} = \pm \ell_z \mp i0, \qquad \ell_0^{3,4} = \pm \sqrt{\ell_z^2 - \ell_\perp^2 + m^2 - i0},$$
 (F.2)

To make the imaginary part more explicit, we expand the $\ell_0^{3,4}$

$$\ell_0^{3,4} = \pm \sqrt{\ell_z^2 - \ell_\perp^2 + m^2} \mp \frac{i0}{\sqrt{\ell_z^2 - \ell_\perp^2 + m^2}}$$
 (F.3)

where $\ell_z^2 > \text{or} < \ell_\perp^2 - m^2$ determines the location of the pole in the complex ℓ_0 plane. The resulting poles are shown in figure F.1. Using the theorem of residues for the different sets of poles, we find

$$\mathcal{M}_{s}^{>} = g^{2} \mu^{2\epsilon} \delta^{ab} g_{\perp}^{\mu\nu} \int_{\sqrt{\ell_{\perp}^{2} - m^{2}}}^{\infty} \frac{\mathrm{d}\ell_{z}}{2\pi} \int \frac{\mathrm{d}^{2-2\epsilon}\ell_{\perp}}{(2\pi)^{2-2\epsilon}} \frac{1}{\ell_{\perp}^{2} - m^{2}} \left[-\frac{1}{\ell_{z}} + \frac{1}{\sqrt{\ell_{z}^{2} - \ell_{\perp}^{2} + m^{2}}} \right],$$

$$\mathcal{M}_{s}^{<} = g^{2} \mu^{2\epsilon} \delta^{ab} g_{\perp}^{\mu\nu} \int_{-\infty}^{\sqrt{\ell_{\perp}^{2} - m^{2}}} \frac{\mathrm{d}\ell_{z}}{2\pi} \int \frac{\mathrm{d}^{2-2\epsilon}\ell_{\perp}}{(2\pi)^{2-2\epsilon}} \frac{1}{\ell_{\perp}^{2} - m^{2}} \left[-\frac{1}{\ell_{z}} - \frac{1}{\sqrt{\ell_{z}^{2} - \ell_{\perp}^{2} + m^{2}}} \right], \quad (F.4)$$

where $\mathcal{M}_s^>$ is valid for $\ell_z^2 > \ell_\perp^2 - m^2$ and $\mathcal{M}_s^<$ for $\ell_z^2 < \ell_\perp^2 - m^2$. In the next step, we want to solve the ℓ_z integral which needs to be regulated. The $1/\ell_z$ terms will combine to a scaleless

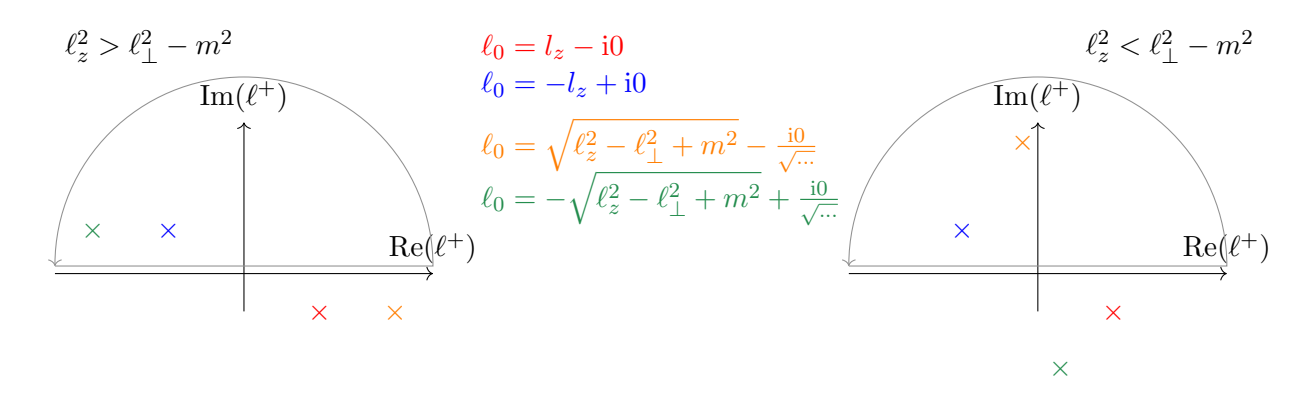


Figure F.1: Pole analysis for the soft LO₀ integral. The poles for $\ell_z^2 > \ell_\perp^2 - m^2$ are shown on the left hand side. Here the square root is positive and the imaginary part of $\ell^{3,4}$ is given by the i0. The right hand side shows the poles for $\ell_z < \ell_\perp^2 - m^2$. In this case the square root is imaginary and the poles change.

integral and can be dropped. For the second term we use the following substitution

$$\cosh x = \frac{\ell_z}{\ell_\perp^2 - m^2}, \qquad d\ell_z = \sinh x \sqrt{\ell_\perp^2 - m^2} \, dx. \tag{F.5}$$

Then,

$$\mathcal{M}_{s}^{>} = g^{2} \mu^{2\epsilon} \delta^{ab} g_{\perp}^{\mu\nu} \int \frac{\mathrm{d}^{2-2\epsilon} \ell_{\perp}}{(2\pi)^{2-2\epsilon}} \int_{\sqrt{\ell_{\perp}^{2} - m^{2}}}^{\infty} \frac{\mathrm{d} \ell_{z}}{2\pi} \frac{1}{\ell_{\perp}^{2} - m^{2}} \left| \frac{2\ell_{z}}{\nu} \right|^{-\eta} \frac{1}{\sqrt{\ell_{z}^{2} - \ell_{\perp}^{2} + m^{2}}}$$

$$= g^{2} \mu^{2\epsilon} \delta^{ab} g_{\perp}^{\mu\nu} \int \frac{\mathrm{d}^{2-2\epsilon} \ell_{\perp}}{(2\pi)^{2-2\epsilon}} \int_{0}^{\infty} \frac{\mathrm{d}x}{2\pi} \frac{1}{\ell_{\perp}^{2} - m^{2}} \left| \frac{2\sqrt{\ell_{\perp} - m^{2}}}{\nu} \right|^{-\eta} \cosh^{-\eta} x$$

$$= \frac{g^{2}}{2\pi} \mu^{2\epsilon} \delta^{ab} g_{\perp}^{\mu\nu} \frac{|\nu|^{\eta}}{\eta} {}_{2}F_{1} \left(\frac{\eta}{2}, \eta; \frac{\eta + 2}{2}; -1 \right) \int \frac{\mathrm{d}^{2-2\epsilon} \ell_{\perp}}{(2\pi)^{2-2\epsilon}} \frac{1}{(\ell_{\perp}^{2} - m^{2})^{1+\frac{\eta}{2}}}. \tag{F.6}$$

The \mathcal{M}_s^{\leq} contribution yields the same result. The ℓ_{\perp} -integral can be evaluated using standard fromulæ, yielding the final result in the $\overline{\text{MS}}$ scheme

$$\mathcal{M}_s = -\frac{i^{\eta} g^2}{4\pi^2} \delta^{ab} g_{\perp}^{\mu\nu} e^{\epsilon \gamma_E} \mu^{2\epsilon} m^{1-2\epsilon-\eta} \frac{|\nu|^{\eta}}{\eta} {}_2F_1\left(\frac{\eta}{2}, \eta; \frac{\eta+2}{2}; -1\right) \frac{\Gamma(\epsilon + \frac{\eta}{2})}{\Gamma(\frac{\eta}{2} + 1)}. \tag{F.7}$$

F.2 Leading-order hard contribution

For the massless triangle in section 5.2.3 we used

$$C_{0} = \int \frac{\mathrm{d}^{d}\ell}{(2\pi)^{2}} \frac{1}{(\ell^{2} + \mathrm{i}0)[(\ell + p_{2})^{2} + \mathrm{i}0][(\ell - p_{1})^{2} + \mathrm{i}0]}$$

$$= \mathrm{i}(4\pi)^{\epsilon - 2} \frac{\Gamma(1 - \epsilon)\Gamma(-\epsilon)\Gamma(1 + \epsilon)}{\epsilon\Gamma(1 - 2\epsilon)} (-2p_{1} \cdot p_{2} - \mathrm{i}0)^{-1 - \epsilon},$$

$$C_{2} = \int \frac{\mathrm{d}^{d}\ell}{(2\pi)^{2}} \frac{\ell^{2}}{(\ell^{2} + \mathrm{i}0)[(\ell + p_{2})^{2} + \mathrm{i}0][(\ell - p_{1})^{2} + \mathrm{i}0]}$$

$$= -\mathrm{i}4^{2\epsilon - 3}\pi^{\epsilon - \frac{3}{2}} \frac{\Gamma(1 - \epsilon)}{(\epsilon - 1)\Gamma(\frac{3}{2} - \epsilon)} (-2p_{1} \cdot p_{2} - \mathrm{i}0)^{-\epsilon} [(2 - \epsilon)\Gamma(\epsilon) + \Gamma(1 + \epsilon)],$$
(F.9)

and rewrote

$$\ell^{\mu}\ell^{\nu} = \frac{1}{d}\ell^2 g^{\mu\nu}.\tag{F.10}$$

The results for C_0 and C_2 agree with the literature.

F.3 NLO loop emission diagrams

In this section, we give some caculational details for the loop emission diagrams d_{LE}^1 and d_{LE}^2 which were discussed in section 5.4.3. For this class of diagrams, the ℓ_{\perp} integral is much more involved: First, these contribution include three propagators and we have to use Feynman parameters in order to combine them. Second, the Lorentz structure is more complicated as for the previous diagrams and features terms with ℓ_{\perp} in the numerator. The structure of the integrals is given by

$$\mathcal{M}_{d_{LE}}^{0,\pm} \sim \int d^{2}\ell_{\perp} \frac{(\#\ell_{\perp}^{\rho} + ...^{\rho})g_{\perp}^{\mu\nu} + g_{\perp}^{\nu\rho}(\#\ell_{\perp}^{\mu} + ...^{\mu}) + ...}{(\ell_{\perp}^{2} - 2\xi k_{\perp} \cdot \ell_{\perp} - m^{2})(\ell_{\perp}^{2} - m^{2})} + \frac{\#\ell_{\perp}^{2}\bar{n}^{\rho}g_{\perp}^{\mu\nu}}{(\ell_{\perp}^{2} - 2\xi k_{\perp} \cdot \ell_{\perp} - m^{2})(\ell_{\perp}^{2} - m^{2})}$$

$$= \mathcal{M}_{\epsilon^{0}, d_{LE}}^{0,\pm} + \mathcal{M}_{\frac{1}{\epsilon}, d_{LE}}^{0,\pm}, \tag{F.11}$$

where the superscripts indicate the regions for \mathcal{R} . The first term in the sum is ϵ finite whereas the the second term exhibits a 1/eps pole. We therefore split the integral in these contributions and treat them separately. Further, the ϵ finite integral contains terms $\sim \ell^{\mu}$ and $\sim \ell^{\rho}$.

We begin with combining the two denominators by introducing a Feynman parameter x. In the next step, we can complete the square and shift $\ell_{\perp} \to \ell'_{\perp}$. At this point, we can drop all terms proportional to ${\ell'}_{\perp}^{\mu}$ and ${\ell'}_{\perp}^{\rho}$ as these integrals with an odd power of ℓ_{\perp} in the numerator vanish. Next, we use standard formulæto evaluate the ${\ell'}_{\parallel}$ integrals.

The Feynman parameter integrals can be done analytically but their results become tedious to work with in the following steps. We therefore complete the square in the Feynman parameter and shift it which leads to a much simpler result

$$\mathcal{I}^{\epsilon+1} \sim \int_0^1 \mathrm{d}x \left(\frac{1}{a_1 x^2 + b_1 x + c_1} \right)^{\epsilon+1} (d_1 x^2 + e_1 x + f_1)$$

$$= \int_{\frac{b}{2a}}^{1 + \frac{b}{2a}} \mathrm{d}y \left(\frac{1}{a_1' y^2 + c_1'} \right)^{\epsilon+1} (d_1' y^2 + e_1' y + f_1'), \tag{F.12}$$

$$\mathcal{I}^{\epsilon} \sim \int_{0}^{1} dx \left(\frac{1}{a_{2}x^{2} + b_{2}x + c_{2}} \right)^{\epsilon} f_{2} = \int_{\frac{b}{2a}}^{1 + \frac{b}{2a}} dy \left(\frac{1}{a'_{2}y^{2} + c'_{2}} \right)^{\epsilon} f_{2}.$$
 (F.13)

These integrals can easily be evaluated in Mathematica. Now the the only remaining integral is the ξ integral. We will use eq. (5.50) to evaluate the integral in the central region \mathcal{R}^0 . For the $\mathcal{R}\pm$ regions only one of the limits is divergent and needs to be regulated. Since $\mathcal{M}^{0,\pm}_{\epsilon^0,d_{LE}}$ and $\mathcal{M}^{0,\pm}_{\frac{1}{\epsilon},d_{LE}}$ have a different pole structure, we will treat them separately.

$\frac{1}{\epsilon\eta}$ contribution

The finite parts of $f_{d_{LE},\frac{1}{\epsilon}}(\xi)$ in eq. (5.50) are too complicated to evaluate them analytically. Even evaluating the η finite piece in ϵ is not sufficient to solve the integrals. The integral over the $\mathcal{O}(1/\epsilon)$ term vanishes and the only missing piece is a ϵ and η finite contribution. In this thesis,

our main focus is on the cancellation of endpoint divergences. We will therefore concentrate on the divergent contributions and indicate the presence of these finite terms in our expression by "+ finite".

For the endpoint-divergent piece we find

$$\mathcal{M}_{\frac{1}{\epsilon}d_{LE}}^{0} = -\frac{(\mathrm{i}f^{abc} - d^{abc})g^{3}}{2^{5-2\epsilon}\pi^{2}}g_{\perp}^{\mu\nu}\bar{n}^{\rho} \left| \frac{\nu}{\omega_{n}} \right|^{\eta} \frac{zm(\epsilon-1)}{\omega_{n}(1-z)} \frac{\Gamma(\epsilon)}{\eta} e^{\epsilon\gamma_{E}} \left(\frac{\mu^{2}}{m^{2}} \right)^{\epsilon} \left(\frac{-m^{2}}{k_{\perp}^{2} - 4m^{2}} \right)^{\epsilon} \\ \times {}_{2}F_{1} \left(\frac{1}{2}, \epsilon, \frac{3}{2}, \frac{k_{\perp}^{2}}{k_{\perp}^{2} - 4m^{2}} \right) + \text{finite}, \qquad (F.14)$$

$$\mathcal{M}_{\frac{1}{\epsilon}d_{LE}}^{0} = -\frac{(\mathrm{i}f^{abc} + d^{abc})g^{3}}{2^{5-2\epsilon}\pi^{2}} g_{\perp}^{\mu\nu}\bar{n}^{\rho} \left| \frac{\nu}{\omega_{n}} \right|^{\eta} \frac{zm(\epsilon-1)}{\omega_{n}(1-z)} \frac{\Gamma(\epsilon)}{\eta} e^{\epsilon\gamma_{E}} \left(\frac{\mu^{2}}{m^{2}} \right)^{\epsilon} \left(\frac{-m^{2}}{k_{\perp}^{2} - 4m^{2}} \right)^{\epsilon} \\ \times {}_{2}F_{1} \left(\frac{1}{2}, \epsilon, \frac{3}{2}, \frac{k_{\perp}^{2}}{k_{\perp}^{2} - 4m^{2}} \right) + \text{finite}, \qquad (F.15)$$

$$\mathcal{M}_{\frac{1}{\epsilon}d_{LE}}^{+} = \frac{(\mathrm{i}f^{abc} - d^{abc})g^{3}}{32\pi^{2}} g_{\perp}^{\mu\nu}\bar{n}^{\rho} \frac{zm(\epsilon-1)}{\omega_{n}(1-z)} \frac{\Gamma(\epsilon)}{\eta} e^{\epsilon\gamma_{E}} \left(\frac{\mu^{2}}{m^{2}} \right)^{\epsilon} \\ \times \left[4^{\epsilon} \left(\frac{-m^{2}}{k_{\perp}^{2} - 4m^{2}} \right)^{\epsilon} {}_{2}F_{1} \left(\frac{1}{2}, \epsilon, \frac{3}{2}, \frac{k_{\perp}^{2}}{k_{\perp}^{2} - 4m^{2}} \right) \left(\frac{1}{z} - 1 \right)^{-\eta} - \eta \log z \right] \\ + \text{finite}, \qquad (F.16)$$

$$\mathcal{M}_{\frac{1}{\epsilon}d_{LE}}^{-} = \frac{(\mathrm{i}f^{abc} + d^{abc})g^{3}}{32\pi^{2}} g_{\perp}^{\mu\nu}\bar{n}^{\rho} \frac{zm(\epsilon-1)}{\omega_{n}(1-z)} \frac{\Gamma(\epsilon)}{\eta} e^{\epsilon\gamma_{E}} \left(\frac{\mu^{2}}{m^{2}} \right)^{\epsilon} \\ \times \left[4^{\epsilon} \left(\frac{-m^{2}}{k_{\perp}^{2} - 4m^{2}} \right)^{\epsilon} {}_{2}F_{1} \left(\frac{1}{2}, \epsilon, \frac{3}{2}, \frac{k_{\perp}^{2}}{k_{\perp}^{2} - 4m^{2}} \right) \left(\frac{1}{z} - 1 \right)^{-\eta} - \eta \log z \right] \\ + \text{finite}. \qquad (F.17)$$

Combining these contributions we find that all endpoint divergences cancel in the $1/\epsilon$ contribution

$$\mathcal{M}_{\frac{1}{\epsilon}d_{LE}} = \mathcal{M}_{\frac{1}{\epsilon}d_{LE}}^{0} + \mathcal{M}_{\frac{1}{\epsilon}d_{LE}}^{+} + \mathcal{M}_{\frac{1}{\epsilon}d_{LE}}^{0} + \mathcal{M}_{\frac{1}{\epsilon}d_{LE}}^{-} = \mathcal{O}(\eta^{0}).$$
 (F.18)

$\frac{\epsilon^0}{n}$ contribution

For the ϵ finite contribution, we have a similar issue as before: the η finite terms are too complicated even after expanding them in ϵ . We could not find a closed form for these terms denote them by "+ finite" as before. The final expressions are given by

$$\begin{split} \mathcal{M}^{0}_{\epsilon^{0}d_{LE}^{1}} &= -\frac{(\mathrm{i}f^{abc}-d^{abc})g^{3}}{2^{5-4\epsilon}\pi^{2-\epsilon}} \left| \frac{\nu}{\omega_{n}} \right|^{\eta} \frac{m}{\omega_{n}(1-z)} \frac{\Gamma(\epsilon+1)}{\eta} \left(\frac{1}{m^{2}}\right)^{\epsilon+1} \left(\frac{-m^{2}}{k_{\perp}^{2}-4m^{2}}\right)^{\epsilon+1} \\ &\times \left\{ \frac{zk_{\perp}^{2}}{3} {}_{2}F_{1} \left(\frac{1}{2},\epsilon+1,\frac{5}{2},\frac{k_{\perp}^{2}}{k_{\perp}^{2}-4m^{2}}\right) g_{\perp}^{\mu\nu} \bar{n}^{\rho} + {}_{2}F_{1} \left(\frac{1}{2},\epsilon+1,\frac{3}{2},\frac{k_{\perp}^{2}}{k_{\perp}^{2}-4m^{2}}\right) \right. \\ & \times \left[4z(z-1)k_{\perp}^{\mu} (\omega_{n}g_{\perp}^{\nu\rho} + k_{\perp}^{\nu}\bar{n}^{\rho}) - 4\omega_{n}(z-1)k_{\perp}^{\nu}g_{\perp}^{\mu\rho} + z(k_{\perp}^{2}-4m^{2})g_{\perp}^{\mu\nu}\bar{n}^{\rho} \right] \right\}, \\ & + \text{finite}, \quad (\text{F}.19) \\ \mathcal{M}^{0}_{\epsilon^{0}d_{LE}^{2}} &= -\frac{\left(\mathrm{i}f^{abc}+d^{abc}\right)g^{3}}{2^{5-4\epsilon}\pi^{2-\epsilon}} \left| \frac{\nu}{\omega_{n}} \right|^{\eta} \frac{m}{\omega_{n}(1-z)} \frac{\Gamma(\epsilon+1)}{\eta} \left(\frac{1}{m^{2}}\right)^{\epsilon+1} \left(\frac{-m^{2}}{k_{\perp}^{2}-4m^{2}}\right)^{\epsilon+1} \end{split}$$

$$\times \left\{ \frac{zk_{\perp}^{2}}{3} {}_{2}F_{1} \left(\frac{1}{2}, \epsilon + 1, \frac{5}{2}, \frac{k_{\perp}^{2}}{k_{\perp}^{2} - 4m^{2}} \right) g_{\perp}^{\mu\nu} \bar{n}^{\rho} + {}_{2}F_{1} \left(\frac{1}{2}, \epsilon + 1, \frac{3}{2}, \frac{k_{\perp}^{2}}{k_{\perp}^{2} - 4m^{2}} \right) \right. \\ \times \left[4z(z-1)k_{\perp}^{\mu} (\omega_{n}g_{\perp}^{\nu\rho} + k_{\perp}^{\nu}\bar{n}^{\rho}) - 4\omega_{n}(z-1)k_{\perp}^{\nu}g_{\perp}^{\mu\rho} + z(k_{\perp}^{2} - 4m^{2})g_{\perp}^{\mu\nu}\bar{n}^{\rho} \right] \right\} \\ + \text{finite}, \quad (F.20)$$

$$\times \left\{ \frac{if^{abc} - d^{abc}}{2^{5-2\epsilon}\pi^{2-\epsilon}} \frac{g^{3}}{\omega_{n}(1-z)} \frac{m}{\eta} \frac{\Gamma(\epsilon+1)}{\eta} \left(\frac{1}{m^{2}} \right)^{\epsilon+1} \left(\frac{-m^{2}}{k_{\perp}^{2} - 4m^{2}} \right)^{\epsilon+1} \\ \times \left\{ \frac{zk_{\perp}^{2}}{3} \left| \frac{\nu}{\omega_{n}} \right|^{\eta} \left(\frac{1}{z} - 1 \right)^{-\eta} {}_{2}F_{1} \left(\frac{1}{2}, \epsilon + 1, \frac{5}{2}, \frac{k_{\perp}^{2}}{k_{\perp}^{2} - 4m^{2}} \right) g_{\perp}^{\mu\nu}\bar{n}^{\rho} \right. \\ + \left. 4^{\epsilon} \eta m^{2}z \log z g_{\perp}^{\mu\nu}\bar{n}^{\rho} + \left| \frac{\nu}{\omega_{n}} \right|^{\eta} \left(\frac{1}{z} - 1 \right)^{-\eta} {}_{2}F_{1} \left(\frac{1}{2}, \epsilon + 1, \frac{3}{2}, \frac{k_{\perp}^{2}}{k_{\perp}^{2} - 4m^{2}} \right) \right. \\ \times \left. \left[4z(z-1)k_{\perp}^{\mu}(\omega_{n}g_{\perp}^{\nu\rho} + k_{\perp}^{\nu}\bar{n}^{\rho}) - 4\omega_{n}(z-1)k_{\perp}^{\nu}g_{\perp}^{\mu\rho} + z(k_{\perp}^{2} - 4m^{2})g_{\perp}^{\mu\nu}\bar{n}^{\rho} \right] \right\} \\ + f \text{finite}, \quad (F.21)$$

$$\times \left\{ \frac{zk_{\perp}^{2}}{3} \left| \frac{\nu}{\omega_{n}} \right|^{\eta} \left(\frac{1}{z} - 1 \right)^{-\eta} {}_{2}F_{1} \left(\frac{1}{2}, \epsilon + 1, \frac{5}{2}, \frac{k_{\perp}^{2}}{k_{\perp}^{2} - 4m^{2}} \right) g_{\perp}^{\mu\nu}\bar{n}^{\rho} \right. \\ + \left. 4^{\epsilon} \eta m^{2}z \log z g_{\perp}^{\mu\nu}\bar{n}^{\rho} + \left| \frac{\nu}{\omega_{n}} \right|^{\eta} \left(\frac{1}{z} - 1 \right)^{-\eta} {}_{2}F_{1} \left(\frac{1}{2}, \epsilon + 1, \frac{3}{2}, \frac{k_{\perp}^{2}}{k_{\perp}^{2} - 4m^{2}} \right) \right. \\ \times \left. \left[4z(z-1)k_{\perp}^{\mu}(\omega_{n}g_{\perp}^{\nu\rho} + k_{\perp}^{\nu}\bar{n}^{\rho}) - 4\omega_{n}(z-1)k_{\perp}^{\nu}g_{\perp}^{\mu\rho} + z(k_{\perp}^{2} - 4m^{2})g_{\perp}^{\mu\nu}\bar{n}^{\rho} \right. \right. \\ \left. + 4^{\epsilon} \eta m^{2}z \log z g_{\perp}^{\mu\nu}\bar{n}^{\rho} + \left| \frac{\nu}{\omega_{n}} \right|^{\eta} \left(\frac{1}{z} - 1 \right)^{-\eta} {}_{2}F_{1} \left(\frac{1}{2}, \epsilon + 1, \frac{3}{2}, \frac{k_{\perp}^{2}}{k_{\perp}^{2} - 4m^{2}} \right) \right. \\ \left. \times \left[4z(z-1)k_{\perp}^{\mu}(\omega_{n}g_{\perp}^{\nu\rho} + k_{\perp}^{\nu}\bar{n}^{\rho}) - 4\omega_{n}(z-1)k_{\perp}^{\nu}g_{\perp}^{\mu\rho} + z(k_{\perp}^{2} - 4m^{2})g_{\perp}^{\mu\nu}\bar{n}^{\rho} \right] \right. \\ \left. + 4^{\epsilon} \eta m^{2}z \log z g_{\perp}^{\mu\nu}\bar{n}^{\rho} + \left| \frac{\nu}{\omega_{n}} \right|^{\eta} \left(\frac{1}{z} - 1 \right)^{-\eta} {}_{2}F_{1} \left($$

Combining these results we find that the diagram class d_{LE} is free of endpoint divergences

$$\mathcal{M}_{\epsilon^0 d_{LE}} = \mathcal{M}^0_{\epsilon^0 d_{LE}^1} + \mathcal{M}^+_{\epsilon^0 d_{LE}^1} + \mathcal{M}^0_{\epsilon^0 d_{LE}^2} + \mathcal{M}^-_{\epsilon^0 d_{LE}^2} = \mathcal{M}_{\epsilon^0 d_{LE}^1} + \mathcal{M}_{\epsilon^0 d_{LE}^2} = \mathcal{O}(\eta^0). \tag{F.23}$$

References

- [1] R. von Kuk, J. K. L. Michel and Z. Sun, Transverse momentum-dependent heavy-quark fragmentation at next-to-leading order, JHEP 07 (2024) 129 [2404.08622].
- [2] P. Cal, R. von Kuk, M. A. Lim and F. J. Tackmann, qT spectrum for Higgs boson production via heavy quark annihilation at N3LL'+aN3LO, Phys. Rev. D 110 (2024) 076005 [2306.16458].
- [3] R. von Kuk, J. K. L. Michel and Z. Sun, Transverse momentum distributions of heavy hadrons and polarized heavy quarks, JHEP **09** (2023) 205 [2305.15461].
- [4] R. von Kuk, K. Lee, J. K. L. Michel and Z. Sun, Towards a Quantum Information Theory of Hadronization: Dihadron Fragmentation and Neutral Polarization in Heavy Baryons, 2503.22607.
- [5] R. von Kuk, J. K. L. Michel, I. W. Stewart, Z. Sun and F. J. Tackmann, *Bottom mass effects in Higgs production at small q_T*, in preparation.
- [6] A. Gavardi, R. von Kuk and M. A. Lim, Resumming transverse observables for NNLO+PS matching in GENEVA, in preparation.
- [7] S. L. Glashow, Partial-symmetries of weak interactions, Nuclear Physics 22 (1961) 579.
- [8] S. Weinberg, A Model of Leptons, Phys. Rev. Lett. 19 (1967) 1264.
- [9] A. Salam, Weak and Electromagnetic Interactions, Conf. Proc. C 680519 (1968) 367.
- [10] G. 't Hooft and M. J. G. Veltman, Regularization and Renormalization of Gauge Fields, Nucl. Phys. B 44 (1972) 189.
- [11] ATLAS collaboration, Observation of a new particle in the search for the Standard Model Higgs boson with the ATLAS detector at the LHC, Phys. Lett. B **716** (2012) 1 [1207.7214].
- [12] CMS collaboration, Observation of a New Boson at a Mass of 125 GeV with the CMS Experiment at the LHC, Phys. Lett. B 716 (2012) 30 [1207.7235].
- [13] P. Higgs, Broken symmetries, massless particles and gauge fields, Physics Letters 12 (1964) 132.
- [14] F. Englert and R. Brout, Broken symmetry and the mass of gauge vector mesons, Phys. Rev. Lett. 13 (1964) 321.
- [15] P. W. Higgs, Broken symmetries and the masses of gauge bosons, Phys. Rev. Lett. 13 (1964) 508.
- [16] G. S. Guralnik, C. R. Hagen and T. W. B. Kibble, Global conservation laws and massless particles, Phys. Rev. Lett. 13 (1964) 585.

- [17] P. W. Higgs, Spontaneous symmetry breakdown without massless bosons, Phys. Rev. 145 (1966) 1156.
- [18] T. W. B. Kibble, Symmetry breaking in non-abelian gauge theories, Phys. Rev. **155** (1967) 1554.
- [19] Particle Data Group collaboration, R. L. Workman and Others, *Review of Particle Physics*, *PTEP* **2022** (2022) 083C01.
- [20] SUPER-KAMIOKANDE collaboration, Y. Fukuda et al., Evidence for oscillation of atmospheric neutrinos, Phys. Rev. Lett. 81 (1998) 1562 [hep-ex/9807003].
- [21] SNO collaboration, Q. R. Ahmad et al., Direct evidence for neutrino flavor transformation from neutral current interactions in the Sudbury Neutrino Observatory, Phys. Rev. Lett. 89 (2002) 011301 [nucl-ex/0204008].
- [22] J. Wess and B. Zumino, A lagrangian model invariant under supergauge transformations, Physics Letters B 49 (1974) 52.
- [23] X. Chen, T. Gehrmann, E. W. N. Glover, A. Huss, B. Mistlberger and A. Pelloni, Fully Differential Higgs Boson Production to Third Order in QCD, Phys. Rev. Lett. 127 (2021) 072002 [2102.07607].
- [24] X. Chen, T. Gehrmann, E. W. N. Glover, A. Huss, P. F. Monni, E. Re et al., Third-Order Fiducial Predictions for Drell-Yan Production at the LHC, Phys. Rev. Lett. 128 (2022) 252001 [2203.01565].
- [25] ATLAS collaboration, Standard Model Summary Plots June 2024, .
- [26] ATLAS collaboration, Observation of $H \to b\bar{b}$ decays and VH production with the ATLAS detector, Phys. Lett. B **786** (2018) 59 [1808.08238].
- [27] ATLAS collaboration, Observation of Higgs boson production in association with a top quark pair at the LHC with the ATLAS detector, Phys. Lett. B **784** (2018) 173 [1806.00425].
- [28] CMS collaboration, Observation of $t\bar{t}H$ production, Phys. Rev. Lett. **120** (2018) 231801 [1804.02610].
- [29] Particle Data Group collaboration, S. Navas et al., Review of particle physics, Phys. Rev. D 110 (2024) 030001.
- [30] ATLAS collaboration, A detailed map of Higgs boson interactions by the ATLAS experiment ten years after the discovery, Nature 607 (2022) 52 [2207.00092].
- [31] ATLAS collaboration, Combined measurements of Higgs boson production and decay using up to 139 fb⁻¹ of proton-proton collision data at $\sqrt{s} = 13$ TeV collected with the ATLAS experiment, .
- [32] D. Dicus, T. Stelzer, Z. Sullivan and S. Willenbrock, Higgs boson production in association with bottom quarks at next-to-leading order, Phys. Rev. D 59 (1999) 094016 [hep-ph/9811492].
- [33] G. Lee and C. E. M. Wagner, Higgs bosons in heavy supersymmetry with an intermediate m_A , Phys. Rev. D **92** (2015) 075032 [1508.00576].
- [34] CMS collaboration, Observation of Higgs boson decay to bottom quarks, Phys. Rev. Lett. 121 (2018) 121801 [1808.08242].

- [35] CMS collaboration, Search for Higgs Boson Decay to a Charm Quark-Antiquark Pair in Proton-Proton Collisions at s=13 TeV, Phys. Rev. Lett. 131 (2023) 061801 [2205.05550].
- [36] ATLAS collaboration, Direct constraint on the Higgs-charm coupling from a search for Higgs boson decays into charm quarks with the ATLAS detector, Eur. Phys. J. C 82 (2022) 717 [2201.11428].
- [37] ATLAS collaboration, Search for the Decay of the Higgs Boson to Charm Quarks with the ATLAS Experiment, Phys. Rev. Lett. 120 (2018) 211802 [1802.04329].
- [38] D. Pagani, H.-S. Shao and M. Zaro, $RIP\ Hb\bar{b}$: how other Higgs production modes conspire to kill a rare signal at the LHC, JHEP 11 (2020) 036 [2005.10277].
- [39] M. A. Ebert, S. Liebler, I. Moult, I. W. Stewart, F. J. Tackmann, K. Tackmann et al., Exploiting jet binning to identify the initial state of high-mass resonances, Phys. Rev. D 94 (2016) 051901 [1605.06114].
- [40] F. Bishara, U. Haisch, P. F. Monni and E. Re, Constraining Light-Quark Yukawa Couplings from Higgs Distributions, Phys. Rev. Lett. 118 (2017) 121801 [1606.09253].
- [41] Y. Soreq, H. X. Zhu and J. Zupan, Light quark Yukawa couplings from Higgs kinematics, JHEP 12 (2016) 045 [1606.09621].
- [42] ATLAS collaboration, Measurement of the total and differential Higgs boson production cross-sections at $\sqrt{s} = 13$ TeV with the ATLAS detector by combining the $H \to ZZ^* \to 4\ell$ and $H \to \gamma\gamma$ decay channels, JHEP **05** (2023) 028 [2207.08615].
- [43] CMS collaboration, Measurements of inclusive and differential cross sections for the Higgs boson production and decay to four-leptons in proton-proton collisions at $\sqrt{s} = 13$ TeV, 2305.07532.
- [44] G. Billis, B. Dehnadi, M. A. Ebert, J. K. L. Michel and F. J. Tackmann, Higgs p_T Spectrum and Total Cross Section with Fiducial Cuts at Third Resummed and Fixed Order in QCD, Phys. Rev. Lett. 127 (2021) 072001 [2102.08039].
- [45] S. Camarda, L. Cieri and G. Ferrera, Drell-Yan lepton-pair production: qT resummation at N3LL accuracy and fiducial cross sections at N3LO, Phys. Rev. D 104 (2021) L111503 [2103.04974].
- [46] E. Re, L. Rottoli and P. Torrielli, Fiducial Higgs and Drell-Yan distributions at N³LL'+NNLO with RadISH, JHEP **09** (2021) 108 [2104.07509].
- [47] W.-L. Ju and M. Schönherr, The q_T and $\Delta \phi$ spectra in W and Z production at the LHC at $N^3LL'+N^2LO$, JHEP 10 (2021) 088 [2106.11260].
- [48] T. Neumann and J. Campbell, Fiducial Drell-Yan production at the LHC improved by transverse-momentum resummation at N4LLp+N3LO, Phys. Rev. D 107 (2023) L011506 [2207.07056].
- [49] G. Billis, J. K. L. Michel and F. J. Tackmann, Drell-Yan Transverse-Momentum Spectra at N³LL' and Approximate N⁴LL with SCETlib, 2411.16004.
- [50] A. Belyaev, P. M. Nadolsky and C. P. Yuan, Transverse momentum resummation for Higgs boson produced via b anti-b fusion at hadron colliders, JHEP 04 (2006) 004 [hep-ph/0509100].
- [51] R. V. Harlander, A. Tripathi and M. Wiesemann, Higgs production in bottom quark annihilation: Transverse momentum distribution at NNLO+NNLL, Phys. Rev. D 90 (2014) 015017 [1403.7196].

- [52] F. Spano, Unfolding in particle physics: a window on solving inverse problems, EPJ Web Conf. 55 (2013) 03002.
- [53] B. R. Webber, Fragmentation and hadronization, Int. J. Mod. Phys. A 15S1 (2000) 577 [hep-ph/9912292].
- [54] G. Zweig, An SU(3) model for strong interaction symmetry and its breaking. Version 1, .
- [55] M. Gell-Mann, A Schematic Model of Baryons and Mesons, Phys. Lett. 8 (1964) 214.
- [56] G. 't Hooft, Renormalization of Massless Yang-Mills Fields, Nucl. Phys. B 33 (1971) 173.
- [57] H. Fritzsch, M. Gell-Mann and H. Leutwyler, Advantages of the Color Octet Gluon Picture, Phys. Lett. B 47 (1973) 365.
- [58] H. D. Politzer, Reliable Perturbative Results for Strong Interactions?, Phys. Rev. Lett. **30** (1973) 1346.
- [59] D. J. Gross and F. Wilczek, Ultraviolet Behavior of Nonabelian Gauge Theories, Phys. Rev. Lett. 30 (1973) 1343.
- [60] L. D. Faddeev and V. N. Popov, Feynman Diagrams for the Yang-Mills Field, Phys. Lett. B 25 (1967) 29.
- [61] C. G. Bollini and J. J. Giambiagi, Dimensional Renormalization: The Number of Dimensions as a Regularizing Parameter, Nuovo Cim. B 12 (1972) 20.
- [62] C. G. Callan, Jr., Broken scale invariance in scalar field theory, Phys. Rev. D 2 (1970) 1541.
- [63] K. Symanzik, Small distance behavior in field theory and power counting, Commun. Math. Phys. 18 (1970) 227.
- [64] W. E. Caswell, Asymptotic Behavior of Nonabelian Gauge Theories to Two Loop Order, Phys. Rev. Lett. 33 (1974) 244.
- [65] D. R. T. Jones, Two Loop Diagrams in Yang-Mills Theory, Nucl. Phys. B 75 (1974) 531.
- [66] O. V. Tarasov, A. A. Vladimirov and A. Yu. Zharkov, The Gell-Mann-Low Function of QCD in the Three Loop Approximation, Phys. Lett. **93B** (1980) 429.
- [67] S. A. Larin and J. A. M. Vermaseren, The Three loop QCD Beta function and anomalous dimensions, Phys. Lett. B303 (1993) 334 [hep-ph/9302208].
- [68] T. van Ritbergen, J. A. M. Vermaseren and S. A. Larin, The Four loop beta function in quantum chromodynamics, Phys. Lett. B400 (1997) 379 [hep-ph/9701390].
- [69] M. Czakon, The Four-loop QCD beta-function and anomalous dimensions, Nucl. Phys. B710 (2005) 485 [hep-ph/0411261].
- [70] P. A. Baikov, K. G. Chetyrkin and J. H. Kühn, Five-Loop Running of the QCD coupling constant, Phys. Rev. Lett. 118 (2017) 082002 [1606.08659].
- [71] T. Luthe, A. Maier, P. Marquard and Y. Schröder, Towards the five-loop Beta function for a general gauge group, JHEP 07 (2016) 127 [1606.08662].
- [72] F. Herzog, B. Ruijl, T. Ueda, J. A. M. Vermaseren and A. Vogt, *The five-loop beta function of Yang-Mills theory with fermions*, *JHEP* **02** (2017) 090 [1701.01404].
- [73] T. Luthe, A. Maier, P. Marquard and Y. Schroder, The five-loop Beta function for a general gauge group and anomalous dimensions beyond Feynman gauge, JHEP 10 (2017) 166 [1709.07718].

- [74] G. F. Sterman and S. Weinberg, Jets from Quantum Chromodynamics, Phys. Rev. Lett. 39 (1977) 1436.
- [75] B. Andersson, The Lund Model, vol. 7. Cambridge University Press, 1998, 10.1017/9781009401296.
- [76] R. D. Field and S. Wolfram, A QCD Model for e+ e- Annihilation, Nucl. Phys. B 213 (1983) 65.
- [77] R. Tarrach, The Pole Mass in Perturbative QCD, Nucl. Phys. B 183 (1981) 384.
- [78] O. V. Tarasov, Anomalous dimensions of quark masses in the three-loop approximation, Phys. Part. Nucl. Lett. 17 (2020) 109 [1910.12231].
- [79] S. A. Larin, The Renormalization of the axial anomaly in dimensional regularization, Phys. Lett. B 303 (1993) 113 [hep-ph/9302240].
- [80] J. A. M. Vermaseren, S. A. Larin and T. van Ritbergen, The four loop quark mass anomalous dimension and the invariant quark mass, Phys. Lett. B 405 (1997) 327 [hep-ph/9703284].
- [81] K. G. Chetyrkin, Quark mass anomalous dimension to O (alpha-s**4), Phys. Lett. B 404 (1997) 161 [hep-ph/9703278].
- [82] P. A. Baikov, K. G. Chetyrkin and J. H. Kühn, Quark Mass and Field Anomalous Dimensions to $\mathcal{O}(\alpha_s^5)$, JHEP 10 (2014) 076 [1402.6611].
- [83] T. Luthe, A. Maier, P. Marquard and Y. Schröder, Five-loop quark mass and field anomalous dimensions for a general gauge group, JHEP 01 (2017) 081 [1612.05512].
- [84] M. Cepeda et al., Report from Working Group 2: Higgs Physics at the HL-LHC and HE-LHC, CERN Yellow Rep. Monogr. 7 (2019) 221 [1902.00134].
- [85] LHC HIGGS CROSS SECTION WORKING GROUP collaboration, D. de Florian et al., Handbook of LHC Higgs Cross Sections: 4. Deciphering the Nature of the Higgs Sector, 1610.07922.
- [86] J. C. Collins, D. E. Soper and G. F. Sterman, Factorization of Hard Processes in QCD, Adv. Ser. Direct. High Energy Phys. 5 (1989) 1 [hep-ph/0409313].
- [87] V. N. Gribov and L. N. Lipatov, Deep inelastic e p scattering in perturbation theory, Sov. J. Nucl. Phys. 15 (1972) 438.
- [88] Y. L. Dokshitzer, Calculation of the Structure Functions for Deep Inelastic Scattering and e+e- Annihilation by Perturbation Theory in Quantum Chromodynamics., Sov. Phys. JETP 46 (1977) 641.
- [89] G. Altarelli and G. Parisi, Asymptotic Freedom in Parton Language, Nucl. Phys. B 126 (1977) 298.
- [90] S. Moch, J. A. M. Vermaseren and A. Vogt, *The Three loop splitting functions in QCD: The Nonsinglet case*, *Nucl. Phys.* **B688** (2004) 101 [hep-ph/0403192].
- [91] A. Vogt, S. Moch and J. A. M. Vermaseren, *The Three-loop splitting functions in QCD: The Singlet case*, Nucl. Phys. **B691** (2004) 129 [hep-ph/0404111].
- [92] S. Moch, B. Ruijl, T. Ueda, J. Vermaseren and A. Vogt, Four-Loop Non-Singlet Splitting Functions in the Planar Limit and Beyond, JHEP 10 (2017) 041 [1707.08315].

- [93] S. Moch, B. Ruijl, T. Ueda, J. A. M. Vermaseren and A. Vogt, Low moments of the four-loop splitting functions in QCD, Phys. Lett. B 825 (2022) 136853 [2111.15561].
- [94] G. Falcioni, F. Herzog, S. Moch and A. Vogt, Four-loop splitting functions in QCD The quark-quark case, Phys. Lett. B 842 (2023) 137944 [2302.07593].
- [95] G. Falcioni, F. Herzog, S. Moch and A. Vogt, Four-loop splitting functions in QCD The gluon-to-quark case, Phys. Lett. B 846 (2023) 138215 [2307.04158].
- [96] G. Falcioni, F. Herzog, S. Moch, A. Pelloni and A. Vogt, Four-loop splitting functions in QCD The quark-to-gluon case, Phys. Lett. B 856 (2024) 138906 [2404.09701].
- [97] T. Mannel, W. Roberts and Z. Ryzak, A Derivation of the heavy quark effective Lagrangian from QCD, Nucl. Phys. B 368 (1992) 204.
- [98] B. Grinstein, The Static Quark Effective Theory, Nucl. Phys. B 339 (1990) 253.
- [99] H. Georgi, An Effective Field Theory for Heavy Quarks at Low-energies, Phys. Lett. B 240 (1990) 447.
- [100] E. Eichten and B. R. Hill, An Effective Field Theory for the Calculation of Matrix Elements Involving Heavy Quarks, Phys. Lett. B 234 (1990) 511.
- [101] C. W. Bauer, S. Fleming and M. E. Luke, Summing Sudakov logarithms in $B \to X_s \gamma in$ effective field theory., Phys. Rev. D 63 (2000) 014006 [hep-ph/0005275].
- [102] C. W. Bauer, S. Fleming, D. Pirjol and I. W. Stewart, An Effective field theory for collinear and soft gluons: Heavy to light decays, Phys. Rev. D 63 (2001) 114020 [hep-ph/0011336].
- [103] C. W. Bauer, D. Pirjol and I. W. Stewart, Soft collinear factorization in effective field theory, Phys. Rev. D 65 (2002) 054022 [hep-ph/0109045].
- [104] C. W. Bauer and I. W. Stewart, *Invariant operators in collinear effective theory*, *Phys. Lett. B* **516** (2001) 134 [hep-ph/0107001].
- [105] M. Beneke, A. P. Chapovsky, M. Diehl and T. Feldmann, Soft collinear effective theory and heavy to light currents beyond leading power, Nucl. Phys. B **643** (2002) 431 [hep-ph/0206152].
- [106] M. Beneke and T. Feldmann, Multipole expanded soft collinear effective theory with nonAbelian gauge symmetry, Phys. Lett. B 553 (2003) 267 [hep-ph/0211358].
- [107] A. V. Manohar and M. B. Wise, *Heavy quark physics*, Cambridge monographs on particle physics, nuclear physics, and cosmology. Cambridge Univ. Press, Cambridge, 2000.
- [108] G. P. Korchemsky and A. V. Radyushkin, Infrared factorization, Wilson lines and the heavy quark limit, Phys. Lett. B 279 (1992) 359 [hep-ph/9203222].
- [109] I. W. Stewart, Lectures on the Soft-Collinear Effective Theory, .
- [110] T. Becher, A. Broggio and A. Ferroglia, *Introduction to Soft-Collinear Effective Theory*, vol. 896. Springer, 2015, 10.1007/978-3-319-14848-9, [1410.1892].
- [111] C. Marcantonini and I. W. Stewart, Reparameterization Invariant Collinear Operators, Phys. Rev. D 79 (2009) 065028 [0809.1093].
- [112] X.-d. Ji, J.-p. Ma and F. Yuan, QCD factorization for semi-inclusive deep-inelastic scattering at low transverse momentum, Phys. Rev. D 71 (2005) 034005 [hep-ph/0404183].

- [113] J.-Y. Chiu, A. Jain, D. Neill and I. Z. Rothstein, A Formalism for the Systematic Treatment of Rapidity Logarithms in Quantum Field Theory, JHEP 05 (2012) 084 [1202.0814].
- [114] J. C. Collins and F. V. Tkachov, *Breakdown of dimensional regularization in the Sudakov problem*, *Phys. Lett. B* **294** (1992) 403 [hep-ph/9208209].
- [115] A. V. Manohar and I. W. Stewart, The Zero-Bin and Mode Factorization in Quantum Field Theory, Phys. Rev. D 76 (2007) 074002 [hep-ph/0605001].
- [116] J. Collins, Rapidity divergences and valid definitions of parton densities, PoS LC2008 (2008) 028 [0808.2665].
- [117] A. Vladimirov, Structure of rapidity divergences in multi-parton scattering soft factors, JHEP **04** (2018) 045 [1707.07606].
- [118] J.-y. Chiu, A. Jain, D. Neill and I. Z. Rothstein, *The Rapidity Renormalization Group*, *Phys. Rev. Lett.* **108** (2012) 151601 [1104.0881].
- [119] M. G. Echevarria, A. Idilbi and I. Scimemi, Factorization Theorem For Drell-Yan At Low q_T And Transverse Momentum Distributions On-The-Light-Cone, JHEP **07** (2012) 002 [1111.4996].
- [120] I. Balitsky, Operator expansion for high-energy scattering, Nucl. Phys. B **463** (1996) 99 [hep-ph/9509348].
- [121] J. Jalilian-Marian, A. Kovner, A. Leonidov and H. Weigert, *The Wilson renormalization group for low x physics: Towards the high density regime*, *Phys. Rev. D* **59** (1998) 014014 [hep-ph/9706377].
- [122] Y. V. Kovchegov, Small x F(2) structure function of a nucleus including multiple pomeron exchanges, Phys. Rev. D 60 (1999) 034008 [hep-ph/9901281].
- [123] J.-y. Chiu, A. Fuhrer, A. H. Hoang, R. Kelley and A. V. Manohar, *Soft-Collinear Factorization and Zero-Bin Subtractions*, *Phys. Rev. D* **79** (2009) 053007 [0901.1332].
- [124] J. Collins, Foundations of perturbative QCD, vol. 32. Cambridge University Press, 11, 2013.
- [125] M. Beneke and T. Feldmann, Factorization of heavy to light form-factors in soft collinear effective theory, Nucl. Phys. B 685 (2004) 249 [hep-ph/0311335].
- [126] T. Becher and G. Bell, Analytic Regularization in Soft-Collinear Effective Theory, Phys. Lett. B 713 (2012) 41 [1112.3907].
- [127] S. Gritschacher, A. H. Hoang, I. Jemos and P. Pietrulewicz, Secondary Heavy Quark Production in Jets through Mass Modes, Phys. Rev. D 88 (2013) 034021 [1302.4743].
- [128] Y. Li, D. Neill and H. X. Zhu, An exponential regulator for rapidity divergences, Nucl. Phys. B 960 (2020) 115193 [1604.00392].
- [129] M. A. Ebert, I. Moult, I. W. Stewart, F. J. Tackmann, G. Vita and H. X. Zhu, Subleading power rapidity divergences and power corrections for q_T , JHEP **04** (2019) 123 [1812.08189].
- [130] J. C. Collins and D. E. Soper, Back-To-Back Jets in QCD, Nucl. Phys. B 193 (1981) 381.
- [131] J. C. Collins and D. E. Soper, Back-To-Back Jets: Fourier Transform from B to K-Transverse, Nucl. Phys. B 197 (1982) 446.

- [132] J. C. Collins, D. E. Soper and G. F. Sterman, Transverse Momentum Distribution in Drell-Yan Pair and W and Z Boson Production, Nucl. Phys. B 250 (1985) 199.
- [133] S. Catani, D. de Florian and M. Grazzini, Universality of nonleading logarithmic contributions in transverse momentum distributions, Nucl. Phys. B **596** (2001) 299 [hep-ph/0008184].
- [134] D. de Florian and M. Grazzini, *The Structure of large logarithmic corrections at small transverse momentum in hadronic collisions*, *Nucl. Phys. B* **616** (2001) 247 [hep-ph/0108273].
- [135] T. Becher and M. Neubert, Drell-Yan Production at Small q_T, Transverse Parton Distributions and the Collinear Anomaly, Eur. Phys. J. C 71 (2011) 1665 [1007.4005].
- [136] M. G. Echevarria, T. Kasemets, P. J. Mulders and C. Pisano, QCD evolution of (un)polarized gluon TMDPDFs and the Higgs q_T-distribution, JHEP 07 (2015) 158 [1502.05354].
- [137] M. A. Ebert and F. J. Tackmann, Resummation of Transverse Momentum Distributions in Distribution Space, JHEP 02 (2017) 110 [1611.08610].
- [138] M. A. Ebert, J. K. L. Michel, I. W. Stewart and F. J. Tackmann, $Drell-Yan \ q_T$ resummation of fiducial power corrections at N^3LL , $JHEP \ \mathbf{04} \ (2021) \ 102 \ [2006.11382]$.
- [139] S. Frixione, P. Nason and G. Ridolfi, Problems in the resummation of soft gluon effects in the transverse momentum distributions of massive vector bosons in hadronic collisions, Nucl. Phys. B **542** (1999) 311 [hep-ph/9809367].
- [140] I. W. Stewart, F. J. Tackmann and W. J. Waalewijn, N-Jettiness: An Inclusive Event Shape to Veto Jets, Phys. Rev. Lett. 105 (2010) 092002 [1004.2489].
- [141] I. W. Stewart, F. J. Tackmann and W. J. Waalewijn, Factorization at the LHC: From PDFs to Initial State Jets, Phys. Rev. D 81 (2010) 094035 [0910.0467].
- [142] I. W. Stewart, F. J. Tackmann and W. J. Waalewijn, The Beam Thrust Cross Section for Drell-Yan at NNLL Order, Phys. Rev. Lett. 106 (2011) 032001 [1005.4060].
- [143] I. W. Stewart, F. J. Tackmann and W. J. Waalewijn, *The Quark Beam Function at NNLL*, *JHEP* **09** (2010) 005 [1002.2213].
- [144] C. Balzereit, T. Mannel and W. Kilian, Evolution of the light cone distribution function for a heavy quark, Phys. Rev. D 58 (1998) 114029 [hep-ph/9805297].
- [145] M. Neubert, Renormalization-group improved calculation of the $B \longrightarrow X(s)$ gamma branching ratio, Eur. Phys. J. C 40 (2005) 165 [hep-ph/0408179].
- [146] S. Fleming, A. H. Hoang, S. Mantry and I. W. Stewart, Top Jets in the Peak Region: Factorization Analysis with NLL Resummation, Phys. Rev. D 77 (2008) 114003 [0711.2079].
- [147] J. Collins, Foundations of perturbative QCD, Cambridge monographs on particle physics, nuclear physics, and cosmology. Cambridge Univ. Press, New York, NY, 2011.
- [148] COMPASS collaboration, M. Alekseev et al., Collins and Sivers asymmetries for pions and kaons in muon-deuteron DIS, Phys. Lett. **B673** (2009) 127 [0802.2160].
- [149] HERMES collaboration, A. Airapetian et al., Multiplicities of charged pions and kaons from semi-inclusive deep-inelastic scattering by the proton and the deuteron, Phys. Rev. D87 (2013) 074029 [1212.5407].

- [150] CLAS collaboration, H. Avakian et al., Measurement of beam-spin asymmetries for π^+ electroproduction above the baryon resonance region, Phys. Rev. D **69** (2004) 112004 [hep-ex/0301005].
- [151] E.-C. Aschenauer, A. Bazilevsky, M. Diehl, J. Drachenberg, K. O. Eyser et al., *The RHIC SPIN Program: Achievements and Future Opportunities*, 1501.01220.
- [152] STAR collaboration, L. Adamczyk et al., Measurement of the transverse single-spin asymmetry in $p^{\uparrow} + p \rightarrow W^{\pm}/Z^{0}$ at RHIC, Phys. Rev. Lett. **116** (2016) 132301 [1511.06003].
- [153] COMPASS collaboration, M. Aghasyan et al., Transverse-momentum-dependent Multiplicities of Charged Hadrons in Muon-Deuteron Deep Inelastic Scattering, Phys. Rev. D97 (2018) 032006 [1709.07374].
- [154] CLAS collaboration, S. Jawalkar et al., Semi-Inclusive π₀ target and beam-target asymmetries from 6 GeV electron scattering with CLAS, Phys. Lett. B **782** (2018) 662 [1709.10054].
- [155] B. Parsamyan, Measurement of longitudinal-target-polarization dependent azimuthal asymmetries in SIDIS at COMPASS experiment, PoS **DIS2017** (2018) 259 [1801.01488].
- [156] HERMES collaboration, A. Airapetian et al., Beam-helicity asymmetries for single-hadron production in semi-inclusive deep-inelastic scattering from unpolarized hydrogen and deuterium targets, Phys. Lett. B 797 (2019) 134886 [1903.08544].
- [157] HERMES collaboration, A. Airapetian et al., Azimuthal single- and double-spin asymmetries in semi-inclusive deep-inelastic lepton scattering by transversely polarized protons, JHEP 12 (2020) 010 [2007.07755].
- [158] CLAS collaboration, S. Moran et al., Measurement of charged-pion production in deep-inelastic scattering off nuclei with the CLAS detector, Phys. Rev. C 105 (2022) 015201 [2109.09951].
- [159] I. Scimemi and A. Vladimirov, Non-perturbative structure of semi-inclusive deep-inelastic and Drell-Yan scattering at small transverse momentum, JHEP 06 (2020) 137 [1912.06532].
- [160] A. Bacchetta, V. Bertone, C. Bissolotti, G. Bozzi, F. Delcarro, F. Piacenza et al., Transverse-momentum-dependent parton distributions up to N³LL from Drell-Yan data, JHEP 07 (2020) 117 [1912.07550].
- [161] M. Bury, A. Prokudin and A. Vladimirov, Extraction of the Sivers function from SIDIS, Drell-Yan, and W^{\pm}/Z boson production data with TMD evolution, JHEP **05** (2021) 151 [2103.03270].
- [162] MAP collaboration, A. Bacchetta, V. Bertone, C. Bissolotti, G. Bozzi, M. Cerutti, F. Piacenza et al., Unpolarized transverse momentum distributions from a global fit of Drell-Yan and semi-inclusive deep-inelastic scattering data, JHEP 10 (2022) 127 [2206.07598].
- [163] M. A. Ebert, I. W. Stewart and Y. Zhao, Determining the Nonperturbative Collins-Soper Kernel From Lattice QCD, Phys. Rev. **D99** (2019) 034505 [1811.00026].
- [164] X. Ji, Y. Liu and Y.-S. Liu, TMD soft function from large-momentum effective theory, Nucl. Phys. B 955 (2020) 115054 [1910.11415].

- [165] P. Shanahan, M. Wagman and Y. Zhao, Collins-Soper kernel for TMD evolution from lattice QCD, Phys. Rev. D 102 (2020) 014511 [2003.06063].
- [166] P. Shanahan, M. Wagman and Y. Zhao, Lattice QCD calculation of the Collins-Soper kernel from quasi-TMDPDFs, Phys. Rev. D 104 (2021) 114502 [2107.11930].
- [167] M. Schlemmer, A. Vladimirov, C. Zimmermann, M. Engelhardt and A. Schäfer, Determination of the Collins-Soper Kernel from Lattice QCD, JHEP 08 (2021) 004 [2103.16991].
- [168] Y. Li et al., Lattice QCD Study of Transverse-Momentum Dependent Soft Function, Phys. Rev. Lett. 128 (2022) 062002 [2106.13027].
- [169] LPC collaboration, M.-H. Chu et al., Nonperturbative Determination of Collins-Soper Kernel from Quasi Transverse-Momentum Dependent Wave Functions, 2204.00200.
- [170] R. Boussarie et al., TMD Handbook, 2304.03302.
- [171] A. Bacchetta, M. Diehl, K. Goeke, A. Metz, P. J. Mulders and M. Schlegel, Semi-inclusive deep inelastic scattering at small transverse momentum, JHEP 02 (2007) 093 [hep-ph/0611265].
- [172] M. A. Ebert, A. Gao and I. W. Stewart, Factorization for azimuthal asymmetries in SIDIS at next-to-leading power, JHEP 06 (2022) 007 [2112.07680].
- [173] A. Bacchetta, U. D'Alesio, M. Diehl and C. A. Miller, Single-spin asymmetries: The Trento conventions, Phys. Rev. D 70 (2004) 117504 [hep-ph/0410050].
- [174] D. W. Sivers, Single Spin Production Asymmetries from the Hard Scattering of Point-Like Constituents, Phys. Rev. D 41 (1990) 83.
- [175] A. M. Kotzinian and P. J. Mulders, Longitudinal quark polarization in transversely polarized nucleons, Phys. Rev. D 54 (1996) 1229 [hep-ph/9511420].
- [176] A. M. Kotzinian and P. J. Mulders, *Probing transverse quark polarization via azimuthal asymmetries in leptoproduction*, *Phys. Lett. B* **406** (1997) 373 [hep-ph/9701330].
- [177] D. Boer and P. J. Mulders, Time reversal odd distribution functions in leptoproduction, Phys. Rev. D 57 (1998) 5780 [hep-ph/9711485].
- [178] P. J. Mulders and R. D. Tangerman, The Complete tree level result up to order 1/Q for polarized deep inelastic leptoproduction, Nucl. Phys. B 461 (1996) 197 [hep-ph/9510301].
- [179] R. Abdul Khalek et al., Science Requirements and Detector Concepts for the Electron-Ion Collider: EIC Yellow Report, 2103.05419.
- [180] J. C. Collins and A. Metz, Universality of soft and collinear factors in hard-scattering factorization, Phys. Rev. Lett. 93 (2004) 252001 [hep-ph/0408249].
- [181] D. Boer, L. Gamberg, B. Musch and A. Prokudin, Bessel-Weighted Asymmetries in Semi Inclusive Deep Inelastic Scattering, JHEP 10 (2011) 021 [1107.5294].
- [182] C. Balazs, H.-J. He and C. P. Yuan, QCD corrections to scalar production via heavy quark fusion at hadron colliders, Phys. Rev. D 60 (1999) 114001 [hep-ph/9812263].
- [183] R. V. Harlander and W. B. Kilgore, *Higgs boson production in bottom quark fusion at next-to-next-to leading order*, *Phys. Rev. D* **68** (2003) 013001 [hep-ph/0304035].
- [184] S. Dittmaier, M. Krämer and M. Spira, *Higgs radiation off bottom quarks at the Tevatron and the CERN LHC*, *Phys. Rev. D* **70** (2004) 074010 [hep-ph/0309204].

- [185] S. Dawson, C. B. Jackson, L. Reina and D. Wackeroth, Exclusive Higgs boson production with bottom quarks at hadron colliders, Phys. Rev. D 69 (2004) 074027 [hep-ph/0311067].
- [186] R. V. Harlander, K. J. Ozeren and M. Wiesemann, *Higgs plus jet production in bottom quark annihilation at next-to-leading order*, *Phys. Lett. B* **693** (2010) 269 [1007.5411].
- [187] R. Harlander and M. Wiesemann, Jet-veto in bottom-quark induced Higgs production at next-to-next-to-leading order, JHEP 04 (2012) 066 [1111.2182].
- [188] S. Bühler, F. Herzog, A. Lazopoulos and R. Müller, The fully differential hadronic production of a Higgs boson via bottom quark fusion at NNLO, JHEP 07 (2012) 115 [1204.4415].
- [189] R. V. Harlander, S. Liebler and H. Mantler, SusHi: A program for the calculation of Higgs production in gluon fusion and bottom-quark annihilation in the Standard Model and the MSSM, Comput. Phys. Commun. 184 (2013) 1605 [1212.3249].
- [190] M. Wiesemann, R. Frederix, S. Frixione, V. Hirschi, F. Maltoni and P. Torrielli, *Higgs* production in association with bottom quarks, *JHEP* **02** (2015) 132 [1409.5301].
- [191] M. Bonvini, A. S. Papanastasiou and F. J. Tackmann, Resummation and matching of b-quark mass effects in $b\bar{b}H$ production, JHEP 11 (2015) 196 [1508.03288].
- [192] M. Bonvini, A. S. Papanastasiou and F. J. Tackmann, Matched predictions for the $b\bar{b}H$ cross section at the 13 TeV LHC, JHEP 10 (2016) 053 [1605.01733].
- [193] S. Forte, D. Napoletano and M. Ubiali, *Higgs production in bottom-quark fusion in a matched scheme*, *Phys. Lett. B* **751** (2015) 331 [1508.01529].
- [194] S. Forte, D. Napoletano and M. Ubiali, *Higgs production in bottom-quark fusion:* matching beyond leading order, Phys. Lett. B **763** (2016) 190 [1607.00389].
- [195] R. V. Harlander, Higgs production in heavy quark annihilation through next-to-next-to-leading order QCD, Eur. Phys. J. C 76 (2016) 252 [1512.04901].
- [196] M. Lim, F. Maltoni, G. Ridolfi and M. Ubiali, Anatomy of double heavy-quark initiated processes, JHEP **09** (2016) 132 [1605.09411].
- [197] A. H. Ajjath, A. Chakraborty, G. Das, P. Mukherjee and V. Ravindran, Resummed prediction for Higgs boson production through $b\bar{b}$ annihilation at N^3LL , JHEP 11 (2019) 006 [1905.03771].
- [198] G. Das, Higgs rapidity in bottom annihilation at NNLL and beyond, 2306.04561.
- [199] T. Gehrmann and D. Kara, The $Hb\bar{b}$ form factor to three loops in QCD, JHEP **09** (2014) 174 [1407.8114].
- [200] A. Chakraborty, T. Huber, R. N. Lee, A. von Manteuffel, R. M. Schabinger, A. V. Smirnov et al., Hbb vertex at four loops and hard matching coefficients in SCET for various currents, Phys. Rev. D 106 (2022) 074009 [2204.02422].
- [201] C. Duhr, F. Dulat and B. Mistlberger, *Higgs Boson Production in Bottom-Quark Fusion to Third Order in the Strong Coupling*, *Phys. Rev. Lett.* **125** (2020) 051804 [1904.09990].
- [202] C. Duhr, F. Dulat, V. Hirschi and B. Mistlberger, Higgs production in bottom quark fusion: matching the 4- and 5-flavour schemes to third order in the strong coupling, JHEP 08 (2020) 017 [2004.04752].
- [203] R. Mondini and C. Williams, Bottom-induced contributions to Higgs plus jet at next-to-next-to-leading order, JHEP 05 (2021) 045 [2102.05487].

- [204] C. W. Bauer, S. Fleming, D. Pirjol, I. Z. Rothstein and I. W. Stewart, *Hard scattering factorization from effective field theory*, *Phys. Rev. D* **66** (2002) 014017 [hep-ph/0202088].
- [205] P. Pietrulewicz, D. Samitz, A. Spiering and F. J. Tackmann, Factorization and Resummation for Massive Quark Effects in Exclusive Drell-Yan, JHEP 08 (2017) 114 [1703.09702].
- [206] B. Dehnadi, I. Novikov and F. J. Tackmann, The photon energy spectrum in $B \to X_s \gamma$ at $N^3 LL'$, 2211.07663.
- [207] M. A. Ebert, J. K. L. Michel and F. J. Tackmann, Resummation Improved Rapidity Spectrum for Gluon Fusion Higgs Production, JHEP 05 (2017) 088 [1702.00794].
- [208] T. Lübbert, J. Oredsson and M. Stahlhofen, Rapidity renormalized TMD soft and beam functions at two loops, JHEP 03 (2016) 168 [1602.01829].
- [209] Y. Li and H. X. Zhu, Bootstrapping Rapidity Anomalous Dimensions for Transverse-Momentum Resummation, Phys. Rev. Lett. 118 (2017) 022004 [1604.01404].
- [210] G. Billis, M. A. Ebert, J. K. L. Michel and F. J. Tackmann, A toolbox for q_T and θ -jettiness subtractions at N^3LO , Eur. Phys. J. Plus 136 (2021) 214 [1909.00811].
- [211] M.-x. Luo, T.-Z. Yang, H. X. Zhu and Y. J. Zhu, Quark Transverse Parton Distribution at the Next-to-Next-to-Next-to-Leading Order, Phys. Rev. Lett. 124 (2020) 092001 [1912.05778].
- [212] M. A. Ebert, B. Mistlberger and G. Vita, Transverse momentum dependent PDFs at N^3LO , JHEP **09** (2020) 146 [2006.05329].
- [213] S. Moch, J. A. M. Vermaseren and A. Vogt, *The Quark form-factor at higher orders*, *JHEP* **08** (2005) 049 [hep-ph/0507039].
- [214] R. Brüser, Z. L. Liu and M. Stahlhofen, Three-Loop Quark Jet Function, Phys. Rev. Lett. 121 (2018) 072003 [1804.09722].
- [215] A. A. Vladimirov, Correspondence between Soft and Rapidity Anomalous Dimensions, Phys. Rev. Lett. 118 (2017) 062001 [1610.05791].
- [216] G. P. Korchemsky and A. V. Radyushkin, Renormalization of the Wilson Loops Beyond the Leading Order, Nucl. Phys. B283 (1987) 342.
- [217] R. Brüser, A. Grozin, J. M. Henn and M. Stahlhofen, Matter dependence of the four-loop QCD cusp anomalous dimension: from small angles to all angles, JHEP 05 (2019) 186 [1902.05076].
- [218] J. M. Henn, G. P. Korchemsky and B. Mistlberger, The full four-loop cusp anomalous dimension in $\mathcal{N}=4$ super Yang-Mills and QCD, JHEP **04** (2020) 018 [1911.10174].
- [219] A. von Manteuffel, E. Panzer and R. M. Schabinger, Analytic four-loop anomalous dimensions in massless QCD from form factors, Phys. Rev. Lett. 124 (2020) 162001 [2002.04617].
- [220] G. Lustermans, J. K. L. Michel, F. J. Tackmann and W. J. Waalewijn, *Joint two-dimensional resummation in q_T and 0-jettiness at NNLL, JHEP {\bf 03} (2019) 124 [1901.03331].*
- [221] Z. Ligeti, I. W. Stewart and F. J. Tackmann, Treating the b quark distribution function with reliable uncertainties, Phys. Rev. D 78 (2008) 114014 [0807.1926].

- [222] R. Abbate, M. Fickinger, A. H. Hoang, V. Mateu and I. W. Stewart, Thrust at N^3LL with Power Corrections and a Precision Global Fit for $\alpha_s(mZ)$, Phys. Rev. D 83 (2011) 074021 [1006.3080].
- [223] I. W. Stewart, F. J. Tackmann, J. R. Walsh and S. Zuberi, Jet p_T resummation in Higgs production at NNLL' + NNLO, Phys. Rev. D 89 (2014) 054001 [1307.1808].
- [224] M. A. Ebert, J. K. L. Michel, F. J. Tackmann et al., SCETlib: A C++ Package for Numerical Calculations in QCD and Soft-Collinear Effective Theory, DESY-17-099 (2018)
- [225] S. Alioli, C. W. Bauer, C. Berggren, F. J. Tackmann and J. R. Walsh, Drell-Yan production at NNLL'+NNLO matched to parton showers, Phys. Rev. D 92 (2015) 094020 [1508.01475].
- [226] S. Alioli, G. Billis, A. Broggio, A. Gavardi, S. Kallweit, M. A. Lim et al., Refining the GENEVA method for Higgs boson production via gluon fusion, JHEP 05 (2023) 128 [2301.11875].
- [227] S. Frixione, Z. Kunszt and A. Signer, Three jet cross-sections to next-to-leading order, Nucl. Phys. B 467 (1996) 399 [hep-ph/9512328].
- [228] V. Del Duca, C. Duhr, G. Somogyi, F. Tramontano and Z. Trócsányi, *Higgs boson decay into b-quarks at NNLO accuracy*, *JHEP* **04** (2015) 036 [1501.07226].
- [229] S. Alioli, A. Broggio, A. Gavardi, S. Kallweit, M. A. Lim, R. Nagar et al., Resummed predictions for hadronic Higgs boson decays, JHEP 04 (2021) 254 [2009.13533].
- [230] OPENLOOPS 2 collaboration, F. Buccioni, J.-N. Lang, J. M. Lindert, P. Maierhöfer,
 S. Pozzorini, H. Zhang et al., OpenLoops 2, Eur. Phys. J. C 79 (2019) 866 [1907.13071].
- [231] J. Gaunt, M. Stahlhofen, F. J. Tackmann and J. R. Walsh, *N-jettiness Subtractions for NNLO QCD Calculations*, *JHEP* **09** (2015) 058 [1505.04794].
- [232] R. Boughezal, C. Focke, X. Liu and F. Petriello, W-boson production in association with a jet at next-to-next-to-leading order in perturbative QCD, Phys. Rev. Lett. 115 (2015) 062002 [1504.02131].
- [233] N. Deutschmann, F. Maltoni, M. Wiesemann and M. Zaro, *Top-Yukawa contributions to bbH production at the LHC*, *JHEP* **07** (2019) 054 [1808.01660].
- [234] S. Bailey, T. Cridge, L. A. Harland-Lang, A. D. Martin and R. S. Thorne, Parton distributions from LHC, HERA, Tevatron and fixed target data: MSHT20 PDFs, Eur. Phys. J. C 81 (2021) 341 [2012.04684].
- [235] F. J. Tackmann, Beyond Scale Variations: Perturbative Theory Uncertainties from Nuisance Parameters, 2411.18606.
- [236] M. A. Ebert and F. J. Tackmann, Impact of isolation and fiducial cuts on q_T and N-jettiness subtractions, JHEP **03** (2020) 158 [1911.08486].
- [237] S. Alioli, C. W. Bauer, C. J. Berggren, A. Hornig, F. J. Tackmann, C. K. Vermilion et al., Combining Higher-Order Resummation with Multiple NLO Calculations and Parton Showers in GENEVA, JHEP 09 (2013) 120 [1211.7049].
- [238] P. F. Monni, P. Nason, E. Re, M. Wiesemann and G. Zanderighi, *MiNNLO*_{PS}: a new method to match NNLO QCD to parton showers, JHEP **05** (2020) 143 [1908.06987].

- [239] J. M. Campbell, S. Höche, H. T. Li, C. T. Preuss and P. Skands, *Towards NNLO+PS matching with sector showers*, *Phys. Lett. B* **836** (2023) 137614 [2108.07133].
- [240] M. Dasgupta, F. A. Dreyer, K. Hamilton, P. F. Monni, G. P. Salam and G. Soyez, Parton showers beyond leading logarithmic accuracy, Phys. Rev. Lett. 125 (2020) 052002 [2002.11114].
- [241] M. van Beekveld et al., A new standard for the logarithmic accuracy of parton showers, 2406.02661.
- [242] F. Herren, S. Höche, F. Krauss, D. Reichelt and M. Schoenherr, A new approach to color-coherent parton evolution, JHEP 10 (2023) 091 [2208.06057].
- [243] S. Höche, F. Krauss and D. Reichelt, *The Alaric parton shower for hadron colliders*, 2404.14360.
- [244] S. Alioli, A. Broggio, S. Kallweit, M. A. Lim and L. Rottoli, Higgsstrahlung at NNLL'+NNLO matched to parton showers in GENEVA, Phys. Rev. D 100 (2019) 096016 [1909.02026].
- [245] S. Alioli, A. Broggio, A. Gavardi, S. Kallweit, M. A. Lim, R. Nagar et al., Precise predictions for photon pair production matched to parton showers in GENEVA, JHEP 04 (2021) 041 [2010.10498].
- [246] S. Alioli, A. Broggio, A. Gavardi, S. Kallweit, M. A. Lim, R. Nagar et al., Next-to-next-to-leading order event generation for Z boson pair production matched to parton shower, Phys. Lett. B 818 (2021) 136380 [2103.01214].
- [247] T. Cridge, M. A. Lim and R. Nagar, $W\gamma$ production at NNLO+PS accuracy in Geneva, Phys. Lett. B 826 (2022) 136918 [2105.13214].
- [248] S. Alioli, G. Billis, A. Broggio, A. Gavardi, S. Kallweit, M. A. Lim et al., *Double Higgs* production at NNLO interfaced to parton showers in GENEVA, JHEP **06** (2023) 205 [2212.10489].
- [249] S. Alioli, A. Broggio and M. A. Lim, Zero-jettiness resummation for top-quark pair production at the LHC, JHEP **01** (2022) 066 [2111.03632].
- [250] S. Alioli, C. W. Bauer, A. Broggio, A. Gavardi, S. Kallweit, M. A. Lim et al., *Matching NNLO predictions to parton showers using N3LL color-singlet transverse momentum resummation in geneva, Phys. Rev. D* **104** (2021) 094020 [2102.08390].
- [251] P. F. Monni, E. Re and P. Torrielli, *Higgs Transverse-Momentum Resummation in Direct Space*, *Phys. Rev. Lett.* **116** (2016) 242001 [1604.02191].
- [252] W. Bizon, P. F. Monni, E. Re, L. Rottoli and P. Torrielli, Momentum-space resummation for transverse observables and the Higgs p_{\perp} at $N^3LL+NNLO$, JHEP **02** (2018) 108 [1705.09127].
- [253] A. Gavardi, M. A. Lim, S. Alioli and F. J. Tackmann, NNLO+PS W⁺ W production using jet veto resummation at NNLL', JHEP 12 (2023) 069 [2308.11577].
- [254] P. Cal, M. A. Lim, D. J. Scott, F. J. Tackmann and W. J. Waalewijn, Jet veto resummation for STXS H+1-jet bins at aNNLL'+NNLO, 2408.13301.
- [255] P. Nason, A new method for combining NLO QCD with shower Monte Carlo algorithms, JHEP 11 (2004) 040 [hep-ph/0409146].

- [256] L. Buonocore, M. Grazzini, J. Haag, L. Rottoli and C. Savoini, Effective transverse momentum in multiple jet production at hadron colliders, Phys. Rev. D 106 (2022) 014008 [2201.11519].
- [257] C. Biello, A. Sankar, M. Wiesemann and G. Zanderighi, NNLO+PS predictions for Higgs production through bottom-quark annihilation with MINNLO_{PS}, Eur. Phys. J. C 84 (2024) 479 [2402.04025].
- [258] A. J. Larkoski, D. Neill and J. Thaler, Jet Shapes with the Broadening Axis, JHEP **04** (2014) 017 [1401.2158].
- [259] I. W. Stewart, F. J. Tackmann, J. Thaler, C. K. Vermilion and T. F. Wilkason, *XCone: N-jettiness as an Exclusive Cone Jet Algorithm*, *JHEP* **11** (2015) 072 [1508.01516].
- [260] D. Bertolini, D. Kolodrubetz, D. Neill, P. Pietrulewicz, I. W. Stewart, F. J. Tackmann et al., Soft Functions for Generic Jet Algorithms and Observables at Hadron Colliders, JHEP 07 (2017) 099 [1704.08262].
- [261] J. Thaler and K. Van Tilburg, *Identifying Boosted Objects with N-subjettiness*, *JHEP* **03** (2011) 015 [1011.2268].
- [262] J. Thaler and K. Van Tilburg, Maximizing Boosted Top Identification by Minimizing N-subjettiness, JHEP **02** (2012) 093 [1108.2701].
- [263] A. Banfi, G. P. Salam and G. Zanderighi, Resummed event shapes at hadron hadron colliders, JHEP 08 (2004) 062 [hep-ph/0407287].
- [264] S. Dulat, T.-J. Hou, J. Gao, M. Guzzi, J. Huston, P. Nadolsky et al., New parton distribution functions from a global analysis of quantum chromodynamics, Phys. Rev. D 93 (2016) 033006 [1506.07443].
- [265] T. Liu and A. A. Penin, High-Energy Limit of QCD beyond the Sudakov Approximation, Phys. Rev. Lett. 119 (2017) 262001 [1709.01092].
- [266] T. Liu and A. Penin, *High-Energy Limit of Mass-Suppressed Amplitudes in Gauge Theories*, *JHEP* **11** (2018) 158 [1809.04950].
- [267] R. Akhoury, H. Wang and O. I. Yakovlev, On the Resummation of large QCD logarithms in Higgs —> gamma gamma decay, Phys. Rev. D 64 (2001) 113008 [hep-ph/0102105].
- [268] A. A. Penin, High-Energy Limit of Quantum Electrodynamics beyond Sudakov Approximation, Phys. Lett. B 745 (2015) 69 [1412.0671].
- [269] Z. L. Liu and M. Neubert, Factorization at subleading power and endpoint-divergent convolutions in $h \to \gamma \gamma$ decay, JHEP **04** (2020) 033 [1912.08818].
- [270] Z. L. Liu, B. Mecaj, M. Neubert and X. Wang, Factorization at subleading power and endpoint divergences in $h \to \gamma \gamma$ decay. Part II. Renormalization and scale evolution, JHEP **01** (2021) 077 [2009.06779].
- [271] Z. L. Liu, M. Neubert, M. Schnubel and X. Wang, Factorization at Next-to-Leading Power and Endpoint Divergences in $gg \to h$ Production, 2212.10447.
- [272] M. Beneke, Y. Ji and X. Wang, Renormalization of the next-to-leading-power $\gamma\gamma \to h$ and $gg \to h$ soft quark functions, JHEP **05** (2024) 246 [2403.17738].
- [273] M. Stahlhofen, Resummation of quark mass effects in $gg \to h$, in SCET 2015: XIIth annual workshop on Soft-Collinear Effective Theory, (2015).

- [274] M. Beneke and V. A. Smirnov, Asymptotic expansion of Feynman integrals near threshold, Nucl. Phys. B **522** (1998) 321 [hep-ph/9711391].
- [275] V. A. Smirnov and E. R. Rakhmetov, The Strategy of regions for asymptotic expansion of two loop vertex Feynman diagrams, Theor. Math. Phys. 120 (1999) 870 [hep-ph/9812529].
- [276] V. A. Smirnov, Applied asymptotic expansions in momenta and masses, Springer Tracts Mod. Phys. 177 (2002) 1.
- [277] M. Spira, A. Djouadi, D. Graudenz and P. M. Zerwas, *Higgs boson production at the LHC*, Nucl. Phys. B **453** (1995) 17 [hep-ph/9504378].
- [278] R. K. Ellis, I. Hinchliffe, M. Soldate and J. J. van der Bij, Higgs Decay to tau+ tau-: A Possible Signature of Intermediate Mass Higgs Bosons at high energy hadron colliders, Nucl. Phys. B 297 (1988) 221.
- [279] C. F. Berger, C. Marcantonini, I. W. Stewart, F. J. Tackmann and W. J. Waalewijn, *Higgs Production with a Central Jet Veto at NNLL+NNLO*, *JHEP* **04** (2011) 092 [1012.4480].
- [280] U. Baur and E. W. N. Glover, Higgs Boson Production at Large Transverse Momentum in Hadronic Collisions, Nucl. Phys. B 339 (1990) 38.
- [281] N. Isgur and M. B. Wise, Weak Decays of Heavy Mesons in the Static Quark Approximation, Phys. Lett. B 232 (1989) 113.
- [282] N. Isgur and M. B. Wise, WEAK TRANSITION FORM-FACTORS BETWEEN HEAVY MESONS, Phys. Lett. B 237 (1990) 527.
- [283] J. G. Korner and G. Thompson, The Heavy mass limit in field theory and the heavy quark effective theory, Phys. Lett. B **264** (1991) 185.
- [284] S. Fleming, A. H. Hoang, S. Mantry and I. W. Stewart, *Jets from massive unstable particles: Top-mass determination*, *Phys. Rev. D* **77** (2008) 074010 [hep-ph/0703207].
- [285] R. L. Jaffe and L. Randall, Heavy quark fragmentation into heavy mesons, Nucl. Phys. B 412 (1994) 79 [hep-ph/9306201].
- [286] A. F. Falk and M. E. Peskin, Production, decay, and polarization of excited heavy hadrons, Phys. Rev. D 49 (1994) 3320 [hep-ph/9308241].
- [287] M. Neubert, Factorization analysis for the fragmentation functions of hadrons containing a heavy quark, 0706.2136.
- [288] M. Fickinger, S. Fleming, C. Kim and E. Mereghetti, Effective field theory approach to heavy quark fragmentation, JHEP 11 (2016) 095 [1606.07737].
- [289] M. G. Echevarria, Y. Makris and I. Scimemi, Quarkonium TMD fragmentation functions in NRQCD, JHEP 10 (2020) 164 [2007.05547].
- [290] M. G. Echevarria, Proper TMD factorization for quarkonia production: $pp \to \eta_{c,b}$ as a study case, JHEP 10 (2019) 144 [1907.06494].
- [291] S. Fleming, Y. Makris and T. Mehen, An effective field theory approach to quarkonium at small transverse momentum, JHEP **04** (2020) 122 [1910.03586].
- [292] B. Mele and P. Nason, The Fragmentation function for heavy quarks in QCD, Nucl. Phys. B 361 (1991) 626.
- [293] A. H. Hoang, A. Pathak, P. Pietrulewicz and I. W. Stewart, *Hard Matching for Boosted Tops at Two Loops*, *JHEP* **12** (2015) 059 [1508.04137].

- [294] A. H. Hoang, C. Lepenik and M. Stahlhofen, Two-Loop Massive Quark Jet Functions in SCET, JHEP 08 (2019) 112 [1904.12839].
- [295] A. Schafer and O. V. Teryaev, Sum rules for the T odd fragmentation functions, Phys. Rev. D 61 (2000) 077903 [hep-ph/9908412].
- [296] S. Meissner, A. Metz and D. Pitonyak, Momentum sum rules for fragmentation functions, Phys. Lett. B 690 (2010) 296 [1002.4393].
- [297] I. I. Balitsky and V. M. Braun, The Nonlocal operator expansion for inclusive particle production in e+ e- annihilation, Nucl. Phys. B **361** (1991) 93.
- [298] V. Moos and A. Vladimirov, Calculation of transverse momentum dependent distributions beyond the leading power, JHEP 12 (2020) 145 [2008.01744].
- [299] K.-m. Cheung and T. C. Yuan, Spin alignment in the production of vector mesons with charm and/or beauty via heavy quark fragmentation, Phys. Rev. D 50 (1994) 3181 [hep-ph/9405261].
- [300] T. C. Yuan, Helicity probabilities for heavy quark fragmentation into excited mesons, Phys. Rev. D 51 (1995) 4830 [hep-ph/9407341].
- [301] P. M. Nadolsky, N. Kidonakis, F. I. Olness and C. P. Yuan, Resummation of transverse momentum and mass logarithms in DIS heavy quark production, Phys. Rev. D 67 (2003) 074015 [hep-ph/0210082].
- [302] M.-x. Luo, T.-Z. Yang, H. X. Zhu and Y. J. Zhu, *Unpolarized quark and gluon TMD PDFs and FFs at N*³LO, *JHEP* **06** (2021) 115 [2012.03256].
- [303] M. A. Ebert, B. Mistlberger and G. Vita, TMD fragmentation functions at N^3LO , JHEP 07 (2021) 121 [2012.07853].
- [304] K. Melnikov and A. Mitov, Perturbative heavy quark fragmentation function through $\mathcal{O}(\alpha_s^2)$, Phys. Rev. D **70** (2004) 034027 [hep-ph/0404143].
- [305] A. Mitov, Perturbative heavy quark fragmentation function through $\mathcal{O}(\alpha_s^2)$: Gluon initiated contribution, Phys. Rev. D 71 (2005) 054021 [hep-ph/0410205].
- [306] F. Yuan and J. Zhou, Collins Fragmentation and the Single Transverse Spin Asymmetry, Phys. Rev. Lett. 103 (2009) 052001 [0903.4680].
- [307] M. A. Ebert, J. K. L. Michel, I. W. Stewart and Z. Sun, Disentangling long and short distances in momentum-space TMDs, JHEP 07 (2022) 129 [2201.07237].
- [308] NNPDF collaboration, R. D. Ball, A. Candido, J. Cruz-Martinez, S. Forte, T. Giani, F. Hekhorn et al., Evidence for intrinsic charm quarks in the proton, Nature 608 (2022) 483 [2208.08372].
- [309] M. Guzzi, T. J. Hobbs, K. Xie, J. Huston, P. Nadolsky and C. P. Yuan, *The persistent nonperturbative charm enigma*, 2211.01387.
- [310] BLFQ collaboration, Z. Zhu, T. Peng, Z. Hu, S. Xu, C. Mondal, X. Zhao et al., Transverse momentum structure of strange and charmed baryons: a light-front Hamiltonian approach, 2304.05058.
- [311] A. Bacchetta and A. Prokudin, Evolution of the helicity and transversity Transverse-Momentum-Dependent parton distributions, Nucl. Phys. B 875 (2013) 536 [1303.2129].

- [312] D. Gutierrez-Reyes, I. Scimemi and A. Vladimirov, Transverse momentum dependent transversely polarized distributions at next-to-next-to-leading-order, JHEP 07 (2018) 172 [1805.07243].
- [313] R. L. Jaffe and A. Manohar, NUCLEAR GLUONOMETRY, Phys. Lett. B 223 (1989) 218.
- [314] A. Bacchetta, D. Boer, M. Diehl and P. J. Mulders, Matches and mismatches in the descriptions of semi-inclusive processes at low and high transverse momentum, JHEP 08 (2008) 023 [0803.0227].
- [315] A. K. Leibovich, Z. Ligeti and M. B. Wise, Comment on quark masses in SCET, Phys. Lett. B 564 (2003) 231 [hep-ph/0303099].
- [316] J. C. Collins, Leading twist single transverse-spin asymmetries: Drell-Yan and deep inelastic scattering, Phys. Lett. B 536 (2002) 43 [hep-ph/0204004].
- [317] M. Diehl, R. Nagar and P. Plößl, Quark mass effects in double parton distributions, 2212.07736.
- [318] Z. L. Liu, B. Mecaj, M. Neubert and X. Wang, Factorization at subleading power, Sudakov resummation, and endpoint divergences in soft-collinear effective theory, Phys. Rev. D 104 (2021) 014004 [2009.04456].
- [319] T. Liu, S. Modi and A. A. Penin, Higgs boson production and quark scattering amplitudes at high energy through the next-to-next-to-leading power in quark mass, JHEP **02** (2022) 170 [2111.01820].
- [320] NNPDF collaboration, R. D. Ball et al., Parton distributions from high-precision collider data, Eur. Phys. J. C 77 (2017) 663 [1706.00428].
- [321] NNPDF collaboration, E. R. Nocera, R. D. Ball, S. Forte, G. Ridolfi and J. Rojo, A first unbiased global determination of polarized PDFs and their uncertainties, Nucl. Phys. B 887 (2014) 276 [1406.5539].
- [322] M. Beneke, M. Garny, S. Jaskiewicz, R. Szafron, L. Vernazza and J. Wang, Large-x resummation of off-diagonal deep-inelastic parton scattering from d-dimensional refactorization, JHEP 10 (2020) 196 [2008.04943].
- [323] D. Boer, R. Jakob and P. J. Mulders, Asymmetries in polarized hadron production in e+e- annihilation up to order 1/Q, Nucl. Phys. B **504** (1997) 345 [hep-ph/9702281].
- [324] A. Metz and A. Vossen, Parton Fragmentation Functions, Prog. Part. Nucl. Phys. 91 (2016) 136 [1607.02521].
- [325] Belle-II collaboration, J. Kahn, The Belle II Experiment, in CERN-BINP Workshop for Young Scientists in e+e- Colliders, pp. 45–54, 2017, DOI.
- [326] BABAR collaboration, J. P. Lees et al., Measurement of Collins asymmetries in inclusive production of charged pion pairs in e⁺e⁻ annihilation at BABAR, Phys. Rev. D **90** (2014) 052003 [1309.5278].
- [327] BABAR collaboration, J. P. Lees et al., Collins asymmetries in inclusive charged KK and $K\pi$ pairs produced in e^+e^- annihilation, Phys. Rev. D **92** (2015) 111101 [1506.05864].
- [328] Belle collaboration, K. Abe et al., Measurement of azimuthal asymmetries in inclusive production of hadron pairs in e+ e- annihilation at Belle, Phys. Rev. Lett. **96** (2006) 232002 [hep-ex/0507063].

- [329] Belle collaboration, R. Seidl et al., Measurement of Azimuthal Asymmetries in Inclusive Production of Hadron Pairs in e+e- Annihilation at $s^{**}(1/2) = 10.58$ -GeV, Phys. Rev. D 78 (2008) 032011 [0805.2975].
- [330] Belle collaboration, H. Li et al., Azimuthal asymmetries of back-to-back $\pi^{\pm} (\pi^0, \eta, \pi^{\pm})$ pairs in e^+e^- annihilation, Phys. Rev. D **100** (2019) 092008 [1909.01857].
- [331] X.-d. Ji, J.-P. Ma and F. Yuan, QCD factorization for spin-dependent cross sections in DIS and Drell-Yan processes at low transverse momentum, Phys. Lett. B **597** (2004) 299 [hep-ph/0405085].
- [332] J. M. Campbell et al., Event Generators for High-Energy Physics Experiments, in Snowmass 2021, 3, 2022, 2203.11110.
- [333] D. Callos, Z.-B. Kang and J. Terry, Extracting the transverse momentum dependent polarizing fragmentation functions, Phys. Rev. D 102 (2020) 096007 [2003.04828].
- [334] Z.-B. Kang, J. Terry, A. Vossen, Q. Xu and J. Zhang, Transverse Lambda production at the future Electron-Ion Collider, Phys. Rev. D 105 (2022) 094033 [2108.05383].
- [335] Z.-B. Kang, X. Liu, F. Ringer and H. Xing, The transverse momentum distribution of hadrons within jets, JHEP 11 (2017) 068 [1705.08443].
- [336] Z.-B. Kang, K. Lee and F. Zhao, *Polarized jet fragmentation functions*, *Phys. Lett. B* **809** (2020) 135756 [2005.02398].
- [337] Y. Makris, D. Neill and V. Vaidya, *Probing Transverse-Momentum Dependent Evolution With Groomed Jets*, *JHEP* **07** (2018) 167 [1712.07653].
- [338] Y. Makris and V. Vaidya, Transverse Momentum Spectra at Threshold for Groomed Heavy Quark Jets, JHEP 10 (2018) 019 [1807.09805].
- [339] I. Scimemi and A. Vladimirov, Matching of transverse momentum dependent distributions at twist-3, Eur. Phys. J. C 78 (2018) 802 [1804.08148].
- [340] L. Bonino, M. Cacciari and G. Stagnitto, Heavy Quark Fragmentation in e^+e^- Collisions to NNLO+NNLL Accuracy in Perturbative QCD, 2312.12519.
- [341] M. Copeland, S. Fleming, R. Gupta, R. Hodges and T. Mehen, *Polarized TMD fragmentation functions for J/\psi production, Phys. Rev. D 109 (2024) 054017 [2308.08605].*
- [342] M. G. Echevarria, S. F. Romera and I. Scimemi, Gluon TMD fragmentation function into quarkonium, JHEP 12 (2023) 181 [2308.12356].
- [343] M. Copeland, S. Fleming, R. Gupta, R. Hodges and T. Mehen, Polarized J/ψ production in semi-inclusive DIS at large Q^2 : Comparing quark fragmentation and photon-gluon fusion, 2310.13737.
- [344] L. Dai, C. Kim and A. K. Leibovich, *Heavy quark transverse momentum dependent fragmentation*, 2310.19207.
- [345] S. Caletti, A. Ghira and S. Marzani, On heavy-flavour jets with Soft Drop, Eur. Phys. J. C 84 (2024) 212 [2312.11623].
- [346] F. Hekhorn, G. Magni, E. R. Nocera, T. R. Rabemananjara, J. Rojo, A. Schaus et al., Heavy quarks in polarised deep-inelastic scattering at the electron-ion collider, Eur. Phys. J. C 84 (2024) 189 [2401.10127].

- [347] Y.-T. Chien, R. Rahn, D. Y. Shao, W. J. Waalewijn and B. Wu, *Precision boson-jet azimuthal decorrelation at hadron colliders*, *JHEP* **02** (2023) 256 [2205.05104].
- [348] M.-S. Gao, Z.-B. Kang, D. Y. Shao, J. Terry and C. Zhang, QCD resummation of dijet azimuthal decorrelations in pp and pA collisions, JHEP 10 (2023) 013 [2306.09317].
- [349] C. Lepenik and V. Mateu, NLO Massive Event-Shape Differential and Cumulative Distributions, JHEP 03 (2020) 024 [1912.08211].
- [350] A. Bris, V. Mateu and M. Preisser, Massive event-shape distributions at N^2LL , JHEP **09** (2020) 132 [2006.06383].
- [351] A. Bris, N. G. Gracia and V. Mateu, *NLO oriented event-shape distributions for massive quarks*, *JHEP* **02** (2023) 247 [2211.10239].
- [352] I. Moult and H. X. Zhu, Simplicity from Recoil: The Three-Loop Soft Function and Factorization for the Energy-Energy Correlation, JHEP 08 (2018) 160 [1801.02627].
- [353] H. T. Li, Y. Makris and I. Vitev, Energy-energy correlators in Deep Inelastic Scattering, Phys. Rev. D 103 (2021) 094005 [2102.05669].
- [354] Z.-B. Kang, K. Lee, D. Y. Shao and F. Zhao, Probing transverse momentum dependent structures with azimuthal dependence of energy correlators, JHEP **03** (2024) 153 [2310.15159].
- [355] A. Gao, H. T. Li, I. Moult and H. X. Zhu, Precision QCD Event Shapes at Hadron Colliders: The Transverse Energy-Energy Correlator in the Back-to-Back Limit, Phys. Rev. Lett. 123 (2019) 062001 [1901.04497].
- [356] A. Gao, H. T. Li, I. Moult and H. X. Zhu, The Transverse Energy-Energy Correlator at Next-to-Next-to-Next-to-Leading Logarithm, 2312.16408.
- [357] J. Collins and T. C. Rogers, Definition of fragmentation functions and the violation of sum rules, Phys. Rev. D 109 (2024) 016006 [2309.03346].
- [358] B. Mele and P. Nason, Next-to-leading QCD calculation of the heavy quark fragmentation function, Phys. Lett. B 245 (1990) 635.
- [359] M. Cacciari, P. Nason and C. Oleari, *Crossing heavy-flavor thresholds in fragmentation functions*, *JHEP* **10** (2005) 034 [hep-ph/0504192].
- [360] A. Jain, M. Procura and W. J. Waalewijn, Fully-Unintegrated Parton Distribution and Fragmentation Functions at Perturbative k_T , JHEP **04** (2012) 132 [1110.0839].
- [361] J. R. Gaunt and M. Stahlhofen, The fully-differential gluon beam function at NNLO, JHEP 07 (2020) 234 [2004.11915].
- [362] S. Catani, S. Dittmaier and Z. Trocsanyi, One loop singular behavior of QCD and SUSY QCD amplitudes with massive partons, Phys. Lett. B **500** (2001) 149 [hep-ph/0011222].
- [363] M. Cacciari and E. Gardi, Heavy quark fragmentation, Nucl. Phys. B 664 (2003) 299 [hep-ph/0301047].
- [364] G. Lustermans, J. K. L. Michel and F. J. Tackmann, Generalized Threshold Factorization with Full Collinear Dynamics, 1908.00985.
- [365] T. Huber and D. Maitre, HypExp: A Mathematica package for expanding hypergeometric functions around integer-valued parameters, Comput. Phys. Commun. 175 (2006) 122 [hep-ph/0507094].

- [366] P. Pietrulewicz and M. Stahlhofen, Two-loop bottom mass effects on the Higgs transverse momentum spectrum in top-induced gluon fusion, 2302.06623.
- [367] S. Moch, J. A. M. Vermaseren and A. Vogt, *Three-loop results for quark and gluon form-factors*, *Phys. Lett. B* **625** (2005) 245 [hep-ph/0508055].
- [368] A. Idilbi, X.-d. Ji and F. Yuan, Resummation of threshold logarithms in effective field theory for DIS, Drell-Yan and Higgs production, Nucl. Phys. B 753 (2006) 42 [hep-ph/0605068].
- [369] T. Becher, M. Neubert and B. D. Pecjak, Factorization and Momentum-Space Resummation in Deep-Inelastic Scattering, JHEP 01 (2007) 076 [hep-ph/0607228].
- [370] W. Bernreuther, R. Bonciani, T. Gehrmann, R. Heinesch, T. Leineweber, P. Mastrolia et al., Two-loop QCD corrections to the heavy quark form-factors: The Vector contributions, Nucl. Phys. B 706 (2005) 245 [hep-ph/0406046].
- [371] J. Gluza, A. Mitov, S. Moch and T. Riemann, The QCD form factor of heavy quarks at NNLO, JHEP 07 (2009) 001 [0905.1137].
- [372] P. Pietrulewicz, S. Gritschacher, A. H. Hoang, I. Jemos and V. Mateu, Variable Flavor Number Scheme for Final State Jets in Thrust, Phys. Rev. D 90 (2014) 114001 [1405.4860].
- [373] M. G. Echevarria, A. Idilbi and I. Scimemi, Unified treatment of the QCD evolution of all (un-)polarized transverse momentum dependent functions: Collins function as a study case, Phys. Rev. D 90 (2014) 014003 [1402.0869].
- [374] J. McGowan, T. Cridge, L. A. Harland-Lang and R. S. Thorne, Approximate N³LO parton distribution functions with theoretical uncertainties: MSHT20aN³LO PDFs, Eur. Phys. J. C 83 (2023) 185 [2207.04739].
- [375] T.-J. Hou et al., New CTEQ global analysis of quantum chromodynamics with high-precision data from the LHC, Phys. Rev. D 103 (2021) 014013 [1912.10053].

Acknowledgments

First, I would like to thank my PhD advisor, Frank Tackmann, for his supervision and support during these three and a half years at DESY. I benefited greatly from countless physics discussions that helped me grow as a physicist. I particularly value that he always made time to discuss, whether it was about a technical detail or a more fundamental physics question. He consistently provided guidance when needed while also allowing me the freedom to pursue my own ideas. Additionally, I really appreciated the collaborative and friendly working environment he fosters in his group. I also want to thank Gudrid Moortgat-Pick for agreeing to co-supervise this thesis.

I am grateful to Alessandro Gavardi, Philip Keicher, Kyle Lee, Matthew Lim, Giulia Marinelli, Johannes Michel, Adi Pathak, Peter Plößl, and Zhiquan Sun for their helpful comments on this thesis. A special thanks goes to Philip for solving my numerous LaTeX problems. Furthermore, I want to thank Pedro Cal, Kyle Lee, Matthew Lim, Johannes Michel, and Iain Stewart for their support and advice, as well as for the interesting and enjoyable physics discussions.

I also want to thank everyone on floor 1b and frequent visitors for the fun times and discussions we shared during lunch, coffee breaks, and after work. This includes Roger Balsach, Pedro Cal, Tom Cridge, Bahman Denahdi, Markus Diehl, Florian Fabry, Alessandro Gavardi, Oskar Grocholski, Matthew Lim, Max Löschner, Giulia Marinelli, Krzysztof Mekala, Johannes Michel, Adi Pathak, Peter Plößl, Simone Rodini, Frank Tackmann, and Kerstin Tackmann. Thank you all for creating such a great working environment.

I am also grateful to the Center for Theoretical Physics at MIT for their hospitality, where parts of the research in this thesis were completed. In particular, I want to thank Iain Stewart, who invited me and acted as my advisor during my time at MIT, and Zhiquan Sun, who made me feel at home in Boston from my very first day. I also want to thank all my friends from MIT, especially Zhiquan, Felix, Wenzer, Patrick, Johannes, and Kyle, for an unforgettable experience. A special thanks again to Zhiquan for the wonderful memories and friendship that began in Boston and continued in Vienna, Hamburg, Kitzbühel, and Madrid – and will continue in Berkeley and Bern. I am also grateful to the Fulbright Foundation for providing me with the opportunity to spend five months at MIT.

Lastly, I am deeply grateful to Philip for his unwavering support—essentially being a homemaker with a full-time job— over the past months, for coming to Hamburg with me, and for joining me again in my next step. You are simply the best. Finally, I want to thank my parents, Arnd and Irina, and my sister, Mascha, for their never-ending support.